FABRICATION OF SILICON NANOPOROUS HUMIDITY SENSORS AND THEIR ELECTRICAL AND SPECTROSCOPIC CHARACTERIZATIONS

by

Seda Oğuz Aytekin

Graduate School of Natural and Applied Sciences

in partial fulfillment of the requirements for the degree of

Doctor of Philosophy

in

Physics Department

Yeditepe University

2014

FABRICATION OF SILICON NANOPOROUS HUMIDITY SENSORS AND THEIR ELECTRICAL AND SPECTROSCOPIC CHARACTERIZATIONS

APPROVED BY:

Prof. Dr. Rabia Ince ....
(Supervisor)

Prof. Dr. Hikmet Yükselici ....

Prof. Dr. Hilmi Ünlü ....

Assoc. Prof. Dr. Ertan Akşahin ....

Assist. Prof. Dr.Vildan Üstoğlu Ünal ....

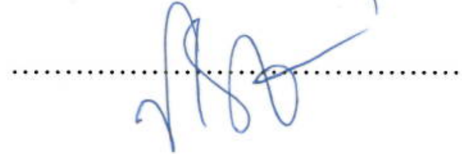

DATE OF APPROVAL: ...... / ...... / ....

ACKNOWLEDGEMENTS

I'd like to take this opportunity to thank a number of people for their contributions to this thesis over the years academic and otherwise, you all have my deepest appreciation.

First and foremost I would like to thank my Ph. D. supervisor Professor Doctor Rabia Ince who not only provided advice, direction and discussion on each aspect of this thesis but also gave freely of her time, encouragement and support from start to finish without which the completion of this work would have been impossible.

I would like to thank also Dr. Alp Osman Kodolbaş for his advice and contribution to this thesis. I'd also like to thank the colleagues from Materials Institute of TÜBİTAK Marmara Research Centre for allowing me access to their laboratory and equipment used throughout this thesis.

I would like to thank also Dr. Ersin Kayahan for his advice and fruitfull discussion on the thesis work, and allowing photoluminescence measurements to be made. I would like to thank also Örsan Aytekin for his fruitfull discussion on the image processing.

Nuray Karaböce, and Dr. Özlem Pehlivan for their advice and friendship.

None of these studies would have been possible without the endless support of my husband, Hasan Serkan Aytekin. Finally, I would like to thank to my mother Nevin Tuncay Oğuz, my father Ali Şuuri Oğuz, and my sister Şeyda Oğuz and Ceyda Oğuz for their continued support.

This thesis is dedicated to my son Emre Kağan Aytekin.

ABSTRACT

FABRICATION OF SILICON NANOPOROUS HUMIDITY SENSORS AND THEIR ELECTRICAL AND SPECTROSCOPIC CHARACTERIZATIONS

This thesis is concerned with fabrication of nanometer to micrometer sized porous silicon structures utilized as a relative humidity sensor by electrochemical anodization method, and Raman spectrometry, image processing, SEM, photoluminescence, AFM, current-voltage and capacitance-voltage experimental methods were used to investigate both structural and electrical properties of porous silicon structures formed in sensors.

Electrochemical anodization conditions affecting the porous structure have been investigated with regard to the fabrication process steps and its effect on the sensitivity of the relative humidity sensors made from porous silicon material.

Nanometer sized structure is analysed by different methods to determine optimized pore diameters for the best sensitive relative humidity sensor; A new analysis method was realised, quantified and reported based on Raman spectroscopy together with the assisting techniques such as SEM, image processing, photoluminescence and AFM in this thesis. This experimental method was then applied to porous silicon samples fabricated in this thesis work and a new application of this experiment was realised. This work shows that using Raman spectroscopy measurements it is possible to determine that the structure contains nanometer-sized porous silicon structures within a sample. It is also possible to state that long-term stability of the sensor in other words its mechanical degradation and relative humidity sensitivity were determined by Raman spectroscopy technique in place of capacitance measuremets. The ability to tailor the porous structure and pore size of the material is investigated, and the parameters effecting the structure and size for a material containing nanometer-sized porous structure are defined and reported.

ÖZET

SİLİSYUM NANOGÖZENEKLİ BAĞIL NEM ALGILAYICI ÜRETİMİ VE ELEKTRİKSEL VE SPEKTROSKOPİK KARAKTERİZASYONU

Bu tez çalışması, nanometre ile mikrometre boyutunda gözenekli silisyum yapının bağıl nem sensörü olarak elektrokimyasal yöntemle üretilmesini ve Raman spektroskopi, görüntü işleme, taramalı elektron mikroskobu, fotolüminesans, atomik güç mikroskobu, akım-gerilim ve kapasitans-gerilim deneysel yöntemleri ile sensör malzemesinde kullanılan gözenekli silisyum malzemenin yapısal ve elektriksel incelenmesini içerir.

Üretim aşamalarından biri olan ve gözenekli silisyum yapıyı etkileyen elektrokimyasal anodizasyon parametreleri incelemiştir. Bu parametrelerin gözenekli silisyum malzemeden üretilen bağıl nem sensörünün duyarlılık değerine etkisi incelenmiştir.

Nanometre boyutundaki yapı farklı metotlar kullanılarak en uygun gözenek çapını ve dolayısıyla en duyarlı bağıl nem sensörünü belirleyebilmek amacıyla analiz edilmiştir. Bu tez çalışmasında, Raman spektroskopi yöntemi ile SEM, görüntü işleme, fotolüminesans ve AFM gibi diğer yardımcı tekniklere dayanan yeni bir analiz metodu gerçekleştirilmiş, analiz sonuçları verilmiş ve değerlendirmeler yapılmıştır. Bu deneysel yöntem, bu tez çalışmasında üretilen tüm gözenekli silisyum numunelere uygulanmış ve bu yöntemin uygulaması gerçekleştirilmiştir. Bu çalışma ile Raman spektroskopi ölçümleri kullanılarak sensördeki nanometre boyutunda yapının belirlenmesinin mümkün olduğu gösterilmiştir. Sensörün uzun dönem karalılığının ya da başka bir ifadeyle yapısal bozulmasının ve bağıl nem duyarlılığının belirlenmesinin kapasitans ölçümleri yerine Raman spektrokopi tekniği ile mümkün olduğu ortaya konmuştur. Gözenekli yapının ve malzemedeki gözenek boyutunun değiştirilmesinin yapılabilirliği araştırılmış ve nanometre boyutunda gözenekli yapıya sahip malzemenin yapısını ve boyutunu etkileyen parametreler tanımlanmış ve raporlanmıştır.

TABLE OF CONTENTS

ACKNOWLEDGEMENTS iii
ABSTRACT iv
ÖZET v
TABLE OF CONTENTS vi
LIST OF FIGURES x
LIST OF TABLES xix
LIST OF TABLES xix
LIST OF SYMBOLS / ABBREVIATIONS xxii
1. INTRODUCTION 1
1.1. HUMIDITY DEFINITIONS 1
1.2. CORRELATION BETWEEN MEASUREMENT TECHNIQUES 3
1.3. HUMIDITY MEASURING INSTRUMENTS 4
1.3.1. Relative Humidity 5
1.3.2. Dew/Frost-Point Temperature 7
1.3.3. Parts Per Million 9
1.4. HUMIDITY MEASURING INSTRUMENTS ACCORDING TO THEIR SENSOR MATERIAL 9
1.4.1. Polymer-Based Humidity Sensors 9
1.4.1.1. Conducting/Semiconducting Polymers 15
1.4.1.2. Hydrophobic Polymer-Based Capacitive Sensors 18
1.4.2. Ceramic Humidity Sensors 19
1.4.3. Metal-oxide Humidity Sensors 21
1.4.3.1. TiO_2 Humidity Sensors 23
1.4.3.2. SiO_2 Humidity Sensors 24
1.4.3.3. Humidity Sensors Based on Spinel Compounds 24
1.4.3.4. Other Ceramic Sensing Materials 25
1.4.4. Semiconducting Humidity Sensors 25
1.4.4.1. SnO_2 26
1.4.4.2. Perovskite Compounds 27
1.4.4.3. In_2O_3 28

1.4.4.4. Other Semiconducting Sensing Materials 28
1.5. CHARACTERISTICS OF HUMIDITY MEASURING INSTRUMENTS 28
1.6. COMPARISON AND ADVANTAGES/DISADVANTAGES OF HUMIDITY MEASURING INSTRUMENTS.. 29
1.7. INTEGRATED HUMIDITY MEASURING INSTRUMENTS 32
1.8. POROUS SILICON INTEGRATED HUMIDITY MEASURING INSTRUMENTS.. 33
1.9. LITERATURE REVIEW OF POROUS SILICON HUMIDITY/GAS SENSORS 36
2. THEORETICAL INFORMATION ON POROUS SILICON FORMATION THEORIES AND CHARACTERIZATION TECHNIQUES 49
2.1. POROUS SILICON FORMATION 49
2.2. POROUS SILICON MORPHOLOGY AND FORMATION THEORIES 64
2.2.1. Formation theories and morphology related with microporous structure 68
2.2.1.1. Quantum Confinement... 70
2.2.2. Formation theories and morphology related with mesoporous structure 72
2.2.3. Formation theories and morphology related with macroporous structure 75
2.3. CHARACTERIZATION OF THE STRUCTURE 77
2.4. OPTICAL MICROSCOPY.. 77
2.5. SCANNING ELECTRON MICROSCOPY 79
2.6. IMAGE PROCESSING 81
2.7. RAMAN SPECTROSCOPY 82
2.7.1. Raman Spectroscopy Principles... 84
2.7.2. Raman Spectroscopy of Crystalline Material 87
2.7.3. Stokes and Anti-Stokes Raman Scattering 88
2.7.4. Phonons.. 90
2.7.4.1. Acoustic Phonons 91
2.7.4.2. Optical Phonons 91
2.7.4.3. Longitudinal- and Transverse- Acoustic/Optical Phonons 92
2.7.5. Phonon Dispersion Curves.. 93

2.7.6. Size effects in quantum dots ... 95
2.7.7. Rule of Mutual Exclusion ... 96
2.7.8. Microscopic Theory of Raman Scattering ... 96
2.7.9. Types of Raman Spectra from Porous Silicon ... 98
2.8. PHOTOLUMINESCENCE SPECTROSCOPY ... 98
2.8.1. Photoluminescence Theory ... 98
2.9. ELECTRICAL CHARACTERIZATION ... 106
2.9.1. Current versus Voltage Measurements ... 106
2.9.2. Capacitance Measurements ... 106
2.9.3. Capacitance Modeling ... 108
3. EXPERIMENTAL PREPARATION OF NANOPOROUS SILICON SAMPLES FOR RELATIVE HUMIDITY SENSING ... 111
3.1. POROUS SILICON BASED MATERIALS FOR HUMIDITY SENSING ... 111
3.2. POROUS SILICON PREPARATION ... 111
3.2.1. Preparation of porous silicon for analysis in this thesis ... 112
3.2.2. Chemical Cleaning ... 113
3.2.3. Thermal Evaporation ... 114
3.3. FORMATION OF POROUS SILICON ... 114
3.4. DESIGN OF ANODIZATION CELL SYSTEM ... 114
4. RESULTS AND DISCUSSION ... 119
4.1. CURRENT VERSUS VOLTAGE (I-V) MEASUREMENT SYSTEM ... 119
4.1.1. Measured I-V curves for varying HF molarities ... 120
4.1.2. Oscillation process during anodization ... 127
4.1.3. Final drying treatment ... 128
4.1.4. Surface passivation ... 132
4.1.5. Thermal evaporation of interdigitated top electrode ... 135
4.2. OPTICAL MICROSCOPE IMAGES OF POROUS SILICON SAMPLES ... 137
4.2.1. Optical Microscope Images of Porous Silicon Samples with <100> wafer orientation, 1-30 Ω.cm, at various anodization current densities and durations ... 138
4.2.2. Optical Microscope Images of Porous Silicon Samples with <111> wafer orientation, 2-20 Ω.cm, and HF:C_2H_5OH concentration of % 25:25:50 ... 141

4.2.3. Scanning Electron Microscope (SEM) Images of Porous Silicon Samples 142
4.2.4. SEM Images of Porous Silicon Samples: Set-A 144
4.2.5. SEM Images of Porous Silicon Samples: Set-B 146
4.2.6. SEM Images of Porous Silicon Samples: Set-C 148
4.3. IMAGE PROCESSING 150
4.4. STRUCTURAL CHARACTERIZATION OF POROUS SILICON SAMPLES USING RAMAN SPECTRUM ANALYSIS 153
4.5. ANALYSIS OF POROUS SILICON SAMPLES USING MATLAB IMAGE PROCESSING OF SCANNING ELECTRON MICROSCOPE (SEM) AND RAMAN SPECTRUM ANALYSIS 153
4.5.1. Raman Peak Wavenumber Variation 159
4.5.2. Raman Peak Width (FWHM) 164
4.5.3. Raman Peak Shift vs FWHM 164
4.5.4. Raman Intensity Variation 166
4.5.5. Comparison of Raman and SEM Results 173
4.6. CAPACITANCE MEASUREMENT RESULTS 174
4.6.1. Equivalent Circuit Model for Porous Silicon Humidity Sensor 175
4.6.2. Response Determination by Variiying Frequencies 176
4.6.3. Sensitivity Determination of Sensors 178
4.6.4. Response Time Determination of Sensors 178
4.6.5. Capacitance Measurements of Sensors 179
4.6.6. Capacitance and Raman Spectra Intensity Change Over Three Months To Gauge Mechanical Stability 181
4.6.7. Comparison of Capacitance Sensitivity and Raman Results 182
4.7. AFM ANALYSIS 184
4.8. PHOTOLUMINESCENCE ANALYSIS 189
5. CONCLUSION 196
6. REFERENCES 203
APPENDIX A: MATLAB IMAGE PROCESSING CODES FOR DIAMETER DETERMINATION 224

LIST OF FIGURES

Figure 1. 1 Scale charts of different humidity measurement parameters at 21 °C air temperature ... 4

Figure 1. 2 Humidity measuring instrument whose measurement principle was based on elongation of substances used as a sensor ... 5

Figure 1. 3 Schematic of electrolytic relative humidity sensor [1] ... 6

Figure 1. 4 A psychrometer with two ideally identical thermometers [2] ... 7

Figure 1. 5 Sensing mechanism of chilled mirror optical dew-point meters ... 8

Figure 1. 6 Commercial resistive-type relative humidity sensors [18] ... 11

Figure 1. 7 Commercial capacitive-type relative humidity sensor [18] ... 12

Figure 1. 8 Brief illustration of the Grotthuss mechanism ... 20

Figure 1. 9 Multi-layer structure of condensed water [5] ... 20

Figure 1.10 Periodic structure of anodic aluminum oxide (AAO) [5] ... 22

Figure 1.11 Two possible mechanism for “donor effect” for n-type. (a) Electrons are attracted by the adsorbed water molecules to the semiconductor surface and the energy bands are bended; (b) Electrons are released by the competitive adsorption. Figure modified, original taken from [5] ... 26

Figure 1.12 Pore radius values calculated from the Kelvin equation for relative humidity values ranging from 0 %rh to 100 %rh ... 35

Figure 1. 13 SEM photograph and device photoluminescence spectrum obtained under a blue light which has an excitation wavelength smaller than 500 nm. Pores diameter and distance between pores are 90 nm and 400 nm, respectively ... 42

Figure 1. 14 Typical SEM surface micrograph of Si-NPPA ... 44

Figure 1. 15 Photograph of the fabricated porous silicon sensor 45

Figure 2. 1 Isotropic and anisotropic etching behaviour of silicon 49

Figure 2. 2 Reaction of porous silicon formation in anodization solution containing HF acid and water (Adapted from [144]) 58

Figure 2. 3 Representative I-V curve for p-type silicon in aqueous HF acid solution (Adapted from [116]) 59

Figure 2. 4 Representative anodic I-V relationships for silicon in HF showing the salient regions of dissolution. In region A pore formation occurs, and in region C silicon electropolishes (Adapted from [112]) 60

Figure 2. 5 Formation conditions and responsible effects for porous formation 65

Figure 2. 6 Effects responsible for the formation of pore wall passivation and passivation breakdown at the pore tip with resulting porous structure (Adapted from Ref. [163]) 66

Figure 2. 7 Energy band diagrams of crystalline silicon, porous silicon, and silicon nanocrystallites (Adapted from Ref. [153]) 67

Figure 2. 8 (1a) Sketch of the interface between porous silicon and bulk silicon. There are two possibilities for hole to cross the interface as shown as arrows. (1b) The corresponding energy band diagrams. The energy required for a hole to enter the anodization solution via the porous silicon structure is larger by E_q than the energy that is required to enter the anodization solution directly. (2a) Photons of energy larger than E_{PS} will be absorbed in the topmost region of a porous silicon layer and will generate an electron hole pair. The electron will move to the bulk if an anodic bias is applied whereas the hole will enter the anodization solution and promote further thinning of the porous structure. (2b) The corresponding energy band diagram 69

Figure 2. 9 Changes in energy levels of a metal with the reduced number of atoms of the material: (a) valence band of bulk metal; (b) large metal cluster

of 100 atoms with opening of band gap; (c) small metal cluster containing three atoms 71

Figure 2. 10 The current density distribution at pore tip 73

Figure 2. 11 The schematic of optical microscope in (a) bright field and (b) dark field modes 78

Figure 2. 12 Schematic of scanning electron microscopy [176] 80

Figure 2. 13 Schematic of Raman spectroscopy [183] 82

Figure 2. 14 Stokes and anti-Stokes Raman scattering mechanisms 89

Figure 2. 15 For a longitudinal wave (a), the displacement is in the direction of motion. For a transverse wave (b), the displacement is transverse to the direction of motion 92

Figure 2. 16 Dispersion curves of silicon (a) in the direction (001) and Raman spectrum of amorphous silicon (b) (Adapted from [205]) 94

Figure 2. 17 Photoluminescence mechanism of indirect band gap semiconductors 99

Figure 2. 18 The schematic of photoluminescence spectroscopy 102

Figure 2. 19 The schematic of porous silicon structure 109

Figure 3. 1 Typical device structure 112

Figure 3. 2 Ohmic contact using Aluminum on crystalline silicon 114

Figure 3. 3 Home-made Teflon anodization cell and platinum spiral shaped electrode 115

Figure 3. 4 A silicon wafer diced into nine pieces 116

Figure 3. 5 Drawing of the Teflon anodization cell 116

Figure 3. 6 Technical drawing of home-made Teflon anodization cell 118

Figure 4. 1 Home-made computer controlled anodization and I-V measurement system 119

Figure 4. 2 Measured I-V curve for p-type silicon in aqueous HF acid solution for a silicon substrate 121

Figure 4. 3 I-V graph from 1 V to 15 V of 1 % HF molarity 123

Figure 4. 4 I-V graph from 1 V to 15 V of 1 % HF molarity 124

Figure 4. 5 I-V graph from -15 V to 15 V of 2 % HF molarity 125

Figure 4. 6 Typical anodic I-V relationship for silicon in ethanoic HF acid showing the salient regions of dissolution. In region A, pore formation occurs, and in region C silicon electropolishes. Region B is a transition zone between regions A and C. Scale units and zeros are arbitrarily chosen and depend on silicon sample and experimental conditions (Adapted from [112]) 126

Figure 4. 7 Pentane drying steps: (a) distilled water rinsing of porous silicon sample (b) ethanol rinsing of porous silicon sample – porous silicon sample was seen at the bottom of the home-made anodization cell (c) pentane rinsing of porous silicon sample after removal of the sample from the anodization cell 130

Figure 4. 8 Silicon samples before etching 131

Figure 4. 9 Silicon samples after etching with porous structure 131

Figure 4. 10 Technical drawing of multiple top electrodes for thermal evaporation of aluminum on porous silicon samples to form humidity sensor 136

Figure 4. 11 Detailed technical drawing of single top electrode 137

Figure 4. 12 Diagram of imaginary areas where images obtained from optical microscope from a porous silicon sample.. 138

Figure 4. 13 Optical microscope images of porous silicon structure with diameters around 2 μm obtained with a current value of 50 mA applied for 5 min 138

Figure 4. 14 Optical microscope images of porous structure with diameters around 1 μm obtained with a current value of 5 mA applied for 4 min (sample number: PS019) 139

Figure 4. 15 Optical microscope images of porous structure with diameters around 1 μm obtained with a current value of 5 mA applied for 5 min 139

Figure 4. 16 Optical microscope images of porous structure with diameters around 1 μm obtained with a current value of 5 mA applied for 6 min (sample number: PS022) 139

Figure 4. 17 Optical microscope images of porous structure with diameters around 1 μm obtained with a current value of 5 mA applied for 6 min (sample number: PS020) 140

Figure 4. 18 Optical microscope images of porous structure with diameters around 1 μm obtained with a current value of 5 mA applied for 30 min (sample number: PS050) 140

Figure 4. 19 Optical microscope images of porous structure with diameters around 1 μm obtained with a current value of 5 mA applied for 30 min, HF:C_2H_5OH concentration of % 12.5:12.5:75 (sample number: PS051) 140

Figure 4. 20 Optical microscope images of porous structure with diameters around 1 μm obtained with a current value of 10 mA applied for 5 min (sample number: PS009) 141

Figure 4. 21 Optical microscope images of porous structure with diameters around 1 μm obtained with a current value of 10 mA applied for 5 min (sample number: PS003); Dark-field mode 141

Figure 4. 22 Optical microscope images (bright field mode) of porous structure with diameters around 1 μm obtained with a current value of 10 mA applied for 5 min (sample number: PS003); Bright-field mode 142

Figure 4. 23 SEM images of porous silicon sample with 50,000 times magnification. Sample was etched at constant voltage of 1 Volt with duration of 5 minutes and annealed at the furnace 142

Figure 4. 24 SEM images of the same porous silicon sample with 150,000 times magnification showing an approximately 10 nm holes 143

Figure 4. 25 Cross section schematic of porous silicon structure formed inside the silicon wafer with a 500 μm thickness 143

Figure 4. 26 Scanning electron microscope top view images from porous silicon sample surfaces A1, A2, A3, A4, and A5, formed at anodization times of 15 min., 30 min., 45 min., 60 min., and 75 min. respectively............. 144

Figure 4. 27 Scanning electron microscope cross section images from porous silicon samples of A1, A2, A3, A4, and A5 145

Figure 4. 28 Top view SEM images of the porous silicon sample surfaces (B1, B2, B3, B4, and B5) with 75,000 times magnification showing granular-type porous structure.. 146

Figure 4. 29 Cross section SEM images of the porous silicon samples (B1, B2, B3, B4, and B5) with 75,000 times magnification showing granular-type porous structure... 147

Figure 4. 30 Top view SEM images of the porous silicon samples (C1, C2, C3, C4, and C5) with 75,000 times magnification showing granular-type porous structure... 148

Figure 4. 31 Cross section SEM images of the porous silicon samples (C1, C2, C3, C4, and C5) with 75,000 times magnification showing granular-type porous structure... 149

Figure 4. 32 (a) Original image A1 (b) Contrast enhanced and filtered image of A1 . 150

Figure 4. 33 Porous silicon samples (A1, A2, A3, A4, A5) and their corresponding histogram graphics showing granul diameter distribution 151

Figure 4. 34 Original Raman spectra of A series samples 160

Figure 4. 35 Diameter of structures from Raman and MATLAB analysis 163

Figure 4. 36 Raman spectra peak shift versus calculated crystallite sizes compared with the literature [181] 163

Figure 4. 37 Experimental Raman peak shift values versus calculated FWHM values 164

Figure 4. 38 Raman peak shift versus FWHM values found in literature [179-181, 246] 165

Figure 4. 39 Raman spectra FWHM values versus calculated crystallite sizes compared with the literature [181] 165

Figure 4. 40 Raman spectra of samples A1, A2, A3, A4, A5 167

Figure 4. 41 Raman spectra of samples B1, B2, B3, B4, and B5 167

Figure 4. 42 Raman spectra of samples C1, C2, C3, C4, and C5 168

Figure 4. 43 Raman spectra of samples anodized at constant current density of 10 $mA.cm^{-2}$ with different anodization times 169

Figure 4. 44 Raman peak intensities together with the depth of the porous silicon structure 170

Figure 4. 45 Raman spectra intensity values and depths of porous structures of the set-A samples 171

Figure 4. 46 Raman spectra intensity degradation over 3 months 171

Figure 4. 47 Raman spectra intensity of sample A3 at 55 %rh and 95 %rh 172

Figure 4. 48 Raman spectra intensity of sample A4 at 55 %rh and 95 %rh 172

Figure 4. 49 Raman spectra intensity of sample A5 at 55 %rh and 95 %rh 173

Figure 4. 50 Fabricated porous silicon humidity sensors 174

Figure 4. 51 Measurement setup for electrical caharacterization of porous silicon humidity sensor in a humidity generator using an LCR meter. 175

Figure 4. 52 Equivalent circuit model for porous silicon humidity sensor 175

Figure 4. 53 Capacitor action for humidity sensing of porous silicon sensor 176

Figure 4. 54 Frequency sweep versus capacitance values of porous silicon relative humidity sensors at 23 °C and 50 %rh. 176

Figure 4. 55 Relative humidity versus capacitance graph of porous silicon humidity sensor at three specific frequency values around 1 kHz. 177

Figure 4. 56 Relative humidity versus dissipation factor graph of porous silicon humidity sensor at three specific frequency values around 1 kHz. 178

Figure 4. 57 Response time measurements of the sensors at varying RH values from 5 %rh to 95 %rh 179

Figure 4. 58 Capacitance values of A-series samples from 0 %rh to 95 %rh 180

Figure 4. 59 AFM of sample A1 with surface roughness values 185

Figure 4. 60 AFM of sample A2 with surface roughness values 185

Figure 4. 61 AFM of sample A3 with surface roughness values 186

Figure 4. 62 AFM of sample A4 with surface roughness values 186

Figure 4. 63 AFM of sample A5 with surface roughness values 186

Figure 4. 64 AFM results of samples A1 to A5, B1 to B5, and C1 to C5.................... 188

Figure 4. 65 Average roughness values from AFM analysis of samples A1 to A5,

B1 to B5, and C1 to C5 188

Figure 4. 66 Photoluminescence spectra of samples from A1 to A5 189

Figure 4. 67 Normalized photoluminescence spectra of samples from A1 to A5 190

Figure 4. 68 Photoluminescence spectra of samples from B1 to B5 191

Figure 4. 69 Normalized photoluminescence spectra of samples from B1 to B5 191

Figure 4. 70 Photoluminescence spectra of samples from C1 to C5 192

Figure 4. 71 Normalized photoluminescence spectra of samples from C1 to C5 193

Figure 4. 72 Anodization time versus particle size calculated from photoluminescence parameters 194

LIST OF TABLES

Table 1. 1 Humidity definitions and units 2

Table 1. 2 Comparison of humidity sensors 29

Table 1. 3 Advantages and disadvantages of capacitive-type humidity sensors 30

Table 1. 4 Advantages and disadvantages of resistive-type humidity sensors 31

Table 1. 5 Advantages and disadvantages of optical-type humidity sensors.............. 31

Table 1. 6 Advantages and disadvantages of psychrometers............ 32

Table 2. 1 Parameter dependences on the properties of porous layer......................... 63

Table 2. 2 Porous silicon photoluminescence bands 102

Table 4. 1 Surface passivation techniques for porous silicon 132

Table 4. 2 Surface passivation techniques for porous silicon 135

Table 4. 3 Formation conditions of porous silicon samples (set-A) 146

Table 4. 4 Formation conditions of porous silicon samples (set B).......................... 147

Table 4. 5 Formation conditions of porous silicon samples (set C).......................... 149

Table 4. 6 Diameter values of granular silicon crystallites and holes in porous silicon samples calculated from image processing of SEM images (set A) 152

Table 4. 7 Formation conditions of porous silicon samples prepared from c-Si wafer with <100> orientation 155

Table 4. 8. Formation conditions of porous silicon samples prepared from c-Si wafer with <111> orientation. 156

Table 4. 9. Raman spectrum evaluation of the porous silicon samples prepared from c-Si wafer with <100> orientation. 156

Table 4. 10. Raman spectrum evaluation of the porous silicon samples prepared from p-type c-Si wafer with <111> orientation. 157

Table 4. 11. Porous silicon samples prepared at different conditions 157

Table 4. 12. Three set of porous silicon samples prepared at different conditions...... 158

Table 4. 13. Raman spectroscopy and MATLAB Image Processing Analysis of Porous silicon samples prepared at different conditions. (calculated using [179] and 181]).. 159

Table 4. 14. Raman (a) Diameter values obtained from MATLAB Image Processing (b) Diameter values calculated from Raman spectra analysis... 161

Table 4. 15. Raman depth of porous silicon structures in the samples at different anodization times obtained from cross section images obtained from SEM 169

Table 4. 16. Capacitance values of porous silicon relative humidity sensors at different anodization times 180

Table 4. 17. Capacitance change of samples over three months with corresponding percentage deteoriation values of mechanical structure 181

Table 4. 18. Peak intensity degradation of Raman spectra from porous silicon humidity sensors fabricated at different anodization times 183

Table 4. 19. Sensitivity of Raman spectroscopy and capacitance measurements and their ratio values... 184

Table 4. 20. Average roughness values of samples anodized at different current densities and anodization times 187

Table 4. 21. Diameter values calculated using photoluminescence parameters 190

Table 4. 22. Diameter values calculated using photoluminescence parameters 192

Table 4. 23. Diameter values calculated using photoluminescence parameters 193

LIST OF SYMBOLS / ABBREVIATIONS

AFM	Atomic force microscope
BCB	Divinyl siloxane benzocyclobutene
BSE	Backscattered electrons
c-Si	Crystalline silicon
C-V	Capacitance versus voltage
CAB	Cellulose acetate butyrate
CB	Conduction band
DI	Deionized
DP	Dew-point
e_w	Water vapor pressure
EDP	Ethylene diamine pyrochatechol
FP	Frost-point
GLAD	Glancing angle deposition
h	Absolute humidity
HF	Hydrofluoric acid
FWHM	Full width at half maximum
HMDSN	Hexamethyldisilazane
HNA	Hydrofluoric nitric acid
HNAA	HF/nitric/acetic acid
IDE	Interdigitated electrode

I-V	Current versus voltage
IPN	Interpenetrating polymer network
ITO	Indium tin oxide
JPSi	Critical current density
LCR	Inductance (L), capacitance (C), and resistance (R)
LED	Light emitting diode
LA	Longitudinal acoustic phonons
LO	Longitudinal optical phonons
LPCVD	Low pressure chemical vapor deposition
NPPA	Nano porous pillar array
OCP	Open circuit potential
PANA	Poly (anthranilic acid)
PANI	Polyaniline
PDEB	Poly(p-diethynylbenzene)
PECVD	Plasma enhanced chemical vapor deposition
PES	Polyethersulphone
PETT	Poly(ethyleneterephthalate)
PL	Photoluminescence
PMMA	Poly(methyl methacrylate)
PPMV	Parts per million by volume
PPMW	Parts per million by weight

PSF	Polysulfone
PSi	Porous silicon
PVA	Polyvinyl alcohol
PVC	Poly(vinyl crotonate)
RCA	Radio Corporation of America
QC	Quantum confinement
RH	Relative humidity
SAW	Surface acoustic wave
SCR	Space charge region
SEM	Scanning electron microscopy
SNC	Silicon nano-crystallites
SNP	Silicon nano-particles
t	Air temperature
TA	Transverse acoustic phonons
TC-PSi	Thermally carbonized porous silicon
TMAH	Tetra methyl ammonium hydroxide
TO	Transverse optical phonons
UIPAC	International Union of Pure and Applied Chemistry
UV	Ultraviolet
VB	Valence band
W	Space charge region width

1. INTRODUCTION

1.1. HUMIDITY DEFINITIONS

Maintenance, realisation, and dissemination of humidity is a primary thermodynamic metrology service, since it is must be closely monitored along with temperature for all primary and industrial measurements. Humidity metrology is a critical requirement in science: hydrology, environmental studies, meteorology, and forecasting for climate studies. In addition, it has a wide range of applications in society: the food processing industry, air-conditioning, and horticulture to name a few.

Humidity is the amount of water vapor contained in the atmosphere or in any gas. Since water or ice can evaporate at any temperature existing on earth, water vapor is always present. Humidity or the amount of water vapor values in air depends on the temperature and pressure. In other words, as the temperature increases, the amount of water vapor that air can hold increases. At the maximum value of the water vapor content, the air or gas is full of water vapor and is said to be saturated. At this contidition, air temperature and pressure are said to be the saturation temperature and saturation pressure. Humidity can be expressed as relative humidity in relative value or percentage, absolute humidity and dew-point temperature.

Relative humidity is a measure for the amount of water vapor at a specified temperature relative to the maximum amount of water vapor at same temperature. Relative humidity value of 50 %rh means that the air or any gas is capable of holding only the half of the water vapor content that it can possibly hold at the specified temperature and pressure. If air has 100 %rh relative humidity, then air is said to be fully saturated with water vapor. In this saturated condition, air can hold maximum amount of water vapor and its relative humidity value is 100 %rh at fixed temperature and pressure values. For example, saturated air (i.e. 100 %rh) at 23 °C can hold just the absolute humidity value of 20.7 $g \cdot m^{-3}$.

Table 1. 1 Humidity definitions and units

Definition	Abbreviation - Symbol	Unit
Relative humidity	RH	%rh
Air temperature	t	°C
Dew-point temperature	DPT, t	°C
Frost- point temperature	FPT, t	°C
Parts per million by volume	PPM_V	-
Parts per million by weight	PPM_W	-
Water vapor pressure	WVP, e	Pa
Absolute humidity	AH, h	$g{\cdot}m^{-3}$

Absolute humidity is the mass of water vapor present in unit volume of moist air. Absolute humidity in air ranges from 5 $g{\cdot}m^{-3}$ to 588 $g{\cdot}m^{-3}$ when the air is saturated at a temperature of 0 °C and 100 °C, respectively. The absolute humidity changes as air temperature or pressure changes.

When an air having a specific water vapor amount is passed over a polished metal surface whose temperature is gradually decreased, air will condense at specific temperature value on the surface. This specific temperature is the dew-point temperature, where condensation of water vapor in air and evaporation of water over the metal surface are in thermal equilibrium. At that temperature air is saturated with respect to liquid water [1].

Dew-point temperature values can be easily converted to other humidity parameters, such as relative humidity, if the air temperature is measured simultaneously. Since measurements are made with temperature sensors, this technique offers the best reproducibility and uncertainty over all humidity measuring instruments. Although it offers lowest uncertainty in humidity measurements, measurements require a qualified person to operate the dew-point meter. The parameters, such as pressure and flow rate

of the system, will affect the measurement results directly. Therefore, if those parameters are not taken into consideration, erroneous results occur inevitably.

Psychrometer is composed of two identical thermometers. One of the sensors surrounded with a moistened wick, while othe was just measuring the air temperature. Evaporation of water from the thermometer sensor by a propeller resulted depression in temperature value, as compared with the thermometer measuring air temperature without any water on its sensor. Depression value is proportional to the air humidity value. Moistened sensor is named as wet-bulb thermometer, while the other is named as dry-bulb thermometer.

1.2. CORRELATION BETWEEN MEASUREMENT TECHNIQUES

The correlation among Relative Humidity (RH), Parts per Million by volume or weight (PPM_V, PPM_W), and the Dew/Frost-Point (DP/FP) temperature is shown in Figure 1.1. The blue double ended arrow shows the relative humidity range from 10 %rh to 100 %rh at air temperature of 21 °C.

While RH values are meaningful in the range of higher humidity values, PPM_V or PPM_W values are meaningful in the range of lower humidity values. In addition, DP/FP temperature and water vapor pressure values cover all the humidity range that is they are meaningful in the whole range. Therefore, relative humidity is constantly used for ease understanding not only for daily life but also for atmospheric or climatic conditioning measurements.

For trace humidity measurement, PPM_v, PPM_w or DP/FP temperature would be better to use for meaningful representation of humidity values, which are related with the absolute amount of water vapor in a gas or air.

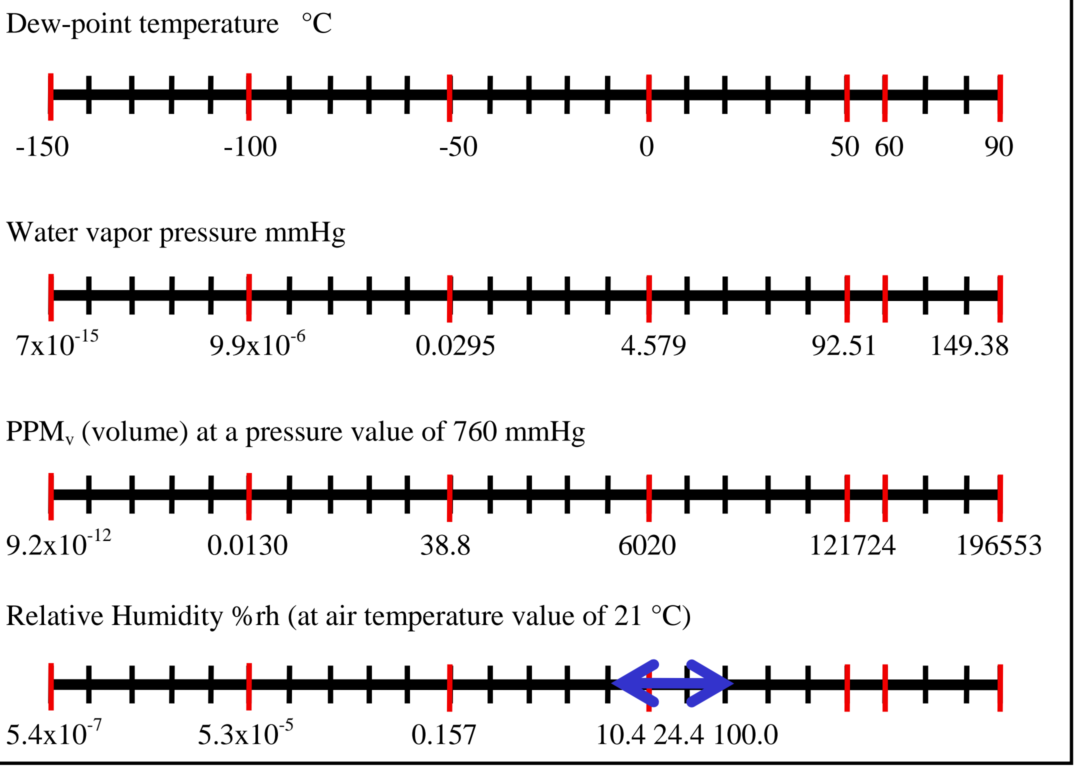

Figure 1. 1 Scale charts of different humidity measurement parameters at 21 °C air temperature

1.3. HUMIDITY MEASURING INSTRUMENTS

Humidity sensors can be divided into categories according to humidity parameters to be measured or according to their sensor material.

Humidity sensors can be divided into three categories according to humidity parameters to be measured:

- Relative humidity
- Dew/Frost-point temperature
- Parts per million

Devices related with each measurement parameter will be described in detail below.

1.3.1. Relative Humidity

Relative humidity can be measured in several methods, including elongation of human hair or nylon film with humidity, wet/dry-bulb method with temperature depression by water evaporation due to humidity, and semiconductor sensor method.

In the 1400's Leonardo daVinci invented the first primitive humidity measuring instrument without any specific denifition of humidity. In 1664, Francesco Folli invented first practical hygrometer. In 1783, Horace Bénédict de Saussure invented a hygrometer that uses human hair to measure humidity. In 1820, John Frederic Daniell invented first dew-point hygrometer using electrical resistance.

The measurement principle of the first humidity measuring instruments was based on the change in the mechanical properties of substances related with water vapor, such as elongation as depicted in Figure 1.2.

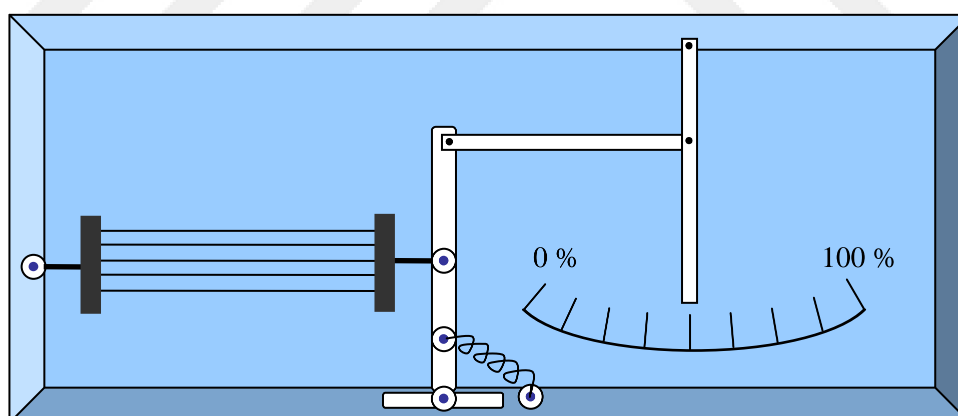

Figure 1. 2 Humidity measuring instrument whose measurement principle was based on elongation of substances used as a sensor

Although such instruments are still in use they are not preferred as reference humidity measuring instruments since calibration of these instruments is sensitive to mechanical shocks and they also suffer from metal fatique in the prolonged usage.

The first electrolytic relative humidity sensors were developed using lithium chloride cells in the 1930's was depicted in Figure 1.3. Although an electrical signal was drawn from these instruments, they had complicated calibration procedures due to their measuring principle.

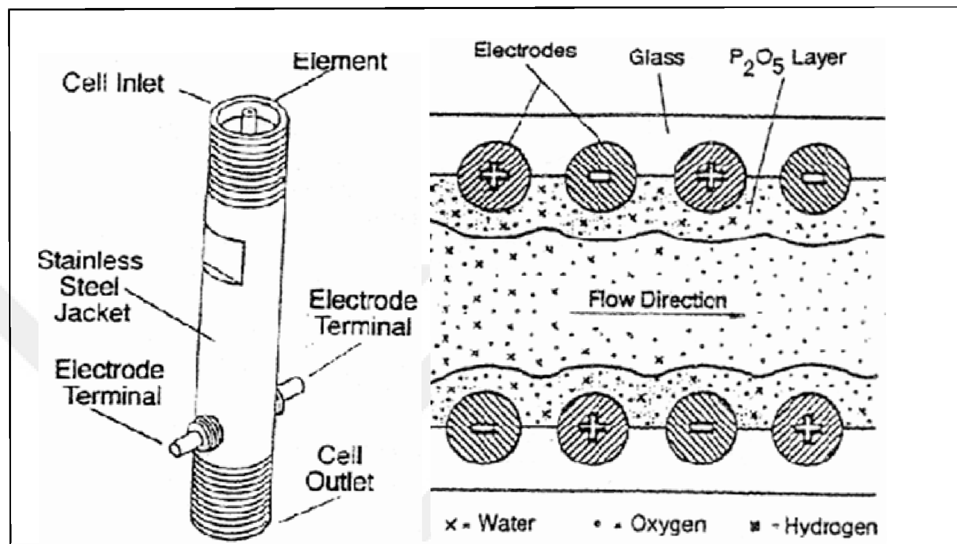

Figure 1. 3 Schematic of electrolytic relative humidity sensor [1]

Hygrometers with either capacitive or resistive type humidity sensors are the most widely used relative humidity measuring instruments in the world. Both type of sensor will be described in the next section extensively.

A secondary level of humidity instruments are psychrometers whose measuring principle is based on evaporation of water vapor.

Psychrometers consist of two ideally identical thermometers namely wet-bulb thermometer and dry-bulb thermometer; one is covered with a cotton wick moistened with distilled water while other thermometer is kept dry to measure air temperature. The former is called as wet-bulb temperature and the latter dry-bulb temperature. The overall system has a propeller to maintain constant air flow over wet-bulb thermometer, which causes a depression in temperature value by evaporative cooling.

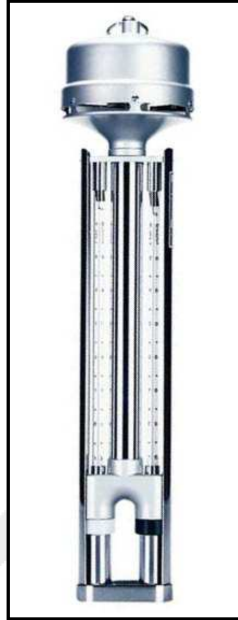

Figure 1. 4 A psychrometer with two ideally identical thermometers [2]

Temperature values measured from both thermometers are used to calculate not only relative humidity, but also other humidity parameters and also some of the thermodynamic parameters related with water vapor, such as specific enthalpy of water vapor. Psychrometric charts are also used for parameter conversions.

1.3.2. Dew/Frost-Point Temperature

There are mainly two types of devices measuring dew-point temperature:

- Chilled mirror dew-point meters
- Metal-oxide sensor based dew-point meters

Another type of humidity measuring device is dew-point meters whose measuring principles are based on condensation of water vapor in a carrier gas (typically air) and then temperature of metal surface where condensation forms are measured as dew-point temperature.

Condensation type dew-point meters are also called as optical dew-point meters, chilled mirror dew-point meters, or chilled mirror hygrometers.

While these instruments are highly accurate and used for primary level calibrations they do not only require regular maintenance but also need a qualified person to operate them. In order to operate this instrument, it must be connected by proper fittings to a pipeline through which carrier gas including water vapor is flowing. They are also used in humidity chambers if their sensors can be separated from the main device. These sensors are operated in both end of the dew/frost-point temperature scale. In addition, these instruments are large and expensive for automation systems with respect to hygrometers [3].

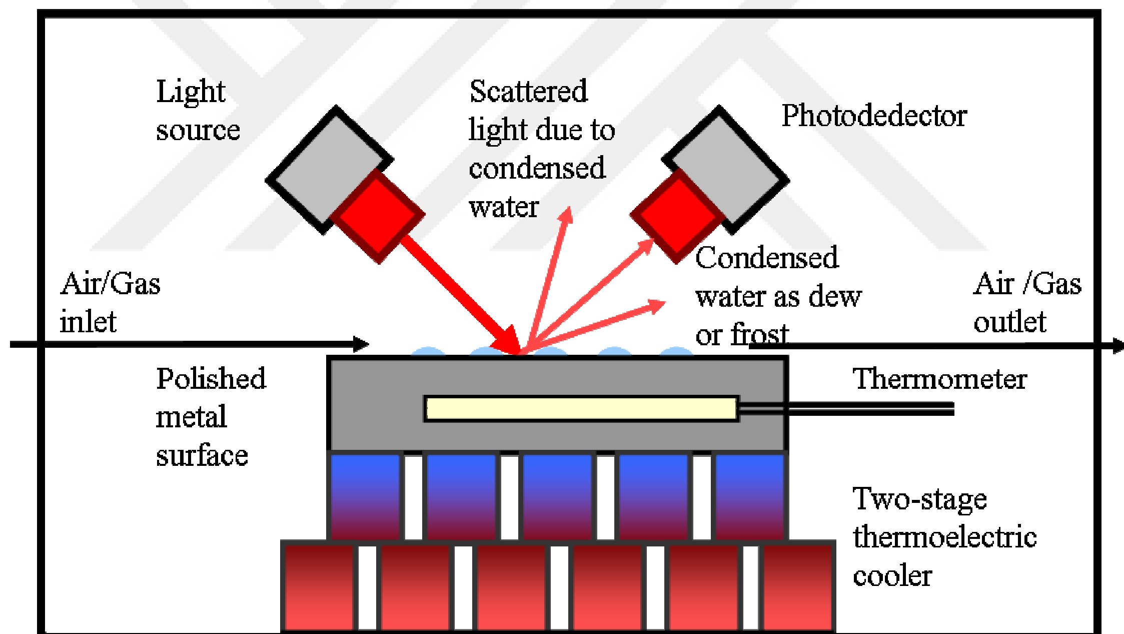

Figure 1. 5 Sensing mechanism of chilled mirror optical dew-point meters

Aluminum-oxide sensor based dew-point meters whose measuring principle based on sensing of water vapor pressure are also used if uncertainty is of second concern. Besides, their operation is more straightforward and they can be used in automation systems. They are used in pipelines with a proper housing or directly in humidity chambers. These sensors must be protected from high humidity values which causes

irreversible results, and finally malfunctioning of the device. These sensors are mostly designed for dew/frost-point temperatures below 10 °C.

1.3.3. Parts Per Million

Parts per million (PPM) represents either water vapor content by volume fraction which is represented as PPM_V or if multiplied by the ratio of the molecular weight of water to that of air, water vapor content by weight fraction which is represented as PPM_W.

Measurements in PPM is rather difficult than relative humidity measurements although it is an absolute measurement. It has extensive applications in industry especially for trace humidity measurement.

1.4. HUMIDITY MEASURING INSTRUMENTS ACCORDING TO THEIR SENSOR MATERIAL

Humidity sensors can be divided into four categories, according to their sensor material. Sensor material can be one of the following:

- Polymer-based
- Ceramic sensing
- Metal-oxide sensing
- Semiconducting sensing materials

1.4.1. Polymer-Based Humidity Sensors

Organic polymers are macromolecules in which a unit structure repeats. Most of the polymers are carbon-hydride compounds or their derivatives. The carbon atoms link each other one by one forming a long chain called the backbone of the polymer. Functional groups are rooted on the backbone. It could be either single atoms such as oxygen or halogen or molecular groups such as –COOH, or $–NO_2$. The functional groups, along with the basic structure of the backbone, determine the chemical and physical properties of the polymers [4, 5].

Artificial polymers are synthesized from monomers that are small molecules. Copolymers are polymers synthesized from two or more different kinds of monomers.

Polymeric humidity sensors have been extensively studied in research areas. They also have been applied in industry for more than 30 years. Most of the sensors are based on porous polymer films thinner than millimeters and their sensing principle is quite similar to that of ceramic sensors. The film is filled with micro-pores for water vapor condensation and some of the measurable physical properties change due to the water absorption.

Almost all of the humidity sensors based on polymers operate at room temperature, due to polymers' high sensitivity to heat. Polymers containing phosphonium have been developed and utilized as a high humidity sensor or dew-point sensor [6, 7]. Crosslinked polyelectrolyte humidity-sensitive films derived from two mutually reactive copolymers have also been developed for humidity sensing [8]. Polymeric electrolyte systems have been used in humidity sensor devices based on variation of the electrical conductivity with water vapor. Conductive polymer-based humidity sensors are attracting considerable attention in research laboratories and industries [9]. In addition, polymeric humidity sensors other than electrical impedance measurements (conductance and capacitance), such as piezoresistive and surface wave acoustic (SAW) devices, are other well known.

Piezoresistive humidity sensor operation relies on the humidity-induced swelling of thin polyimide layers [10, 11]. The shift in the SAW velocity in a SAW device owing to the changes in mass loading, conductivity, permittivity, and viscosity over the SAW path can be employed in sensing applications. Many researchers have reported SAW humidity sensors based on polyvinyl-alcohol as sensing medium in SAW resonator, polyXIO film in SAW delay line, polyaniline (PANI) nanofibres as sensing medium in SAW resonator, tungsten tri oxide as sensing medium in SAW device, a multi-walled carbon nanotube/Nafion (MWCNT/Nafion) composite material prepared as humidity-sensitive films deposited on the surface of an SAW device, and N-isopropylacrylamide

(NIPAAm) nanogel as sensing medium deposited on SAW Resonator and SAW delay line [12, 13, 14, 15, 16, 17].

Sensing mechanism of the humidity sensor is either electronic or protonic. According to transduction type, polymeric humidity sensors are divided into two fundamental categories:

- Resistive-type
- Capacitive-type

The former responds to water vapor variation by changing its conductivity while the latter responds to water vapor by varying its dielectric, ε.

Resistive-type humidity sensors respond to humidity variation by changing its conductivity while capacitive-type humidity sensors respond to water vapor by varying its dielectric constant. Sensing mechanism of resistive-type humidity sensors are based on the conductivity change with humidity change. Resistive-type relative humidity sensors were developed a result of the advancements in the technology of the sensor production.

Figure 1. 6 Commercial resistive-type relative humidity sensors [18]

Capacitive sensors are usually more expensive than resistive sensors due to their high fabrication cost. However, with excellent linear response, capacitive sensors are far more attractive than resistive sensors. For this reason, these sensors are the main topic in this research work. This linear response is due to a very simple principle described as follows. For insulating polymers, the absorbed water, the weight of which is proportional to relative humidity, occupies the free space between the polymeric

molecules. Therefore the change of the dielectric of the hygroscopic polymer is linearly proportional to the amount of water absorbed [5].

Hysteresis problem in capacitive sensors comes from clusters of absorbed water inside the bulk polymer. This must be quantified for each sensor before proceeding with measurements.

The first capacitive-type relative humidity sensors were developed in 1973. This development was opened a new era in the humidity sensing and measuring. Today, almost 75 % of all the fabricated humidity sensors are based on the capacitive measuring principle. The ease of fabrication led to a widespread use of these sensors. Typical capacitive-type humidity sensors are given in Figure 1.7.

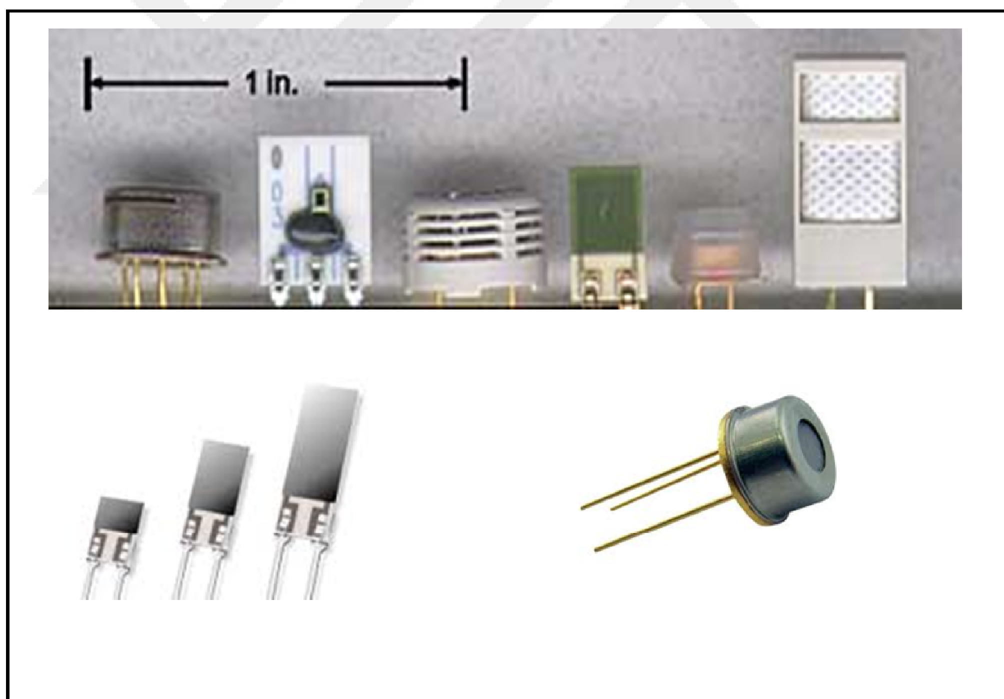

Figure 1. 7 Commercial capacitive-type relative humidity sensor [18]

Sensing mechanism of capacitive-type humidity sensors are based on the dielectric change with humidity [19].

$$S = \frac{\Delta \varepsilon_w}{\Delta RH} \tag{1.1}$$

In the above equation, S is the sensitivity, $\Delta\varepsilon_w= \varepsilon_{wRHmax}-\varepsilon_{wRHmin}$, is the dielectric change which is the difference between maximum and minimum dielectric values, $\Delta RH=RH_{max}-RH_{min}$, is the relative humidity change which is the difference between maximum and minimum relative humidity values.

Capacitive-type relative humidity sensors consist of a substrate where a thin film of polymer or metal oxide is deposited between two conductive electrode layers. The sensing surface is coated with a porous metal electrode to protect it from contamination and exposure to condensation. The substrate is glass, ceramic, or silicon. The incremental change in the dielectric constant of a capacitive-type humidity sensor is directly proportional to the relative humidity of the surrounding atmosphere. The typical capacitance change is in between 0.2 pF and 0.7 pF for a 1 %rh change for commercial sensors in the market.

Capacitive-type relative humidity sensors are easily produced in a wide range of specifications, sizes, and shapes including integrated electronics. Therefore, they are widely used in industrial, commercial, and weather telemetry applications.

Transduction of water vapor concentration into an electrical measurement by the sensing film is a five-step process consisting of:

- Physical interaction of water vapor molecules with the film surface
- Chemical interaction of water vapor molecules with the film surface
- Surface modifications of the film due to water vapor accumulation on the film
- Bulk modifications of the film due to water vapor diffusion into the film
- Electrical or mechanical property of the film changes due to its interaction with water vapor

Most of the polymeric resistive humidity sensors are based on two types of materials: polyelectrolytes and conjugated polymers.

For both types of materials, the conductivity of most polymers decreases with increasing humidity level. However, the conductivity of the former is always lower, due to its ionic functional groups. Generally speaking, polyelectrolytes are hydrophilic or even watersoluble, while conjugated polymers (conducting or semiconducting polymers) are rather hydrophobic and unable to absorb much water. To fabricate humidity sensors based on polyelectrolytes, it is reasonable to use some methods to avoid deformation caused by dissolving and to enhance the sensitivity by lowering the intrinsic conductivity [5, 19]. For sensors based on conducting and semiconducting polymers, dispersing some ions inside the materials leads to reduction in resistivity at low RH and thus generates greater absolute signals. The configuration of most resistive sensors, as well as of capacitive sensors that will be discussed later, is either a sandwiched structure with electrodes on both sides or interdigitated electrodes with deposited polymer films in between. For the sandwiched structure, the top electrode is always a vapor-permeable thin metal film such as gold, platinum, and silver. Polyelectrolytes are polymers with electrolytic groups, which could be salts, acids, and bases. To absorb moisture, the polyelectrolytes are usually prepared as porous thin films. Ammonium and sulfonate salts are traditional polyelectrolytes used in moisture sensing. During the last few years, phosphonium salts have been developed.

Over 150 years ago in 1839, Charles Goodyear vulcanized natural rubber using sulfur by cross-linking the isolated polymeric rubber chains into an intensive network [20]. For humidity sensing polyelectrolytic films, the same method (cross-linking) is used to enhance the mechanical properties of the sensors, as well as preventing dissolving of ions and strengthening the adherence to the substrate. The diaminoalkane forms a "bridge" that connects two polymer chains together so that a dense, insoluble, and intensive polymer network is resulted. Note that the crosslinking reagent (diaminoalkane) becomes the electrolytic (humidity-sensitive) group of the network and the crosslinking and ammonium-quaternization are accomplished at the same time.

Graft-polymerizing, in which electrolytic groups are grafted on a pre-prepared polymer backbone that comprises a porous film, is also a good method to make the sensing film resistive to water [21]. The cross-linking and interpenetrating polymer network (IPN) are primarily dealing with the solubility and deformation, but have little to do with

enhancement of sensitivity. The sensitivity becomes quite low at high humidity due to its low resistivity at low RH.

This problem can be solved by adding an insulating content into the conductive polyelectrolytes [6, 8, 22]. Hygroscopic insulating polymers, such as polyvinyl alcohol (PVA) and polyesters are always favored. This method is proved to be effective for lowering the conductivity of polyelectrolytes at low RH and enhancing sensitivity at high RH. A typical synthesis reaction for preparing a copolymer is mixing two monomers in appropriate solvent under proper conditions. Humidity-sensitive copolymer films can also be crosslinked to enhance the performance [6, 22].

Cross-linked copolymers resulted from mutually reactive polymers have been also developed in the past few years [8, 22]. Different from traditional cross-linking, in which chains of the same polymer are joined together, two different polymers (mutually reactive polymers) are bridged together in this process. There is no bridging reagent or radiation needed in the cross-linking process and the connection between the two reagents is accomplished by direct reactions.

The cross-linked structure from mutually reactive polymers may have mechanical properties as good as IPNs, of which the process is much more complicated. Based on polyelectrolytes, many humidity sensors are able to respond to RH from 20 %rh to 90 %rh with good linearity [8, 22, 23, 24].

1.4.1.1. Conducting/Semiconducting Polymers

In polymers and single molecules, sometimes double bonds and single bond may occur alternately along the main chain. This structure is called conjugation, which is a key thing for semiconductive and conductive polymers. A conjugation structure existing along the entire main chain is named universal conjugation.

Conductive polymers were first reported in 1977 [25]. The band gap of conductive polymers is the narrower as the degree of conjugation is greater because more bonding electrons are delocalized which is verified by theories and experiments [26]. Band gap of highly conjugated polymers is small (~2 eV) and that of saturated polymers is high

(~10 eV). The reason for the decreasing band gap is that the conjugating structure delocalizes the bonding electrons and the system energy is reduced. If the conjugation is universal, its degree can be represented by the degree of polymerization. For highly conjugated polymers with high polymerization degree, the intermolecular resistance becomes negligible in the bulk. This is because the intermolecular energy gap for charge carrier to overcome is quite small, which is usually less than 0.1 eV for high degree of polymerization due to the Van der Waals force that increases with mass. Like intrinsic silicon, despite containing universally conjugated chains the intrinsic conducting polymers are not very conductive because of shortage of free charge carriers. Also, radiation with photon energy higher than the band gap could enhance the conductivity by exciting electrons from the valence band to the conduction band. The conducting mechanism of intrinsic polymers could be interpreted by the principles of electron–hole pair traveling under electric field [27]. However, the traveling is one-dimensional rather than three-dimensional due to the structure of conjugated polymers. Since most conductive polymers lack completely equivalent carbon sites along the main chain, some charges are localized and the band gap is therefore enlarged. The sites that trap the carriers are named polarons (a polaron with two charges is called a "bipolaron") and the process in which carriers overcome the polaron barrier(s) is called "hopping." At room temperature, the conductivity of intrinsic polyacetylene is very low, only 10^{-7} $S{\cdot}cm^{-1}$ to 10^{-8} $S{\cdot}cm^{-1}$ (that of intrinsic silicon is about $4{\times}10^{-6}$ $S{\cdot}cm^{-1}$). Similar to inorganic semiconductors, the conductivity of polymers can be considerably enhanced by doping. The doping of polymers is actually to oxidize (p-type doping) or reduce (n-type doping) the backbone by chemical agents [28, 29]. The oxidation/reduction also generates by-products, like positive or negative ions. These ions become part of the polymer to keep the net charge to be zero. They are usually called "counter ions". It is expected that a p-type polymer semiconductor may contain negative counter ions and an n-type one may contain positive counter ions. In case that sufficient amount of water is absorbed on the doped polymers, one may expect that polymers may show some ionic conduction with the counter ions as the carriers. It is known that the conductivity of extrinsic silicon is very high (>1000 $S{\cdot}cm^{-1}$). However, for general polymers (polyacetylene or polyphenylene) with moderate doping (either p-type or n-type), the conductivity may vary from 0.1 to 1 $S.cm^{-1}$. In recent years, several devices based on

conducting/semiconducting polymers were built, including LEDs, [30] solar cells, [31] and field-effect transistors [32].

Water is well known for its protonation and the released proton interacts with universally conjugated C-C double bonds. This effect was discovered and used for humidity sensing [33, 34]. As conducting polymers, polyaniline (PANI) and its derivatives have been found to be humidity sensitive for a long time [35]. Due to polymerization by some strong oxidant (e.g., $(NH_4)_2S_2O_8$), the PANI structure contains two basic forms: non-oxidized (reduced) and oxidized structures. The PANI synthesized in this way may be regarded as p-type doping. Due to the un-bonded electron pair on the nitrogen atom, both forms can be protonated: $NH \rightarrow NH^{+2}$ and $N \rightarrow NH^{+}$. The humidity sensing property of PANI to water vapor can be regarded as electron hopping assisted by proton exchange. Its conduction is both electronic and ionic. The ionic conduction is favorable as long as mobile counter ions (for example, Cl^{-}) exist in the polymer [36]. Although it is verified that PANI and its derivative are sensitive to humidity, the response is very low due to weak hygroscopicity, at most one order of magnitude change in conductivity [37, 38]. Using a similar methodology in polyelectrolytes, some researchers combine (o-phenylenediamine) (PoPD, a close structure to PANI) with hygroscopic polymers like PVA to enhance the response [39, 40]. The hygroscopic PVA absorbs water molecules from poly in the drying stage and provides water molecules to PoPD as humidity increases.

The composite PoPD/PVA is able to detect RH below 10 %rh [39]. Some hysteresis is observed in this type of sensor after long-term operation or short exposure to high humidity. It is attributed to a layer of sulfuric acid that is formed from the dopant (fuming sulfuric acid) [39]. A major drawback of PANI is its poor processibility. It is reported that converting PANA (Poly (anthranilic acid)) into PANI by heat treatment turns to be a convenient method for fabricating PANI with good humidity-sensing property [41]. The doped composite film of poly(o-anisidine)/PVA, which is also a derivative of PANI, is reported also to be humidity-sensitive [42]. Poly(p-diethynylbenzene) or PDEB is a conducting polymer due to its long-chain conjugated structure. Other conducting polymers, such as p-diethynylbenzene-co-propargyl alcohol, and ethynylbenzene-copropargyl alcohol (copolymer), are also good candidates

for humidity sensing as reported in the given references. These copolymers respond to relative humidity over 30 %rh [43, 44]. The merit of ethynylbenzene-copropargyl alcohol is that for RH over 30 %rh the logarithm of the capacitance of the film changes linearly with humidity and its sensitivity is very high [44]. The sensing mechanism may be due to the interaction between protons or dopant ions and the universally conjugated structure [43].

1.4.1.2. Hydrophobic Polymer-Based Capacitive Sensors

Unlike resistive sensors based on polyelectrolytes, capacitive polymer films for humidity-sensing are made from hydrophobic organic materials that are somewhat hygroscopic in order to absorb moisture [45]. In other words, the polymers for capacitive sensors should be both non-ionic and highly polar macromolecules. In the market, capacitive sensors are usually more expensive than resistive sensors due to their high fabrication cost [46]. However, with excellent linear response, [46–48] capacitive sensors are far more attractive than resistive sensors. This linear response is due to a very simple principle described as follows.

For insulating polymers, the absorbed water, the weight of which is proportional to relative humidity, occupies the free space between the polymeric molecules. Therefore the change of the dielectric constant of the hygroscopic polymer is linearly proportional to the amount of water absorbed. To be non-ionic but very polar, polyimides, [46–49] and esters are also good candidates, such as cellulose acetate butyrate (CAB), [50-51] poly (methyl methacrylate) (PMMA), [52, 53] poly (vinyl crotonate) (PVC), [54] and poly (ethyleneterephthalate) (PETT) [55].

Hysteresis is usually a serious problem in capacitive sensors. Hysteresis comes from clusters of absorbed water inside the bulk polymer [45, 56]. Formation of clusters indicates that hygroscopicity of some polymers is too high and relatively large voids exist in the polymeric structures. The water clusters may also deform the polymers and shorten the lifetimes of the sensors. The application of cross-linking is used to solve the deformation and aging caused by water absorbed in polyelectrolytes. For capacitive sensors, the cross-linking method, [52, 54, 57, 58] in which hygroscopicity is lowered and the resistance is enhanced due to temperature change, [54] is also used to against

the hysteresis. Some hygroscopic cross-linking agents can also enhance the sensitivity of the film [52].

Polyimides, which are used as insulators in integrated circuits, [59, 59] are the most commonly used group of materials for capacitive humidity sensors [45, 46–49] and the response is always linear with the detection limit generally below 20 %rh. In addition, polyimides can also be used as substrates for humidity sensors [49]. The polyimide (Kapton) can be doped with carbon to become conductive. Between the polyimide substrate and the sensing film (made of other polymers), the adherence is strong and the mismatch in thermal coefficients is small. It is also reported that carbon filled polysulfone can be used as good electrodes for humidity sensors based on polyimides [47].

Other polymers suitable for capacitive humidity sensors include polyethersulphone (PES), [46] polysulfone (PSF), [61] divinyl siloxane benzocyclobutene (BCB), [62] hexamethyldisilazane (HMDSN), [63] etc.

The capacitive humidity sensors have linear response as low as 15 %rh [54, 46, 60] and some have very low hysteresis (<2 %rh) [46, 48, 61].

1.4.2. Ceramic Humidity Sensors

Humidity sensors based on water-phase protonic ceramic materials are used widely as a humidity sensor in industry and research laboratories. The adsorbed water condensed on the surface of the materials and protons will be conducted in the formed aquatic layers. For ionic sensing materials, if the humidity increases, the conductivity decreases, and the dielectric constant increases [5, 64]. In bulk water, proton is the dominant carrier responsible for the electrical conductivity. The conduction is due to the Grotthuss mechanism, through which protons tunnel from one water molecule to the next via hydrogen bonding that universally exists in liquid-phase water.

This mechanism was reported more than 200 years ago [65]. The mechanism of protonic conduction inside the adsorbed water layers on the surface of the sensing materials was discovered in study of titanium dioxide based sensors.

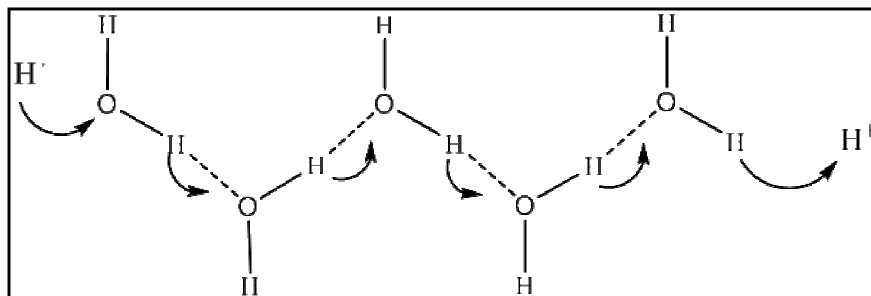

Figure 1. 8 Brief illustration of the Grotthuss mechanism

As shown in Figure 1.9, at the first stage of adsorption, a water molecule is chemically adsorbed on an activated site to form an adsorption complex, which subsequently transfers to surface hydroxyl groups. Then, another water molecule comes to be adsorbed through hydrogen bonding on the two neighboring hydroxyl groups as shown in Figure 1.9.

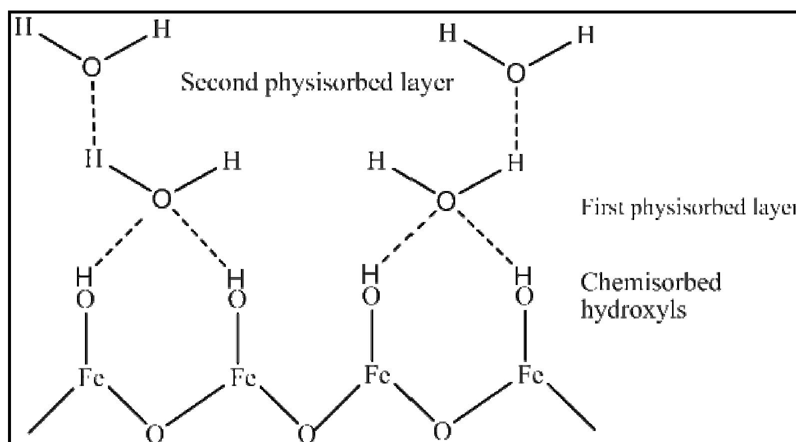

Figure 1. 9 Multi-layer structure of condensed water [5]

The top water molecule condensed cannot move freely due to the restriction from the two hydrogen bonding. Thus this layer or the first physically-adsorbed layer is immobile and there are not hydrogen bonds formed between the water molecules in this layer. Therefore, no proton could be conducted in this stage. An extra layer on top of the

first physically adsorbed layer forms as water continues to condense on the surface of the ceramic. This layer is less ordered than the first physically-adsorbed. For example, there may be only one hydrogen bond locally. If more layers condense, the ordering from the initial surface may gradually disappear and protons may have more and more freedom to move inside the condensed water through the Grotthuss mechanism.

In other words, from the second physisorbed layer, water molecules become mobile and finally almost identical to the bulk liquid water, and the Grotthuss mechanism becomes dominant. This mechanism indicates that sensors based purely on water-phase protonic conduction would not be quite sensitive to low humidity, at which the water vapor could rarely form continuous mobile layers on the sensor surface. The two immobile the chemisorbed and the first physisorbed layers, while cannot contribute to proton conducting activity, could provide electron tunneling between donor water sites. The tunnelling effect, along with the energy induced by the surface anions, facilitates electrons to hop along the surface that is covered by the immobile layers and therefore contributes to the conductivity. This mechanism is quite helpful for detecting low humidity levels, at which there is not effective protonic conduction. Nonetheless, the tunnelling effect is definitely not the semiconducting mechanism that will be discussed later.

1.4.3. Metal-oxide Humidity Sensors

There are four basic types of oxide-based sensing materials which are Al_2O_3, TiO_2, SiO_2, and spinel compounds. The basic preparation methods, humidity-sensing properties, and their advantages and disadvantages will be given briefly [5].

Al_2O_3 is one of the most favorable ceramic sensing materials due to its independence of temperature at nearly all range of relative humidity from 25 °C to 80 °C. The small pore radius makes Al_2O_3 sensitive to very low water vapor pressure. Due to the electron tunneling effect inside the condensed immobile water layers, porous Al_2O_3 is a competitive candidate for sensing low humidity levels.

Two out of several phases for Al_2O_3 are commonly used in humidity sensing: γ-Al_2O_3 (amorphous) and α-Al_2O_3 (corundum). Since the former has high porosity it is more sensitive than the latter. The latter is the most thermodynamically stable phase. The growth of humidity sensitive porous α-Al_2O_3 is important for sensors with long-term stability and non-regenerate applications because of the change of γ-phase Al_2O_3 to γ-$Al_2O_3 \cdot H_2O$ (boehmite). It has a gradual decrease of surface area and porosity.

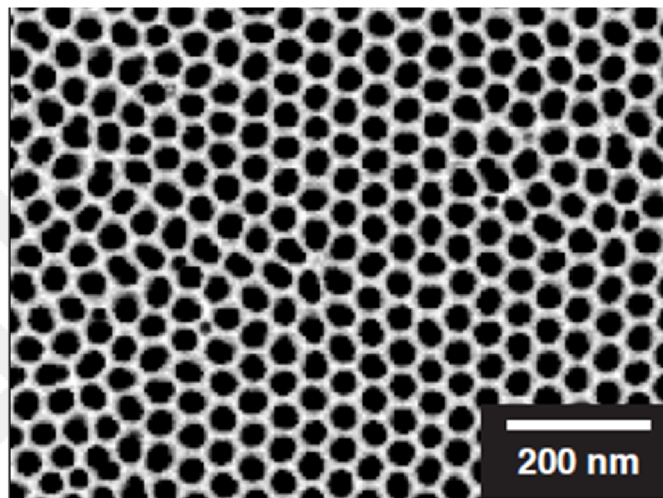

Figure 1.10 Periodic structure of anodic aluminum oxide (AAO) [5]

Many of the Al_2O_3 humidity sensors are fabricated through anodization. Because of its low-cost and easy process, anodic Al_2O_3 has great advatages over other materials. Al_2O_3 layer consisting of hexagonal closepacked cylindrical pores perpendicular to the metal surface is formed under low voltage anodization at certain conditions in acidic electrolyte solution. The diameters and depths of the pores can be controlled by tuning the anodization conditions. Therefore, the detection limit could be set very low by shrinking the pore size [66, 67].

The α-Al_2O_3 sensors fabricated by anodic spark deposition (usually >100 V) showed very high sensitivity and very fast response at RH range (<5 s). Their response time and long-term stability are also examined over one year and the results were satisfactory for a humidity sensor.

Unfortunately, similar to the films formed at low-voltage anodization, Al_2O_3 films prepared by vacuum methods at lower substrate temperatures are usually γ-phase or amorphous, which suffers from degradation. An effective method to obtain stable porous α-Al_2O_3 for humidity sensing is reactive evaporation at elevated substrate temperatures such as from 800 °C to 1300 °C, in which the metal aluminum is evaporated and oxidized before the oxide particles are deposited on the substrate.

1.4.3.1. TiO_2 Humidity Sensors

TiO_2 has three phases: anatase, rutile, and brookite. The third one is seldom used in humidity sensing. When heated strongly (~1000 °C), anatase automatically transforms to the rutile structure. Rutile is the most common phase of TiO_2, while anatase is very rare in nature. At high temperature (~600 °C), anatase is an n-type semiconductor but rutile is a p-type one. Because humidity sensing is usually realized by the adsorbed proton-conducting water layers on the porous structure at room temperature, both phases should behave approximately the same in resistance or capacitance changes. TiO_2 can be considered as a surface protonic/ionic conducting material, not a semiconducting sensing material [68].

For humidity sensing applications, anatase TiO_2 are usually made by a sol–gel method. The sintering must be at low temperatures (e.g., <500 °C) for short time. Otherwise, TiO_2 may be turned into rutile. Due to its higher water adsorption capacity, anatase is a preferred humidity sensing material.

Because of its protonic conducting sensing mechanism, doping with alkali ions may improve the conductivity of TiO_2. Adding SnO_2 increases its porosity and thus enhances the sensitivity at high RH range (>70 %rh). Doping of electrolytes or ions, e.g., P_2O_5 or potassium may considerably enhance the sensitivity. However, most TiO_2-based sensors are not sensitive at low humidity levels and have limited detection ranges from 10 %rh to 30 %rh. A TiO_2 nanowire sensor is capable of detecting relative humidity levels down to 11 %rh.

1.4.3.2. SiO_2 Humidity Sensors

Although SiO_2 grown by wet or dry oxidation has been used as an insulator in electronics for a long time, it is definitely not suitable for humidity sensing because it is a dense material. Humidity sensors based on porous silicon oxide were fabricated using bulk-sintering processes, especially traditional sol–gel method, in which SiO_2 is precipitated by hydrolysis of certain alkoxide of silane. It was reported that sol–gel fabricated SiO_2 sensors could detect humidity as low as 4 %rh [69] and most reported works showed that only humidity over 20 %rh can be detected [70-72].

The most prominent merit of SiO_2 as a humidity sensing material is its compatibility with the current microelectronics industry. Similar to other porous ceramic materials, the humidity sensitivity of SiO_2 can be enhanced by adding electrolyte dopants, such as LiCl.

Glancing angle deposition (GLAD) method used for deposition of the SiO films were not sensitive to humidity levels lower than 15 %rh, the response and recovery times are as short as in milliseconds. These may be the fastest humidity sensors ever reported.

1.4.3.3. Humidity Sensors Based on Spinel Compounds

The spinel compounds belong to a large group of oxides with a general composite of AB_2O_4. A can be a divalent metal element, especially in group II, group IIB, and VIIIB. X generally represents a trivalent metal, e.g., iron, chromium, and aluminum. The structure of this group is tetrahedron (diamond) always with high density of defects. Although spinel oxides are semiconductors, most of the reported humidity sensors based on these materials have ionic sensing properties probably due to their low operating temperatures (<100 °C).

In case that the pore size is very small (100-300 nm), the lower detection limit can be down to 1 %rh [73, 74]. Like other humidity sensing ceramics based on proton-conducting mechanism, doping with alkali ions facilitates formation of hydrated protons.

1.4.3.4. Other Ceramic Sensing Materials

A p-type semiconductor (LiCl-doped $MnWO_4$) was reported to have good linear response to relative humidity over 30 %rh in short response (~3 s) and recovery (~15 s) time at room temperature. Scanning electron microscopy (SEM) showed different grain and pore sizes of the material in relation to the amount of added LiCl. Despite their short response/recovery time, thin films are less sensitive than thick films due to their lack of capillary structures [75, 76]. Boron phosphate calcinated at 350 °C was found to be sensitive to RH over 35 %rh. The phosphate cations might dissolve in the adsorbed water and help the formation of protons. The α-Fe_2O_3 (hematite) used for humidity sensing was back in the 1960's. After doping with silicon and sintering at 850 °C - 950 °C, the average pore size of α-Fe_2O_3 is ~25 Å. The α-Fe_2O_3 sensors can response to RH below 5 %rh.

1.4.4. Semiconducting Humidity Sensors

Some ceramic oxides or composite oxides such as SnO_2, ZnO, and In_2O_3, etc. are wide-bandgap semiconductors. H_2O is adsorbed on the oxide surface in molecular and hydroxyl forms. Water molecules are observed to increase the conductivity of n-type ceramics and to decrease the conductivity of p-type ceramics. This effect has been attributed to the donation of electrons from the chemically adsorbed water molecules to the ceramic surface [77, 78]. Another mechanism proposed was suggested that water molecules replace the previously adsorbed and ionized oxygen (O^-, O^{2-}, etc.) and therefore release the electrons from the ionized oxygen. Because the conductivity is caused by the surface concentration of electrons, this sensing mechanism is usually called “electronic type” [79, 80]. However, the water layer formed by the physical adsorption may be somewhat protonconductive. Therefore, at room temperatures the conductivity of ceramic semiconducting materials is actually due to addition of both electrons and protons (ionic), unless at high temperatures (>100 °C) moisture cannot effectively condense on the surface. The conductivity increment is produced by surface electron accumulation resulting from the preferential alignment of the water dipoles. Hydrogen atoms contact the surface (mostly at the oxygen sites) and attract electrons outward.

Since adsorbed water molecules increase the conductivity of n-type ceramic semiconductors, most of the experimental works deal with n-type ceramics. It was reported that the change of conductivity was linear to certain exponential based on the proposed surface reaction mechanism.

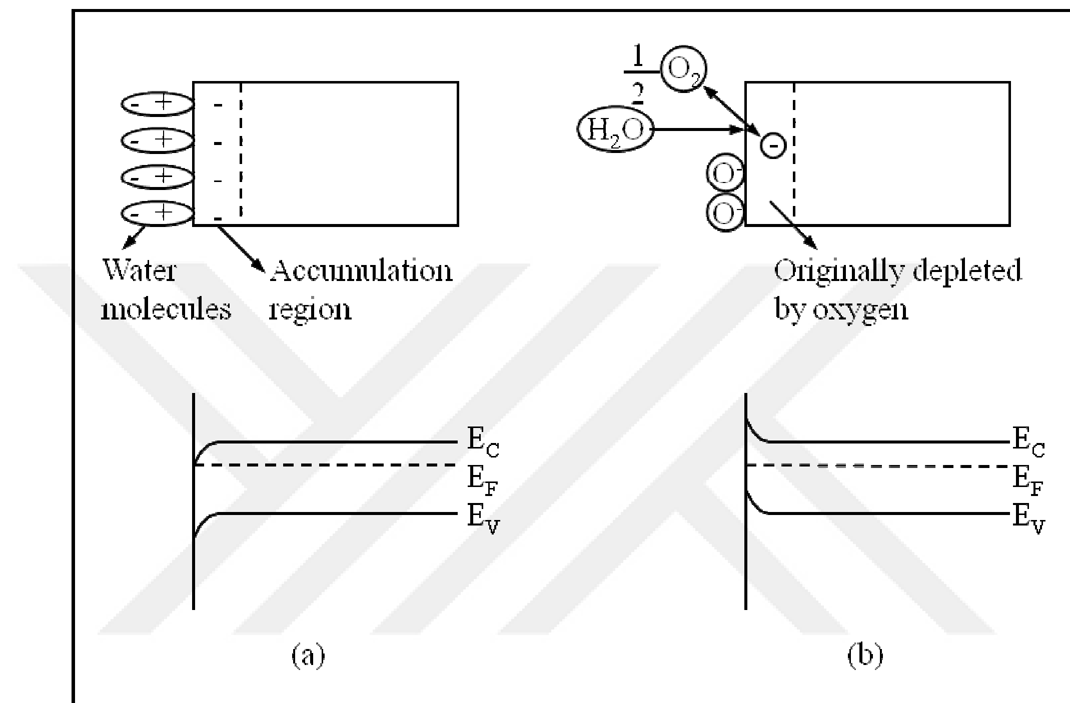

Figure 1.11 Two possible mechanism for “donor effect” for n-type. (a) Electrons are attracted by the adsorbed water molecules to the semiconductor surface and the energy bands are bended; (b) Electrons are released by the competitive adsorption. Figure modified, original taken from [5]

1.4.4.1. SnO_2

Stannic oxide (SnO_2) is an n-type wide-bandgap semiconductor. H_2O is adsorbed on the oxide surface in molecular and hydroxyl forms and the mechanism was identified to be electronic [77, 81]. Different from TiO_2 and other high-temperature semiconducting ceramics, SnO_2 shows electronic conductivity at rather low temperature (even at room temperatures). Therefore, SnO_2 humidity sensors based on semiconducting properties are expected. A transitional behavior was also observed in step-like humidity changes for sensors based on SnO_2 at high temperatures. This is caused by fast competitive

adsorption between H_2O and adsorbed oxygen species (O^{2-}, O^{-}, etc.) and desorption of the adsorbed oxygen species and releasing of free electrons.

The electronic conduction mechanism promotes this phenomenon and also confirms the contribution of competitive adsorption between H_2O and adsorbed oxygen to the conductivity increase. For sensors based on ultra-thin SnO_2 films (60 nm - 90 nm) prepared by sol–gel process, the response time ranged from 8 s to 17 s for different humidity changes and the recovery time was only about 1 s, due to their ultra-thin films. However, most of the SnO_2 sensors are only sensitive to RH higher than 30 %rh. In addition to sensing water vapor, SnO_2 is widely used for multiple gases, especially harmful oxides such as NO_X, CO, PbO_2.

1.4.4.2. Perovskite Compounds

Large group of oxides with general composition of AXO_3 are named as the perovskite compounds. The A can be any metal element with +2 valence electrons, e.g., group II, group IV, and rare earth metals. The X represents titanium, niobium, and iron. All members of this group have the same basic isometric structure [82]. Perovskite oxides type ceramics exhibit interesting properties and promising applications. N-type perovskite semiconductors exhibit electrical conductivity variation as humidity changes and have high sensitivity to water partial pressure down to 0.006 atm. However, the humidity-sensing property of perovskite oxides is only effective at elevated temperatures (400 °C - 700 °C). Therefore, the perovskite oxide humidity sensing devices, based on electron-conducting mechanism, are operated at the temperature of hundreds of Celsius [83, 84]. At room temperature, some porous perovskite oxides still demonstrate humidity sensitivity. Because the sensing mechanism is no longer electron-conducting but ion-conducting, they are only sensitive to humidity higher than 8 %rh - 20 %rh [84-86]. In these cases, the porous perovskite oxides operating at room temperature may be regarded as simple resistive or capacitive ceramics, in which the group II elements may serve as metal ions to improve the conductivity in moisture. Most humidity sensitive perovskite oxides were fabricated by bulk-sintering of the mixture of two or more metal oxides/carbonates.

1.4.4.3. In_2O_3

In industry, smooth and transparent films made of indium oxide, an n-type ceramic semiconductor, are used as infrared-reflectors or electrodes for liquid crystals. There are a couple of methods for fabrication of rough and porous In_2O_3 layers that are sensitive to humidity. The humidity-sensing is due to the porous water adsorbing structure inside the gaps. Using thermal deposition in high vacuum was found to obtain In_2O_3 films with granular sizes ranging from 1 μm to 10 μm. However, In_2O_3 humidity sensors are not able to sense relative humidity lower than 25 %rh and the response may take a couple of minutes. This type of devices still needs improvement. Although we categorize In_2O_3 as a semiconducting (electronic conducting) material, its humidity-sensing mechanism is still not very clear [87-90].

1.4.4.4. Other Semiconducting Sensing Materials

Homogeneously mixed and sintered $ZnO\text{-}Y_2O_3$ was found to be a humidity-sensitive n-type semiconductor [91, 92]. Doping with Li^+ shows linear behavior in the entire humidity range from 5 %rh to 98 %rh at room temperatures. The composite materials were found to be n-type and the electrical conduction due to the water donors was thought to be the dominant mechanism in the low humidity range.

1.5. CHARACTERISTICS OF HUMIDITY MEASURING INSTRUMENTS

In order to satify a wide range of applications the following general requirements must be fulfilled by a humidity sensor [1, 93]:

- Good sensitivity over a wide range
- Good uncertainty
- Good accuracy
- Short response time
- Good repeatability
- Good reproducibility
- Good long-term stability
- Low hysteresis
- Fitness to circuitry

- Tough durability and long life
- Ability to recover from condensation
- Resistant to chemical and physical contaminants
- Low temperature dependence
- Simple structure, simple fabrication
- Small size
- Suitable for measurement system of user
- Cost effectiveness

1.6. COMPARISON AND ADVANTAGES/DISADVANTAGES OF HUMIDITY MEASURING INSTRUMENTS

In this work, the properties of various types of humidity sensors reviewed in the previous sections were researched, compared, and contrasted from various publications containing literature and manufacturer data sheets to determine their suitability as a humidity sensor. Comparison of four different types of humidity measuring instruments is given in Table 1.2.

Table 1. 2 Comparison of humidity sensors

Capacitive type [1, 5, 64, 93]	Resistive type [1, 5, 93]	Optical type [1, 5, 93]	Psychrometer [1, 93]
Ease of use	Ease of use	Complex	Complex
Integral memory	Integral memory	None / Software	Only new electronic versions
Transfer standard	Transfer standard	Reference standard	Transfer standard
Low cost	Low cost	Expensive	Low to medium cost
No maintenance	No maintenance	Regular maintenance	Regular maintenance
Tolerate condensation	No tolerance to condensation	Tolerate condensation	Tolerate condensation

Drift / Hysteresis	Drift / Hysteresis	Low drift / Low hysteresis	Low drift / Low hysteresis
Temperature dependence	Temperature dependence	No temperature dependence	No temperature dependence
No sensitivity to flow rate	No sensitivity to flow rate	Sensitive to air/gas flow rate	Sensitive to air flow rate
Measurement range: 1 %rh to 99 %rh	Measurement range: 5 %rh to 95 %rh	Measurement range: 0 %rh to 100 %rh	Measurement range: 0 %rh to 100 %rh
Sensitivity: 0.2 pF·%rh^{-1} - 0.6 pF·%rh^{-1}	Sensitivity (kOhm.%rh^{-1}): 1 (90 %rh - 60 %rh) 6 (60 %rh - 50 %rh) 50 (50 %rh - 40 %rh) 450 (40 %rh - 20 %rh)	Sensitivity (°C.%rh^{-1}): 0.5	Sensitivity (°C.%rh^{-1}): 1.0
Accuracy: [1, 93] 2 %rh – 4 %rh	Accuracy: [1,93] 3 %rh – 5 %rh	Accuracy: [1,93] 0.5 %rh ; 0.1 °C (dew-point temperature)	Accuracy: [1,93] 3 %rh – 5 %rh

In addition, advantages and disadvantages of capacitance type humidity sensors, resistive-type humidity sensors, optical-type humidity sensors, and psychrometers are given in Table 1.3, Table 1.4, Table 1.5, and Table 1.6, respectively.

Table 1. 3 Advantages and disadvantages of capacitive-type humidity sensors

Advantages [1, 5, 64, 93]	Disadvantages [1, 5, 64, 93]
Resistant to chemicals	Hysteresis
Full recovery from condensation	Drift due to response to substances other than water vapour
Low temperature coefficient	Temperature dependency

Easy fabrication	Possible damage of strong acidic or basic chemicals
Response time ranges from 30 s to 60 s for a 63 %rh step change	Calibration shift at temperatures above 40 °C and at relative humidity values above 85 %rh
Long-term storage options	Distance between the sensor and the signal conditioning circuitry has a practical limit (less than 3.05 m.)
Ease of use	Direct field interchangeability can be a problem
Cost effective	
Tolerate condensation	

Table 1. 4 Advantages and disadvantages of resistive-type humidity sensors

Advantages [1, 5, 93]	Disadvantages [1, 5, 93]
Ease of use	Hysteresis
Integral memory	Drift due to response to substances other than water vapor
Low cost	Temperature dependency
No maintenance	Possible damage of strong acidic or basic chemicals
Interchangeability of the sensor within 2 %rh	Intolerant to condensation
	Non-linear response (logarithmic)

Table 1. 5 Advantages and disadvantages of optical-type humidity sensors

Advantages [1, 5, 93]	Disadvantages [1, 5, 93]
Reference standard	Complex and expensive
Traceable to temperature standards	Requires pressure measurement and correction
Low drift	Requires regular maintenance

Low hysteresis	Sensitive to incoming air/gas flow rate
No temperature dependence	None / Software
Tolerate condensation	Requires longer times for stabilization after condensation occurs
	Requires qualified person to operate

Table 1. 6 Advantages and disadvantages of psychrometers

Advantages [1, 93]	Disadvantages [1, 93]
Transfer standard	Complex
No temperature dependence	Require suitable chart or software in order to convert temperature values to humidity related definitions
Tolerate condensation	Regular maintenance
Low drift	Sensitive to built-in air flow rate
Low hysteresis	Requires continuous water supply
Low/moderate cost	

As a conclusion drawn from Table 1.2, Table 1.3, Table 1.4, and Table 1.5, it can be observed that although capacitive humidity sensors suffer from hysteresis and most of them have some temperature dependency, they are inexpensive, easily fabricated, and accurate sensors.

1.7. INTEGRATED HUMIDITY MEASURING INSTRUMENTS

An immense number of humidity measuring devices were arisen from the diversity of humidity measuring techniques. Among them absolute humidity, dew-point and relative humidity are the commonly used terms and also names of measuring devices. Approximately 75 % of the market offers resistive or capacitive type relative humidity sensors for measuring relative humidity. In addition integrated relative humidity sensors are still growing in demand in industry.

Integrated sensors refer to the implementation of the sensing element and associated electronics on the same substrate. Integrated relative humidity sensors are not widely available because of the incompatibility of the sensing material and the silicon substrate required for the electronic circuitry. In this respect porous silicon has attracted great attention due to its compatibility with the electronic circuitry as a sensory material.

After the discovery of luminescent properties of porous silicon [94-95], its use has been extended to sensing applications. Morphology of the porous silicon structure had attracted much attention from the researchers because of its suitability not only as a sensor material for humidity and gas sensing, but also for a material that can be used in biotechnology applications, such as in drug delivery.

1.8. POROUS SILICON INTEGRATED HUMIDITY MEASURING INSTRUMENTS

Porous silicon has a myriad of channels or holes with nanometer to micrometers dimensions etched into silicon to create a sponge, tunnel or mixed structure which is suitable for humidty sensing. This structure leads to a high surface to volume ratio or high void to bulk ratio. There are five basic reasons to use porous silicon as a humidity sensing material:

- Since it is compatible with bulk silicon, a fully integrated sensor can easily be implemented
- Batch fabrication is possible with low cost and easy fabrication
- The material can be tailored to suit a particular sensing application, since the properties of porous silicon layer can be easily manipulated
- The high surface to volume ratio allows the miniaturization of the active sensing region
- Control of nanometer sized pore and/or crystalline islands is required to produce a sensor with humidity properties desired

Water and water vapour in nanometer sized porous structure is trapped during various relative humidity values. The mechanism is the diffusion of water and water vapour in this structure. Diffusion is the net movement of a substance (e.g., water vapor) from a region of high concentration to a region of low concentration. Knudsen diffusion, surface diffusion, and capillary condensation are the main considerations when there is diffusion in "small" cylindrical pores which means that the pore diameter is of the same order of magnitude as the molecular size of molecules entering the pore. Knudsen diffusion and surface diffusion involve only gases. Capillary condensation involves the conversion from a gas into a liquid and it results from the altered vapor pressure of a liquid inside a pore. This increased vapor pressure p is given by the Kelvin equation.

In order to verify suitable diameter values of porous structure for humidity sensors, the Kelvin equation (1.2) was utilised [96]. The Kelvin equation gives the basis for calculation of optimum pore size "*r*" as a function of relative humidity. According to the Kelvin equation, the ideal pore sizes required for sensing of relative humidity values from 20 %rh to 95 %rh range from 0.8 nm to 40 nm, respectively. Diameter ($d=2*r$) values were calculated for relative humidity values ranging from 0 %rh to 100 %rh, and were generated in the Figure 1.12 at various temperature values.

$$ln \frac{p}{p_0} = \frac{2\gamma V_m}{rRT} \tag{1.2}$$

In the above equation, p is the vapour pressure, p_0 is the saturation vapour pressure, γ is the surface tension, V_m is the molar volume of the liquid, R is the universal gas constant, T is temperature in Kelvin, r is radius of the pore where the liquid is trapped. Since, porous silicon is the material for sensing relative humidity; water is the liquid which was taken into account for all the parameters stated above.

Using the Kelvin equation given above, diameter values was calculated and the results were presented in the following log-linear graph. These values show the pore diameter of the sensing material suitable for humidity sensors in the range from 0 %rh to 100 %rh.

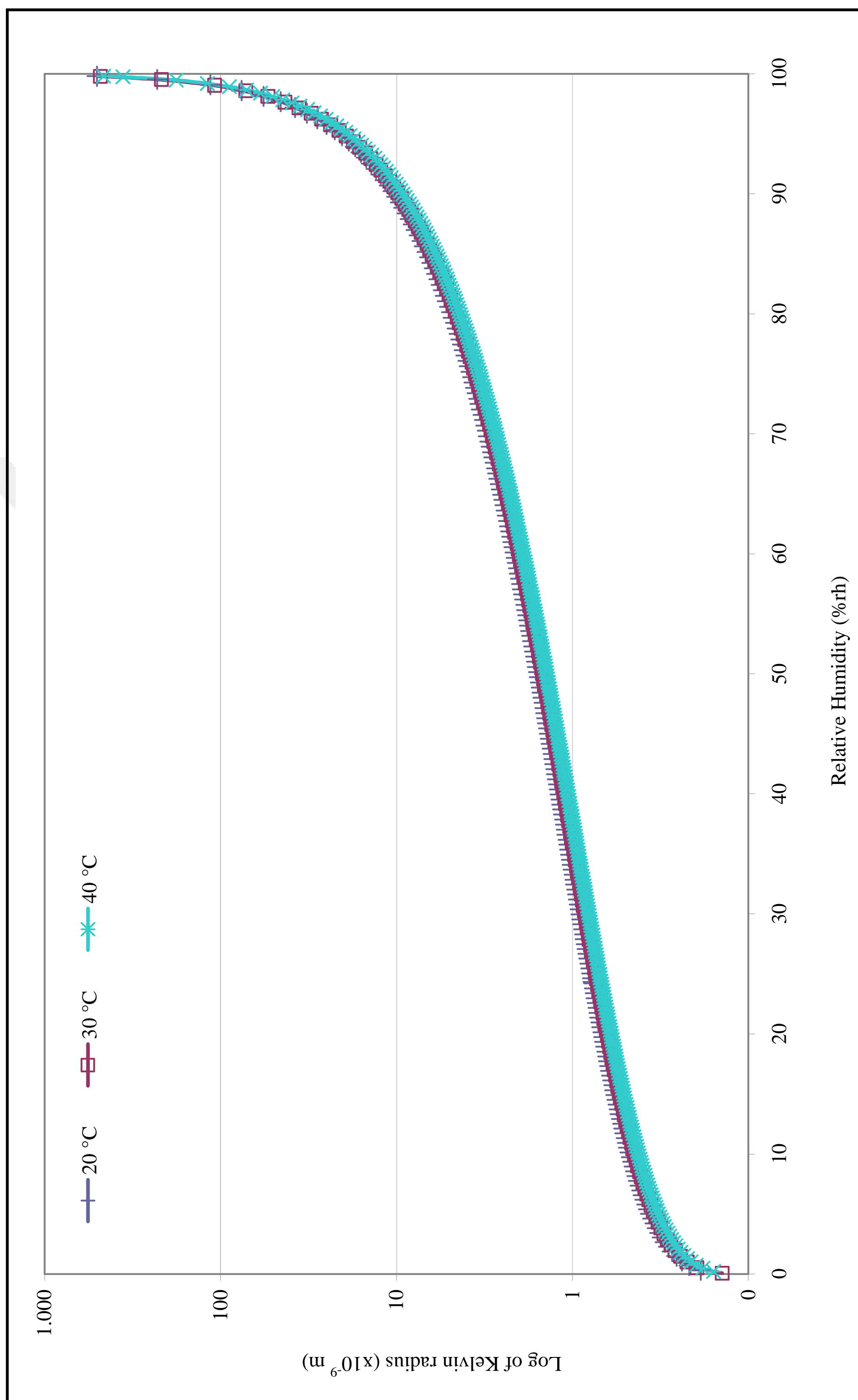

Figure 1.12 Pore radius values calculated from the Kelvin equation for relative humidity values ranging from 0 %rh to 100 %rh

It is observed from the graph depicted in Figure 1.12 that various diameters must be available in a humidity sensor structure.

1.9. LITERATURE REVIEW OF POROUS SILICON HUMIDITY/GAS SENSORS

Porous silicon (PSi) has promising features as a gas sensor, and especially as a relative humidity sensor working in the range from 10 %rh to 99 %rh. Porous silicon (PSi) was discovered in 1956 by Uhlir during studies of electrochemical polishing of silicon wafers using hydrofluoric (HF) acid containing electrolyte [97] who suggested that this was a thin film deposited on the surface. In 1958, fabrication of porous Si was next reported by Turner [98]. In 1972 Theunissen reported that the colouration was due to pore formation in the silicon [99]. Although PSi was first discovered by Uhlir in 1956, small interest shown in porous silicon from the mid-1970's and throughout the 1980's relates almost exclusively to its use for device isolation in integrated circuits [100]. A significant interest in this material is more recent due to its room temperature photoluminescence demonstrated by Canham [95]. Since this time the majority of research into porous silicon has focussed on observations of and explanations for the mechanism of both photoluminescence and electroluminescence from this material, and its potential optoelectronic applications. Proposed, generally accepted and experimentally verified mechanism for the photoluminescence from room temperature porous silicon comes from primarily from quantum confinement in nanocrystalline silicon domains formed during the anodisation process. Photoluminescencs of this type is called "S" band, where S stands for "slow", because the emission lifetime for this material is on atimescale of microseconds. It has been widely studied mainly for its optical properties, but since the interest of the scientific community has been triggered to its potential sensor applications. PSi has shown many advantages with respect to standard materials. The most noticeable is the very large specific area, reaching 900 $m^2 \cdot cm^{-3}$ for nanometer sized porous silicon. This structure can serve as a gas sensing depending on the pore morphology and additional catalyts. In particular porous silicon appears to be a good candidate for coupling with biological molecules because of its peculiar characteristics [101, 102, 103, 104]. The nanoporous structure allows the

loading of large amounts of biological material in a very small volume and the possibility to easily tailor the pore size and morphology as a function of the kind of molecules to be introduced.

When the literature on porous silicon was surveyed in this work, thousands of studies were observed to have been carried out in this field, which was started by Uhlir in 1956 [97]. There were also tens of review papers [105-118] and several books [119-124] regarding formation and characterization of PSi structure. There were also tens of papers concerning porous silicon as a gas sensor or a relative humidity sensor [125-141]. This literature concerning porous silicon as a relative humidity sensor has been reviewed and a summary is given below:

In 1990 Anderson et al., [126] produced a porous layer on p-type (111) silicon wafer with 0.01 Ω·cm resistivity value, in a Teflon assembly at a current density of 10 $mA\cdot cm^{-2}$. They found a 440 % increase in capacitance in response to a humidity change from 0 %rh to 100 %rh.

O'Halloran et al., produced a relative humidity sensor using porous silicon in a membrane type design. Silicon substrates of p-type <100> with resistivity of 2-4 Ω·cm were anodized for 5 minutes in a 40 % HF solution (1:1 ethanol) with a current density of 30 $mA\cdot cm^{-2}$. Using these conditions a porous layer of roughly 1 μm thickness with a porosity pf approximately 65 % is expected, with the majority of pores less than 5 nm in diameter. After porous formation, the silicon was rinsed in DI water and allowed to stand for 2 minutes in a water/ethanol solution to prevent capillary cracking of the porous structure. Besides several upper electrode designs were deposited before anodization to get the best response. But the fabrication of the sensor is complicated including low pressure chemical vapor deposition (LPCVD) and plasma etching [127].

In 2000, Foucaran also developed a humidity sensor from n-type <100> silicon wafer with resistivity of 6×10^{-3} Ω·cm [128]. A gold layer of 200 nm was coated on its back surface. This gold layer forms an ohmic contact with the silicon wafer. This wafer was then cut into squares of 15 mm x 15 mm dimensions. The anodic current density was 30 $mA\cdot cm^{-2}$. The electrolyte used for the porous formation was a mixture of one volume of

ethanol (98 %) and 6 volumes of HF (40 wt. %). These fabrication conditions led to the formation of 54 % porosity. Anodization of samples was performed in a single-tank Teflon circular cell, with a diameter of 0.9 mm, at room temperature. The relative humidity sensor was characterized in a climatic chamber from 10 %rh to 90 %rh. The capacitance of the sensor was measured using a HP-4275A LCR meter at a frequency of 100 kHz. Capacitance change in the specified relative humidity range was 2.6 pF·%rh^{-1}.

Kim has reported [129] the fabrication of humidity sensors using porous silicon layer with mesa structure on the same year.

A small single crystal with several intrinsic junctions is called a mesa. The name mesa, meaning table in Spanish, originates from the similarity in shape with natural mesas, hills with a flat top and steep sides. Apart from larger crystals which might have impurities and crystal defects within the layers, a smaller mesa has a quite homogeneous structure which makes it more suitable for reproducible measurements [129].

To create porous silicon layer, p-type silicon wafers with (100) direction and 0.02 Ω·cm resistivity were used as a substrate. The fabrication of the sensor has mainly ten steps including low pressure chemical vapor deposition (LPCVD). Anodization to form the porous silicon layer was carried out in 25 % HF solution mixed with ethanol at a constant current density of 13 mA·cm^{-2} for 120 s. For capacitance measurements, HP 4263A LCR meter was used at frequencies of 120 Hz, 1 kHz, 10 kHz, and 100 kHz. LCR meter is a measuring instrument of a component with the following measurands namely, inductance (L), capacitance (C), and resistance (R). The capacitance response was inspected in the range of the relative humidity from 25 % rh to 95 % rh. The capacitance response was 18.6 pF·%rh^{-1} at 120 Hz, 11.4 pF·%rh^{-1} at 1 kHz, 3.6 pF·%rh^{-1} at 10 kHz, and there was no change in capacitance values at 100 kHz.

Mai et al. fabricated porous silicon humidity sensors on silicon substrates by anodization with a current density of 5 mA·cm^{-2} for 30 min and 60 min in 2000 [130]. Gold electrodes were prepared on the top surface of porous films by vacuum evaporation. HP4192A-LF impedance analyzer was used to measure conductance and

capacitance of sensors vs. frequency. Samples were annealed at 400 °C in nitrogen ambient. Conductance response was 3.2 $mS\cdot\%rh^{-1}$ at 200 Hz, and 14.0 $mS\cdot\%rh^{-1}$ at 1 kHz. Besides, capacitance change was observed only in the annealed samples.

The same year, Rittersma fabricated a novel surface-micromachined capacitive porous silicon humidity sensor [131]. This fabrication process is rather complex and had many steps. Humidity sensitive area was defined by patterning a 1 µm thermal oxide and a 200 nm LPCVD Si_3N_4 on low-doped 2-10 Ω·cm p-type silicon wafers. The Si_3N_4 was patterned with BHF, followed by a 1 % HF dip. The back surface of the wafers was implanted with a high dose of boron and covered with a metal. The patterning of the metallization follows with the meshed capacitor electrode in one layer. This patterning was done with lift-off process. Chromium, gold and again chromium was deposited. Finally, the free silicon between the meshes of the top electrode is turned into porous silicon with electrochemical etching. Anodization was performed in a 1:1 mixture of 50 % HF and 98 % ethanol. The current density was varied between 5 $mA\cdot cm^{-2}$ and 30 $mA\cdot cm^{-2}$, and the formation time was varied between 30 s and 2 min. The capacitance response was 2.7 $pF\cdot\%rh^{-1}$ at 100 kHz.

In 2001 Das et al. have developed porous silicon humidity sensors on a p-type (100) orientation with resistivity in the range of 1-2 Ω·cm [132]. The anodization was performed in a cell specifically developed for the purpose. The wafers act as a seal between the front and rear regions of the cell. The front region was filled with the mixture of HF and CH_3OH while the rear portion was immersed in KCl solution. The back contact metallization was done by screen printing of silver-aluminium paste and its subsequent thermal annealing. The anodization current density was varied from 2 $mA\cdot cm^{-2}$ to 50 $mA\cdot cm^{-2}$ and HF concentration in methanol was varied from 24 % to 48 %. The capacitance response was 0.09 $nF\cdot\%rh^{-1}$ at 170 Hz, 0.04 $nF\cdot\%rh^{-1}$ at 720 Hz and 1 kHz, 0.01 $nF\cdot\%rh^{-1}$ at 10 kHz, 66 kHz and 103 kHz.

In 2002, E. J. Connolly et al. investigated the suitability of porous polysilicon and porous silicon carbide (SiC) as materials for sensing humidity [133]. They have used two different materials for fabrication of humidity sensors. Thin films of p-type polysilicon and silicon carbide were deposited on standard silicon wafers. Polysilicon

was deposited using LPCVD and silicon carbide using PECVD (plasma enhanced chemical vapor deposition), and doped in situ. The thickness of the films were 4000 °A (polysilicon) and 5000 °A (SiC), and both were doped with boron. Aluminium was evaporated on the back surface of the wafer. The samples made porous by electrochemical etching/anodization using various HF concentrations, anodization current densities in the range 1 $mA \cdot cm^{-2}$ - 50 $mA \cdot cm^{-2}$, and anodization times between 30 s and 10 min. An HP 4194 impedance/gain-phase analyzer meter operated at frequencies between 100 Hz and 100 kHz was used for capacitance measurements. The capacitance response was 100 $pF \cdot \%rh^{-1}$ for polysilicon, and 0.1 $pF \cdot \%rh^{-1}$ for silicon carbide. Although silicon carbide was not found to be as sensitive as porous polysilicon, it had a good linearity over the range from 10 %rh to 90 %rh. Besides, the response time of the porous silicon carbide samples were faster than single-crystal silicon.

Fürjes et al. proposed a new design for porous silicon relative humidity sensor [134]. The structure of this sensor had many steps. First of all, crystalline n-Si islands embedded in the porous silicon layer to get reliable contacts. Aluminium or Cr/Au lines of 10 μm - 12 μm width were contacted to n^+ region formed by additional phosphorous implantation in the n electrodes. A 500 nm $SiN_{1.05}$ layer was used for masking and electrical insulation. The formation of porous silicon was the final step in wafer processing. To improve the mechanical stability, a thin capping layer was formed on the top. Normalized capacitance values of the relative humidity sensor had a variation of 50 over the range from 10 %rh to 95 %rh values.

Yarkin et al. described electrical impedance of humidity sensitive metal/PS/n-Si structures with unoxidized and oxidized porous silicon layer [135]. Frequency and voltage dependencies of impedance will be analyzed in detail which will be useful for better understanding of both fundamental electrical properties of PSi and operation principles of PSi-based humidity sensors. Studied samples were fabricated from n-type c-Si substrates. The back surface of the substrates was ion-implanted to make ohmic contacts. PS layers were formed by electrochemical etching of the substrates. The anodization was performed in HF (48%):C_2H_5OH = 1:1 solution accompanied by halogen lamp illumination of etched surface. Etching current density and time were 5 $mA \cdot cm^{-2}$ and 480 s correspondingly. After anodization the samples were rinsed in

ethanol and dried. The contacts for electrical measurements were formed by Al evaporation on the back surface of the substrate (bottom contact) and on the PS surface (top contacts). Top contact was thin (about 20 nm) and has an area of 3×10^{-2} cm^2. Conductance and capacitance of metal/PS/n-Si structures were measured by HP 4192 impedance analyzer in equivalent parallel circuit mode. Frequency dependence of capacitance was obtained for various oxidation temperatures. Porous silicon structures oxidized at low temperatures had linear capacitance dependence while structures oxidized at higher temperatures showed capacitance change on the order of two to three.

In 2004 Bjorkqvist et al., studied the response of a capacitance-type humidity sensor in which thermally carbonized porous silicon (TC-PSi) layer was used as a humidity sensing material [136]. Humidity behavior of TC-PSi found to be highly dependent on carbonization temperature. The PS layer was made by anodizing boron-doped p+-type Si (1 0 0) wafers with a resistivity of 0.015 Ω·cm - 0.025 Ω·cm in an HF (40 %) and ethanol mixture (1:1 (v/v)). They used 1 min etching time with 50 $mA\cdot cm^{-2}$ current density to achieve a 2.8 µm thick PS layer. The carbonization of PS layer was carried out in a quartz tube (300 ml) under continuous nitrogen gas flush (0.5 $l\cdot min^{-1}$) to which acetylene (C_2H_2) flush (1 $l\cdot min^{-1}$) was added for 15 min before the heat treatment and during it. The thermal treatment (10 min) was performed at 520 °C, in a constant temperature oven. Carbonized PS was cooled down to room temperature under N_2 flow before contact with ambient air. After carbonization, gold electrodes (20 nm thick) were sputtered on the top of the TC-PS surface. The distance between the rectangular electrodes was 0.5 mm. The electrical parameters were measured using a 1920 Precision LCR Meter (QuadTech) operated at 0.1 V. A number of frequencies from 35 Hz to 100 kHz were used. Capacitance change of 120 nF was observed during relative humidity values from 6 %rh to 84 %rh. Hysteresis effect was examined at three different frequencies, namely at 55 Hz, 120 Hz and 1 kHz while changing relative humidity values from 5 %rh to 95 %rh. At 84 %rh there was a hysteresis of approximately 50 nF.

In 2005, Di Francia et al. fabricated porous silicon based relative humidity sensor [137]. Single-crystal <100> phosphorus-doped, n-type silicon wafers with 1 Ω·cm resistivity, and 525 µm thick has been used in this work.

Figure 1. 13 SEM photograph and device photoluminescence spectrum obtained under a blue light which has an excitation wavelength smaller than 500 nm. Pores diameter and distance between pores are 90 nm and 400 nm, respectively

Before anodization, a 1500 °A thick indium tin oxide (ITO) back contact has been deposited on substrates by e-beam evaporation. Porous silicon samples have been fabricated by electrochemical etching, using a solution of hydrofluoric acid: water: 2-propanol (35:40:25, wt %), at a constant current density of 90 $mA \cdot cm^{-2}$, under the light of a 300 W Hg lamp positioned at 15 cm from the sample. The etching time was 2 min. After the etching, samples have been rinsed in pentane and dried using N_2. Porous silicon samples chosen for the realization of our sensor are 10 μm thick and show a porosity of about 30 %. Pores diameter and distance between pores are 90 nm and 400 nm, respectively (see Fig. 1.13).

Porous silicon shows photoluminescence at wavelengths ranging from the ultraviolet to the infrared due to radiative recombination of the carriers confined in nanometer-sized clusters of Si formed and embedded into the PSi layer. Visible PL band (500 nm – 800 nm) requires silicon crystallites to get visible PL from porous silicon. Therefore, PL spectrum suggests that the material has a sponge-like morphology, characterized by nanoporous phase with nanostructure dimension less than 5 nm. Over these samples, Au contacts have been deposited. It consisted of a 1500 °A ITO back contact, the n-type silicon bulk, the porous layer, and the gold contacts.

The relative humidity response was characterized by current versus voltage measurements. At positive bias voltage there was no change in the current value while changing relative humidity from dry air (0 %rh) to 30 %rh. At negative bias voltages current value changes from 10^{-10} A to 10^{-9} A from dry air (0 %rh) to 30 %rh change. Di Francia et al. proposed a novel and simple way to use n-type porous silicon as active material for humidity sensing. The sensor design was very simple regarding fabrication steps.

In 2005, Xu et al. fabricated porous silicon capacitive humidity sensor [138]. Silicon structure was nano porous pillar array (NPPA). These samples were prepared by hydrothermally etching (1 1 1) oriented, boron-doped, single crystal silicon (sc-Si) wafers with an area of 20 mm × 20 mm in hydrofluoric acid containing ferric nitrate. The resistivity of the initial sc-Si wafers was 0.15 Ω·cm - 0.2 Ω·cm. The hydrothermal etching was carried out in a mixed solution, with the concentrations of HF and $Fe(NO_3)_3$ are 12.4 $mol \cdot l^{-1}$ and 0.04 $mol \cdot l^{-1}$, respectively. The hydrothermal treatment is performed at 140 °C for 40 min. After the etching process, the Si-NPPA samples are washed with distilled water and dried at room temperature. The electrodes were formed by magnetron sputtering aluminium at 150 °C for 10 min and subsequently heat-treated at 350 °C for 10 min. Different humidity levels were obtained from a series of standard saturated salt (LiCl, $MgCl_2$, $Mg(NO)_3$, NaCl, KCl, and KNO_3) solutions in conical flasks with stopper. The experiments of the capacitance response of Si-NPPA sensor to humidity were carried out by using a LCR Databridge 8501 at two electrical signal frequencies, 100 Hz and 1000 Hz.

The typical morphology of Si-NPPA detected by scanning electron microscope (SEM) is presented in Fig. 1.14. Clearly large quantities of regular, uniformly distributed silicon pillars, which are perpendicular to the surface and well-separated, were generated. The lateral SEM measurement also shows that the thickness of the Si-NPPA layer is about 3 μm, and transmission electron microscopy measurement discloses that all the pillars are nano-porous, similar to the structural characteristics of normal PSi.

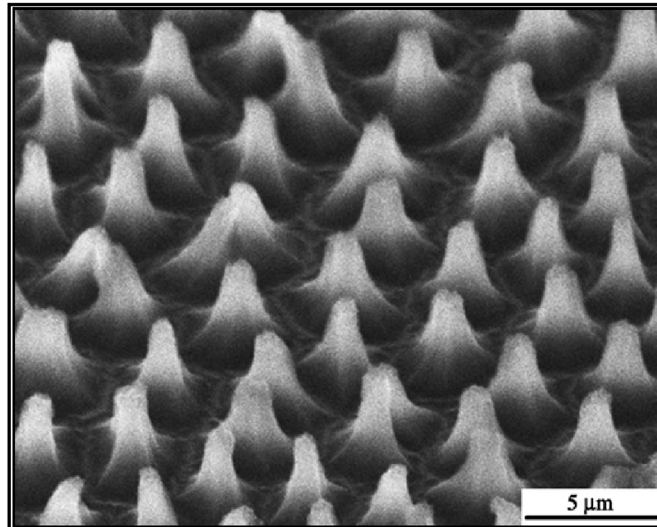

Figure 1. 14 Typical SEM surface micrograph of Si-NPPA

Variation of capacitance with relative humidity from 10 %rh to 95 %rh at 100 Hz and at 1 kHz was found to be 450 nF and 175 nF respectively.

In 2006 Bjorkqvist et al. studied different possibilities to reduce hysteresis in thermally carbonized porous silicon (TC-PS) humidity sensor [139]. Modification of the contact angle, pore size enlargement, and heating of the sensor were all possible ways to diminish the condensation of water into the porous structure of PS.

The PS layer was prepared by anodizing boron-doped p-type Si (100) wafer with a resistivity of 0.015 Ω·cm - 0.025 Ω·cm in an HF (38 %) and ethanol mixture (1:1 by volume). Current density of 50 $mA \cdot cm^{-2}$ was used, which produces porosity of about 65 %. Both free-standing films and samples on substrate were prepared. Free-standing films were etched for 8 min and layers on substrate (humidity sensor) for 1 min, which led to the film thickness of about 20 μm and 3 μm, respectively. After etching, the PSi was dried for 2 h and then thermally carbonized by acetylene. The carbonization was carried out in a quartz tube in a constant temperature oven. Several different temperatures between 520 °C and 835 °C were used to produce variation on the surface chemistry and thus, on a contact angle.

Pore size enlargement of the porous silicon by annealing at high temperature was found to be a usable method to reduce and tune the hysteresis loop into the higher relative humidity values. TC-PS humidity sensor with larger pores showed only slight hysteresis above 75 %rh. Operation of the sensor a few degrees above room temperature also reduced hysteresis significantly. In each case, reduced hysteresis is mostly based on a smaller amount of condensed water. In capacitive-type sensor, this also means lower sensitivity. However, the sensitivity of the TC-PS humidity sensor is still adequate for accurate humidity measurements and better than sensitivity in most commercial capacitive sensors.

Variation of capacitance with relative humidity from 6 %rh to 75 %rh at three different temperatures, 22.0 °C, 25.3 °C and 28.7 °C, was found to be 47 nF, 37 nF and 33 nF respectively.

In 2007, Islam et al fabricated a porous silicon humidity sensor on a p-type silicon wafer <1 0 0> with resistivity of 1 Ω·cm - 2 Ω·cm by standard electrochemical etching in HF-based electrolyte using specially designed PSi formation cell [141].

Figure 1. 15 Photograph of the fabricated porous silicon sensor

The cell was PC interfaced through data acquisition system to control the current density and etching time precisely. Anodization was carried on in dark with the formation parameters of current density 10 mA·cm^{-2}. HF concentration and etching time

were 48 % and 7 min, respectively. Top coplanar inter-digital metal contacts were fabricated by silver screen printing technique with subsequent firing at 500 °C for 40 s. Length of each inter-digital electrode is of 4 mm, thickness of electrodes is 0.5 mm and spacing between each electrode is 0.5 mm. Porosity of the PSi sample was determined by gravimetric technique and is found to be 60 %. The thickness of the PSi layer is 7 μm. Fig. 1.15 shows the photograph of the actual PSi humidity sensor.

Three types of porous silicon layer were studied for analyzing the drift due to aging of the sensors. First one was washed in deionized water immediately after anodization, second one was post oxidized in H_2O_2 solution immediately after anodization for 48 h at room temperature, and last one was post oxidized after washing in deionized water kept at room temperature for 1 year. For all the three samples the formation parameters were the same. For measuring the long-term drift of PS humidity sensor, experiment was performed at a fixed humidity and at room temperature for several days. The experiments were repeated at different humidity level for different periods with all the samples. Change of capacitive impedance with the variation of RH was measured by phase detection circuit.

As a result of measurements, at the end of 15 days sensor output change was 1 V at 98 %rh, at 95 %rh for another 8 days a voltage change of 0.3 V and at 35 % rh for another 10 days a voltage change of 0.3 V was observed. For the sensor oxidized in H_2O_2 solution at 98 %rh, a voltage change of 0.3 V was observed during period of ten days. The last sensor oxidized at room temperature in one year, a voltage change of 0.5 V at 98 %rh was observed during period of ten days.

The drift behavior increased non-linearly on the long-term basis as time progresses for the freshly prepared sample. This may be due to the fact that the sample has highly unstable $Si\text{-}H_x$ bonds, which are easily replaced by more stable Si-O-Si bonds. The rate of oxidation for the fresh sample was faster than the oxidized sample leading to large change in morphology. When the sensor was sufficiently oxidized, the drift for the next 8 days at lower RH was drastically reduced. When a post-oxidized sample was used for the same study, the drift was much smaller in comparison to sample I. This was due to the fact that in highly oxidized environment the sample was sufficiently oxidized and

the PSi layer was appreciably stabilized. Last sample was kept to get oxidized at normal atmosphere for 1 year, the drift showed almost similar nature as in the case of the sample oxidized in H_2O_2. This may be due to the fact that oxidation was a slow process and oxidation at normal atmosphere takes a much longer time. If the data compared for the experimental drift behavior it was apparent that though on a longterm basis the drift was non-linear in nature, in the short-term basis it was assumed to be linear.

As a conclusion, what was observed from the literature is that although porous silicon is used widely as a relative humidity sensor material and much research has been done on this subject, the formation mechanisms of the porous silicon structure is still controversial and subject to both experimental and theoretical work.

As another conclusion, in the literature although some studies have simple procedures, resulting in good capacitance values, they result in structural instability. There are other studies with complex fabrication techniques which tend to finalize their procedures with different and/or complex treatments such as a capping or coating to achieve stable structures. In this work, since the main aim is to fabricate porous silicon with simple fabrication techniques including simple stabilization treatments, a procedure was applied to all fabricated samples unless otherwise stated. This simple fabrication procedure is given in Chapter 2.

In the scope of the thesis work, silicon based porous thin film capacitive type relative humidity sensors are the main concern. The thesis will describe the porous silicon, its structural characterization by means of both microscopic and spectroscopic methods and its electrical characterization as a humidity sensor.

The main motivation of the work done in this thesis was to fabricate a nanoporous silicon relative humidity sensor, to determine its sensitivity (capacitance change with respect to relative humidity), linearity, hysteresis, and mechanaical strength via the capacitance transduction principle, spectroscopy, and structural measurement techniques, and to find a relation between its sensitivity, Raman spectrum parameters, and pore diameter. Pore diameter was determined by image processing and Raman spectroscopic techniques. A simple fabrication procedure together with a good

capacitance change over relative humidity range from 20 %rh to 95 %rh is the main concern.

Under these circumstances, the second chapter pertains to the theory of porous silicon formation and characterization techniques. The pre-fabrication and fabrication steps of porous silicon sensors during the experiments carried on for this thesis work will be given in the third chapter. Also the electrochemical anodization process and the equipment used during the fabrication and characterization will be described in the same chapter.

All the results obtained during the study will be given and discussed in Chapter 4. This chapter includes the evaluations of Raman spectra based on Richter's equations including Raman spectra peak shift, peak intensity, and full width at half maximum (FWHM) values. The outputs of both image processing and Raman spectra analysis used to investigate the diameter of the porous silicon structure is also given. Capacitance values are given for relative humidity range between 20 %rh to 90 %rh. Since SEM and Raman spectra measurements were performed over a limited area upto 2 μm, AFM analysis was also applied in order to determine surface homogeneity upto 10 μm. Finally, photoluminescence spectroscopy was applied in order to confirm that the structure contains nanometer-sized clusters of silicon formed and embedded into the porous silicon layer.

The final chapter summarizes and concludes the results obtained during the study. It also includes suggestions for future work.

2. THEORETICAL INFORMATION ON POROUS SILICON FORMATION THEORIES AND CHARACTERIZATION TECHNIQUES

This chapter pertains to the theories of porous silicon formation in historical order and theoretical information on characterization techniques of porous silicon used throughout this thesis work including Raman spectroscopy, scanning electron microscopy (SEM), optical microscopy, photoluminescence (PL) techniques, and current versus voltage (I-V), capacitance versus voltage (C-V) measurement systems.

2.1. POROUS SILICON FORMATION

Porous silicon (PSi) layer prepared by electrochemical or chemical etching of crystalline silicon in acid or alkali based solutions [122, 142]. Silicon can be etched in either isotropic or anisotropic form depending on the acidic or alkali based etchant in anodization solution, respectively. Etching behavior of silicon is represented in Figure 2.1 depending on the material used in solution.

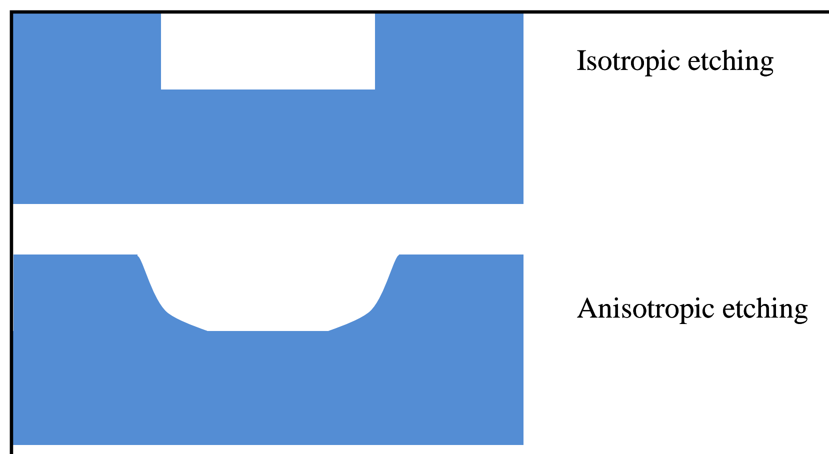

Figure 2. 1 Isotropic and anisotropic etching behaviour of silicon

Anodization solution materials, such as hydrofluoric (HF) acid, potassium hydroxide (KOH), Tetra Methyl Ammonium Hydroxide (TMAH), HF/Nitric/Acetic acid (HNAA),

Ethylene Diamine Pyrochatechol (EDP), Hydrofluoric Nitric acid (HNA), and Phosphoric acid (H_3PO_4) can be used during etching of the silicon wafer [119, 122, 142].

Silicon is thermodynamically unstable in air or water, and it tends to react spontaneously to form a native oxide layer. The simple empirical formula is silicon dioxide, SiO_2.

$$Si + O_2 \rightarrow SiO_2 \tag{2.1}$$

Silicon dioxide on the surface of a silicon wafer protects the underlying silicon from further oxidation. Therefore, since it is an electrical insulator, it forms passivating films on crystalline silicon. If the surface of a material is passive then it is less affected by environmental factors such as air. Therefore formation of porous silicon requires an additive in the solution to dissolve the oxide layer and allow electrochemical reaction to continue. Si-F bond is the only bond stronger than Si-O bond, and it drives the main chemical dissolution reaction. In the presence of HF acid together with water, silicon dioxide spontaneously dissolves as SiF_6^{-2}.

$$SiO_2 + 6HF \rightarrow SiF_6^{-2} + 2H^+ + 2H_2O \tag{2.2}$$

The silicon hexafluoride ion (SiF_6^{-2}) is stable dianion that is highly soluable in water. Thus fluoride is the most important material of the anodization solution used in the formation of porous silicon. In the absence of fluoride, dissolution of insulating oxide is impossible which led to cease of the electrochemical corrosion reaction [122].

The reaction of silicon with water is analogous to the reaction of metallic sodium in water: elemental silicon is electronegative enough to spontaneously liberate hydrogen from water. However, silicon does not dissolve in acidic solutions, even if fluoride ion present which removes the passivating layer of SiO_2. Dissolution of silicon in aqueous HF is slow unless strong oxidizing agents such as O_2 or NO_3^- are present in the anodization solution or the reaction is driven by electrochemistry, because corrosion becomes kinetically limited by the passivating nature of surface hydrates.

As a summary, since silicon is stable in acidic solutions and its surface is passivated by a native oxide, it can only be etched in a solution containing fluoride. In addition of an anisotropic etching characteristic, HF acid is preferred as a basic component in anodization solution which was also used throughout this work.

Hydrogen gas is evolved as a by-product from the chemical reaction between silicon and HF acid. If only HF acid is present in the anodization solution, hydrogen gas bubbles are going to stick onto the silicon, which causes retardation the reaction but also to induce lateral and in-depth inhomogeneity. To improve the porous silicon layer uniformity, these hydrogen gas bubbles must be removed. This problem is solved by adding a surfactant agent to the anodization solution containing HF acid. Mostly used surfactant or wetting materials are laboratory grade ethanol, acetic acid, Mirasol or Triton. Most widely used surfactant agent is laboratory grade ethanol. For efficient hydrogen gas bubble elimination, at least 15 % ethanol must be contained in the anodization solution. Ethanol is used as a surfactant throughout this work.

Porous silicon (PSi) is formed on a silicon wafer in aqueous or non-aqueous electrolytes containing hydrofluoric (HF) acid. Electrolytes containing fluoride, silicon is stable at open circuit potential, while electrochemical dissolution takes place for anodic potentials. For anodic current densities below the critical current density J_{PSi} porous silicon is formed and the electrolyte-electrode interface is covered by Si-H bonds which were determined by IR spectroscopy. During the dissolution process silicon interface atoms have one Si-O bond and three Si–Si bonds as given in chemical reaction (2.5) and as depicted in Figure 2.2. If a silicon atom at the surface establishes a bond to a fluorine atom it is immediately removed from the surface. This fast removal of Si–F species can be ascribed to the weakening of the Si backbonds induced by the strong polarizing effect of F. Therefore, the main reactions responsible for the formation of porous silicon are the reactions of Si-Si, Si-H, Si-O, and Si-F bonds at the surface of the silicon crystal.

Valence band holes are the key oxidizing equivalents in the reaction which are driven to the surface by the applied electric field and by diffusion. The migration of electrons and holes is influenced by the pore morphology; sharp pore tips generate enhanced electric fields that attract charge carriers. Once a valence band hole makes it to a surface Si atom,

the atom is susceptible to attack by nucleophiles in the solution, primarily F^{-}, and H_2O. A nucleophile is a chemical species that donates an electron pair to an electrophile to form a chemical bond in relation to a reaction. Electrophiles are positively charged species that are attracted to an electron rich centre. In chemistry, an electrophile (literally electron-friend) is a reagent attracted to electrons that participates in a chemical reaction by accepting an electron pair in order to bond to a nucleophile.

The electrochemically driven reaction requires an electrolyte containing hydrofluoric acid. Application of anodic current oxidizes a surface silicon atom, which is then attacked by fluoride. The net process is a 4 electron oxidation, but only two equivalents are supplied by the current source. The other two equivalents come from reduction of protons in the solution by surface SiF_2 species. Pore formation occurs as Si atoms are removed in the form of SiF4, which reacts with two equivalents of F^{-} in solution to form $SiF^{2-}{}_6$.

The electronegativity of these elements together with the relative strengths of these bonds determines the relative stability of each bond on a silicon surface. The Si-F bond is highly reactive. Oxygen and fluoride are electronegative elements and form more polar silicon bonds which make silicon atom susceptible to nucleophilic attack. Si-H and Si-C species tend to passivate the silicon surface in aqueous solutions. The surface of freshly prepared porous silicon is covered with a passivating layer of Si-H bonds, together with Si-F and Si-O species in minor quantities.

Electrochemical reaction occurred at silicon surface involves a competition between Si-O, Si-F, and Si-H bond formation. Si-O bonds are chemically attacked by F^{-}, and only form when the diffusion of F^{-} to the silicon surface cannot keep up with the rate of delivery of valence band holes, as in the case of electropolishing. Electropolishing, which occurs at high current density values or at low HF concentration in anodisation solution, involves the complete dissolution of silicon without pore formation. When the concentration of HF in the anodisation solution is low, oxidized silicon aoms are generated at the surface too rapidly to be attacked by F^{-}, and water molecules take over the role of nucleophile. The reaction mechanism shifts to Si-O formation, and reaction transitions from 2-electron to 4-electron. The lack of fluoride ions means that the oxide cannot be removed from the surface, and this insulating oxide terminates pore propagation. The valence band holes are

then required to move into the porous silicon structureto oxidize a silicon atom which is accessible to the fluoride ions in the anodisation solution. The result is thinning of the silicon filaments close to the porous silicon/crystalline silicon interface, undercutting the porous silicon layer.

Summary of the important pore-forming mechanisms in porous silicon can be listed as:

- The (100) crystallographic face contains strained Si-H bonds, and it tends to be more prone to dissolution compared to other orientations.
- Si-H bonds in the (111) face, which are perpendicular to the surface, are more stable.
- Different reactivity of the faces leads to “crystallographic” priority during pore propagation resulted that (100) is the main direction of propagation.
- The high radius of curvature at the bottom of a pore generates a region of enhanced electric field which attracts valence band holes.
- The space-charge region is a region in which carriers are depleted due to band bending at the silicon/electrolyte interface. It increases with decreasing dopant density, therefore this mechanism is a primary determinant of macropore size for low-doped n-type Si.
- As the diameter of a silicon filament decreases, its resistance for transport of valence band holes increases. At a critical filament diameter (typically a few nm for p-type silicon), injection of the hole into the solution becomes more favorable, and holes do not propagate further down the length of the nanowire. This mechanism is responsible for the lack of electrochemical dissolution of a microporous layer, once it is formed.
- The increased band gap resulting from quantum-confinement excludes valence band holes from these smallest regions of the porous silicon matrix.
- If there are no fluoride ions available at the silicon/solution interface, silicon oxide forms at the interface. Valence band holes are then excluded from this region and they continue to oxidize the silicon/porous silicon interface. This causes pore widening and, ultimately, lift-off of the porous layer (electropolishing).

In contrast to a semiconductor where a current is caused by the movement of free electrons and holes, an electrolyte can be understood as a phase through which charge is carried by the movement of ions.

Any transfer of a charge between the electrode and the host ion in the electrolyte is accompanied by a chemical reaction. If an electron moves from the electrode to the solution, the host ion is reduced. If it moves in the other direction the host ion is oxidized. The electron is a term used in physics as well as chemistry. This is in contrast to the concept of a hole, a positive charge carrier, which describes the behavior of an electron vacancy in the periodic potential of a semiconductor crystal. This term, however, loses its meaning at the interface to the electrolyte. Concerning the chemical reaction, any hole crossing the interface can be replaced by an electron going in the other direction. Energetically, however, there is a difference, because the injection of an electron from the host ion into the silicon conduction band (CB) requires energy 1.1 eV larger than that required for a hole in the valence band (VB) going in the other direction. In many cases the interaction of holes with the electrode surface can be understood if two holes at the interface are replaced by one broken bond of a surface atom.

The movement of charges in space and changes in energy occur in different ways in the semiconductor and the electrolyte. In a solution the energy levels itself fluctuate in energy due to thermal fluctuations of the surrounding solvent dipoles, carrying the electron with it.

The current-voltage (I-V) characteristic of a semiconductor-electrolyte contact is determined by both the semiconducting nature of the electrode, as well as by the ionic and molecular species present in the electrolyte. The current density at the electrode for a certain potential is limited by the reaction kinetic at the interface, or by the charge supply from the electrode or the electrolyte.

The silicon atoms of the electrode do not participate in the chemical reaction in the cathodic currents regime. A p-type electrode which is kept in the dark shows only a small reverse current density in the cathodic regime. If defects are present in the electrode surface, this small dark current increases by orders of magnitude.

In the open circuit potential (OCP) region, the electrode is inert for an HF electrolyte without an oxidizing agent, because no chemical reaction occurs at the front (emitter) at this potential range. The OCP depends on illumination condition, substrate doping density, HF concentration, and dissolved oxygen concentration.

When a semiconductor electrode is brought in contact with an electrolyte, equilibrium is established through a mechanism of charge transport between the two phases, leading to a band bending which continues until the Fermi level of the semiconductor equals the Redox Fermi level of the electrolyte. This transport is carried out by electron transfer through the conduction band or by hole transfer through the valence band. In general, the net result of the redistribution of charges at the interface is the formation of an electric double-layer, with three distinct zones: the space charge region (SCR) in the semiconductor side, the Helmholtz region (HR) and the diffuse region (DR) in the solution side. If the Fermi level of the semiconductor is grater than the Redox Fermi level of the electrolyte, the process called inversion take place: there is a flow of electrons from the semiconductor into the electrolyte. As a consequence, electrons are drained from the surface, giving rise to a depletion layer in the semiconductor, (SCR), which typically extends from a few tens to a few hundreds of nm in depth. Since surface is depleted from electrons, it remains positively charged. The electric field in this region is a function of the distance from the surface. The space charge region within the semiconductor leads to a dependence of electron energy on distance, which is referred to as band bending at the surface. Band bending causes the majority carriers at the surface to move towards the bulk of the semiconductor, while holes are attracted to the surface. The semiconductor electrodes is then said to be in depletion mode because electrons are drained away from the surface. Therefore, it can be assumed that the number of thermally generated minority carriers is not sufficient to produce inversion; the electrode is therefore under depletion if kept in the dark.

A hole approaching the interface initiates the divalent electrochemical dissolution of a silicon surface atom at the emitter in the regime of anodic current densities below J_{PSi}. The dissolution proceeds under formation of H_2 and electron injection, as given in Equation (2.3). The formation of PSi structures is confined to this region.

Under anodic potentials in acidic electrolytes free of fluoride, silicon is passivated by formation of an anodic oxide under consumption of four holes (h^+), according to the reaction:

$$Si + 2H_2O + 4h^+ \rightarrow SiO_2 + 4H^+ \qquad (2.3a)$$

$$SiO_2 + 6HF \rightarrow H_2SiF_6 + 2H_20 \qquad (2.3b)$$

In acidic electrolytes with fluoride, silicon is stable at open circuit potential (OCP), while electrochemical dissolution takes place for anodic potentials. For anodic current densities below the critical current density, J_{PSi}, PSi is formed and the electrolyte-electrode interface is found to be Si–H covered. Species active in the dissolution process are HF, $(HF)_2$ and HF_2^- . A dissolution reaction proposed for this regime is:

$$Si + 4HF_2^- + 2h^+ \rightarrow SiF_6^{2-} + 2HF + H_2 \qquad (2.4)$$

For anodic current densities above J_{PS} tetravalent electrochemical dissolution of the electrode is observed. The chemical reaction proceeds in two steps, first the electrode is anodically oxidized, and then the oxide is chemically dissolved in HF. Overall reactions, as given in Eqs. (2.3) and (2.5), show that the dissolution of one silicon atom consumes four holes. If the anodic potential is increased, the current density becomes larger than J_{PS} and dissolution occurs via an intermediate anodic oxide film. Hence the reaction can be separated into electrochemical oxide formation according to reaction (2.2) and chemical dissolution of the oxide due to HF, $(HF)_2$ or HF_2^- [143]:

$$SiO_2 + 2HF_2^- + 2HF \rightarrow SiF_6^{2-} + 2H_2O \qquad (2.5)$$

For the p-type substrate, which is kept in the dark, a significant number of electrons are collected at the backside which indicates that electrons are injected during the tetravalent dissolution reaction. In the regime of oscillations the electron injection current is found to oscillate.

In this regime, the current density exceeds J_{PS} and the simple diode behavior disappears. I-V characteristic shows a more complex structure with another current maximum and a region of current oscillations. These features of the I-V curve are related to the properties of a thin anodic oxide present on the electrode surface. The current is not limited by charge supply from the electrode any more, but by diffusion in the electrolyte.

When silicon is chemically or electrochemically etched in HF acid containing solutions, the exposed silicon surface becomes terminated with H atoms. A characteristic feature of a hydrogen-terminated silicon surface is its water repelling property. Such a surface exhibits a large contact angle for a drop of water and is therefore called hydrophobic. Ethanol used as a surfactant served to enhance the wettability of porous silicon. The term “surfactant” is derived from the words “surface activity” and is used to describe chemical compounds used for the purpose of modifying the surface properties of solutions, specifically in reducing the surface tension. Surface tension arises in a solution due to the attraction between its constituent molecules. This gives the fluid surface a property similar to a stretched elastic membrane. Water has a high surface tension and in organic solutions, actions are known to increase the surface tension of the solution, fluoride ions are known to be particularly effective in this process.

Porous layers formed in ethanoic HF acid solution were more uniform than those formed in HF acid alone. In the anodic dissolution process, hydrogen gas is released from the dissolving silicon surface which was given in reaction (2.4). Therefore, if the surface tension is high, the hydrogen gas is effectively trapped on the silicon surface. The hydrogen bubbles then screen the underlying silicon from solution, preventing etching. Reducing the surface tension has two effects. Firstly, it will reduce the size of the hydrogen bubbles, and secondly allow the formed bubbles to escape more easily from the solution. In addition, HF acid find a way to penetrate into the formed layer more easily, and therefore attack the underlying silicon, increasing the amount of etchant at the etch front and therefore the etch rate. Hydrogen bubbles can also be trapped within the forming pores disrupts the silicon/electrolyte contact resulting in the current flow being diverted away from the main pore tip thereby causing more side-pore growth.

Therefore, electrochemistry of silicon in an anodization solution must contain HF acid, water and ethanol. Complete electrochemical anodization reaction is still not clear but the most recent reaction mechanism proposed by Kolasinski [144] is given in Figure 2.2.

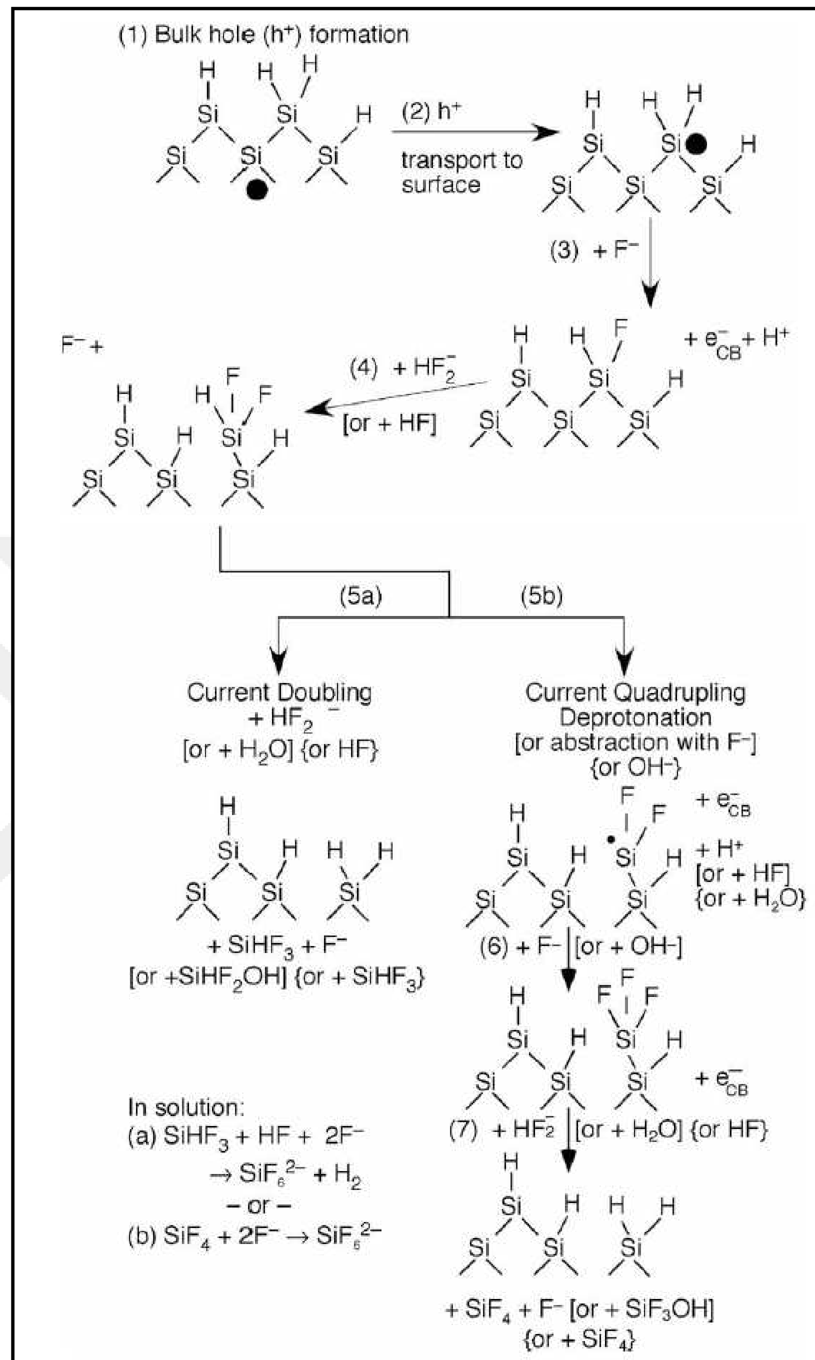

Figure 2. 2 Reaction of porous silicon formation in anodization solution containing HF acid and water (Adapted from [144])

HF normally etches SiO_2 and terminates on Si. By biasing the Si positively, holes can be injected by an external circuit which will oxidize the Si and form hydroxides which the HF can then dissolve. This produces an excellent polishing etch. If the etching is performed in

very concentrated HF (48 % HF, 98 % EtOH), then the silicon does not fully oxidize when etched, and porous silicon is formed, which appears brownish.

Increasing the wafer bias above the OCP will increase the etch rate by supplying holes which will oxidize the Si. Increasing the wafer bias further will reach the passivation potential (PP) where SiO_2 forms. This passivates the surface and terminates the etching. The HF acid and H_2O solution does not exhibit a passivation potential, since the SiO_2 is dissolved by the HF.

Current is the driving force in the reaction pushing the charge carriers to the silicon surface where the reactions occur. Higher currents will cause a greater flux of carriers and therefore will accelerate the reaction – however if too many carriers arrive, the oxidation of the surface will greatly exceed dissolution of silicon, and electropolishing will dominate. It is known that the charge supplied to the silicon is proportional to the amount of porous silicon formed.

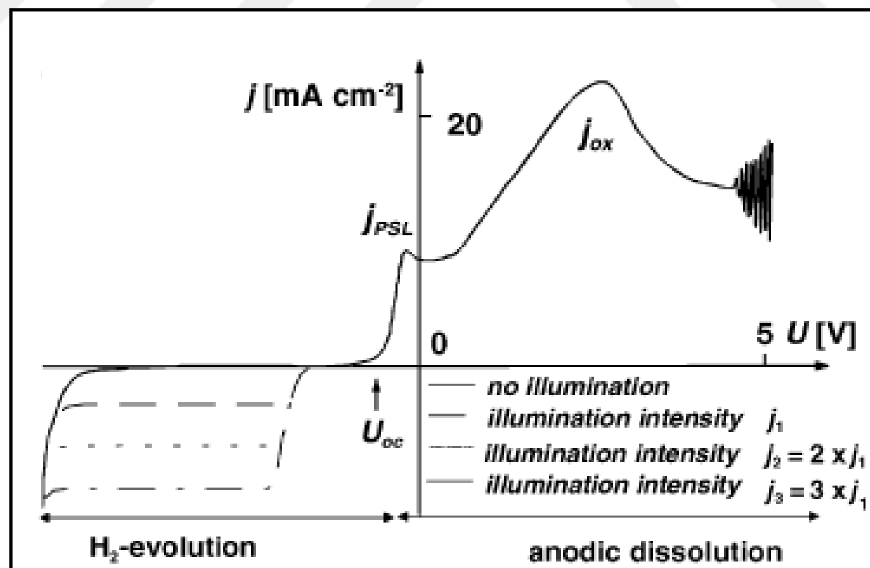

Figure 2. 3 Representative I-V curve for p-type silicon in aqueous HF acid solution (Adapted from [116])

The main understanding of porous silicon formation still comes from I-V relationships and a basic knowledge of silicon electrochemistry is essential to understand the fundamentals

of pore formation. I-V relationship of p-type silicon substrates formed with aqueous HF acid solutions exhibit the same trend as given in Figure 2.3 and Figure 2.4 [112, 116].

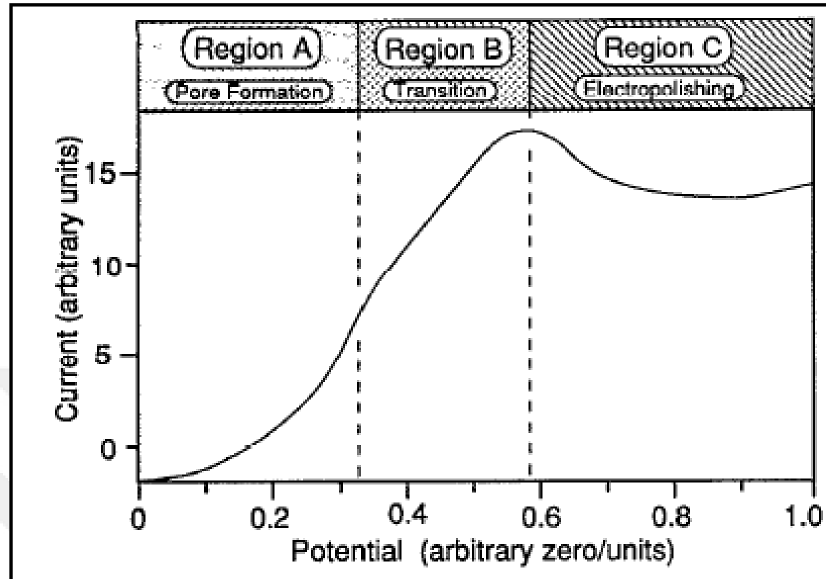

Figure 2. 4 Representative anodic I-V relationships for silicon in HF showing the salient regions of dissolution. In region A pore formation occurs, and in region C silicon electropolishes (Adapted from [112])

Electrochemical anodization of silicon samples has three characteristic regions. The region up to first peak is named as pore formation. The region up to second peak is named as transition where there are two competing reactions namely pore formation and electropolishing of silicon. After the second peak the region is named as electropolishing which lead to smoothing of the surface. Region B is a transition zone between regions A and C. Scale units and zeros are arbitrarily chosen and depend on silicon sample and experimental conditions.

Electropolishing and electrochemical pore formation are two main reactions observed in electrochemistry of silicon. In the former case the rate-limiting species in the chemical reaction is HF, it is obvious that hillocks will dissolve faster than depressions because they are more exposed to the source of the rate-limiting species. If the reaction is limited by charge (holes) supply from the electrode as in the latter case, the center of a depression will dissolve faster. This process will lead to pore formation. [145]. Electropolishing of

semiconductors commonly involves the presence of a thin oxide film as in the case of silicon. In the electropolishing region further from the peak value, there are oscillations at higher voltages. Current oscillations at silicon electrodes under potentiostatic conditions in HF were already reported in one of the first electrochemical studies of silicon electrodes [98] and ascribed to the presence of a thin anodic silicon oxide film. Several groups have studied this phenomenon since this early work, and a common understanding of its basic origin has emerged, but details of the oscillation process are still controversial.

A key to understanding the oscillation process is the observation that two forms of anodic oxide are present on the electrode: a dense, slow dissolving type of anodic oxide and a soft, fast dissolving type.

A first indication of different dissolution rates is the shape of the I-V curve itself. For current densities above J_{PSi} it is mainly determined by the dissolution rate of the thin anodic oxide. The existence of the current maximum (first peak in Fig. 3.4) and the current minimum (first bump in Figure 2.4) can be interpreted as an indication of anodic oxides of different dissolution rates [147].

The oxide etch rates at different times of the oscillation cycle can be determined in situ, if the time delay between switching the electrode to OCP and the appearance of hydrophobic surface conditions is measured. Despite the fact that the oxide thickness changes by only about 20 %, the time required for etching of the total oxide thickness varies by a factor as high as 3. This modulation of the oxide etch rate itself is sufficient to generate an oscillation loop.

The initial formation of an oxide with a low dissolution rate leads to an increase in potential under galvanostatic conditions with increasing oxide thickness. If the potential across the oxide is constant over the whole sample area, which is fulfilled for a good conductivity of electrolyte and substrate, the oxide becomes very homogeneous in thickness. This is a self-adjusting process, because the electric field across a thin oxide would be higher than for an area with a thicker oxide, generating a higher oxide growth rate at the thin spot until a homogeneous oxide thickness is reached. This effect is sufficient to synchronize the oscillations.

At a certain thickness a change in the oxide morphology occurs, which transforms the dense oxide into the soft, porous form. After this change the anodic oxide shows a high permeability for ions of the electrolyte. This leads to the sudden drop in the potential and an increase in etch rate. The etch rate exceeds the growth rate and the total oxide thickness decreases until the fast etching layer is etched away. The next slow etching oxide is exposed to the electrolyte and its thickness increases again, and so on.

There is strong evidence for such a layered structure of the oxide and the transient behavior of their etch rate, which is proposed to be the driving force of the oscillation process [148, 149]. However, the microscopic origin of this change in oxide morphology is as yet unidentified. Different oscillation models are under discussion.

Typically, etch rates for silicon with different are: (100) > (110) > (111). There is an etching hierarchy from easily etched to hardly etched regarding doping of silicon starting from n+, p+, p and n illuminated, p in dark, n in dark.

The rate of porous formation is unaffected by the concentration of HF acid, but the porosity changes dramatically, increasing with a decrease in the HF acid concentration.

The porosity of the porous silicon layer can be varied by changing the current density. Fronhoff et al. determined the porosity values for different current densities for p-, p and p+ silicon material ranging from 20 % up to 80 % [150].

The influences of parameters on porous silicon layer properties were given in Table 2.1. Porosity, etching rate, electropolishing threshold information gathered from literature given in references [105-143].

This information was also supported by the work carried out in this thesis work as given in the experimental and also in the results sections.

Table 2. 1 Parameter dependences on the properties of porous layer

Increase of	Porosity	Etching rate	Electropol-ishing threshold	Raman spectrum peak wavenumber shift	PL spectrum peak energy
HF concentration	decrease	decrease	increase	decrease	decrease
Ethanol concentration	decrease	decrease	increase	decrease	decrease
Current density	increase	increase	-	increase	increase
Anodization time	increase	Almost constant	-	increase	increase
Wafer doping (p-type)	decrease	increase	increase	NA	NA
Wafer doping (n-type)	increase	increase	-	NA	NA
Temperature	-	-	increase	-	-

Porous silicon (PSi) is obtained by partial electrochemical dissolution (anodic) of Si substrates in hydrofluoric acid (HF) based solutions. In this process, the amount of material etched from the substrate surface can range from 20 % to 90 %, and layers characterized by a wide range of porosity are obtained. The silicon wafers with resistivities of 0.005 $\Omega\cdot$cm to 15 $\Omega\cdot$cm are expected to have doping concentrations of 3.62×10^{19} atoms$\cdot$cm^{-3} to 1.03×10^{15} atoms$\cdot$cm^{-3}, respectively. The space charge region (SCR) width of the wafers under the etching conditions is critically determined by the distribution of dopants in the wafers. In addition, the charge carrier transfer type is also varied during the etching process with the doping concentrations [151]. As a result, such difference in the doping levels seems to bring up the morphological variation. Porous silicon (PSi) formation is still a controversial phenomenon and there is no unique theory which explains all the structural features resulted from the anodization processes which have different formation parameters.

2.2. POROUS SILICON MORPHOLOGY AND FORMATION THEORIES

Proposed formation theories are mostly related to the pore dimensions which were defined in UIPAC document as follows [152]:

- Microporous structure (1 nm – 10 nm)
- Mesoporous structure (10 nm – 50 nm)
- Macroporous structure (50 nm – 100 nm)

Pore dimensions are also identified according to their pore diameters as follows:

- Nanoporous silicon (1 nm – 100 nm)
- Microporous silicon (1 μm – tens of μm)
- Hybrid micro-nanoporous silicon

The terms “nanoporous”, “nanopore”, and so on have become commonly used in recent years. It would be meaningless to follow the SI convention for the Greek prefixes, which would require that a nanopore be 1000 times smaller than a micropore. While it currently carries no officially accepted definition, general usage indicates that a “nanomaterial” has structural features of the order of 100 nm or less. Thus the term nanoporous can be considered to be a general descriptor referring to any of the above macro - , meso - , or microporous materials with pore sizes less than 100 nm. In fact, this is more in line with the original Greek meaning of nano, which translates as “dwarf” [14-117, 153].

The basic conditions for electrochemical pore formation in a homogeneous electrode are a passive state of the pore walls and an active state, which promotes dissolution, at the pore tip. Dissolution of a silicon electrode in hydrofluoric acid will occur if holes (h^+) are present at the surface. Consequently a surface area which is depleted of holes will be passivated.

Hole depletion will only occur if any hole that reaches the interface is immediately consumed in the dissolution reaction. This requires that the chemical reaction is not limited by mass transfer in the electrolyte. This condition is fulfilled if the current density is below

a critical value J_{PS} which is given by the following equation, in which J_{PS} is in A·cm^{-2}, c in wt.% HF, T in K, E_a = 0.345 eV, k = 8.6171 x 10^{-5} eV·K^{-1} and A = 3300 x (wt.% HF)$^{-3/2}$ A·cm^{-2}:

$$J_{PS} = A \cdot \exp(-E_a/kT) \cdot c^{3/2} \tag{2.6}$$

Figure 2.5 shows which kind of porous structure can be expected depending on current density and doping density of the bulk silicon. For example for a low doped n-type electrode anodized at a current density smaller than J_{PS}, a superposition of a microporous and macroporous structures can be expected.

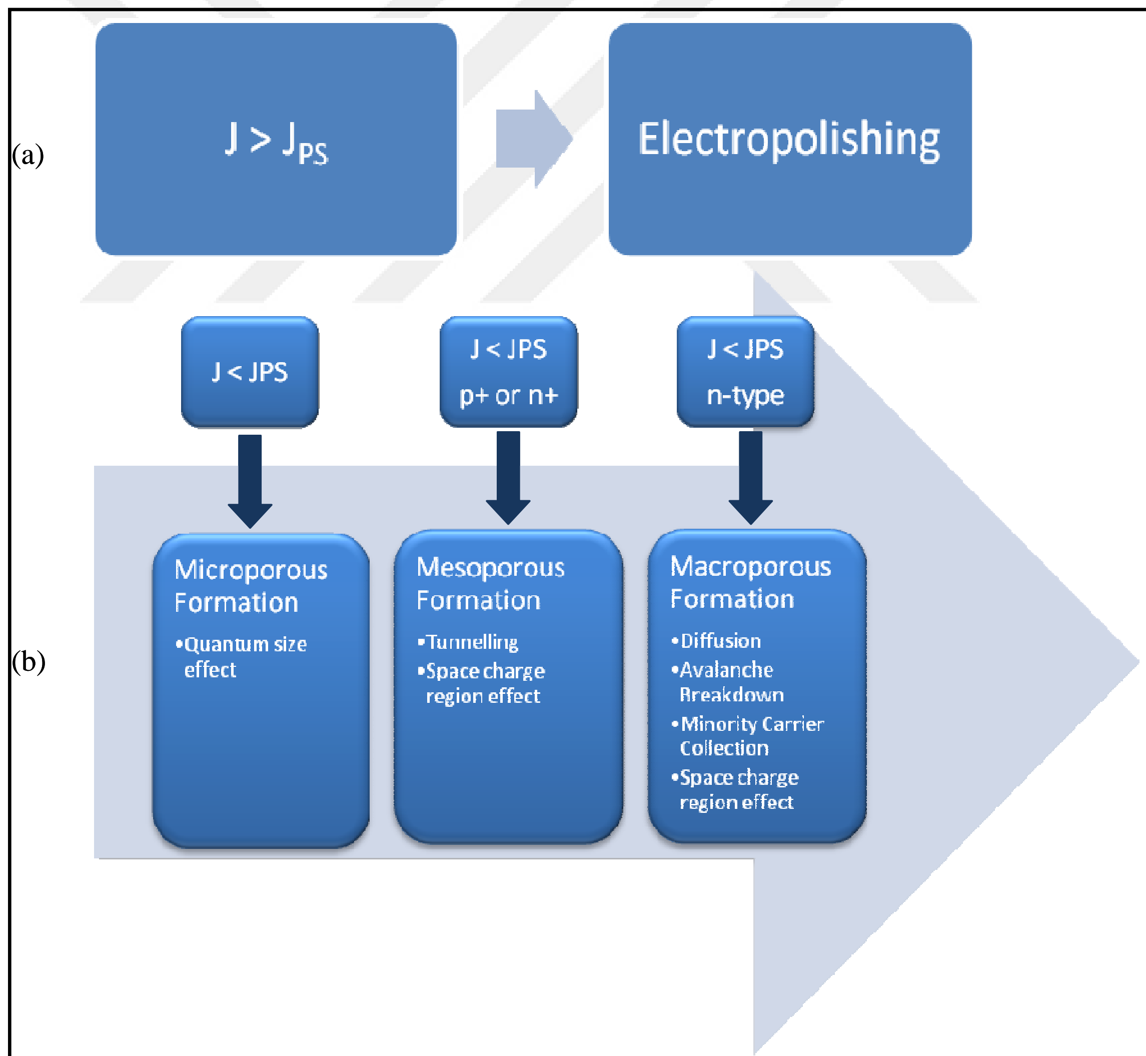

Figure 2. 5 Formation conditions and responsible effects for porous formation

It also gives information on which effect is responsible for the formation of micro-, meso, and macroporous silicon structure. Quantum-size effect is responsible for the formation of microporous structure. Space charge region (SCR) effect is responsible for the formation of both mesoporous and macroporous structure.

For current densities greater than J_{PS} the reaction is limited by ionic mass transfer, which will lead to a surface charge of holes and to a smoothing of the electrode surface (electropolishing).

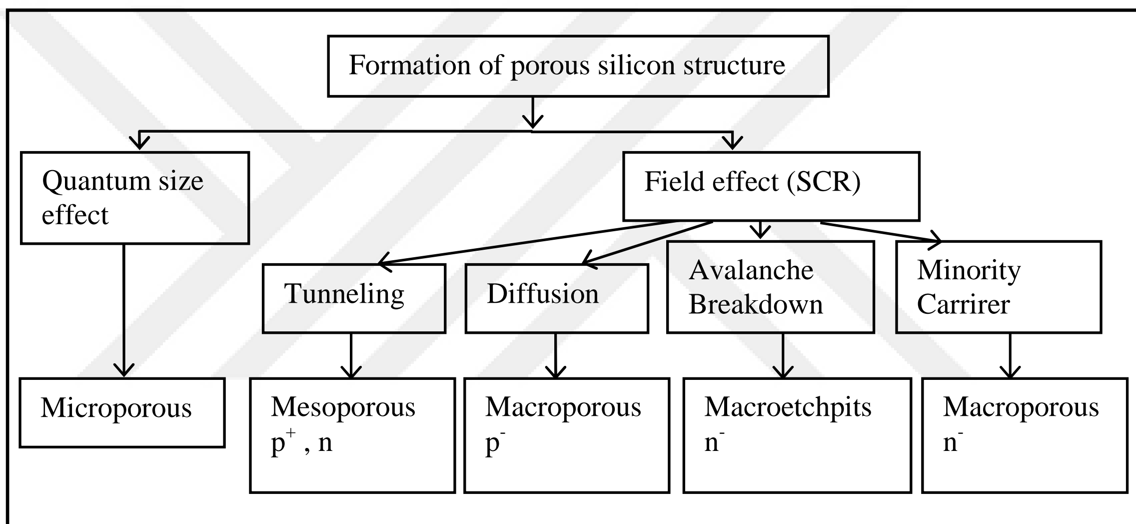

Figure 2. 6 Effects responsible for the formation of pore wall passivation and passivation breakdown at the pore tip with resulting porous structure (Adapted from Ref. [163])

Figure 2.6 give about the effects which are responsible for the formation of pore wall passivation (second row) and passivation breakdown at the pore tip (third row) with resulting porous structure together with substrate doping type (bottom row). For current densities smaller than J_{PS} holes are depleted at the surface due to two different mechanisms:

i) A surface region which is depleted of mobile charge carriers (space charge region) will form if a semiconductor electrode is in contact with an electrolyte. Under anodic bias this layer is thick for low doped n-type, is thin for highly doped p-type or n-type, and does not exist for p-type silicon. Consequently, the size of the pores will scale according to the

depletion region width and therefore to resistivity. These pores are designated according to their size macroporous or mesoporous.

ii) A depletion of holes is also expected, if the dimension of a semiconductor particle, wire, or sheet is below the Bohr radius of an exciton (a few nm). In this case holes are depleted independently of doping density due to quantum confinement. These small pores are designated microporous.

Both mechanisms i) and ii) are independent of each other and may coexist, resulting in a superposition of microporous and mesoporous or macroporous and silicon structures.

Energy band diagram of crystalline silicon, porous silicon, and silicon nanocrystallites is depicted in Figure 2.7.

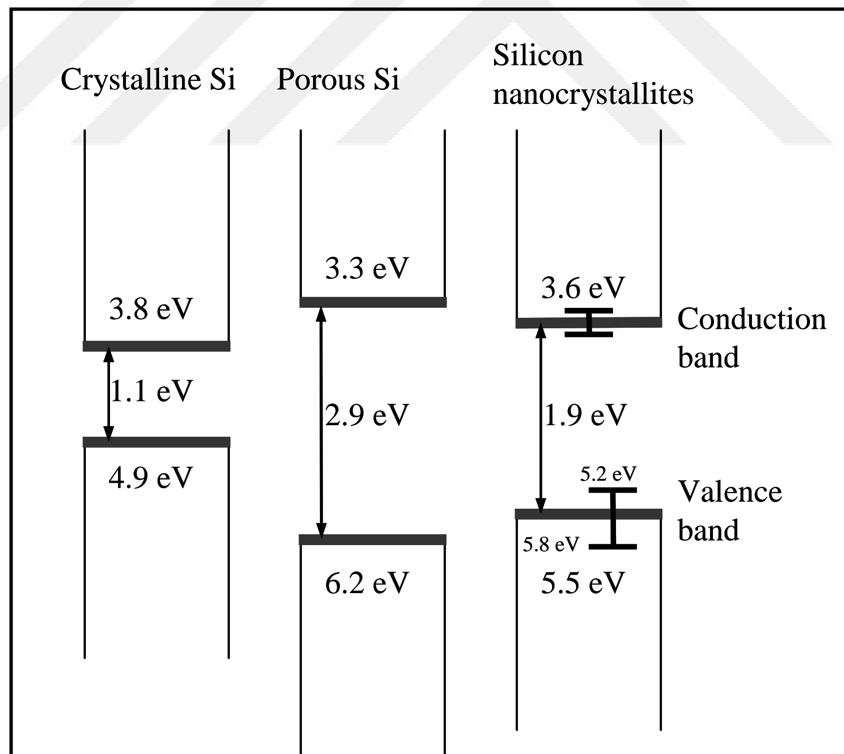

Figure 2. 7 Energy band diagrams of crystalline silicon, porous silicon, and silicon nanocrystallites (Adapted from Ref. [153])

2.2.1. Formation theories and morphology related with microporous structure

In 1992, Lehmann proposed a formation mechanism for microporous silicon which is based on a depletion of holes in the porous region due to quantum confinement. This theory allows predictions concerning the dependence of the porous morphology on the formation conditions [154].

Microporous structures formed by hole depletion due to quantum confinement (QC) effect was published in the literature extensively [95, 112, 114, 119-124, 142, 155-163]. The proposed formation mechanism of microporous silicon is based on the fact that holes are necessary for the electrochemical dissolution process of silicon.

If the dimensions of a silicon crystallite are reduced to a few nanometers, its bandgap increases as a result of quantum confinement effect which is explained in the next section. The same holds true for the thin silicon walls separating the micropores.

Since the band gap in porous silicon is increased compared to bulk silicon, holes need the additional energy E_q to penetrate into the porous layer. Band gap energies of crystalline silicon, porous silicon, and silicon nanocrystallites were depicted in Figure 2.7. The increase in bandgap energy E_q in the wall region compared to the bulk electrodes produces an energy barrier for holes E_{PS}. If E_q is larger than the bias-dependent energy of holes, the porous region becomes depleted of holes and therfore passivated against further dissolution. This is sketched in Figure 2.8.

It is then energetically more favorable for a hole to enter the electrolyte directly (solid arrow), than via the porous structure (dotted arrow). For the case of pore formation due to QC no additional effect is required to explain the active state of the pore tip, which is in contrast to passivation by a space charge region (SCR). The pore tip is active, because it is in contact with the unconfined bulk electrode, while the pore walls are passive due to the close spacing of the pore tips. These will result in a distinct porous-bulk interface, and significant porosity values. If the formation current density is increased, the bandgap of the porous structure is expected to increase. A higher current density requires an increase in the anodization bias, thus holes have more enrgy to cross the barrier E_q. Since E_q is a

function of the size of the microparticles that form the porous skeleton, one can conclude that an increase of the formation bias will result in an increased band gap and a decrease of particle size in the porous layer. Additional holes are generated in the porous layer while the anodic bias is applied, which will promote further thinning of the skeleton. Therefore, the nanometer sized structures that form the porous skeleton will be etched further, until their bandgap energy is large enough to become passivated again. The described effect can only be expected for photon energies that are in excess of the gap energy in the microporous silicon layer.

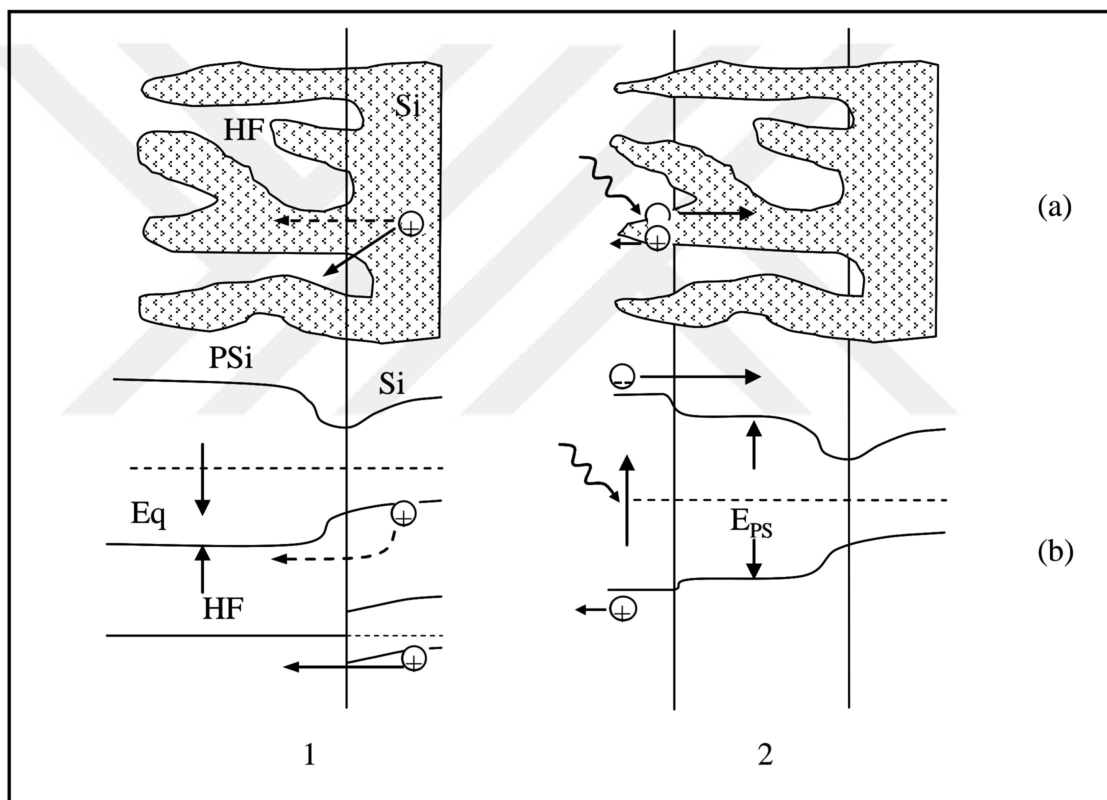

Figure 2. 8 (1a) Sketch of the interface between porous silicon and bulk silicon. There are two possibilities for hole to cross the interface as shown as arrows. (1b) The corresponding energy band diagrams. The energy required for a hole to enter the anodization solution via the porous silicon structure is larger by E_q than the energy that is required to enter the anodization solution directly. (2a) Photons of energy larger than E_{PS} will be absorbed in the topmost region of a porous silicon layer and will generate an electron hole pair. The electron will move to the bulk if an anodic bias is applied whereas the hole will enter the

anodization solution and promote further thinning of the porous structure. (2b) The corresponding energy band diagram

An increase of the band gap in PSi will produce a measurable blue shift of the optical absorption edge. A blue shift of the photoluminescence (PL) peak position due to an increased band gap is also expected for a direct recombination process or a recombination process via centers that show an energy distribution.

An extension of QC model, including tunneling probabilities between the confined crystallites and the bulk, has been developed by Fronhoff [164].

2.2.1.1. Quantum Confinement

Every atom posesses specific, discrete energy levels for electrons. These levels are either empty or occupied by one or two electrons according to the Pauli Exclusion Principle. The energy of the levels can be found by solving the Schrödingers equation. Exact solutions, however, can only be obtained for single electron atoms.

If many atoms are bound together, like in a crystal, their atomic orbitals overlap and form energy bands with a high density of states. Different bands may be separeted by gaps of forbidden energy for electrons. The calculation of electron levels in the periodic potential of a crystal is a many-electron problem and requires several parroximations for a solution.

When a metal particle having bulk properties is reduced in size to a few hundred atoms, the density of states (DOS) in the conduction band changes dramatically, because there is less atoms. The continuous DOS in the band is replaced by a set of discrete energy levels, which may have energy level spacings larger than the thermal energy, k_BT. Eventually a size is reached where the surfaces of the particles are separated by distances which are in the order of the wavelengths of the electrons. In this situation the energy levels can be modelled by the quantum-mechanical treatment of a particle in a box. This is referred as the quantum size effect. The emergence of new electronic properties can be understood in terms of the Heisenberg uncertainty principle, which states that the more an electron is spatially confined the broader will be its range of momentum. The average energy will not be determined so much by the chemical nature of the atoms, but mainly by the dimension

of the particle. Quantum size effect occurs in semiconductors at larger sizes because of the longer wavelength of conduction electrons and holes in semiconductor due the larger effective mass. In a semiconductor the wavelength can approach one micrometer, whereas in a metal it is in the order of 0.5 nm.

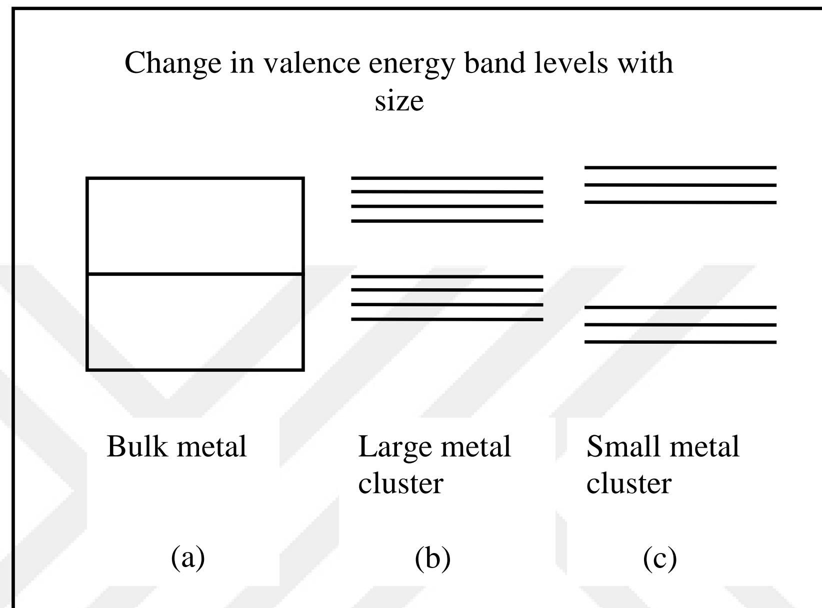

Figure 2. 9 Changes in energy levels of a metal with the reduced number of atoms of the material: (a) valence band of bulk metal; (b) large metal cluster of 100 atoms with opening of band gap; (c) small metal cluster containing three atoms

The minute network structure of microporous silicon is in between the two extremes of a single atom and a large crystal. A crystallite of a few hundred silicon atoms is large enough to have a rich electronic band structure but is still small enough to show an increase in the energy of an electron-hole pair due to quantum confinement. The effect of an increase in fundamental bandgap due to size quantization is not specific to silicon, but common to all semiconductors.

Photoluminescence, which is the light emission coming from recombination of quantum confined electron-hole pairs in nanocrystalline silicon domains, was observed during characterization of porous silicon samples and the results were presented in results and discussion section.

The vibrational properties of a crystal determine much macroscopic behaviour: thermal properties, transport properties, and the interaction with radiation, for example in infra-red absorption and Raman scattering.

Raman spectrum of crystalline silicon, the only Raman active mode is zone centre ($\vec{q} = 0$) optical phonon mode due to the conservation of phonon momentum $\vec{q}$. The localization of phonon in silicon crystals affects the $\vec{q} = 0$ selection rule allowing transitions with $\vec{q} \neq 0$ which leads to the broadening and the redshift.

The effects of strong phonon confinement, redshift and broadening, were found on the Raman spectra and the blueshift of the photoluminescence peak was observed by reducing the crystalline sizes. Vibrational and optical findings were analysed within the existing models of confinement for silicon nanocrystals in order to determine diameter of the silicon nanocrystallites, and the findings were presented in the results and discussion section.

2.2.2. Formation theories and morphology related with mesoporous structure

A common feature of all pore formation mechanisms in silicon electrodes is a dissolution reaction limited by hole supply. The hole transfer rate is determined by the electronic properties of the semiconducting electrode. It is therefore possible to describe a solid state equivalent for any interface condition present during electrochemical pore formation. The passivation of microporous silicon against electrochemical dissolution, for example, can be understood if compared to the charge carrier distribution in a quantum well structure. The latter material shows local variations of the bandgap energy. As a consequence the free charge carriers populate the quantum wells, while regions with a large bandgap become depleted. For an anodized silicon electrode, this corresponds to a populated bulk and a depleted, and therefore passivated, microporous region. All remaining mechanisms for pore formation, responsible for meso- and macropore formation are due to charge carrier depletion caused by a space charge region. The solid state equivalent is therefore a Schottky diode with a non-planar interface [165].

Pore formation in silicon electrodes is only observed under anodic conditions in HF acid for current densities below J_{PS}. In this case a depletion region is present in silicon electrodes independent of type and density of doping. With increasing doping density the electric field strength increases and the width of the depletion region decreaases. This enables charge carriers to pass through the space charge region by band-to-band tunneling. The currents in the electrochemical cell are always limited by mass transport of chemical reactants in the electrolyte and by reaction kinetics. The electric field depends on doping, applied bias, and geometry. Around a depression in the elctrode the depletion region width is decreased and the field strength is increased, which increases tunneling probability of charge carriers and thereby the local current density. This effect becomes significant if the radius of curvature of the etch pit is smaller than the SCR width.

Tunneling is expected to dominate all pore formation in the mesoporous regime and extends into the lower macropore regime, while avalanche breaskdown is expected to produce structures of macropore size. Space charge region effect is another proposed mechanism for the formation of mesoporous silicon structures resulted from electrochemical anodization process on silicon wafer.

The current density decreases from the tip towards the wall according to a cosine law and becomes zero when the pore wall is truly cylindrical as depicted in Figure 2.10.

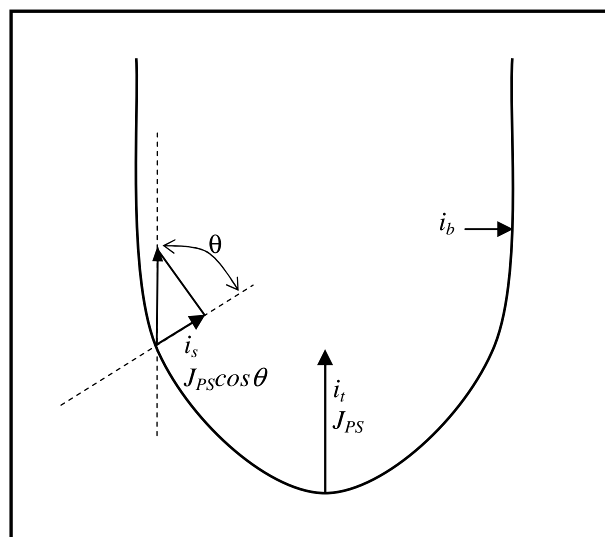

Figure 2. 10 The current density distribution at pore tip

Oxide formation and dissolution tend to occur at the pore tips at a lower potential than at the side of the pore bottom. There is a distribution of the kind of reactions along the pore bottom. For a pore to propagate under a steady state the current density on the side of the pore bottom, i_s, and that at the pore tip, i_t, as illustrated in Figure 2.10 have the following relation.

$$i_s = i_t \cos\theta + i_b \tag{2.7}$$

In the above equation, i_b is the extra current mostly due to the anisotropic effect and is responsible for the formation of side pores. The current density at different sites on the bottom depends on the angle "θ". It is the largest at the tip where θ=0, and is the smallest on the boundary of the bottom where θ=90°. Such a distribution of current density is provided by the distribution of radius of curvature along the pore bottom, which determines the field at the silicon surface and the nature of the reactions.

At the wall segment that is close to being cylindrical, the current density becomes small, but not zero. Because any current flow is associated with the breakdown condition, the pore diameter increases until the limiting value for tunneling at the pore wall is reached.

The consequences of type and density of substrate doping on pore geometry and pore spacing will be given below. The concept of a homogeneous SCR with a constant width independently of the absolute value of the doping density is considered. The width and the electric field in the SCR are therefore inhomogeneous and it can be assumed that the growth of a mesopore depends on the local field distribution.

If the distances between the pores become significantly larger than twice the SCR width W, the pore wall regions will no longer be depleted. This enables branching at the pore tips and side pores would penetrate this region until depletion is established again. As a result of this mechanism, pores tend to space themselves at distances below 2W. In highly doped p-type silicon the pore diameter is comparable to W, and so mesoporous layers of significant porosity are formed.

The doping density and the type of doping are important, because it determines whether the silicon electrode is under forward or reverse conditions. A p-type silicon electrode is under forward conditions in the anodic regime. The solid- state equivalent is a forward-biased non-planar Schottky junction. Depending on doping density the forward current of a Schottky diode is dominated by diffusion, thermionic emission over the barrier, or by tunneling through the barrier.

The field at a spherical pore tip is significantly larger than in the planar case and mesopore formation due to tunneling is observed for p-type doping densities up to 3 x 10^{17} cm^{-3}. Avalanche breakdown in p-type electrodes is, of course, confined to the cathodic regime, and is therefore not relevant to formation of pore.

2.2.3. Formation theories and morphology related with macroporous structure

This section is devoted to the formation mechanisms that have been proposed as being responsible for formation of macropores on p-type silicon electrodes. First models for macropore formation on p-type Si electrodes were based on surface passivation by organic molecules [166] or on electrostatic considerations [167]. These models, however, were found to contradict experimental observations [168].

It was first believed that macropores in Si were restricted to rather peculiar electrolytes (especially water-free Acetonitrile) and Si with a high-resistivity, it was later discovered that many electrolytes are suitable including diluted HF and that the doping is not decisive. The nucleation of macropores in p-type Si is sometimes difficult, and in some electrolytes the macropores are filled with meso- or nanoporous silicon [169].

Macropore formation on p-type silicon electrodes was first observed for anodization in water-free mixtures of anhydrous HF [170, 171]. Later it was observed that aqueous HF electrolytes [168, 172], are also sufficient for the formation of macropores on p-type Si electrodes. This indicates that macropore formation on such electrodes cannot be ascribed to the chemical identity of a certain electrolyte. Only the presence of HF in the electrolyte is required, as is the case for the other pore size regimes. The pore morphology and stability of pore growth, however, depend on electrolyte composition and concentration, as

well as on additives such as surfactants [168, 173]. The morphology of macroporous layers formed on p-type Si electrodes can be understood as a consequence of the stringent requirement for pore wall passivation in low doped p-type substrates: pore walls are depleted if their thickness is less than twice the SCR width W. Width depends on doping density and applied bias.

For p-type silicon, the dependence of macropore density on doping density is linear. However, the absolute values of pore density observed on nonstructured p-type substrates are about one order of magnitude larger than for n-type electrodes. This produces high values of porosity ($p > 0.5$) for random p-type macropore structures as well as for arrays [167, 168]. The pore walls become fragile if the doping density is increased above 10^{16} cm^{-3} and usually only a roughening of the electrode surface is observed for anodization in aqueous HF.

For macropore formation on low doped p-type substrates, the applied bias and current density are coupled: a change in the applied bias produces a corresponding change in anodization current density. For macropore growth on p-type electrodes an increase in the current density has little effect on pore diameter, but produces a roughly proportional increase in pore growth rate [168]. Concerning growth rate and the dissolution valence, macropore formation on p-type silicon shows similarities to micro PSi formation. This can be understood as a consequence of the fact that depletion in p-type substrates is only present for an applied bias significantly lower than that corresponding to the critical current density J_{PS}. Thus J_{PS} is never reached at the pore tips or pore walls during macropore formation on p-type Si electrodes. This is supported by the observation that microporous silicon covers not only the macropore walls but also the pore tips. For higher HF concentrations the whole pore volume can be filled with micro PSi.

The dependence of pore morphology on crystal orientation is found to be weak in aqueous HF. Some faceting can be observed at the pore tips. At high HF concentrations or in mixtures with organic solvents, most of the pore volume is found to be filled with micro PSi. The presence of an oxidizing species, like water, reduces the amount of pore filling [174].

The growth of a macropore on a p-type substrate can be initiated by artificial etch pits. The growth of predefined pore arrays is observed to be more stable than the growth of random pores on flat electrodes [168, 173].

In conclusion it can be said that the flexibility of pore array design on low doped p-type Si is less than that for macropore formation on n-type substrates, because of the limitations in array porosity and substrate doping range.

2.3. CHARACTERIZATION OF THE STRUCTURE

Characterization of porous silicon structures was accomplished by optical microscopy, scanning electron microscopy, Raman spectroscopy, and photoluminescence spectroscopy techniques. Brief introduction to these techniques was given in the following sections.

2.4. OPTICAL MICROSCOPY

The first instrument to determine any structural changes in the silicon wafer was the optical microscope after the application of electrochemical anodization process. The images taken from optical microscopy can be taken either of two different modes: bright field or dark field.

In the bright field microscopy, the light impinges vertically on the sample. Horizontal surfaces reflect most of the light while slanted or vertical surfaces reflect less. The convex lenses bend light rays in a peculiar manner so that light hitting the center of the lens goes straight through. But light hitting other areas is bent toward a focal point. This bending allows the view at a specific distance from an object to see the image as larger than it would appear to the eye as depicted in Figure 2.11 (a).

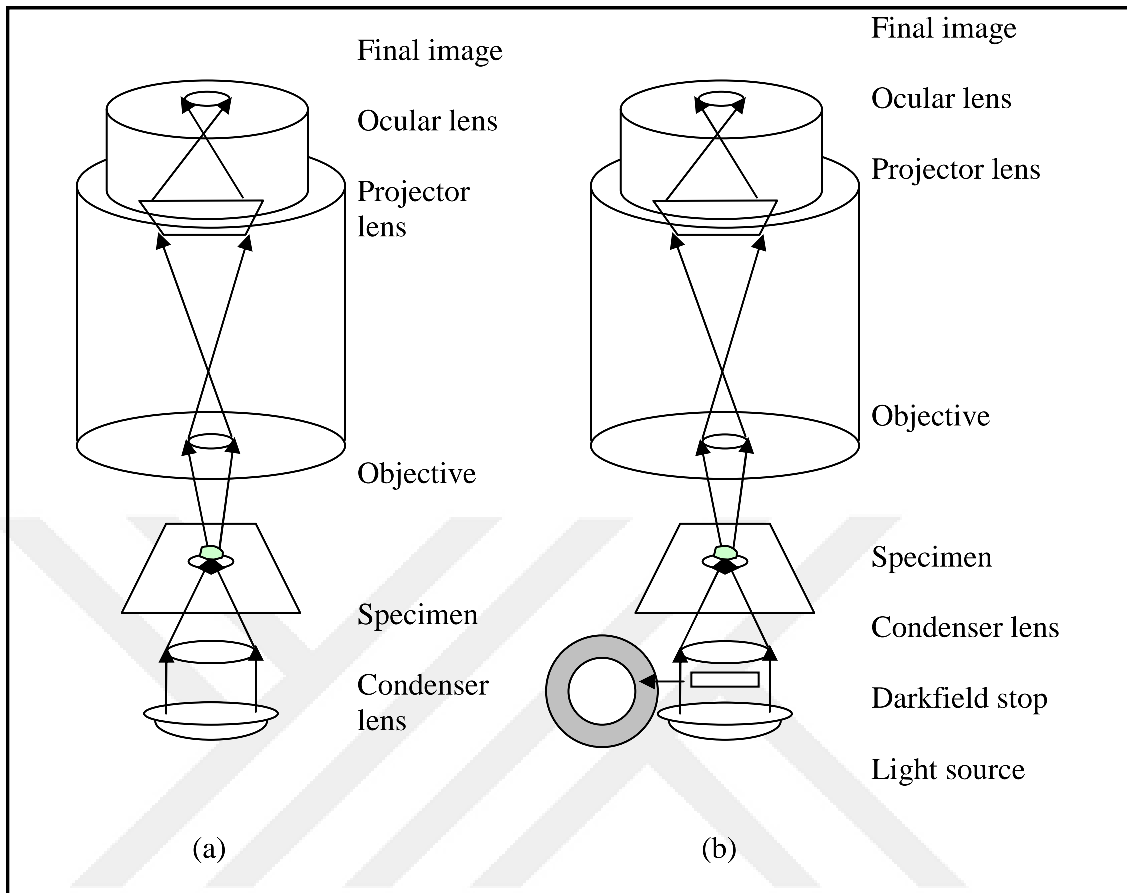

Figure 2. 11 The schematic of optical microscope in (a) bright field and (b) dark field modes

Light is first emitted by the light source and is directed by the condenser lens on to the specimen. The light from the specimen then passes through the objective lens. This lens is the main determinant for the level of magnification. It bends the light rays and sends them to a projector lens, which reverses their direction so that when the image reaches the eye it will not appear "upside-down". The light rays' then travel to the ocular lens or "eye piece". This is often a 10X magnification lens, meaning it magnifies the magnified image an additional ten times. The image is then projected into the eye.

In dark-field microscopy, the light impinges at a shallow angle on the sample. Light from horizontal sample surfaces does not reach the lens, but light from slanted and vertical surfaces does. The image contrast is the reverse of that of bright light imaging. Dark field microscopy is especially useful to bring out small surface irregularities that are difficult or

impossible to see with bright light microscopy. Dark field microscopy is akin to seeing dust in the air in a darkened room when bright sunlight falls into the room, scattering light from dust particles. The schematic of optical microscope in dark field mode is depicted in Fig. 2.11 (b).

Dark field microscopy excludes the unscattered beam from the image. As a result, the field around the specimen is generally dark. In optical microscopy, dark field describes an illumination technique used to enhance the contrast in unstained samples. It works by illuminating the sample with light that will not be collected by the objective lens, and thus will not form part of the image. This produces the classic appearance of a dark, almost black, background with bright objects on it [175].

The light path through a dark field microscope:

- Light enters the microscope for illumination of the sample.
- A specially sized disc, (dark field stop) blocks some light from the light source, leaving an outer ring of illumination.
- The condenser lens focuses the light towards the sample.
- The light enters the sample. Most is directly transmitted, while some is scattered from the sample.
- The scattered light enters the objective lens, while the directly transmitted light simply misses the lens and is not collected due to a direct illumination block.
- Only the scattered light goes on to produce the image, while the directly transmitted light is omitted.

2.5. SCANNING ELECTRON MICROSCOPY

SEM is a non-destructive method, which probes the surface area of the material. The microscope used throughout this thesis work was JEOL 6335F scanning electron microscope (SEM). The schematic of scanning electron microscope is depicted in Fig. 2.12. Although SEM resolution is 1 nm, blurred images obtained for resolutions lower than 10 nm during porous silicon measurements.

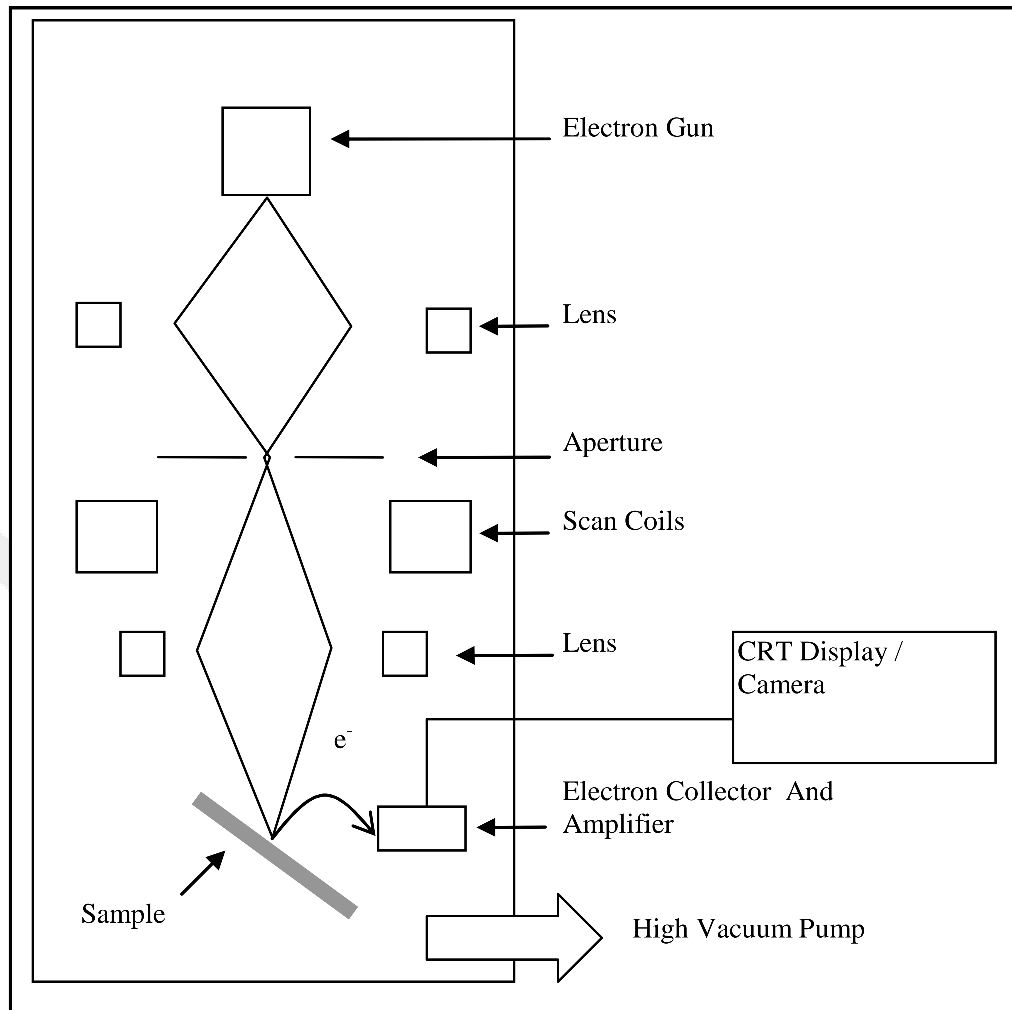

Figure 2. 12 Schematic of scanning electron microscopy [176]

When an electron beam from the electron gun encounters a specimen in the specimen chamber, several important kinds of emissions take place. The most useful emissions are emissions of backscattered electrons, secondary electrons, photons cathodoluminescence), and X-rays. The number of backscattered electrons emitted from a material bombarded by the electron beam (and thus the brightness of the backscattered image) is a function of the average atomic number of the material. Therefore, BSE images are useful for distinguishing among different minerals in a specimen. The emission of secondary electrons is related to topography of the specimen. Consequently, secondary electron images are useful for studying the shapes of crystals or other objects [177].

SEM was used to obtain the surface and cross-sectional images from porous silicon structure throughout this study. SEM images obtained from porous silicon samples with 75,000 magnifications were depicted in the experimental section.

2.6. IMAGE PROCESSING

An image processing algorithm developed in the MATLAB environment was applied to determine the granule diameters of SEM images taken from porous Silicon samples formed under different anodization conditions.

Size distributions, including the diameter of nanometer sized silicon crystalline islands or granules, were determined from the algorithm developed in a MATLAB environment. MATLAB Image Processing Toolbox functions were initially used to reduce the noise, while preserving the edges of the circular shapes of the granules. Then, contrast of the grayscale images was enhanced, and finally morphological opening together with the circular structuring element were performed on these images.

The algorithm was based on the use of the 'Granulometry' function, which determines the size distribution of objects in an image, without explicitly segmenting and detecting each object first. This enabled a calculation of the size distribution of objects in any given image obtained from SEM. Granulometry estimates the intensity surface area distribution of an image as a function of granule size. Granulometry likens image objects to stones. Their sizes can be determined by sifting them through screens of increasing size. In granulometry, image objects are sifted by opening the image with a circular structuring element of increasing size. Counting what remains after passing through screens of successively increasing aperture corresponds to counting the remaining intensity surface area after each opening in granulometry [178].

Size distributions, including the diameter of nanocrystallites were determined from image processing of the SEM images using an algorithm developed in the MATLAB environment and given in Appendix A. The algorithm was used to reduce the noise, while preserving the edges of the circular shapes of the granules. After contrast enhancement a morphological opening was performed. These outlines enabled calculation of the size

distribution of objects in any given SEM image to be obtained. Diameter values obtained from the algorithm written in the MATLAB Image Processing Toolbox environment were presented in the experimental section, in the form of histogram gather information about the diameter values of the granules versus number of objects at that diameter value found in the SEM images of crystalline silicon samples.

2.7. RAMAN SPECTROSCOPY

Atomic vibrations in a solid have a profound effect on its properties. For example, heat is transported via atomic vibrations and the specific heat of a material is determined mostly by the spectrum of allowed vibrational modes. Furthermore, under certain conditions, electro-magnetic radiation can interact with atomic vibrations for example in Raman scattering, thereby directly determining the optical properties of the material. In crystals, vibrational modes can be classified in terms of the wavevector because of lattice periodicity. The schematic of Raman spectroscopy is depicted in Figure 2.13.

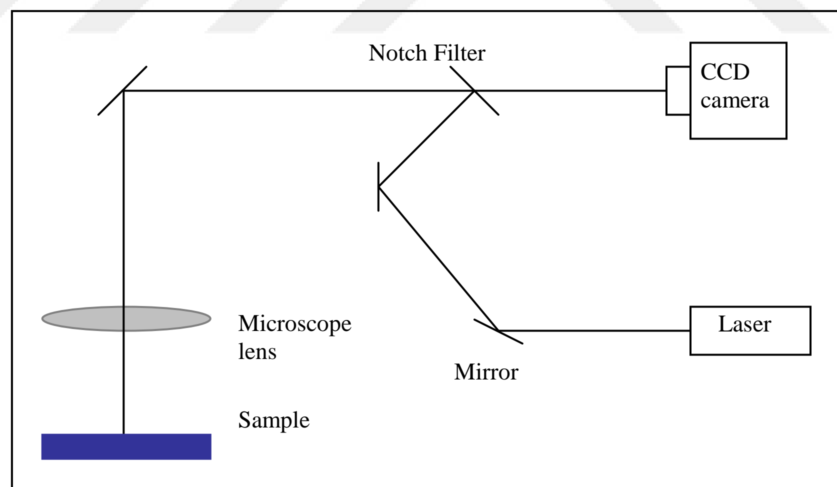

Figure 2. 13 Schematic of Raman spectroscopy [183]

Raman spectroscopy is a non-destructive method that has been used to investigate the morphology of porous silicon structure. Raman characterization have a probing volume which depends on the laser wavelength, laser spot size and the beam penetration depth. It probes a volume of the material with a resolution much better than 10 nm, essentially

together with the model used in this thesis work, changes in nanocrystallite diameters of 1 nm could be detected [123, 179-182].

Raman spectroscopy measurements were carried out with a laser having excitation wavelength of 514 nm which has a penetration depth of 762 nm in silicon, together with a 2 μm laser spot diameter resulted in a probing volume of approximately 2 μm^3 [184]. Since the diameter and the penetration depth of the Raman laser spot are approximately 1-2 μm, the Raman intensity measured on this volume is the summation of intensities contributed by each nanocrystallite within the specified Raman laser spot.

The diameter of granular type nanocrystallites was calculated using a model presented by Zi et al in 1996 and developed by Lu et al in 2010 [179, 182]. Dimensions for silicon spheres were calculated by Lu et al ranges from 1.4 nm to 4.9 nm. It is assumed that the calculation of the size of the spheres can be extended up to 16 nm according to the results obtained from Faraci et al [180]. The Richter equation was also used to show an asymmetric Raman spectrum line shape and wavenumber downshifts with decreasing nanowire diameter from 20 nm to 3 nm [173]. The Richter equation, which is assumed to approximate well up to 20 nm, is used throughout this paper. An analytic form of this model was used, as shown in Equation 2.8.

$$\Delta\omega = \omega_{PSi} - \omega_{cSi} = -A \cdot \left(\frac{a}{L}\right)^{\gamma} \tag{2.8}$$

In the above equation, ω_{PSi} (cm^{-1}) and ω_{cSi} (521 cm^{-1}) are the characteristic Raman band positions of or the frequency of the Raman phonon in porous silicon nanocrystallites and c-Si respectively. The parameters A and γ are used to describe the vibrational confinement due to the finite size in a nanocrystallite. The values of the two parameters were obtained by fitting them to the calculated values for Si spheres [179]. For spherical Si nanocrystallite, $A = 47.41$ cm^{-1}, $\gamma = 1.44$ [179]. "a" is the lattice constant of silicon and is equal to 0.543 nm.

In single crystalline silicon only first-order scattering at the optical phonon in the center of the Brillouin zone is allowed, which produces a sharp Raman peak at 521 cm^{-1} [185]. Confinement of the phonon leads to a momentum uncertainty, and so the Raman peak

broadens and shifts to lower energy. This effect can be used to determine the size of silicon nanocrystallites using Raman measurements [122].

Comparison of Raman spectra of all the samples with the Raman spectrum of crystalline silicon showed a red (down) shift in the optical phonon mode after porous silicon formation due to the phonon confinement effect. This indicates that nanometer sized silicon crystallites in the silicon samples were formed as a result of electrochemical anodization process. Such structures exhibit red shifts from crystalline silicon (c-Si) in Raman spectra when nanometer sized structures are present.

In general, Raman scattering is a complicated process to describe theoretically, since a multiple scattering of photons, electrons, and phonons is involved. Any microscopic theory, attempting to explain the Raman Effect in a solid, should take into account the dynamical correlation between the atomic motions, the local polarizability of the bonds and the changes of the dipole moments on every atomic site. Due to the fact that the wave vector of the light is very small compared with the relevant reciprocal distances in the crystal, the momentum conservation rule allows participation of phonons around the Γ point only [186].

2.7.1. Raman Spectroscopy Principles

The phenomenon of inelastic scattering of light was first postulated by Smekal in 1923 and first observed experimentally in 1928 by Raman and Krishnan [187]. Name was given after the Nobel wining Indian physicist Raman who reported the effect. Since then, the phenomenon has been referred to as Raman spectroscopy. Raman Effect constituted an excellent tool to study excitations of molecules and molecular structures. In addition to these studies, systematic investigations of single crystals in order to obtain information for the semi-empirical treatment of their lattice dynamics was also drew attention. The first- and second-order scattering in silicon with the 4880 A° line of the Ar^+ laser by Parker et al. is one of the breakthroughs in the history of Raman spectroscopy [188]. Raman spectroscopy also gives valuable information especially the crystallite size of the nanostructures. Porous silicon is one of the materials studied extensively to characterize the pore sizes by Raman spectroscopy [123, 180-182, 185, 189-191].

Light scattering techniques provide an exceedingly useful tool to study fundamental excitations in solids, such as phonons, because light can be scattered from solids inelastically, whereby the incident and scattered photons have different frequencies.

Inelastic light scattering became an important tool for the study of excitations in solids in the mid-1960's with the advent of laser light sources, because the inelastically scattered light is typically only $\sim 10^{-7}$ of the intensity of the incident light. When electromagnetic radiation (light) interacts with matter, most of the radiation (photon) continues along its original path, but a tiny amount is scattered in other directions. Some portion of the radiation may also be absorbed.

Light that is scattered without a change in energy is called Rayleigh scattering. Light scattering accompanied by vibrations or rotations in molecules or in crystals is called Raman scattering. Raman spectroscopy is based on the so called Raman Effect which describes the inelastically scattered light on elementary excitation of a solid material like lattice vibrations, i.e., phonons.

Raman is an inelastic light-scattering process in which small fractions of the incident photons from an arbitrary light source are scattered with a spectral frequency (energy) shift that is characteristic of the scattering medium. A linearly polarized laser light source with electric field, E, induces an oscillating dipole moment, or polarization, upon the electron charge field in the scattering medium in the linear light-scattering processes. The radiating dipole emits in the characteristic pattern with zero emission along the dipole axis and radiation maxima at normal angles to the dipole. For linear light-scattering processes, the total light scattering is proportional to the strength of the induced dipole moment and the incident laser field.

$$E_s \approx P = \varepsilon_0 \alpha E_l \qquad (2.9)$$

In the above equation, ≈ indicates proportionality, ε_0 is the free-space permittivity, E_s is the scattered electric field, P is the induced polarization, E_l is the incident laser field and α

is termed the electric polarizability, which quantifies how readily the scattering medium is polarized by the incident laser field.

In general, the electric fields and induced polarization are vector quantities so that α is a rank-2 tensor. The polarizability is generally expanded in terms of the equilibrium and displaced positions of the medium's atomic structure,

$$\alpha = \alpha_0 + \left(\frac{\partial \alpha}{\partial Q}\right)\delta Q \tag{2.10}$$

In the above equation, Q is a time-varying internuclear displacement and α and $(\partial\alpha/\partial Q)$ are the equilibrium polarizability and time-varying polarizability derivative, respectively. If the incident laser field is at frequency, ω, and the internuclear separation is oscillating at some natural frequency, Ω, then $E_l \approx E_{l,o}\cos\omega t$ and $\delta Q = \delta Q_o \cos\Omega t$ such that the scattered electric field is now written as,

$$E_s \approx \alpha_o E_{l,o}\cos\omega t + \left(\frac{\partial \alpha}{\partial Q}\right)E_{l,o}\cos\omega t\cos\Omega t \tag{2.11}$$

The above equation may be rewritten in this manner following application of a simple trigonometric identity,

$$E_s \approx \alpha_o E_{l,o}\cos\omega t + \left(\frac{\partial \alpha}{\partial Q}\right)E_{l,o}\left[\cos(\omega+\Omega)t + \cos(\omega-\Omega)t\right] \tag{2.12}$$

The first term in Equation (2.12) is the elastic, or Rayleigh, scattering contribution, which represents dipole scattering at the incident laser frequency, ω. The Rayleigh peak is by far the strongest of the linear scattering processes. The second term represents the inelastic, or vibrational Raman components, which are spectrally shifted to the Stokes ($\omega - \Omega$) and anti-Stokes ($\omega + \Omega$) sides of the probe laser by characteristic vibrational resonances of the scattering medium. In this manner, Raman is species selective since different compounds display distinct molecular resonance frequencies that are readily identifiable in Raman spectra.

In solid-state materials, Raman scattering arises through the interaction of probe laser light with quantized lattice vibrations, or phonons such that Ω in Eq. (2.12) now represents the optically coupled phonon-mode frequency.

Raman selection rules describe the change in frequency, ω (energy), and wave vector, k (momentum), for the inelastic scattering process.

$$\omega_R = \omega \pm \Omega \quad (2.13a)$$

$$k_R = k \pm K \quad (2.13b)$$

In the above equations, ω_R and k_R refer to Raman-scattered photons, ω and k refer to the probe-laser beam, and Ω and K refer to the phonon. In the Stokes process, $\omega_R = \omega - \Omega$, and a red-shifted Raman photon results from the creation of an optical phonon at Ω with a loss of optical energy. The anti-Stokes process, $\omega_R = \omega + \Omega$, creates a blue-shifted Raman photon from the annihilation of a thermally generated optical phonon and a gain of optical energy [192-197].

2.7.2. Raman Spectroscopy of Crystalline Material

In crystalline solids, the Raman Effect is caused by phonons. There is an incident photon-electron interaction followed by an electron-lattice interaction. An incoming photon excites an electron, causing an excited electron-hole pair. The latter is scattered at the lattice, inducing a phonon in the solid and causing the electron-hole pair to return to the origin state by emitting a photon. The latter is reduced in energy compared to the incident photon by the amount lost in the scattering event.

For every crystal symmetry class, it is possible to calculate which phonons are Raman active, and in which measurement geometry, i.e. for which direction of polarization of the incident and scattered light, relative to the crystallographic axis.

In nanocrystalline materials, the phonons are of similar dimensions to the nanostructures, and so are confined. As a result, Raman spectra display the macro size crystalline Raman

features broadened and shifted by phonon confinement. Nanometer sized silicon structures are known to exhibit red shifted Raman spectra [180-182, 185, 189-191]. By using an adequate model, it is possible to estimate the size of the nanocrystals [198].

The critical result of small size effect in nanocrystallite structures is the breaking of translation symmetry, which results in the losing of phonon momentum conservation and the relaxation of phonon wavevector selection rule of $q \approx 0$ in their Raman scattering. Crystalline semiconductors exhibit first-order scattering only by phonons with $k \approx 0$. Phonons with large k must be observed in second order. Many of the tetrahedral semiconductors, however, may be prepared in amorphous form for which k conservation no longer holds. Thus, in the amorphous materials the first-order Raman spectrum is broad and corresponds to the density of one-phonon states [199].

Another fortunate circumstance is the fact that this density of states is often a broadened version of that of the corresponding crystalline material. This implies a large amount of conservation of short range order [199].

2.7.3. Stokes and Anti-Stokes Raman Scattering

Two situations arise with Raman scattering:

- Scattered photons have a lower energy (Stokes scattering – phonon emitted). Molecule absorbs energy: Stokes scattering. The resulting photon of lower energy generates a Stokes line on the red side of the incident spectrum.

- Scattered photons have a higher energy (anti-Stokes scattering – phonon absorbed). Molecule loses energy: Anti-Stokes scattering. Incident photons are shifted to the blue side of the spectrum, thus generating an anti-Stokes line

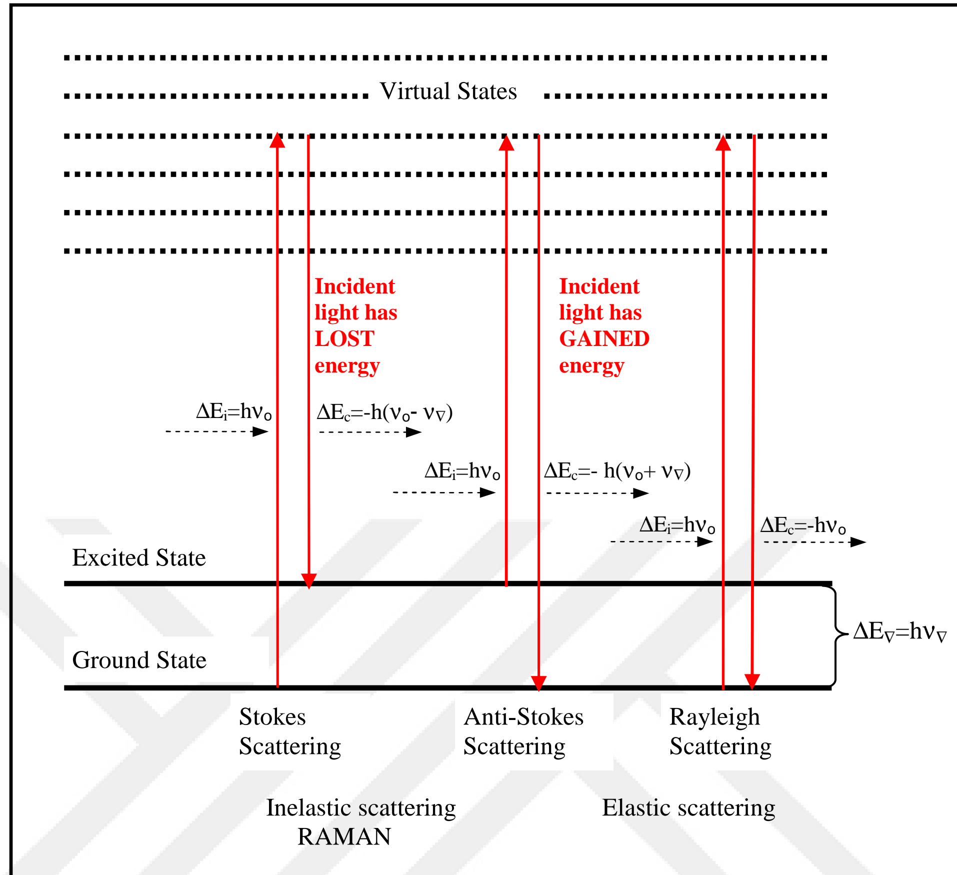

Figure 2. 14 Stokes and anti-Stokes Raman scattering mechanisms

In Stokes–Raman scattering the incident photons coupled with phonon-induced changes in the polarizability of the solid, causing the scattered photons to lose a quantum of lattice energy or phonon relative to the incident photons. Regarding to the conservation of momentum, only phonons close to the Γ-point of the Brillouin zone are excited in such processes [200]. Moreover, the frequency ω of the excited phonons is described as:

$$\omega = [1/\lambda_i - 1/\lambda_s] \tag{2.14}$$

In the above equation, λ_i and λ_s are the wavelength of the incident and scattered radiation respectively. The Raman shift is that described as the value of ω and is generally have a unit of cm^{-1}. Then the Raman spectrum can be produced as a graph of the scattered intensity as a function of the Raman shift and contains information about the physical and chemical characteristic of the solid. A presence of mechanical stress/strain can cause this frequency of Raman modes to change, and lifts their degeneracy. Tension will change the

peaks of Raman shift to a lower wavenumber than the stress free frequency; in contrary a Raman shift higher than stress-free frequency indicates compressive stress [200].

A direct measure of strain of a microstructure can be determined using Raman spectroscopy. For a cubic diamond lattice crystalline structure of silicon, Loudon [201] derived three Raman tensors; in a crystal coordinate system x = [100], y = [010] and z = [001] they are given by:

$$R_x = \begin{pmatrix} 0 & 0 & 0 \\ 0 & 0 & d \\ 0 & d & 0 \end{pmatrix} \quad R_y = \begin{pmatrix} 0 & 0 & d \\ 0 & 0 & 0 \\ d & 0 & 0 \end{pmatrix} \quad R_z = \begin{pmatrix} 0 & d & 0 \\ d & 0 & 0 \\ 0 & 0 & 0 \end{pmatrix} \tag{2.15}$$

For back scattering from a (001) surface, and correspond to scattering by transverse optical phonons (TO), polarized along x and y respectively, and corresponds to scattering by longitudinal optical phonons (LO), polarized along z. For an unstressed condition, the corresponding three degenerate Raman-active optical phonon modes of single crystal silicon have the same frequency of about 521 cm^{-1}. Then the total Raman intensity is given by:

$$I = \left| p_s R_j p_i \right|^2 \tag{2.16}$$

In the above equation, p_i and p_s are the polarizations of the incident laser and the collected scattered photons, respectively. All quantitative measure of all unknown stress states can be revealed by evaluating particular crystal orientation and monitoring various scattering polarization [202].

2.7.4. Phonons

A phonon is a quantized mode of vibration occurring in rigid atomic lattices, such as those in crystalline solids. In lattice dynamics, there are a finite number of vibrational modes, and the energy of each mode is quantized. So, phonons are also these normal modes. Also, although phonons are exclusively a property of periodic media, vibrations exist in all

solids. The properties of long-wavelength phonons give rise to sound in solids (hence the name phonon).

Phonons participate in many of the physical properties of materials, including heat capacity and thermal/electrical conductivities, e.g. the propagation of phonons is responsible for the conduction of heat in electrical insulators [203].

There are two types of phonons: acoustic phonons, denoted with the subscript A, and optical phonons, denoted with the subscript O.

2.7.4.1. Acoustic Phonons

Acoustic phonons have frequencies that become small for long wavelengths and correspond to sound waves in the lattice which is a property of phonon dispersion relation [204].

These long wavelengths correspond to bulk translations. Acoustic phonon means that all basis atoms in the primitive cell move in phase i.e., no relative motion among themselves.

Longitudinal- and transverse-acoustic phonons are often abbreviated as LA and TA phonons, respectively.

2.7.4.2. Optical Phonons

Optical phonons, which arise in lattices with more than one atom per unit cell, always have some minimum frequency of vibration, even when their wavelength is infinite [204]. The two atoms in the unit cell are vibrating with a phase difference of □ which usually creates a dipole moment, and therefore couples to electromagnetic waves, hence the name of optical for these modes.

In ionic crystals (such as NaCl) they are also excited very easily by light (such as infrared radiation). This is because they correspond to a mode of vibration where positive and negative ions at adjacent lattice sites move, thus creating a time-varying electric dipole moment. Optical phonons that interact in this way with light are called infrared active. Optical phonons, which are known as Raman active, can also interact indirectly with light,

through Raman scattering (an inelastic scattering of a photon that creates or annihilates an optical phonon). Optical phonons are often abbreviated as LO and TO for the longitudinal and transverse varieties, respectively.

In the diamond-type lattices there are two atoms per primitive unit cell, and hence there are six phonon branches. These are divided into three acoustic phonon branches (the three lower energy curves) and three optical phonon curves. Suppose there are N atoms in the primitive cell. Since each atom has 3 degrees of freedom, there are 3 acoustic phonon branches (1 longitudinal and 2 transverse) and 3N-3 optical phonon branches.

2.7.4.3. Longitudinal- and Transverse- Acoustic/Optical Phonons

Under the influence of a pressure wave, displacement of atomic planes will occur. Along high-symmetry directions (such as the [100] and [111] directions in Si) the phonons can be classified as transverse or longitudinal according to whether their displacements are perpendicular or parallel to the direction of the wave vector q.

For a three-dimensional crystal, for each longitudinal wave there are two transverse waves. The dashed lines represent the equilibrium positions, and the solid lines indicate the deflected positions at a given time.

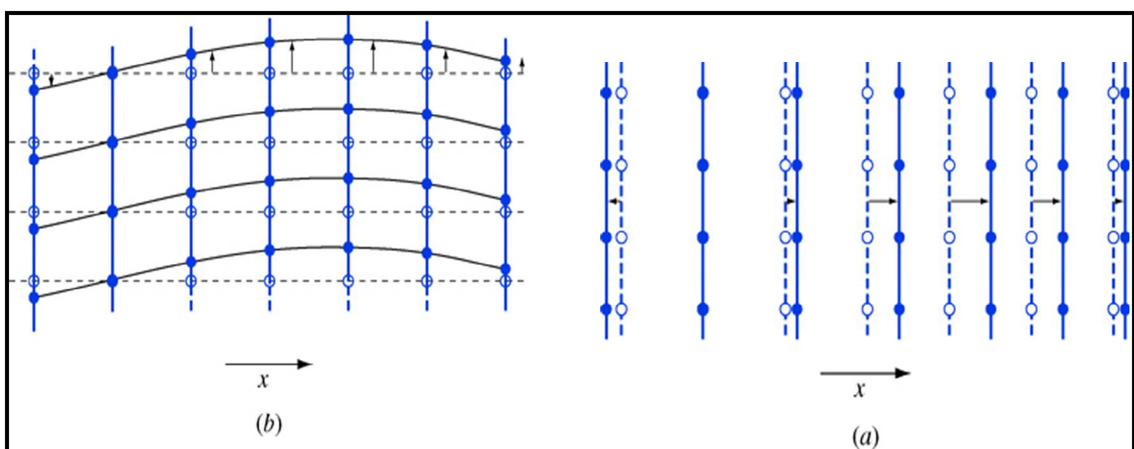

Figure 2. 15 For a longitudinal wave (a), the displacement is in the direction of motion. For a transverse wave (b), the displacement is transverse to the direction of motion

In a solid the long-wavelength transverse acoustic (abbreviated as TA) phonons are shear sound waves while the longitudinal acoustic (LA) phonons correspond to compressional sound waves. The velocities of these sound waves are determined by the shear and bulk elastic moduli, respectively. Since it is usually easier to shear than to compress a crystal, the TA phonons travel with lower velocities than the LA phonons.

Two special features of the TA phonons in the diamond-type semiconductors are: (1) their dispersion curves are relatively flat near the zone edge; and (2) their energies are much lower than the LA phonon energy near the zone edge.

In Si the two atoms in the unit cell are identical so the bonding is purely covalent and the two atoms do not carry charge. As a result there is no additional restoring force associated with LO phonons and the transverse optical (TO) phonons and the longitudinal optical (LO) phonons are degenerate at the zone center.

Vibrational modes in a crystal can be symmetrized according to the space group symmetry of the crystal just like the electronic states. A phonon mode is defined by the displacements of the atoms inside the unit cell. Thus the symmetry of the phonon must belong to the direct product of the representation of a vector and the representation generated by a permutation of the positions of equivalent atoms in the unit cell [194].

2.7.5. Phonon Dispersion Curves

The dispersion curve of Si can be regarded as representatives of semiconductors with the diamond-type lattices. Specially treated silicon wafer is also used in the calibration of Raman spectrometers. Phonon dispersion curves in crystals along high-symmetry directions of the Brillouin zone can be measured quite precisely by inelastic neutron scattering and more recently by high resolution inelastic x-ray scattering.

Photon-phonon interaction is easily described from the dispersion curves. An example showing the longitudinal and transverse optical and acoustical modes (LO-TO and LA-TA respectively) of silicon is given in Figure 2.16.

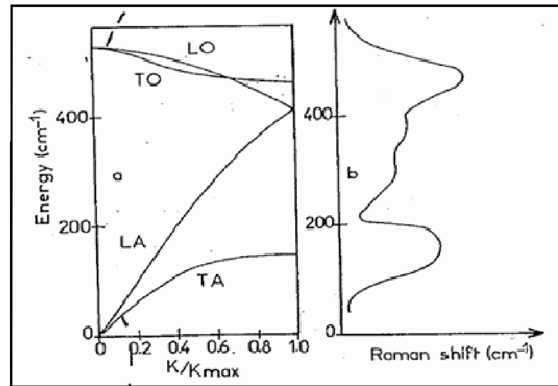

Figure 2. 16 Dispersion curves of silicon (a) in the direction (001) and Raman spectrum of amorphous silicon (b) (Adapted from [205])

Optical and acoustical modes interact with laser light ($E=h\upsilon$) to give an inelastic scattering. Near $K=0$, for silicon these dispersion curves can be approximately described by a parabola, $\omega= A\text{-}BK^2$ for optical modes and $\omega= v_s K$ for acoustical modes, v_s being the sound velocity.

In the bulk material the wave vectors and energy conservation laws between the phonons K and the incident k, and scattered k', photons ($k=2\pi/\lambda$) are expressed as:

$$k = k' + K \qquad (2.17a)$$

$$h\upsilon = h\upsilon' \pm h\omega \qquad (2.17b)$$

Due to the small values of the k and k' wavevectors for the visible light compared to the K_{max} wavevector ($|K|_{max} = \Pi/\ 2a$) the photon-phonon interactions are limited to the center of the Brillouin zone $K=0$. Selection rules taking into account the given symmetry of the semiconductor (m3m for silicon) show further that the only first order Raman transition allowed corresponds to the triply degenerate (1 LO+2 TO) phonon at 521 cm^{-1}, at $K=0$. Second order effects involving pairs of phonons with opposite K vectors give rise in the bulk material too bands of lower intensity [206].

The energy of a phonon is generally given in terms of its wave vector κ_p, and by use of the phase velocity, it can also be given in terms of its angular frequency ω_p and direction s_α.

For photons, generally the frequency $\omega_p h$ (or wavelength λ) is used. Regardless of their specific presentations, these carriers contain continuous and discrete energies and exchange these energies through various interactions.

2.7.6. Size effects in quantum dots

The direct consequence of the confinement effects in quantum dots is due to lack of long range order. The wavefunction e^{-iKr} of the infinite crystal is now replaced by:

$$\Psi = e^{-iKr} \, x W(r, \Lambda) \tag{2.18}$$

In the above equation, the limited correlation length Λ corresponds to the limited size of the crystal.

The effect of this spatial damping factor is first to relax the $K=0$ selection rule [195]. In the case of the amorphous silicon this relaxation leads to a Raman spectrum which clearly reflects the density of states (Figure 2.16). Amorphous silicon, where only the short range order is retained, can be considered as the limit case of a nanocrystal.

When the size of nanocrystals decreases an increasing part of the dispersion curve is able to interact with light. The detailed behavior of Raman line with decreasing has been extensively used these last years in the case of porous silicon with the objective to characterize the nanostructures. From the results of Richter et al [185] and Campbell and Fauchet [189], it has been shown that it is possible to reproduce the broadened nanocrystal Raman line in porous silicon by a simple model which considers the curvature of the LO dispersion curves. It was shown that by the above authors that the Raman intensity of the line is given by:

$$I(\omega) = \int \frac{|C(0,K)|^2 \, d^3K}{(\omega - \omega(K))^2 + \Gamma_0/2} \tag{2.19}$$

In the above equation, $C(0,K)$ is a Fourier coefficient obtained from the $W(r, \Lambda)$ function.

2.7.7. Rule of Mutual Exclusion

If a molecule has a centre of symmetry, then Raman active vibrations are IR inactive, and vice versa. If there is no centre of symmetry then some (but not necessarily all) vibrations may be both Raman and IR active. Note that this does not mean that a mode which is not Raman active must be IR active: in fact, it is still possible that a mode of a particular symmetry is neither Raman nor IR active.

2.7.8. Microscopic Theory of Raman Scattering

Classical theory correctly predicts that Raman scattering should be weaker than Rayleigh scattering and that there is a simple linear dependence of Raman scattering on incident intensity and on sample concentration. With classical theory, Stokes and anti-Stokes intensity ratio is predicted to be:

$$[(\nu_0 - \nu_k)/(\nu_0 + \nu_k)]^4 \qquad (2.20)$$

However, Boltzmann distribution will be major factor in determining relative Stokes and anti-Stokes intensity. The excited vibrational state will be only thermally populated, and Stokes intensity will be much larger than anti-Stokes.

State of the three systems involved has to be specified in order to describe microscopically inelastic scattering of light by phonons in a semiconductor:

- Incident and scattered photons with frequencies ωi and ωs, respectively;
- Electrons in the semiconductor;
- The phonon involved in the scattering.

In the initial state /*i*> (before scattering occurs) there are, respectively, $N(\omega_i)$ and $N(\omega_s)$ photons with the frequencies ω_i and ω_s. There are also N_q phonons present in the semiconductor (assumed to be at a nonzero temperature *T*) while the electrons are all in their ground states (i. e., the valence bands are completely filled and the conduction band

empty). In the final state |*f*>, after Stokes Raman scattering, $N(\omega_i)$ has decreased by one while $N(\omega_s)$ and N_q have both increased by one. The electrons remain unchanged. At first sight it seems that this scattering process does not involve electrons and therefore it can be described by an interaction Hamiltonian involving photons and phonons only. The strength of this interaction, however, is very weak unless the photons and phonons have comparable frequency.

When visible photons are used to excite Raman scattering in a semiconductor, they couple by-and-large only to electrons via the electron–radiation interaction. The scattering proceeds in three steps.

1. The incident photon excites the semiconductor into an intermediate state |a> by creating an electron–hole pair (or exciton).
2. This electron–hole pair is scattered into another state by emitting a phonon via the electron–phonon interaction Hamiltonian. Thi intermediate state is denoted by |b>.
3. The electron–hole pair in |b> recombines radiatively with emission of the scattered photon.

Thus electrons mediate the Raman scattering of phonons although they remain unchanged after the process. Since the transitions involving the electrons, are virtual they do not have to conserve energy, although they still have to conserve wavevectors [194].

Crystalline silicon has only one Raman active phonon mode. This mode is three-fold degenerate. Its frequency is, at room temperature, 521 cm^{-1} for Si. The wave vector k of the mode which is excited with conventional lasers is negligible as compared to the size of the Brillouin zone: other phonons with finite *k* are Raman forbidden as a result of the translational symmetry. These phonons can, however, be observed as two phonon processes in the second-order Raman spectrum. In this case only the sum of the *k*'s of the two phonons must be vanishingly small and hence the whole Brillouin zone contributes to the Raman spectrum. In amorphous Si the translational invariance is broken by the lack of long-range order. As a result the *k*-conservation selection rule breaks down and all phonon modes become first-order Raman allowed [208].

2.7.9. Types of Raman Spectra from Porous Silicon

Raman spectroscopy has been widely used to characterize both amorphous silicon (a-Si) and microcrystalline silicon (c-Si). Raman shift values are 480 cm^{-1} and 521 cm^{-1}, respectively. Their full widths at half maximum (FWHM) values are 20-30 cm^{-1}, and 3-5 cm^{-1}, respectively, at the temperature values of 300 K and 80 K [119]. If the structure within porous silicon material resembles to a-Si or c-Si, the Raman spectrum of porous silicon should resemble to that of a-Si or c-Si.

Raman spectra obtained from porous silicon material is divided into two categories. For one type of structure, the Raman shift is very similar to c-Si and shifted by about 2-4 cm^{-1} compared to c-Si. But the full width at half maximum (FWHM) value is larger than in c-Si, around 7-9 cm^{-1}. Second type of Raman spectrum has a large shift to lower energies by around 7-10 cm^{-1} or even more, and their FWHM values are much larger than the first type of Raman spectrum, around 10-40 cm^{-1} [119].

The dimension of the porous silicon structure is calculated using Raman spectrum parameters (Raman peak shift, and FWHM values) which lead to dimensions 2-3 nm upto 20 nm. Confinement of the phonon leads to a momentum uncertainty, and so the Raman peak broadens and shifts to lower energy. This effect can be used to determine the size of silicon crystallites using Raman measurements. Dimensions calculated from Raman spectrum is found to be correlated well with the photoluminescence spectrum of the porous silicon material. The diameter of the porous silicon structure can also be analysed using electron microscopy techniques staring from 2-3 nm upto several hundred micrometers.

2.8. PHOTOLUMINESCENCE SPECTROSCOPY

2.8.1. Photoluminescence Theory

The luminescent material must have a semiconductor structure with a nonzero band gap energy E_g and energy must be imparted to this material before luminescence take place. The mechanism of photoluminescence in semiconductors is schematically depicted in Figure 2.17, which plots the *E*-*k* diagrams for an indirect gap material, where *E* and *k* are

the kinetic energy and wave vector (momentum vector) of the electron or hole, respectively. Upon absorption of an UV or visible photon with an energy $\hbar\omega_{exc}$ exceeding the band gap energy of the material, an electron-hole pair is created and the hole (electron) is excited to states high up in the valence (conduction) band. During a photon absorption process in semiconductors, both energy and momentum are conserved. For an indirect band gap material of which the conduction band minimum and the valence band maximum have different *k* values, conservation of momentum implies that the photon absorption process must be assisted by either absorbing or emitting a phonon (a quantum of lattice vibration), because the electron wave vector must change significantly in jumping from the valence band in state to a state in the conduction band, and the absorption of a photon alone can not provide the required momentum change since photon wave vector is much smaller than the difference between initial and final wave vectors.

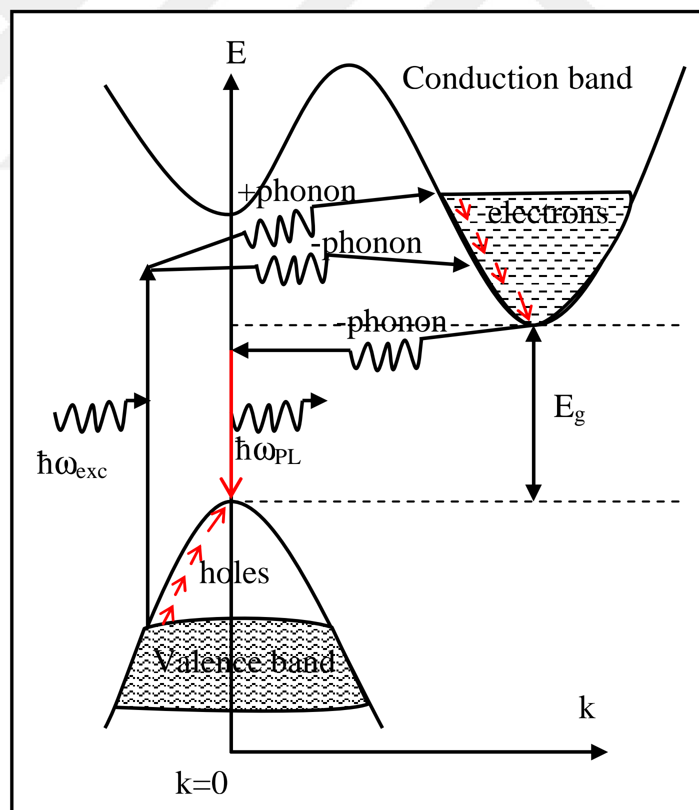

Figure 2. 17 Photoluminescence mechanism of indirect band gap semiconductors

The excited electron and hole will not remain in their initial excited states for very long; instead, they will relax very rapidly (~ 10^{-13} s) to the lowest energy states within their respective bands by emitting phonons. When the hole (electron) arrives at the top (bottom) of the valence (conduction) band, the electron-hole pair can recombine radiatively with the emission of a photon (luminescence). In an indirect gap material, the excited electron located in the conduction band undergoes a change in momentum state before it can recombine with a hole in the valence band; conservation of momentum demands that the electron-hole recombination must be accompanied by the emission of a phonon, since it is not possible to make this recombination by the emission of a photon alone. The PL efficiency is determined by the competition between radiative and nonradiative recombination. For an indirect gap material, the PL process, which requires a change in both energy and momentum for the excited electron and hence involves both a photon and a phonon, is a second-order process with a long radiative lifetime (~ 10^{-5} -10^{-3} s), and therefore a relatively small efficiency because of the competition with nonradiative combination.

However, for particles in the nanometer size domain, substantial changes are expected in both the efficiency and the peak energy of the photoluminescence due to the quantum confinement effect. This can be understood in terms of the Heisenberg uncertainty principle. Unlike in bulk materials the electrons and holes are free to move within their respective bands in all three directions, in nanoparticles the electrons and holes are spatially confined and hence their motion is quantized in all three dimensions. The spatial confinement of a particle of mass m to a region in a given direction of length Δx introduce an uncertainty in its momentum $\hbar/\Delta x$ and increase its kinetic energy. The quantum confinement effect would lead to a progressive widening of the band gap of a nano-sized semiconductor as its size is reduced, along with a broadening of the electron-hole pair state in momentum space (i.e. an increased overlap between the electron and hole wavefunctions), and a decreasing probability for the pair to find a nonradiative recombination center, provided that the surface dangling bonds are passivated which would otherwise act as traps for the carriers and quench the PL. While the former would shift the PL peak to higher energies, the latter two effects would greatly enhance the electron-hole radiative recombination probability and result in a higher PL efficiency. This is one of the main reasons why silicon nanocrystals are studied recently since they are capable of

luminescing very efficiently (with essentially 100% quantum efficiency) in the energy range (~ 1.4 eV - 2.4 eV), while bulk silicon, an indirect gap semiconductor with a band gap of ~ 1.17 eV at T = 0 K, does not luminesce.

Since visible photoluminescence is the most attractive technological property of porous silicon, photoluminescence measurement is one of the characterization technique used in this work. The basic principle is the optical excitation of an electron-hole pair, followed by radiative emission. While basic principle of electroluminescence is electrical excitation of an electron-hole pair, followed by radiative emission.

The broad PL band from porous silicon has been observed experimentally and studied theoretically, and a quantum confinement model has been proposed. It is now mostly accepted that with reducing the size of silicon QDs the zero-phonon direct band-to-band transition becomes partially allowed and therefore the effective red band originates from two kinds of luminescent mechanisms: direct band-to-band recombination and phonon-assisted indirect recombination in parallel. With reducing size of the nanoparticles the quantum confinement effect is enhanced. However, unlike other direct band-gap semiconductor nanostructures in which most of the optical properties follow the predictions of the quantum confinement model, many of the basic properties of silicon nanocrystals do not follow this model. Thus some different physical mechanisms in addition to the quantum confinement effect involved in the effective room temperature emission in silicon nanostructures have been proposed. It is now generally agreed that photoluminescence from porous silicon domain can derive from a combination of quantum confinement and surface effects. To date there is still controversy concerning the origin and nature of the radiative states that contribute to the PL and the detailed physical processes are still unclear and under debate. This is most likely due to the variability in sample structure and the many possible states in silicon nanostructures [209-223].

Photoluminescence from porous silicon is an indication that the optical physics of the nanocrystallites in the porous silicon material differs from bulk crystalline silicon. Photoluminescence in the visible region of the spectrum corresponds to energies significantly larger than the band gap energy of silicon. The band gap energy of silicon is 1.17 eV, with corresponding wavelength of 1100 nm. The photon energy of

photoluminescence from porous silicon falls mainly between 1.6 eV to 2.2 eV. The "energy of the peak" of the photoluminescence which is higher than the band gap energy of 1.17 eV of crystalline bulk silicon can be explained in terms of quantum confinement effects. Quantum confinement effects are also responsible for the formation of nanometer sized structure in silicon and this lead to an increase in the band gap of this structure [119].

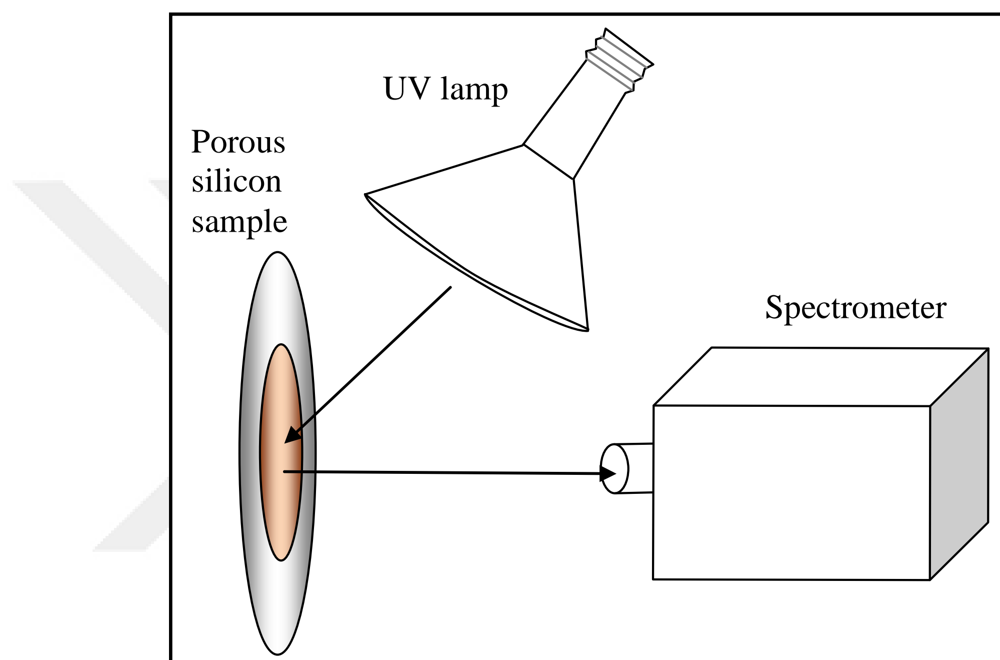

Figure 2. 18 The schematic of photoluminescence spectroscopy

The schematic of photoluminescence spectroscopy is depicted in Fig. 2.18.

Table 2. 2 Porous silicon photoluminescence bands

Spectral range	Peak wavelength nm	Luminescence band label	PL	EL
UV	~ 350	UV band	yes	no
Blue-green	~470	F band	yes	no
Blue-red	400-800	S band	yes	yes
Near IR	1100-1500	IR band	yes	no

Canham reported strong PL from porous silicon at room temperature and suggested the quantum confinement (QC) model for its mechanisms in 1990 [95]. He demonstrated efficient visible photoluminescence (PL) in Si for the first time and its shift from the infra-red to red as the porosity of the sample increased which is assumed to be a proof of quantum confinement. He also showed that the fabrication process is simple and low cost regarding that electronics and optics could be integrated onto the same chip. Since then there has been a long debate for the PL mechanisms of PSi [209-2011]. It was suggested that more than one type of mechanism were needed in interpreting photoluminescence from PSi. It was suggested that for the S-band luminescence the QC model works but the F-band luminescence is very likely to originate from contaminated or defective Si oxides [212]; and that for nanometer silicon particles with larger sizes, the QC model works, but for nanometer silicon particles with smaller sizes, Si=O bond plays the key role [213-214].

Quantum confinement of carriers in Si nanostructures was the first model proposed to explain PS luminescence [95]. The various models can be grouped in six different categories which assume an extrinsic origin for the luminescence, except for the quantum-confined model: The hydrogenated amorphous silicon model, the surface hydrides model, defect model, siloxene model, surface states model, and quantum confinement model. Quantum confinement effects result in an enlargement of the band gap, in the relaxation of the momentum-conserving rule, and in the size dependence of the PL energy that naturally explains the efficient luminescence, the up-shift, and the tunability of the PL band in PS. Many other experimental results support the quantum confinement model. Structural characterization has proven that PS is crystalline in nature. Observations of nanocrystal of nanometric dimensions have been reported. The band gap up-shift is clearly visible in absorption spectra, and the luminescence blue shift after further chemical dissolution in HF is easily explained by further reduction of nanocrystal dimensions. Fresh structures can be theoretically modeled as quantum wires, while aged structures are usually more dot-like [215-216].

The spatial confinement of excitons in small nanocrystals breaks the k-conservation rule for indirect transitions. Thus no-phonon assisted transitions, which are forbidden in bulk

silicon, have the same probability as TO phonon-assisted processes at a confinement energy of > 0.8 eV.

However, it is becoming increasingly clear that, even in the quantum confinement framework, the emission peak wavelength is not only related to size effects. Freshly etched and very high porosity samples which have not been exposed to the air have luminescence peak energies in the 3 eV range while as soon as they get into contact with air their luminescence peak moves to the usual 2 eV range [217-218].

The photoluminescence from porous silicon can originate from a combination of quantum confinement and surface effects. Contribution of defects, interfacial oxides, hydrides, and chemical impurities to photoluminescence spectrum are also found in the literature. The four main observed spectral ranges for photoluminescence spectrum is given in Table 2.2. An orange photoluminescence at room temperature comes primarily from quantum confinement in nanocrystalline silicon domains and it is designated by “S” label which stands for “slow”, because the emission lifetime for this material is on a timescale of microseconds. In the blue-green spectral range, PL emission lifetime is in a few nanoseconds. Therefore “F” label stands for “fast” for this range. The UV and IR bands are labeled for the region of the spectrum in which they appear. Since the UV and F bands are only seen in oxidized porous silicon, they are thought to originate from oxide-based defects. The IR band has been ascribed to dangling bond states or a silicon atom that is bonded to three other atoms rather than its usual complement of four atoms. Thus it is not passivated, it is “active”.

To obtain a bright S band (orange) photoluminescence, porous silicon domain must contain a large number of quantum-sized silicon crystallites, which cannot be quenched by surface species or defects. Studies have shown that the commonly observed red/orange visible luminescence band is due to direct radiative recombination of carriers in the crystalline nanostructures. The shift of the bandgap into the visible is due to quantum confinement. The quantum structure also results in the formation of a pseudo-direct gap increasing the efficiency of radiative recombination by over 10^5.

Formation conditions including wafer cleaning procedure affect the efficiency of the photoluminescence spectrum. It also stated in the literature that, PL spectra can not be obtained from porous silicon structure including nanometer scale silicon features. But, to display bright S band photoluminescence, samples must contain a large number of quantum-sized silicon crystallites which cannot be quenched by surface species or defects [124]. S-band has the most technological significance since it can be electrically excited and it can be tuned in the visible band from 400 nm to 800 nm.

The main problem in luminescent porous silicon is the degradation of the luminescence. Treatments for stable and efficient photoluminescence have been studied extensively in the literature [219-220]. High pressure water vapour annealing was found to be the most effective solution for stable photoluminescence in porous silicon material [221].

The photoluminescence spectrum of light given off from porous silicon structure can be tuned by changing the formation parameters such as anodization current density, anodization time, and HF acid concentration in the anodization solution.

A set of PL spectra were obtained from the samples of A-series, B-series, and C-series which were produced during this study given in the experimental section. Those spectra were interpreted as a manifestation of quantum confinement effects. PL spectrum is in correlation with nanometer sized structure. Radius of crystallites which can emit photons with an energy E was calculated by the following formulas given by Yorikawa et al. in 1998, [222] and by Ledoux et al. in 2000 [223].

$$R(E) = \left[\gamma / \left(E - E_g^0\right)\right]^{1/n} \tag{2.21}$$

In the above equation, γ=24.0 (eV Å^n), n=1.25 and $E_g^{\,0}$ =1.17 eV.

$$E_{PL}(d) = E_0 + \left(3.73 / d^{1.39}\right) \tag{2.22}$$

In the above equation, E_0 =1.17 eV, d is the particle diameter in nanometers, $E_{PL}(d)$ is the photoluminescence peak energies obtained from porous silicon samples.

Equation (2.21) given by Yorikawa et al. stated that this equation is found to be underestimated the particle diameter when the equation parameters set to γ=14.8 (eV $Å^n$), n=1.25 and E_g^0 =1.17 eV. Equation (2.21) and Equation (2.22) was used for the calculation of the diameter values of porous silicon structures. The results were given in the next section.

2.9. ELECTRICAL CHARACTERIZATION

2.9.1. Current versus Voltage Measurements

Current versus voltage measurements were carried out with a Keithley SourceMeter model 2400. Constant current values were also supplied from Keithley SourceMeter model 2400 during the anodization process. Current source was connected to the home made Teflon anodization cell with a suitable wiring. Silicon sample was utilised as anode, while spirally wounded platinum wire was utilised as cathode in this system.

I-V relationship of p-type silicon substrates formed with aqueous HF acid solutions exhibit the same trend as given in Figure 2.3 and Figure 2.4 [112, 116].

Measured I-V curves for p-type silicon in aqueous HF acid solution for different silicon substrates are given in the next section.

2.9.2. Capacitance Measurements

Capacitance measurements were carried out with an LCR meter with model 7600 from QuadTech in a thermally isolated chamber of a humidity generator from Thunder Scientific and the results were given in Table 3 and Figure 8. Relative humidity values from 20 %rh to 95 %rh at specified temperature value were generated using a “two-pressure, two-temperature” humidity generator from Thunder Scientific model 2500ST.

Relative humidity sensors are characterised mostly in terms of their sensitivity, linearity, and capacitance change [41, 42, 224, 225]. Nanoporous silicon relative humidity sensors

were characterized in terms of its sensitivity from 20 %rh to 95 %rh relative humidity values. Nanoporous silicon relative humidity sensors are characterized in terms of normalized percentage capacitance change (*NPCC*) in the range from 20 %rh to 95 %rh [226]. Normalized percentage capacitance change was calculated using the below stated equation and the results were given in the results section.

$$NPCC_{\%RH} = \left(\left(C_{RHhigh} - C_{RHlow}\right)/C_{RHlow}\right) \cdot \left(1/\Delta RH\right) \cdot 100 \tag{2.23}$$

In the above equation, *NPCC* is the normalized percentage capacitance change, C_{RHhigh} is the capacitance at highest relative humidity value, C_{RHlow} is the capacitance at lowest relative humidity value, and ΔRH is the relative humidity change.

Sensitivities values of sensors were calculated using Eq. (2.23) as given below and from the measured capacitance values at above specified relative humidity range. The calculated sensitivity values were given in the results section.

$$S = \Delta C_p / \Delta RH \tag{2.24}$$

$$\Delta C_p = C_{RHhigh} - C_{RHlow} \tag{2.25}$$

$$\Delta RH = RH_{high} - RH_{low} \tag{2.26}$$

In the above equation, *S* is the sensitivity, ΔC_p is the capacitance change, ΔRH is the relative humidity change, C_{RHhigh} is the capacitance at highest relative humidity value, C_{RHlow} is the capacitance at lowest relative humidity value, RH_{high} is the highest relative humidity value, and RH_{low} is the lowest relative humidity value.

The parallel plate capacitor model ($C= \varepsilon A/d$) can be utilised here to understand the change in capacitance (*C*) of the NPS sensor (with effective surface sampling area *A*) with humidity. Here *d* is the sample thickness and ε the electric permittivity of the dielectric materials (silicon, air, water) between the electrodes. Since electric permittivity of water is greater than that of air, the increase of capacitance across the sensor with humidity

corresponds to an increasing electric permittivity of the sensor as the percentage of water filled pores increases at the expense of air filled pores; as they are in parallel, a linear combination of the dielectric materials is assumed.

It should also be noted that the effective cross-section area would increase for a capacitor with a very high porosity, the effective surface area can increase the apparent surface area by up to a million times [226].

Capacitance measurements also gauge the quality of the mechanical structure of the NPS layers. This is critically important, since it determines the time period over which the sensor can be reliably utilised. Thus, after the measurements were completed on each sample, they were kept at ambient conditions for three months and their performance over the humidity range was again determined to gauge their mechanical stability over time.

2.9.3. Capacitance Modeling

The parallel plate capacitance of a material is given in the following equation.

$$C = \varepsilon A / d \tag{2.27}$$

A series combination of capacitors C_i causes an equivalent capacitance, $C_{Series} = 1 \big/ \sum_i (1/C_i)$, and a parallel combination of capacitors causes an equivalent capacitance, $C_{Parallel} = \sum_i C_i$.

These combinations can be utilised here to gain insight into the change in capacitance of the NPS sensor (with effective surface sampling area A=1 cm^2) with humidity. Here d is substrate thickness and ε the electric permittivity of the dielectric between the electrodes.

Cross-sectional SEM images of the five samples (presented in the experimental section), reveal the structure shown in Figure 2.19.

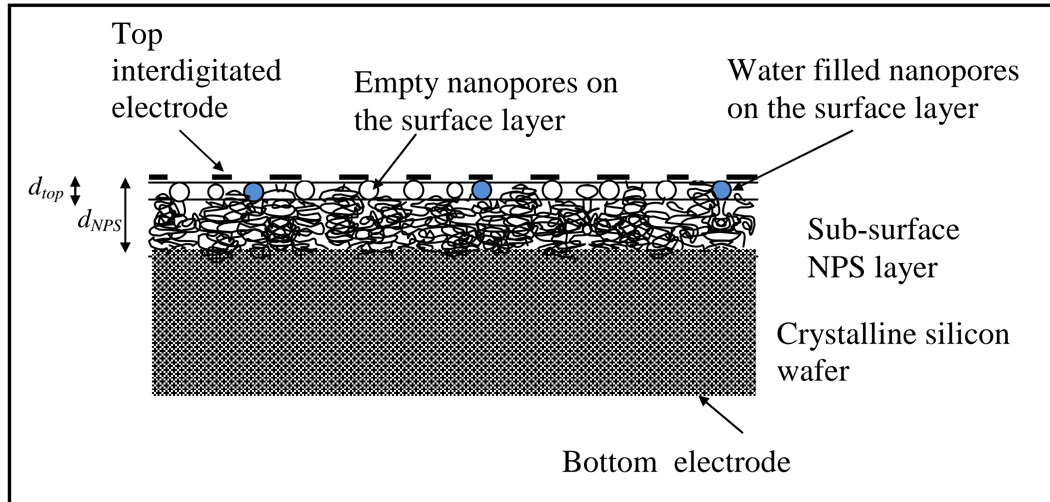

Figure 2. 19 The schematic of porous silicon structure

Once the NPS layer is formed the new dielectric material is a combination: air, SNC, and water. Since electric permittivity of water (ε_{water} = 7.12x10^{-10} F·m^{-1}) is greater than that of air (ε_{air} = 8.9x10^{-12} F·m^{-1}), the capacitance increase across the NPS sensor with RH corresponds to increasing electric permittivity of the sensor as the fraction of water filled pores increases at the expense of air filled pores. It should also be noted that the 'effective' cross-section area A is much greater than A_h for a capacitor with high porosity ($A = k_A A_h$); factor k_A may increase to 10^6 [226].

Since the area (A) of the sample is measured as 1 cm^2 (10^{-4} m^2) and the crystalline silicon wafers had a stated thickness of d = 500 µm, it was straightforward to calculate the theoretical capacitance of the silicon wafer with electrical permittivity of silicon, ε_{Si} = 1.053x10^{-10} F·m^{-1}.

During modelling of the measurements, it was assumed that during sensing water diffusion only occupies a fraction x of d_{NPS} ($d_{top} = x\ d_{NPS}$) giving rise to capacitance C_{top}. Beneath this, the second sub-surface NPS layer has a thickness $(1-x)d_{NPS}$ giving rise to capacitance C_{NPS}. In addition, these two upper layers are themselves combinations of dielectrics: (i) thin surface layer composed of three dielectrics (water, air, and NPS) (ii) sub-surface layer composed of two dielectrics (air and NPS).

Thus, each layer has its own capacitance: C_{top}, C_{NPS}, and the bottom layer C_{si}. A combination of these three causes C_{Sense}. Even allowing for a slight decrease in d due to formation of d_{NPS}, $C_{si} > C_{sense}$. Thus, C_{top} and C_{NPS} must be acting as a series connection of capacitors, since a parallel connection would increase, rather than decrease C_{Sense}. A simple mathematical model of the theoretical total capacitance C_{Sense} of the three layers is shown in Equation (2.28).

$$C_{Sense} = 1/\left(\left(1/C_{top}\right) + \left(1/C_{NPS}\right) + \left(1/C_{Si}\right)\right) \tag{2.28}$$

The capacitance values of water (C_w), air (C_{air}), and NCS (C_{NCS}) within each of the top two layers (i) and (ii) for a typical value of d_{NPS} = 10 μm were calculated from Equation (2.28). It was assumed that each layer had at least $k_A = 10^6$, and that water displaced air in the nanopores of the surface layer by a fraction f. Calculated values of water (C_w), air (C_{air}), and NCS (C_{NCS}) are presented in the results section, where x and f were variables in the model.

Since x is a fraction, all capacitances (except C_w) are greater than C_{si} since they are much thinner layers. Thus, in order that $C_{sense} < C_{si}$, capacitances within layer (i) must act as a series capacitor combination. This must also be the case for layer (ii) since, except water, its structure is similar to layer (i). Thus, Equation (2.28) is modified to give a total theoretical capacitance as follows.

$$C_{Total} = 1/\left(\left(\left(\left(1/C_w\right) + \left(1/C_{air}\right) + \left(1/C_{NCS}\right)\right) + \left(\left(1/C_{air}\right) + \left(1/C_{NCS}\right)\right) + \left(1/C_{Si}\right)\right)\right) \tag{2.29}$$

By fixing d_{NPS} and k_A and varying x and f, the theoretical data fitted to the measured C_{Sense} values are calculated.

3. EXPERIMENTAL PREPARATION OF NANOPOROUS SILICON SAMPLES FOR RELATIVE HUMIDITY SENSING

3.1. POROUS SILICON BASED MATERIALS FOR HUMIDITY SENSING

Porous silicon (PSi) is a material prepared by electrochemical or chemical etching of crystalline silicon in acid or alkali based solutions. Porous silicon structures contain nanometer to micrometer sized not only columnar pores but also granular islands and sponge-like structure.

Since porous silicon (PSi) has several unique properties, it has been extensively studied for many applications. After the discovery of its efficient photoluminescence in the visible region in 1990 by Canham [95], the main interests were focused on optoelectronic applications. After that, the field of interest has also expanded in micromachining [227] and biomaterial applications [228-230], among others.

Due to its large specific surface area, porous silicon has also been found to be a potential material for gas and humidity sensors. [125-141]

3.2. POROUS SILICON PREPARATION

A crystalline silicon (c-Si) wafer with (100) orientation and of p-type is preferred for the experiments done throughout this thesis work. A crystalline silicon wafer with (100) orientation is preferred since structure is mainly dependent on orientation [231]. Porous structure created on c-Si wafer having (100) orientation produce perpendicular structures to the plane surface of the wafer. A crystalline silicon (c-Si) wafer of p-type is preferred since it doesn't require an excitation source such as light to generate hole which is required to start the reaction takes place between c-Si wafer and a solution containing hydrofluoric acid to produce porous structure.

Porous silicon (PSi) structure is formed on crystalline silicon (c-Si) wafers which are divided into nine pieces having similar dimensions. Divided c-Si wafer pieces are named as samples hereafter. These samples are diced so as to adapt well with a hole of the anodization cell designed accordingly.

The typical device structure for porous silicon thin film relative humidity sensors used in this work is presented in Figure 3.1.

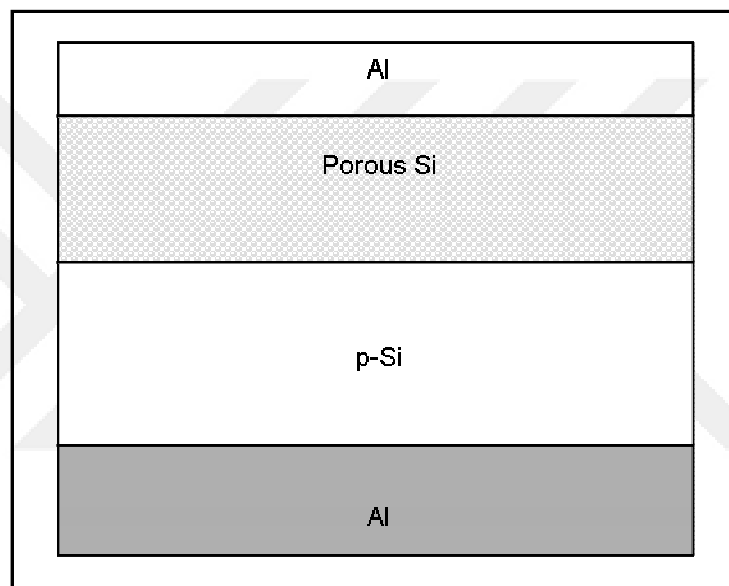

Figure 3. 1 Typical device structure

3.2.1. Preparation of porous silicon for analysis in this thesis

Silicon substrates of p-type which have 1-30 Ohm·cm and 1-20 Ohm·cm resistivity, and (100) orientation with thickness of 500 µm were used for the formation of porous silicon structures. Polished surface of the wafer is named as front surface of the wafer, and unpolished surface of the wafer is named as rear surface of the wafer thereafter.

Formation of porous silicon steps are given as:

- Chemical cleaning of silicon wafer
- Thermal evaporation of metal in vacuum to the rear surface of the wafer

- Formation of porous silicon on the front surface of the wafer
- Design of anodization system regarding solution and reactions
- Setting up current versus voltage (IV) measurement system
- Final drying treatment of the porous silicon structure
- Surface stabilization of porous silicon samples
- Thermal evaporation of metal interdigitated electrode (IDE) in vacuum on front surface of the porous silicon structure

3.2.2. Chemical Cleaning

The first step of the fabrication of porous silicon is a standard RCA cleaning of the silicon wafer. RCA clean developed by Werner Kern working for the Radio Corporation of America (RCA) in 1965. After that, it is named as RCA cleaning method, and it is accepted as a standard set of wafer cleaning procedure. RCA cleaning for silicon wafers has five basic steps:

- Removal of organic and inorganic contamination,
- Removal of certain organic and metal surface contamination,
- Removal of native oxide layer and any contamination in the oxide,
- Removal of certain ionic and metal surface contamination, and
- Drying with nitrogen purge.

First cleaning was accomplished by using a mixture of sulfuric acid and hydrogen peroxide. Second cleaning was performed in a 5:1:1 ratio mixture of deionized (DI) water, ammonium hydroxide, and hydrogen peroxide. Third step was a 30 second dip in 1:20 hydrofluoric acid (HF) and DI water. Fourth step was a cleaning of wafer in 10 minutes in a 6:1:1 ratio mixture of DI water, hydrogen chloride (HCl) and hydrogen peroxide mixture. Each step was ended by rinsing in deionized water for 10 minutes.

After RCA cleaning silicon wafers were dried with nitrogen gas purge. As soon as the drying was completed, samples were placed inside the physical vapor deposition system to deposit aluminum on unpolished surface of the crystalline wafer.

3.2.3. Thermal Evaporation

After drying of the silicon wafer, unpolished side of the wafer was coated with aluminum by physical vapor deposition technique. This technique is a vacuum evaporation of metals such as aluminium on silicon wafer.

Coating of aluminum is required for the humidity sensor structure. In order to make an ohmic contact between silicon wafer and aluminium, the silicon wafer was put in a furnace having a temperature value of 400 °C with time duration of 30 minutes.

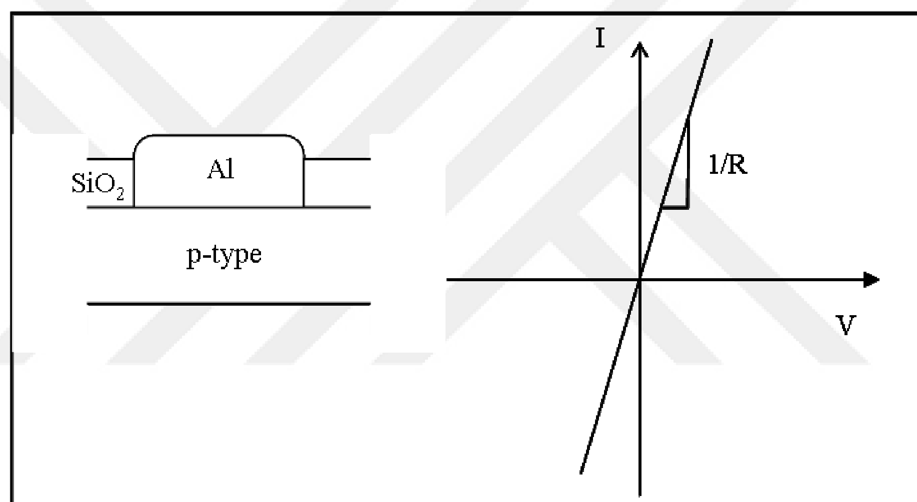

Figure 3. 2 Ohmic contact using Aluminum on crystalline silicon

Procedures described up to this point were applied to each silicon wafer used for the formation of porous silicon structure.

3.3. FORMATION OF POROUS SILICON

3.4. DESIGN OF ANODIZATION CELL SYSTEM

Home-made system was designed to enable the current to pass through the cell at the same time as given in Figure 3.3. Technical drawing of the Teflon anodization cell design was given in Figure 3.6.

An isolated, closed system is required into which the silicon sample can be placed and the solution containing hydrofluoric (HF) acid can act on it to produce the nano-sized porous or granular structures. Since HF acid was choosen as an anodization medium, materials compatible with HF acid must be chosen. Thus platinum and Teflon were chosen as they withstand HF acid.

A home-made Teflon cylindrical cell together with platinum electrode, named as the electrochemical anodization system used in this thesis work, were designed for the formation of porous silicon.

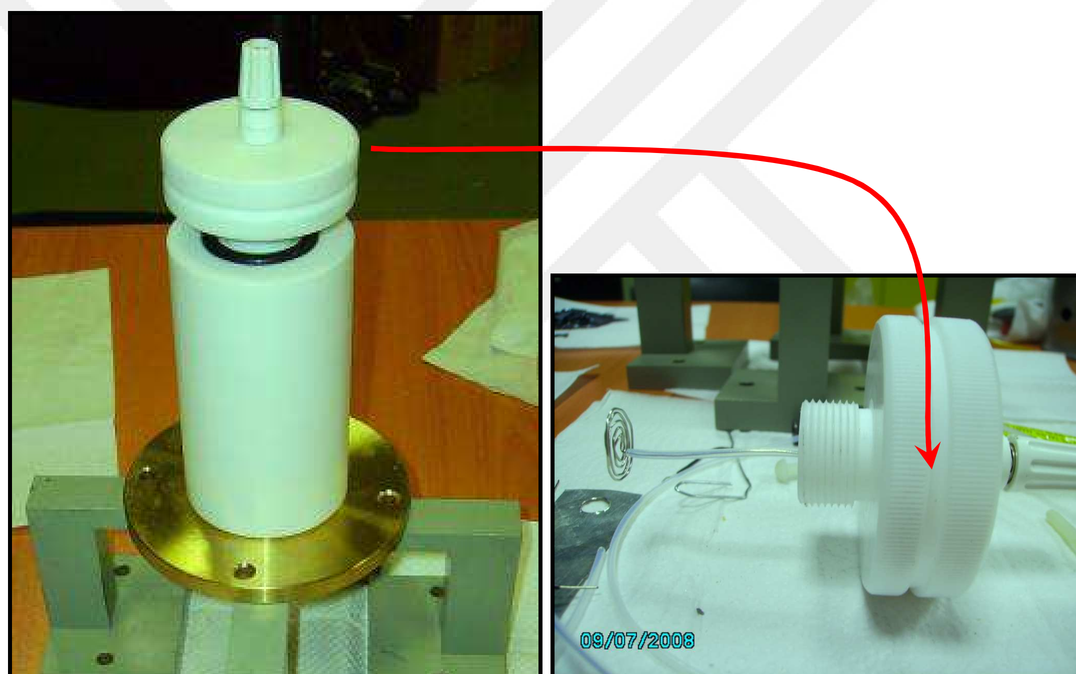

Figure 3. 3 Home-made Teflon anodization cell and platinum spiral shaped electrode

A silicon wafer was diced into nine pieces as evenly as possible as given in Figure 3.4. Each piece had an appropriate size in order to fit into Teflon cell in the anodization system. Platinum wire act as cathode while crystalline slicon act as an anode in the chemical reaction. Anodization solution, platinum electrode, and silicon were the main parts of the system as figured out in Figure 3.5. Detailed drawing of the system is given in Figure 3.6.

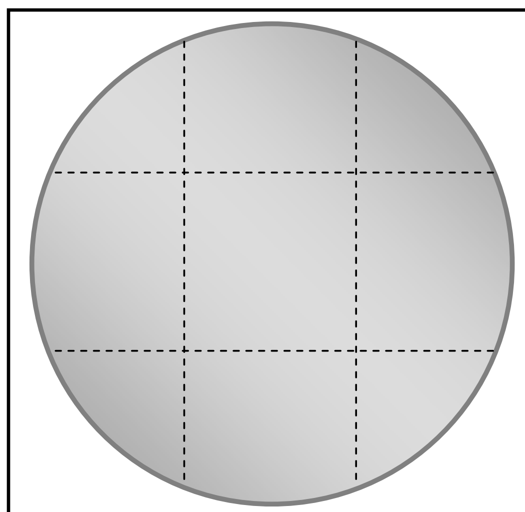

Figure 3. 4 A silicon wafer diced into nine pieces

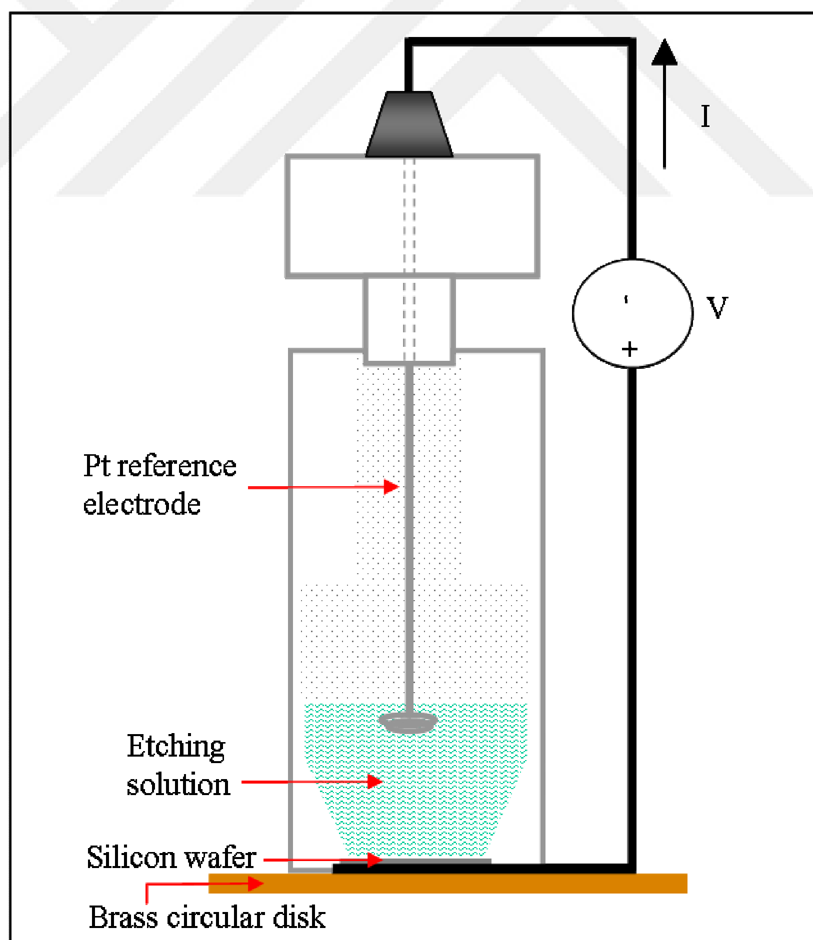

Figure 3. 5 Drawing of the Teflon anodization cell

As a third step, formation of porous structure on silicon wafer is conducted with the anodization system. The most common way of producing porous silicon structure is based on the electrochemical etching of crystalline silicon (c-Si) in aqueous hydrofluoric (HF) acid solutions by passing specific current values. In the anodic dissolution process, it is known that hydrogen gas is released from the dissolving silicon surface, so if the surface tension of the anodization solution is high, the hydrogen gas is effectively trapped on the silicon surface. Thus the reaction ceased. Besides, since silicon is hydrophobic, hydrogen bubbles will then mask the underlying silicon surface from the HF acid based anodization solution. In order not to cease the reaction and maintain a homogenous structure it is necessary to use another material namely a surfactant that reduces the surface tension of the anodization solution. The term "surfactant" is derived from the words "surface activity" and is used to describe chemical compounds used for the purpose of modifying the surface properties of solutions, specifically in reducing the surface tension. Surface tension arises in a solution due to the attraction between its constituent molecules. This gives the fluıid surface a property similar to a stretched elastic membrane. Reducing the surface tension has two effects on the anodization process. Firstly it will reduce the size of the hydrogen bubbles, secondly allow the formed bubbles to escape more easily from the surface of the silicon and the solution. Surfactants such as Triton or ethanol are the materials used for this purpose. Ethanol was used for the formation of porous structure on silicon substrate throughout the experimental work done in this thesis work. HF acid, DI water and ethanol were the main components of the anodization solution. The variation of HF acid concentration affects the structure formed on silicon substrates.

HF is diluted with ethanol since silicon is organophilic and hydrophobic, the use of ethanol guarantees a higher homogeneity, due to a better wettability of the surface than deionized water. Ethanol was used unless otherwise stated.

Chemical reaction of silicon with HF acid for the formation of nanocrystallite porous structure is given in theoretical section from Equation (2.1) to Equation (2.5) and in Figure (2.2).

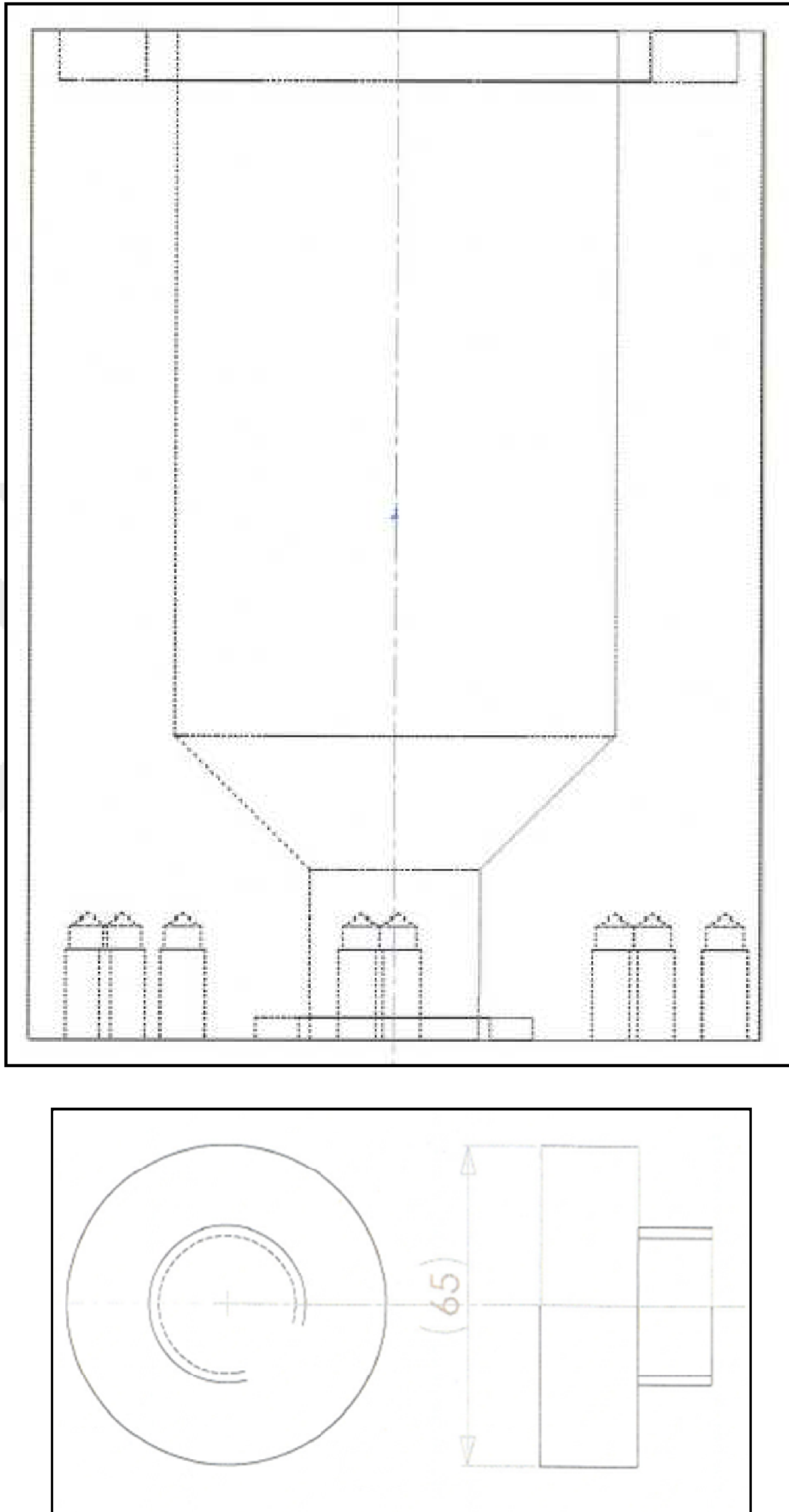

Figure 3. 6 Technical drawing of home-made Teflon anodization cell

4. RESULTS AND DISCUSSION

4.1. CURRENT VERSUS VOLTAGE (I-V) MEASUREMENT SYSTEM

Current versus voltage (I-V) measurement system was set up which is used both for determining the anodization current density value and for applying the determined current density value to obtain porous structure on each silicon sample.

Computer controlled source and measure unit was integrated to the home-made anodization system as given in Figure 4.1.

The current was applied in dark to produce porous structure on crystalline silicon in all the samples fabricated throughout this work. Samples were produced with specific current density values between 5.0 mA·cm^{-2} and 50.0 mA·cm^{-2} in time durations between 1 minute to 75 minutes.

Figure 4. 1 Home-made computer controlled anodization and I-V measurement system

I-V relationship of p-type silicon substrates formed with aqueous HF acid solutions obtained throughout this study which are given in the Figure 4.2 to Figure 4.5 exhibits the same trend with the literature which is depicted in Figure 4.6 [116].

4.1.1. Measured I-V curves for varying HF molarities

Representative I-V curves for p-type silicon in aqueous HF acid solution are given in Figure (2.3) and Figure (2.4) [116, 112].

I-V measurement graph obtained during the experiments performed on crystalline silicon samples were given in Figure 4.3. Anodization solution contains HF acid and ethanol in equal proportions of volume. Voltage values starting from -25 V until +25 V was applied in order to get the I-V curve which is a characteristic I-V curve of the crystalline silicon sample used throughout this study. Current value for the formation of porous silicon structure was obtained using this I-V curve. The first peak in this I-V curve is called as the maximum current in order to get the porous silicon structure, which is almost 50 mA. Therefore, current values smaller than 50 mA must be used in order to get the porous structure within the crystalline silicon samples whose specifications given in the Section 3.2.1.

An experimental representative I-V curve was obtained from a sample which was diced from a single wafer before electrochemical anodization process.

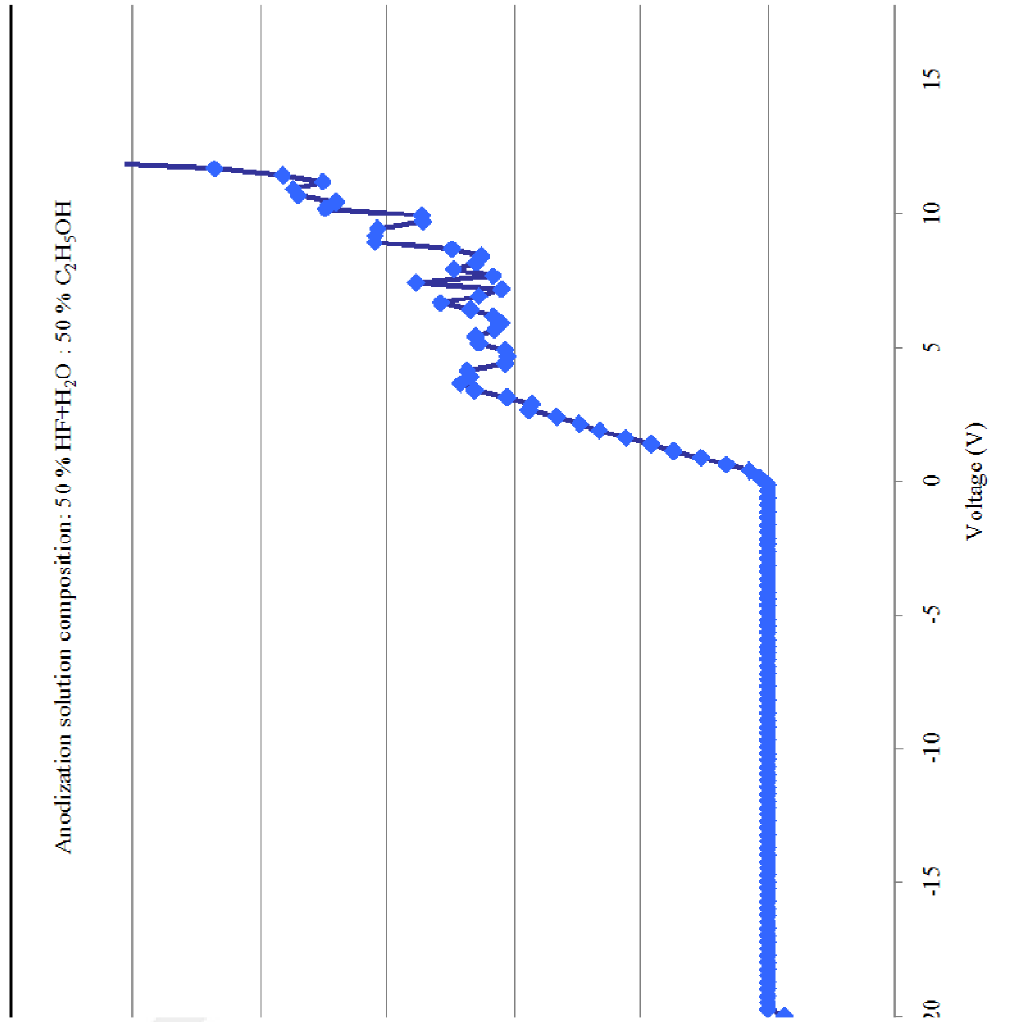

Figure 4. 2 Measured I-V curve for p-type silicon in aqueous HF acid solution for a silicon substrate

I-V measurements of various HF molarities were performed and graphs for these measurements are given in the Figure 4.3, Figure 4.4, and Figure 4.5.

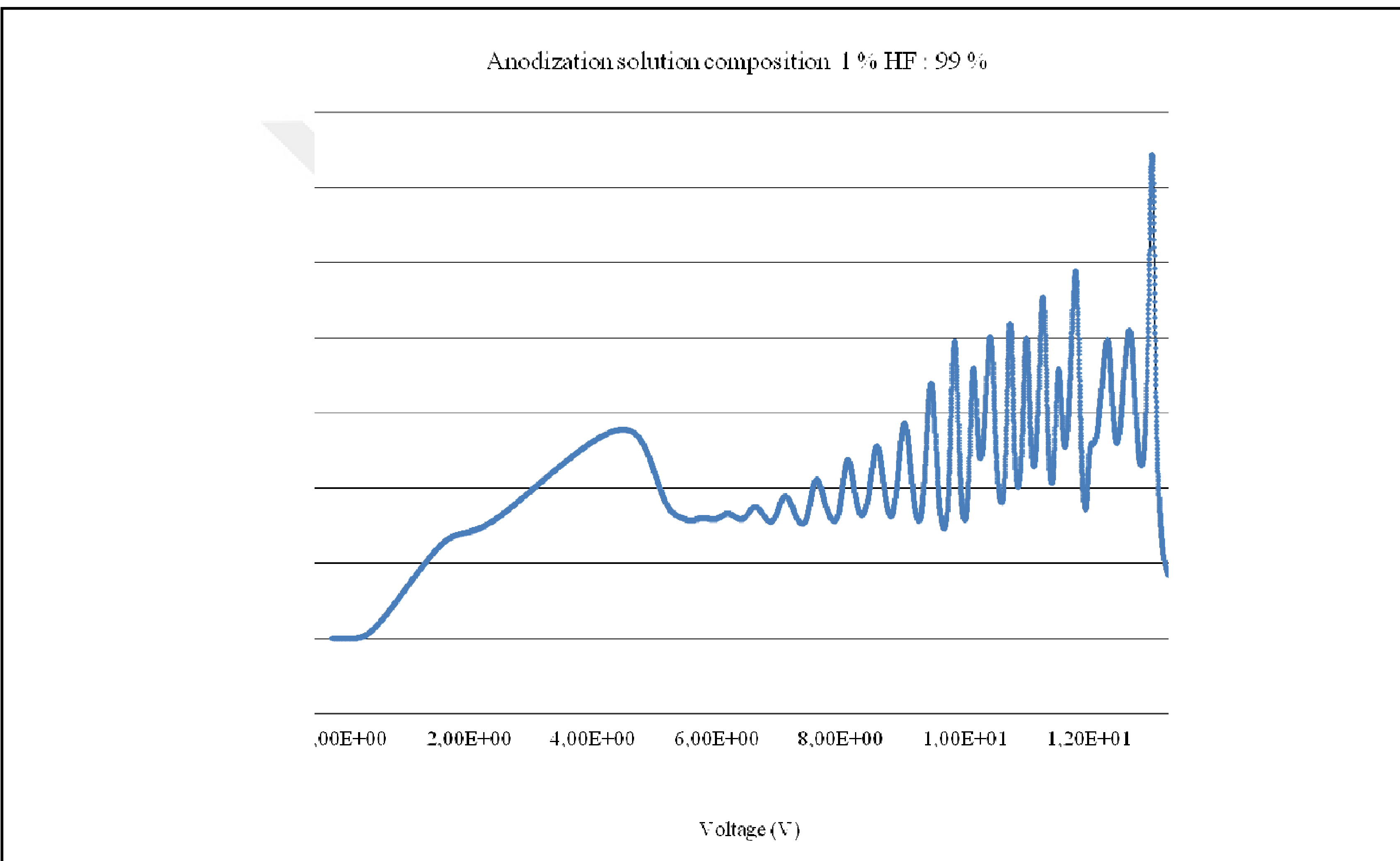

Figure 4. 3 I-V graph from 1 V to 15 V of 1 % HF molarity

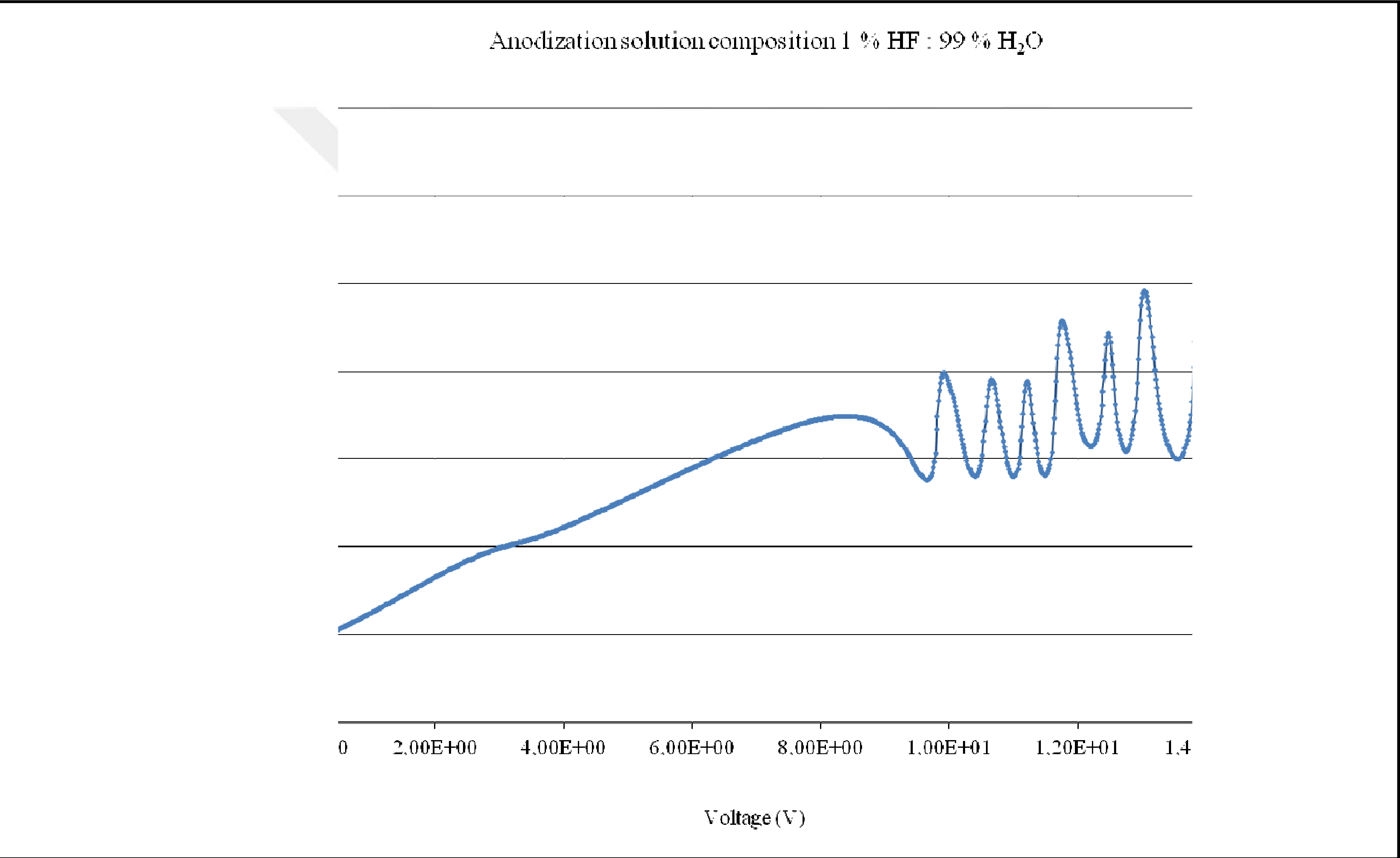

Figure 4. 4 I-V graph from 1 V to 15 V of 1 % HF molarity

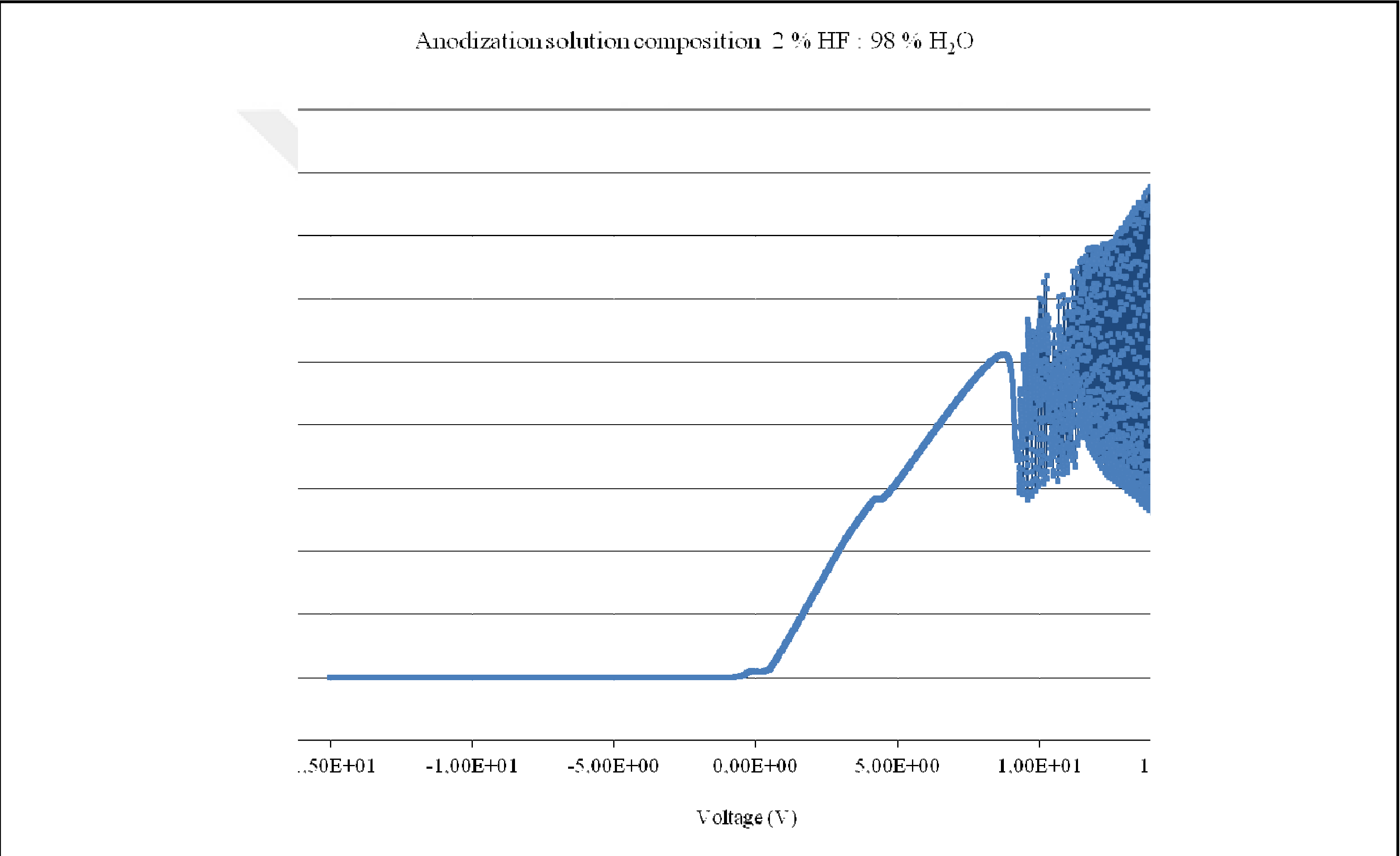

Figure 4. 5 I-V graph from -15 V to 15 V of 2 % HF molarity

Graphs obtained from silicon samples have three characteristic regions as seen both from Figure 4.2, Figure 4.3, Figure 4.4, and Figure 4.5 and from literature as given in the references between 142 and 159.

Upto first peak the region is named as pore formation. Upto second peak the region is named as transition where there are two competing reactions namely pore formation and electropolishing of silicon. After the second peak the region is named as electropolishing.

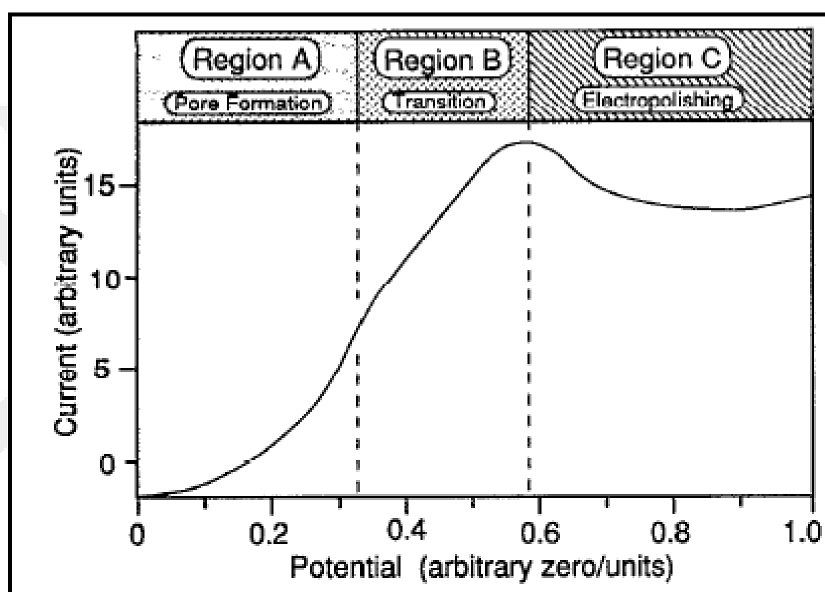

Figure 4. 6 Typical anodic I-V relationship for silicon in ethanoic HF acid showing the salient regions of dissolution. In region A, pore formation occurs, and in region C silicon electropolishes. Region B is a transition zone between regions A and C. Scale units and zeros are arbitrarily chosen and depend on silicon sample and experimental conditions (Adapted from [112])

In some ways electropolishing and electrochemical pore formation can be understood as the two competing reactions. In the first case the rate-limiting species in the chemical reaction is HF, while in the second it is the supply of holes from the electrode. If we assume a rough silicon wafer surface and a reaction that is limited by the diffusion of HF, it is obvious that hillocks will dissolve faster than depressions because they are more exposed to the source of the rate-limiting species. If the reaction is limited by charge supply from the electrode, the center of a depression will dissolve faster. The latter process

will lead to formation of pore while the former will lead to smoothing of the surface [116]. However, this is a simplified picture of the electropolishing effect; real systems are more complex and electropolishing of metal and semiconductors commonly involves the presence of a thin oxide film.

Current oscillations at silicon electrodes under potentiostatic conditions in HF were already reported in one of the first electrochemical studies of silicon electrodes. [98] They were ascribed to the presence of a thin anodic silicon oxide film in first place. High current values causes competing silicon oxide removal and etching reactions, but details of the oscillation process are still controversial. [142-149]

4.1.2. Oscillation process during anodization

A key to understanding the oscillation process is the observation that two forms of anodic oxide are present on the electrode: A dense, slow dissolving type of anodic oxide and a soft, fast dissolving type. A first indication of different dissolution rates is the shape of I-V curve itself. For current densities above JPSL it is mainly determined by the dissolution rate of the thin anodic oxide. [147] The oxide etch rates at different times of the oscillation cycle can be determined in situ, if the time delay between switching the electrode to open circuit potential (OCP) and the appearance of hydrophobic surface conditions is measured. Despite the fact that the oxide thickness changes by only about 20 %, the time required for etching of the total oxide thickness varies by a factor as high as three. This modulation of the oxide etch rate itself is sufficient to generate an oscillation loop. The initial formation of an oxide with a low dissolution rate leads to an increase in potential under galvanostatic conditions with increasing oxide thickness. If the potential across the oxide is constant over the whole sample area, which is fulfilled for a good conductivity of electrolyte and substrate, the oxide becomes very homogeneous in thickness. This is a self-adjusting process, because the electric field across a thin oxide would be higher than for an area with a thicker oxide, generating a higher oxide growth rate at the thin spot until a homogeneous oxide thickness is reached. This effect is sufficient to synchronize the oscillations. At a certain thickness a change in the oxide morphology occurs, which transforms the dense oxide into the soft, porous form. After this change the anodic oxide shows a high permeability for ions of the electrolyte. This leads to the sudden drop in the potential and

an increase in etch rate, a wavy pattern in I-V graphs. Now the etch rate exceeds the growth rate and the total oxide thickness decreases until the fast etching layer is etched away. The next slow etching oxide is exposed to the electrolyte and its thickness increases again, and so on. There is strong evidence for such a layered structure of the oxide and the transient behavior of its etching rate, which is proposed to be the driving force of the oscillation process [148, 149]. However, the microscopic origin of this change in oxide morphology is as yet unidentified. Different oscillation models are under discussion.

4.1.3. Final drying treatment

After anodization process, porous silicon samples have to be dried. Due to large capillary stress, drying of samples is a critical step and can result in extended cracking if special procedures are not followed. Drying procedure was applied to all of the samples in order to cease the anodization (etching) reaction to prevent cracking of the nanometer sized structure. Deionized (DI) water was used for termination of the reaction. But it is insufficient for the surface stability of the porous silicon structure since evaporation of water vapor from nanoporous structure will result collapse of the structure because of the high pressure exerted by water vapor pressure due to its high surface tension.

The origin of the cracking is the large capillary stress associated with evaporation from the pores. During evaporation a liquid-gas interface forms inside the pores. The surface tension at liquid-gas interface is responsible for the pressure decrease in a capillary liquid, which is given by the Laplace equation

$$\Delta P = -\left(2\gamma \cos\theta / r\right) \tag{4.1}$$

In the above equation, ΔP is the pressure decrease in liquid, γ is the surface tension of the liquid-gas interface, θ is the contact angle with the surface, and r is the radius of the capillary.

The pressure decrease given by Equation (4.1) will lead to high force per unit area on the capillary walls in contact with the capillary fluid. As the pressure decrease is limited to the pores, the average strees in the film is approximately Equation (4.1) multiplied by the

porosity of the structure. If a structure having a specific surface area of 600 $m^2 \cdot cm^{-3}$, then 13.2 MPa was calculated for ethanol [232-233].

Therefore, a material with a lower surface tension than water is required such as pentane. But since pentane and water are immiscible, an intermediate step is also required. Ethanol was chosen since it is miscible with water and pentane and also it has a surface tension value in between water and pentane. As a result, all the samples were rinsed and kept in DI water, ethanol, and pentane for 5 minutes, respectively. Hence a process called pentane drying was applied to all the porous silicon samples throughout this thesis work.

In the literature there are three different processes for the drying of porous silicon to reduce or eliminate the capillary stress:

- Pentane drying [114, 165]
- Freeze drying [114, 234, 235]
- Supercritically drying [114, 211, 236, 237]
- Slow evaporation rates [114, 165]

Among them pentane drying is the most suitable one for our purposes not only it requires simple equipment and material but also it is applied at room temperature. Pentane has a very low surface tension, and shows no chemical interaction with porous silicon unlike ethanol. Using pentane as drying liquid enables to reduce strongly the capillary tension inside the porous structure and exhibit no cracking pattern after drying. On the contrary, freeze and supercritically drying requires complicated equipment, special materials and cannot be applied at room temperature.

Some photographs of drying process which was applied to all the samples produced in this thesis work were shown in the Figure 4.7.

(a)

(b)

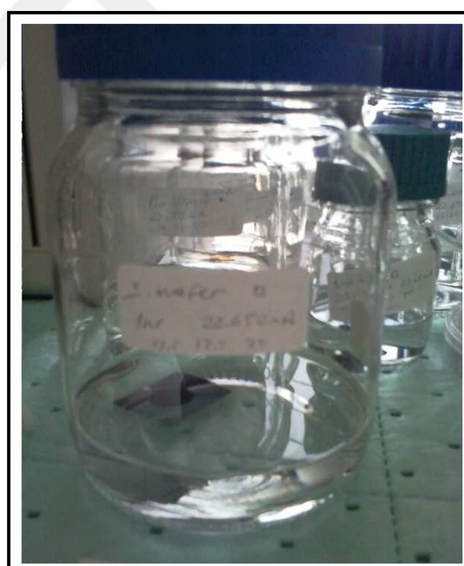

(c)

Figure 4. 7 Pentane drying steps: (a) distilled water rinsing of porous silicon sample (b) ethanol rinsing of porous silicon sample – porous silicon sample was seen at the bottom of the home-made anodization cell (c) pentane rinsing of porous silicon sample after removal of the sample from the anodization cell

Silicon samples diced from a single silicon wafer were shown in Figure 4.8.

Figure 4. 8 Silicon samples before etching

Porous silicon samples after anodization and drying process were shown in Figure 4.9.

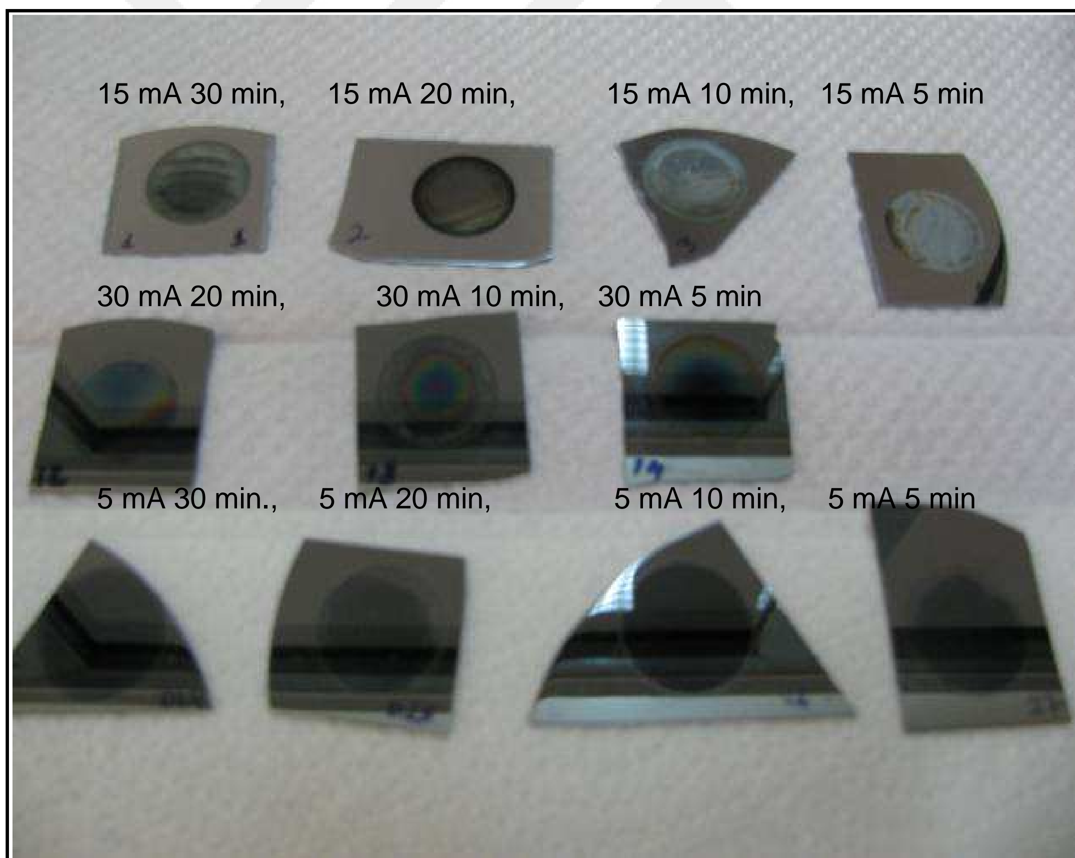

Figure 4. 9 Silicon samples after etching with porous structure

4.1.4. Surface passivation

In the literature there are many methods for the surface passivation of porous silicon surface as given in the Table 4.1.

Table 4. 1 Surface passivation techniques for porous silicon

Method	Procedure	Result
Oxidation	• Slow ageing in the dark (weeks or months) [120] • Anodic oxidation in a non-fluoride electrolyte [120] • Chemical oxidation (hydrogen peroxide, nitric acid) [120] • Thermal oxidation (300 °C - 900 °C) [120] • Thermal annealing at 400 °C in nitrogen ambient [130]	• -- • Electronic passivation; red to orange light emission [120] • Blue shift of luminescence [120] • Electronic surface passivation [120] • Conductance and capacitance of the annealed PS sensor become more stable [120]
Nitridation	• Rapid thermal annealing in N_2 or NH_3 (more efficient) (1100 °C, 30 s) [120] • Annealing above 400 °C converts surface into nitride [120] • Annealing at 300 °C in O_2 [120] • Annealing at 1000 °C in NH_3 [120] • Annealing at 600 °C several hours [120]	The humidity absorption behaviour is only slightly improved after thermal nitridation. [238]
Halogenation	• Exposure to halogen vapor for few minutes [120]	• Photoluminescence quenched [120]
Modifications involving metals	• Deposition of metal from the solution [120]	• Strong luminescence quenching [120]

Organic chemical derivatization	• PS react with 1-alkenes, non-conjugated dienes and aldehydes at 85 °C - 115 °C [239] • Derivatization by organic groups offers an alternative possibility to oxidation [120] • Thermal derivatization with alcohols [120] • Partial methoxylation by immersing in boiling methanol [120] • Grafting alkoxy groups by immersing in methanol, ethanol or propanol, irradiation of few minutes using 6W UV lamp located 2 cm away [120]	• Aging in ambient has no effect on PL [239] • -- • -- • Modification is accompanied by some oxidation [120] • Slight decrease and a red shift of luminescence. Alkoxy species covalently bind to the surface probably oxidized to some extent. [120]
Electrochemical derivatization	• Derivatization with formate groups (HCOOH+1M HCOONa 2 mA·cm^{-2}, 10-20 min) • Grafting with trifluoroacetate groups (CF_3COOH+1M CF_3COONa) [120] • Methoxy derivatization by anodisation of PS in anhydrous methanol electrolyte (10 mA/cm^2, 20 s) [120]	• Some oxide is created. SiOC bonding and loss of SiH groups [120] • These modifications are detrimental to the photoluminescence intensity. Reaction breaking Si-Si bonds rather than Si-H bonds. [120] • Dissolution occurs by chemical attack of Si-Si back-bonds at a methoxylated Si site. The silicon ends dissolve as $Si(OCH_3)_3$ and the surface is rehydrogenated behind. Luminescence intensity is preserved; stability to ageing is improved by about a factor of 2. [120]

	• Direct methyl grafting by anodization of PS in diethylether with $CH_3Li.LiI$ or CH_3MgI. (1-10 mA/cm^2, 10 min.) [120]	• Substitution efficiency of –H by $–CH_3$ is over 80 %, and only a few percent of the surface Si atoms get oxidized. Luminescence intensity is preserved and stability to ageing is improved by about an order of magnitude. [120]
Impregnation	• Indium plating [120] • Polymerization by polypirrole	• PL blue shift, intensity increased by about a factor of 20. [120] • EL efficiency and stability increased. [120]
Lewis acid hydrosilylation	• Hydrosilylation of unsaturated carbon-carbon bonds on the native hydride terminated PS can be induced by the Lewis acid $EtAlCl_2$ or white light illumination at room temperature in a matter of minutes or hours. [240]	• Porous structure is mainly unaffected [240]
Ozone oxidation	• By placing PS in a stream of ozone for 1 hour. [120]	• Hydrophilic surface [120]
Carbonization	15 min. acetylene room temperature & nitrogen 15 min 500 °C nitrogen till room temperature 10 min. 820 °C 15 min. acetylene room temperature & nitrogen 10 min. 820 °C nitrogen till room temperature [241]	• Excellent long term stability against ageing [241] • Resistant against harsh corrosives like HF and NaOH [241] • Stable in humid air [139] • Change hydrophobic PS surface to hydrophilic [139] • Enlarging pores [242] • Sensitivity of the sensor decreases [242] • Capacitance does not vary as much as the resistance during ageing [242]

Among them below stated methods are found to be cost effective and do not require complex experimental procedures.

Table 4. 2 Surface passivation techniques for porous silicon

Method	Procedure	Result
Oxidation	Chemical oxidation (hydrogen peroxide, nitric acid)	Blue shift of luminescence
Oxidation	Thermal annealing at 400 °C in nitrogen ambient.	Conductance and capacitance of the annealed PS sensor become more stable.
Impregnation	Indium plating	PL blue shift, intensity increased by about a factor of 20.
Impregnation	Polymerization by polypirrole	EL efficiency and stability increased.

As a result of the literature search, the most suitable and cost-effective process was choosen as the thermal annealing process. A set of porous silicon samples was then annealed in the furnace at 300 °C for two hours.

4.1.5. Thermal evaporation of interdigitated top electrode

After the formation of porous silicon, an interdigitated electrode (IDE) was vacuum evaporated on top of the structure. Designed IDE was the final step for the fabrication of humidity sensor. Multiple and single technical drawings of IDE were given in Figure 4.10 and Figure 4.11. Nine samples were coated with aluminium by evaporation in a single run by using IDE array as depicted in Figure 4.10.

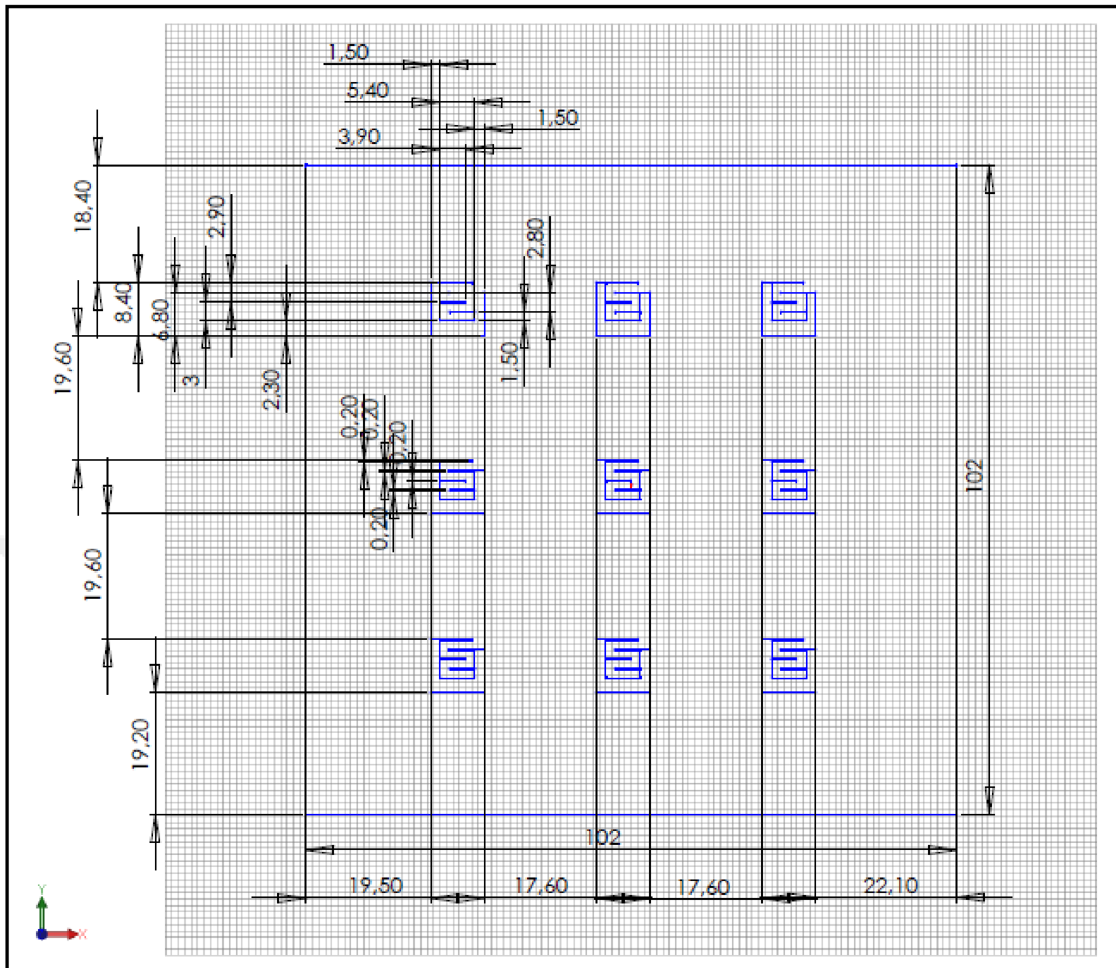

Figure 4. 10 Technical drawing of multiple top electrodes for thermal evaporation of aluminum on porous silicon samples to form humidity sensor

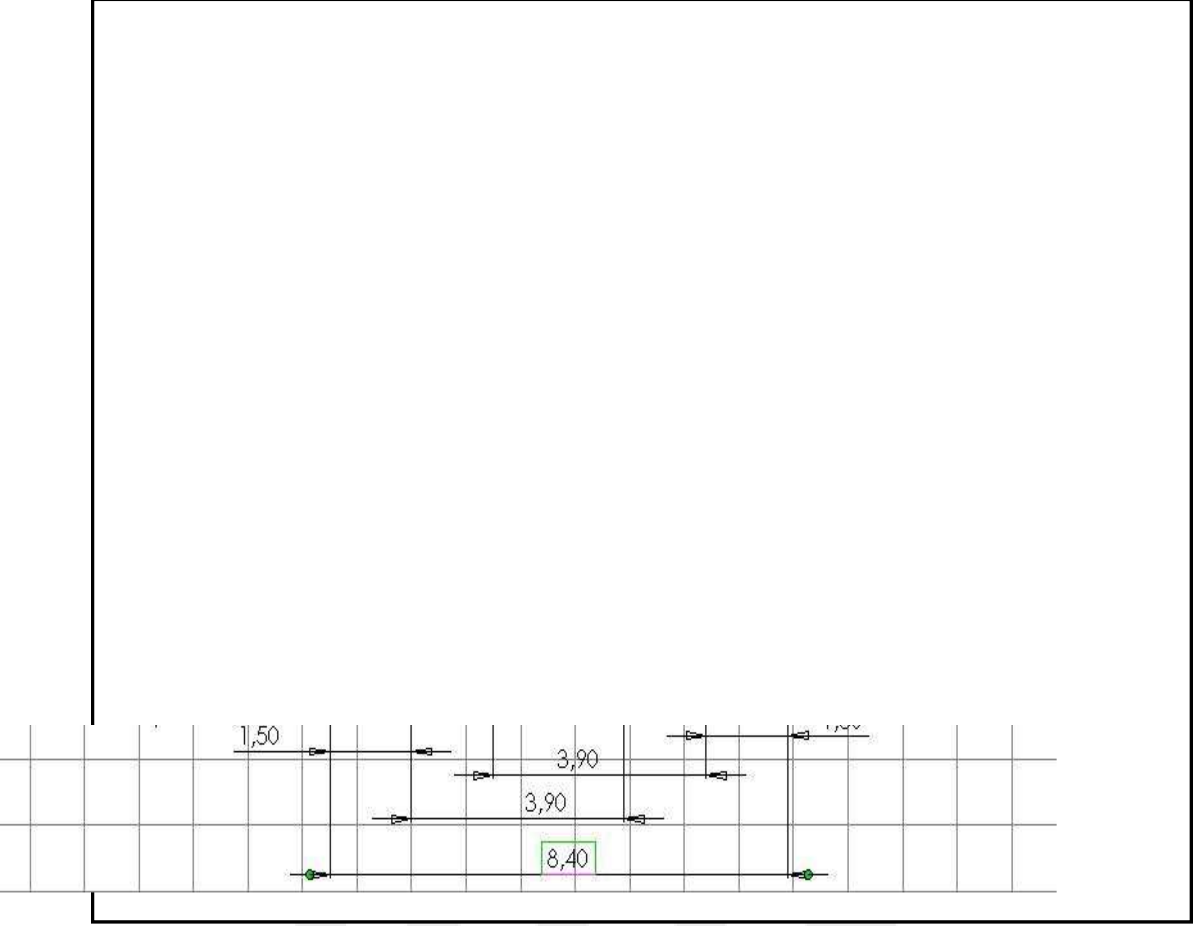

Figure 4. 11 Detailed technical drawing of single top electrode

4.2. OPTICAL MICROSCOPE IMAGES OF POROUS SILICON SAMPLES

All optical microscope images were taken from the middle area “e” of the sample porous silicon structure as shown in the diagram given below.

Before characterization measurements carried out, each silicon sample was cut into two pieces through an imaginary red line as shown in Figure 4.12. One piece was treated for relative humidity sensor, Raman spectroscopy, and photoluminescence spectroscopy, while the other half was used for SEM studies.

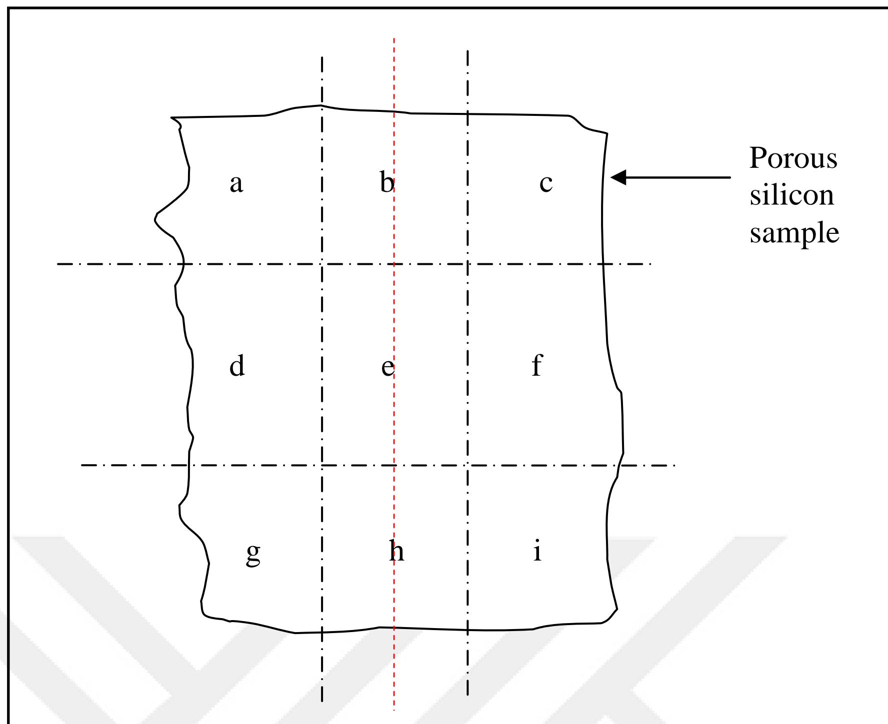

Figure 4. 12 Diagram of imaginary areas where images obtained from optical microscope from a porous silicon sample

4.2.1. Optical Microscope Images of Porous Silicon Samples with <100> wafer orientation, 1-30 Ω.cm, at various anodization current densities and durations

50 mA current applied in 5 min duration

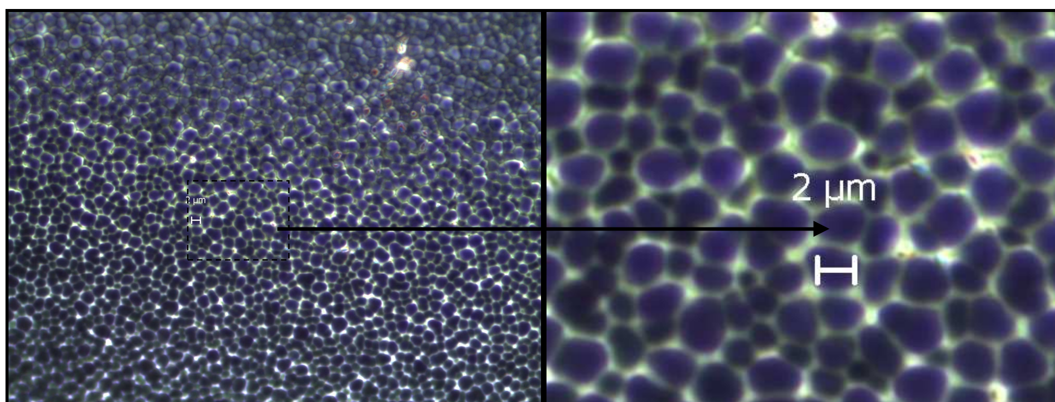

Figure 4. 13 Optical microscope images of porous silicon structure with diameters around 2 µm obtained with a current value of 50 mA applied for 5 min

5 mA current applied in 4 min, 5 min, 6 min, and 30 min durations

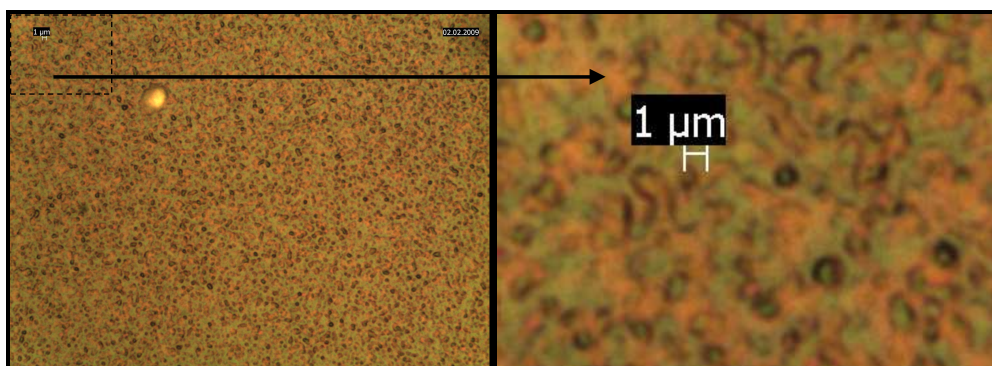

Figure 4. 14 Optical microscope images of porous structure with diameters around 1 µm obtained with a current value of 5 mA applied for 4 min (sample number: PS019)

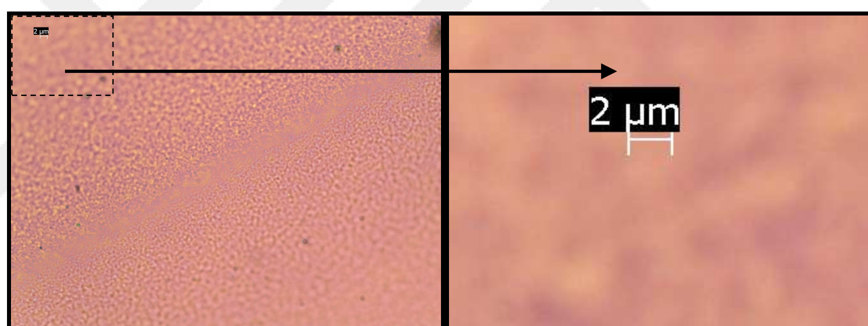

Figure 4. 15 Optical microscope images of porous structure with diameters around 1 µm obtained with a current value of 5 mA applied for 5 min

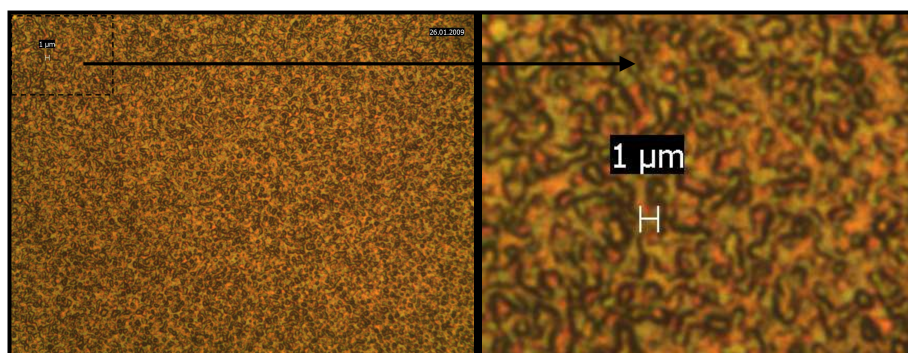

Figure 4. 16 Optical microscope images of porous structure with diameters around 1 µm obtained with a current value of 5 mA applied for 6 min (sample number: PS022)

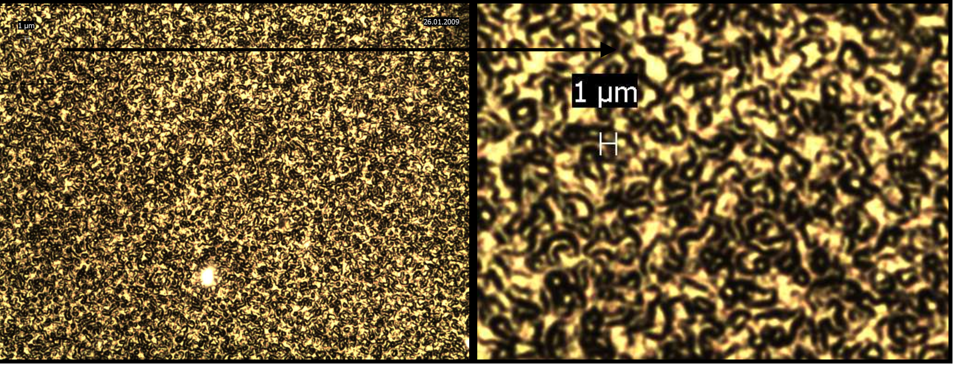

Figure 4. 17 Optical microscope images of porous structure with diameters around 1 µm obtained with a current value of 5 mA applied for 6 min (sample number: PS020)

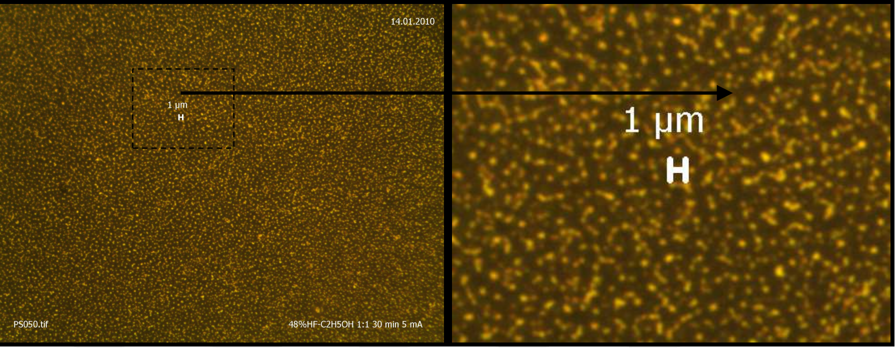

Figure 4. 18 Optical microscope images of porous structure with diameters around 1 µm obtained with a current value of 5 mA applied for 30 min (sample number: PS050)

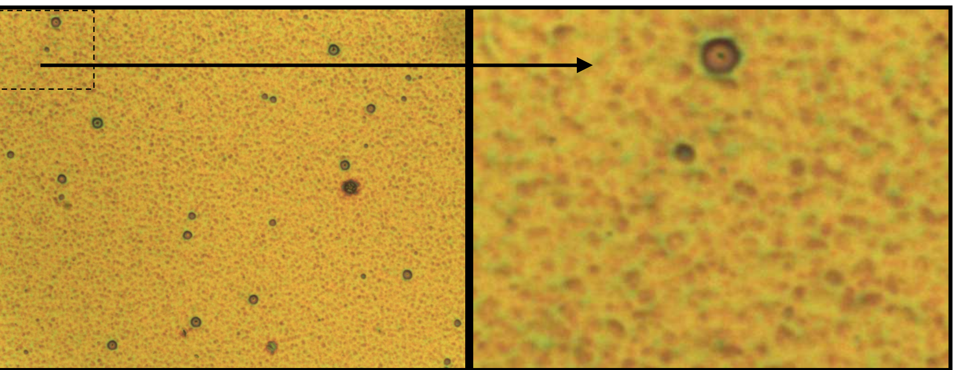

Figure 4. 19 Optical microscope images of porous structure with diameters around 1 µm obtained with a current value of 5 mA applied for 30 min, $HF:C_2H_5OH$ concentration of % 12.5:12.5:75 (sample number: PS051)

4.2.2. Optical Microscope Images of Porous Silicon Samples with <111> wafer orientation, 2-20 Ω.cm, and HF:C_2H_5OH concentration of % 25:25:50

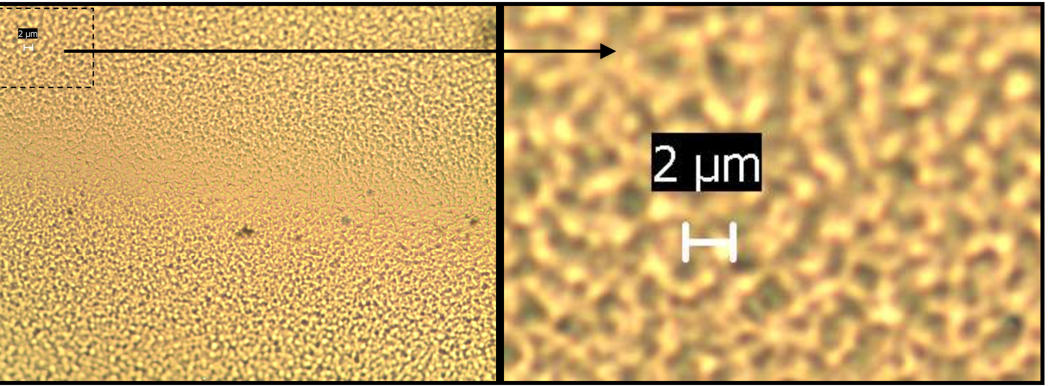

Figure 4. 20 Optical microscope images of porous structure with diameters around 1 µm obtained with a current value of 10 mA applied for 5 min (sample number: PS009)

Figure 4.21 and Figure 4.22 was presented below in order to demonstrate the difference between the images taken from the bright-field and dark-field modes.

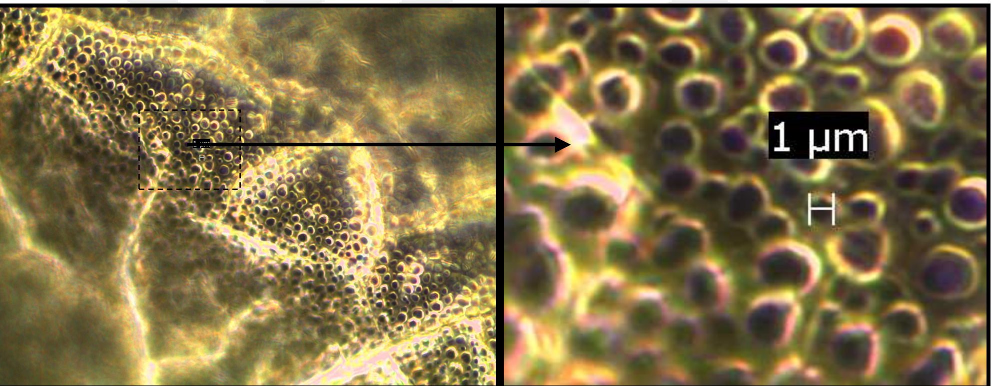

Figure 4. 21 Optical microscope images of porous structure with diameters around 1 µm obtained with a current value of 10 mA applied for 5 min (sample number: PS003); Dark-field mode

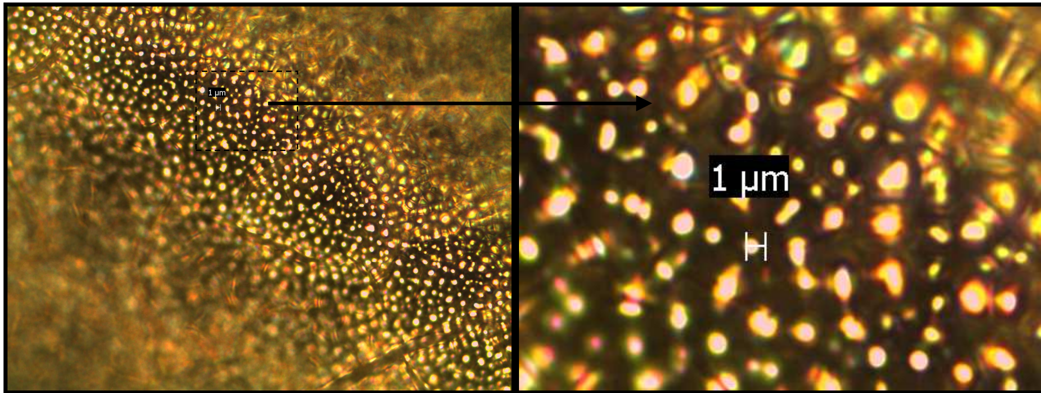

Figure 4. 22 Optical microscope images (bright field mode) of porous structure with diameters around 1 µm obtained with a current value of 10 mA applied for 5 min (sample number: PS003); Bright-field mode

4.2.3. Scanning Electron Microscope (SEM) Images of Porous Silicon Samples

Since optical microscope is not sufficient to resolve nanometer sized structures scanning electron microscope images were also taken and given below.

1 V 5 min furnace annealed sample with 50,000 times magnification:

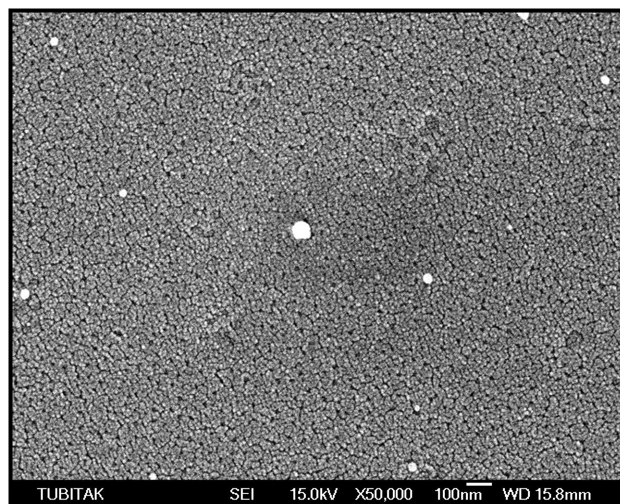

Figure 4. 23 SEM images of porous silicon sample with 50,000 times magnification. Sample was etched at constant voltage of 1 Volt with duration of 5 minutes and annealed at the furnace

1 V 5 min furnace annealed sample with 150,000 times magnification

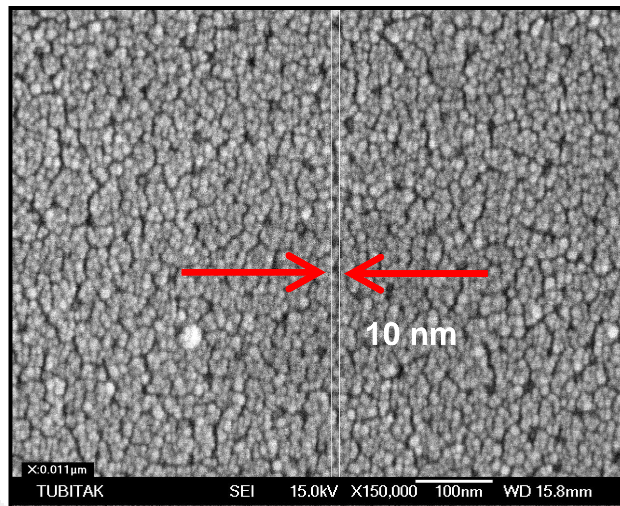

Figure 4. 24 SEM images of the same porous silicon sample with 150,000 times magnification showing an approximately 10 nm holes

The arrows in Figure 2.24 indicates the pores is approximately 10 nm obtained from the microscope software.

Schematic of cross section porous silicon structure was given in Figure 4.25.

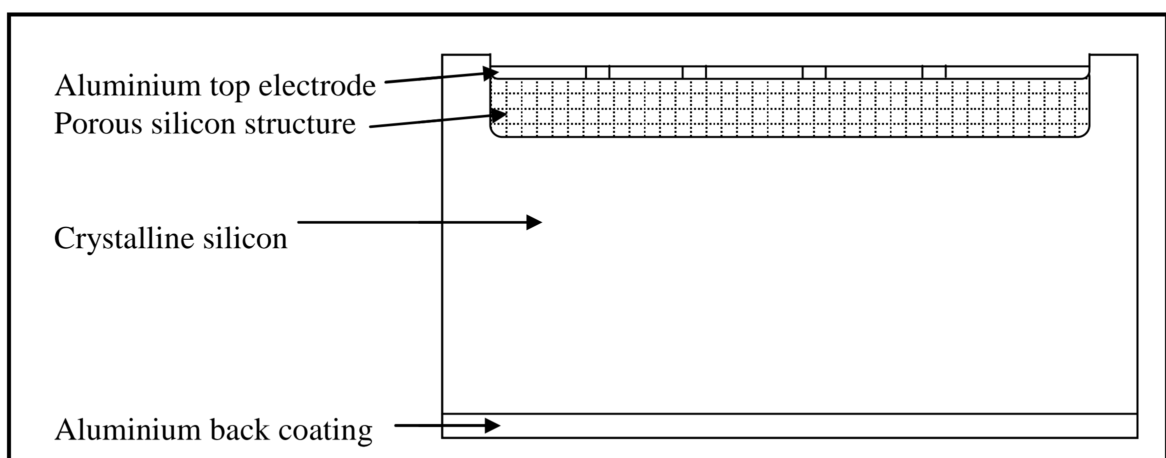

Figure 4. 25 Cross section schematic of porous silicon structure formed inside the silicon wafer with a 500 µm thickness

JEOL 6335F scanning electron microscope (SEM) was used to obtain both surface and cross section area images from porous silicon structure. SEM images of set of samples prepared at conditions described explicitly in the Table 4.3, Table 4.4, and Table 4.5 were presented in the figures depicted from Figure 4.26 to Figure 4.31.

The images showed nanometer sized silicon crystalline granular structure. In the SEM images, granules composed of tiny granules but they cannot be resolved clearly due resolution set by SEM.

4.2.4. SEM Images of Porous Silicon Samples: Set-A

SEM surface area images of set-A samples prepared at conditions described explicitly in the Table 4.3 was presented in the Figure 4.26.

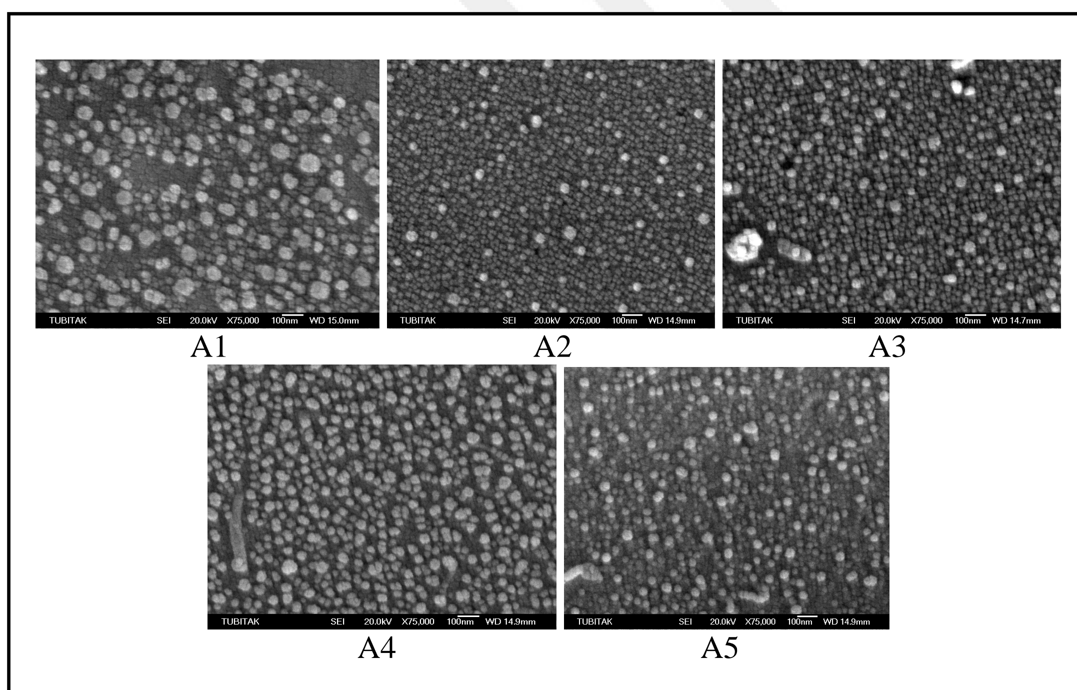

Figure 4. 26 Scanning electron microscope top view images from porous silicon sample surfaces A1, A2, A3, A4, and A5, formed at anodization times of 15 min., 30 min., 45 min., 60 min., and 75 min. respectively

SEM cross section area images of set-A samples prepared at conditions described explicitly in the Table 4.3 was presented in the Figure 4.27.

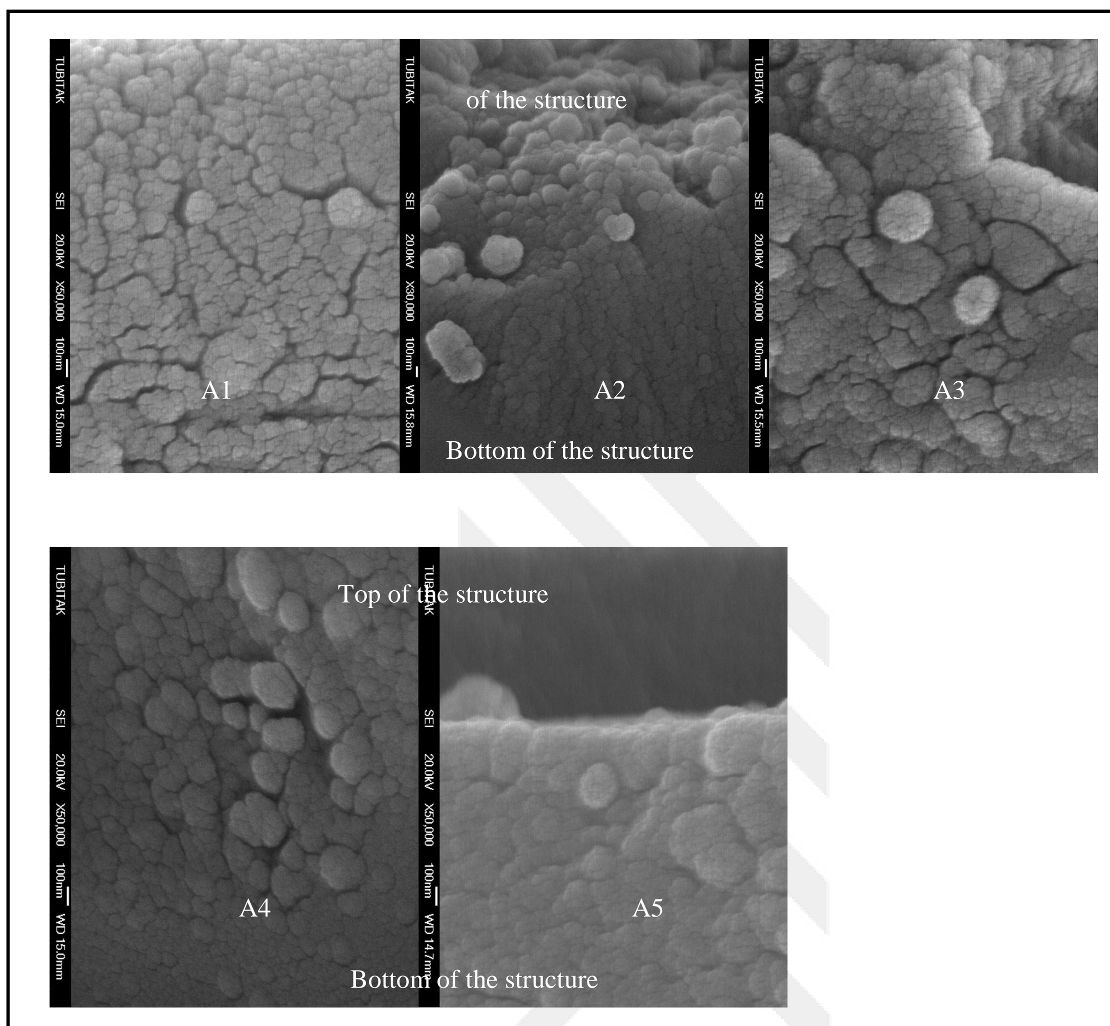

Figure 4. 27 Scanning electron microscope cross section images from porous silicon samples of A1, A2, A3, A4, and A5

Half of the samples were designed to be a relative humidity sensor, and capacitance measurements were performed, while the other halves were used for the measurements of Raman spectra, photoluminescence spectra, AFM, and SEM proceses. The structure of samples from set A has nanometre sized granular silicon crystallites and nanometer sized holes between these granular silicon crystallites whose diameters were calculated by image processing software in MATLAB environment, and from Raman and PL spectroscopy measurements.

Table 4. 3 Formation conditions of porous silicon samples (set-A)

Sample name	Anodisation current, mA	Anodisation time, min	$HF:C_2H_5OH$ concentration, %
A1	5	15	25:25:50
A2	5	30	25:25:50
A3	5	45	25:25:50
A4	5	60	25:25:50
A5	5	75	25:25:50

4.2.5. SEM Images of Porous Silicon Samples: Set-B

SEM surface area images of set-B samples prepared at conditions described explicitly in the Table 4.4 was presented in the Figure 4.28.

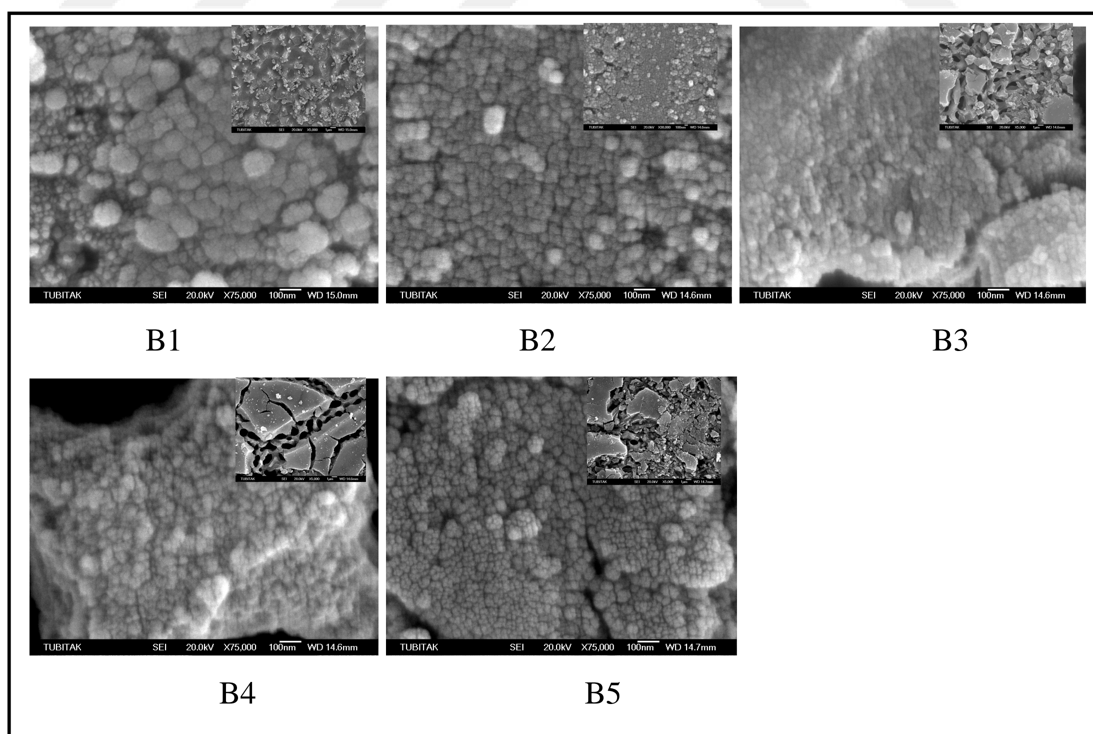

Figure 4. 28 Top view SEM images of the porous silicon sample surfaces (B1, B2, B3, B4, and B5) with 75,000 times magnification showing granular-type porous structure

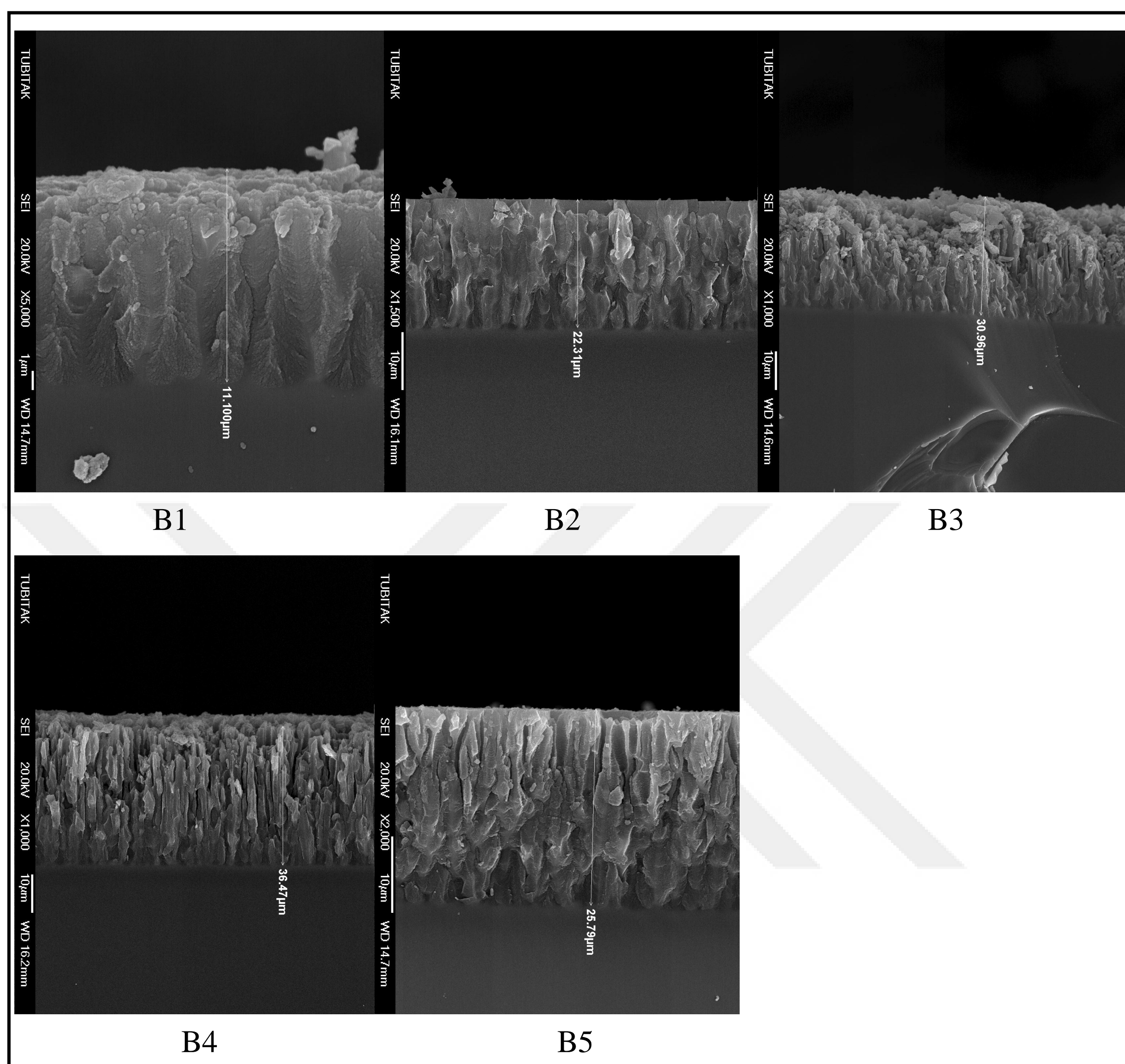

Figure 4. 29 Cross section SEM images of the porous silicon samples (B1, B2, B3, B4, and B5) with 75,000 times magnification showing granular-type porous structure

Table 4. 4 Formation conditions of porous silicon samples (set B)

Sample name	Anodisation current, mA	Anodisation time, min	$HF:C_2H_5OH$ concentration, %
B1	22	15	25:25:50
B2	22	30	25:25:50
B3	22	45	25:25:50
B4	22	60	25:25:50
B5	22	75	25:25:50

SEM cross section area images of set-B samples prepared at conditions described explicitly in the Table 4.4 was presented in the Figure 4.29.

Samples were cut into two pieces. One half of the samples were designed to be a relative humidity sensor, and capacitance measurements were performed, while the other halves were used for the measurements of Raman spectra, photoluminescence spectra, AFM, and SEM proceses. The structure of samples from set B has both nanometre sized granular silicon crystallites and micrometer sized holes whose diameters were calculated by image processing software in MATLAB environment, and from Raman and PL spectroscopy measurements.

4.2.6. SEM Images of Porous Silicon Samples: Set-C

SEM surface area images of set-C samples prepared at conditions described explicitly in the Table 4.5 was presented in the Figure 4.30.

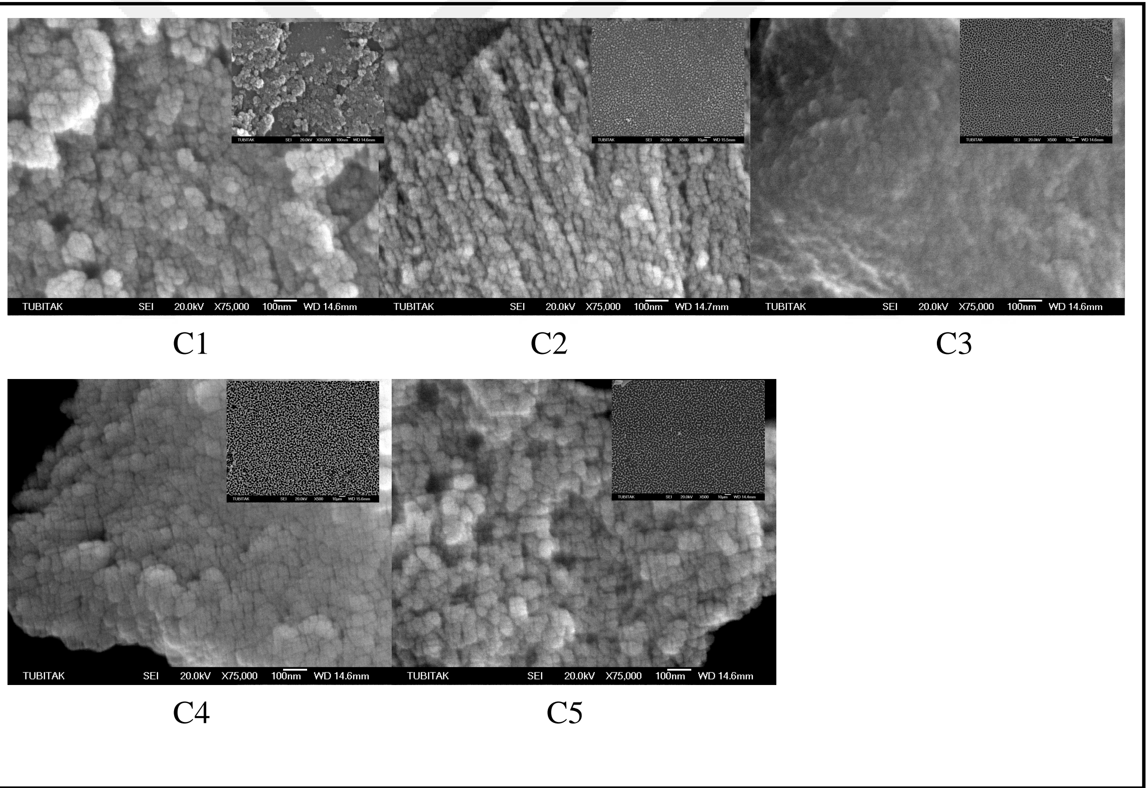

Figure 4. 30 Top view SEM images of the porous silicon samples (C1, C2, C3, C4, and C5) with 75,000 times magnification showing granular-type porous structure

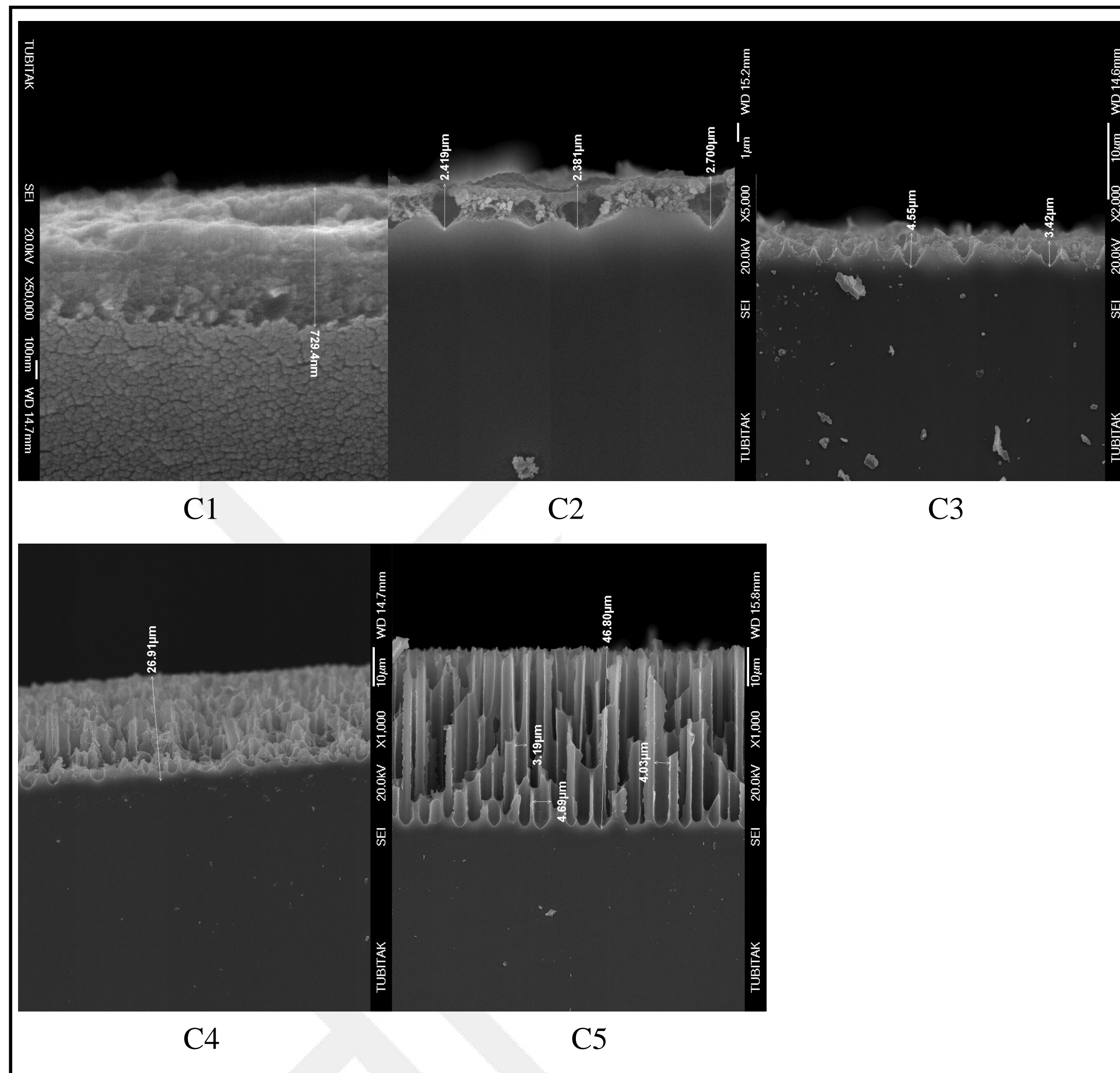

Figure 4. 31 Cross section SEM images of the porous silicon samples (C1, C2, C3, C4, and C5) with 75,000 times magnification showing granular-type porous structure

Table 4. 5 Formation conditions of porous silicon samples (set C)

Sample name	Anodisation current, mA	Anodisation time, min	$HF:C_2H_5OH$ concentration, %
C1	22	15	12.5:12.5:75
C2	22	30	12.5:12.5:75
C3	22	45	12.5:12.5:75
C4	22	60	12.5:12.5:75
C5	22	75	12.5:12.5:75

SEM surface area images of set-C samples prepared at conditions described explicitly in the Table 4.5 was presented in the Figure 4.30. SEM cross section area images of set-C samples prepared at conditions described explicitly in the Table 4.5 was presented in the Figure 4.31. The inset images in the Figure 4.28 and Figure 4.30 were surface images of the samples with magnification of 500. The corresponding area is 181 μm x 240 μm.

Half of the samples were designed to be a relative humidity sensor, and capacitance measurements were performed, while the other halves were used for the measurements of Raman spectra, photoluminescence spectra, AFM, and SEM proceses. The structure of samples from set C has mainly micrometer sized holes but the walls of these holes were found to be composed of nanometre sized granular silicon crystallites whose diameters were calculated by image processing software in MATLAB environment, and from Raman and PL spectroscopy measurements.

4.3. IMAGE PROCESSING

Microscope images of porous silicon structures having holes and/or granular islands ranging from micrometer to nanometer sizes obtained from different formation parameters were given in Section 4.5. Images of porous silicon structures having micrometer sizes were obtained from optical microscope. Images of porous silicon structures having nanometer sizes were obtained from scanning electron microscope.

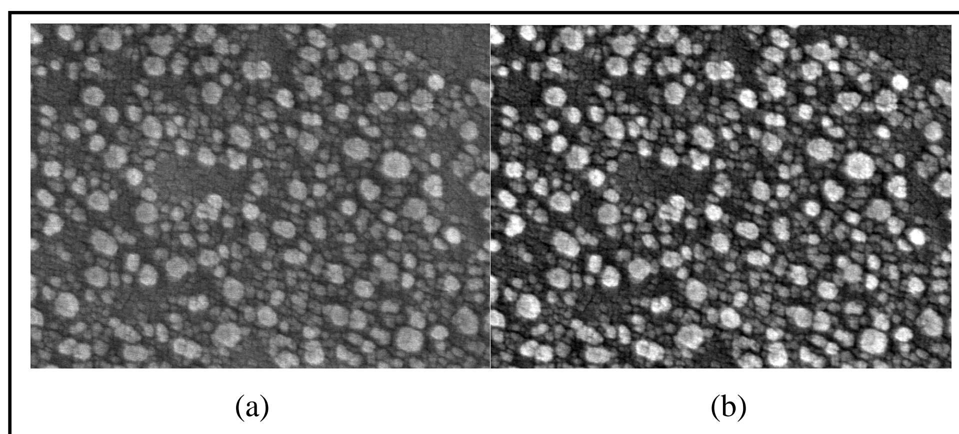

(a) (b)

Figure 4. 32 (a) Original image A1 (b) Contrast enhanced and filtered image of A1

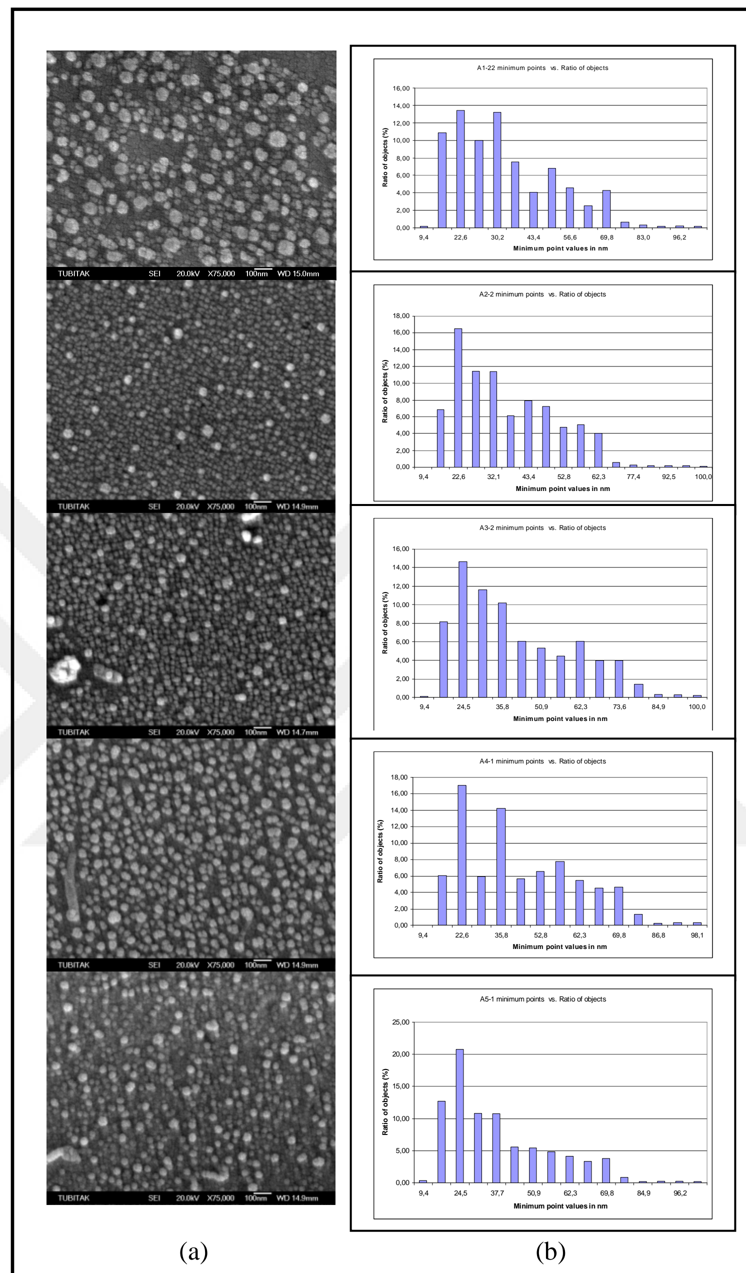

Figure 4. 33 Porous silicon samples (A1, A2, A3, A4, A5) and their corresponding histogram graphics showing granul diameter distribution

Size distributions, including the diameter of nanocrystallites were determined from image processing of the SEM images using an algorithm developed in the MATLAB environment and given in Appendix A. The algorithm was used to reduce the noise, while preserving the edges of the circular shapes of the granules. After contrast enhancement a

morphological opening was performed on these images as described elsewhere [243, 244]. An example of contrast enhanced and filtered image compared with the original one is shown in Figure 4.32.

These outlines enabled calculation of the size distribution of objects in any given SEM image to be obtained. The output of the program was a histogram of the size distribution, which is given in Figure 4.33; the average nanocrystal diameter of each sample was calculated from these histograms, and results were given in Table 4.6.

Table 4. 6 Diameter values of granular silicon crystallites and holes in porous silicon samples calculated from image processing of SEM images (set A)

Sample name	Etching time min	Average nanocrystallite diameter obtained from MATLAB Image Processing nm	Average hole diameter obtained from MATLAB Image Processing nm
A1	15	25.5	15.0
A2	30	28.0	13.0
A3	45	29.0	14.0
A4	60	32.0	14.0
A5	75	30.0	14.0

Diameter values obtained from the algorithm written in the MATLAB Image Processing Toolbox environment were presented in the analysis section, in the form of histogram gather information about the diameter values of the granules versus number of objects at that diameter value found in the SEM images of crystalline silicon samples.

Calculated average diameter values of holes which are in between the nanocrystallites were found to be smaller than the nanocrystallite diameters which are also apparent from the SEM images. Different algorithms were used in order to calculate the average diameter values of both nanocrystallites and holes. Calculated average dimater values of both granules and holes are cross checked with the diameter values obtained during SEM analysis.

4.4. STRUCTURAL CHARACTERIZATION OF POROUS SILICON SAMPLES USING RAMAN SPECTRUM ANALYSIS

In single crystalline silicon only first-order scattering at the optical phonon in the center of the Brillouin zone is allowed, which produces a sharp Raman peak at 521 cm^{-1}. [119] Confinement of the phonon leads to a momentum uncertainty, and so the Raman peak broadens and shifts to lower energy. In Raman scattering, a multiple scattering of photons, electrons, and phonons is involved. The wave vector of the light is very small compared with the relevant reciprocal distances in the crystal; the momentum conservation rule allows participation of phonons around the Γ point only. [245]

Raman spectroscopy is a non-destructive method that has been used to investigate the morphology of nanoporous silicon, and to determine the size of silicon nanocrystallites. In order to evaluate the dimensional parameters, in particular the pore or nanometer sized granular island diameter, the full width half maximum (FWHM), maximum peak intensity, and Raman shift values for each of the samples prepared at different current density values, at different duration of times, and at different concentrations of solution was evaluated by a model which relates the photon-phonon interaction in crystals with the aid of Origin software. Enhancement of the Raman spectra intensity due to increased density of nanometer sized crystalline silicon inside the structure of anodized silicon samples was also observed.

4.5. ANALYSIS OF POROUS SILICON SAMPLES USING MATLAB IMAGE PROCESSING OF SCANNING ELECTRON MICROSCOPE (SEM) AND RAMAN SPECTRUM ANALYSIS

Porous silicon (PSi) is a material with voids and channels in it. PSi structure is produced on the crystal silicon by the electrochemical anodization of silicon wafers in aqueous HF which leads to the formation of a layer containing a large number of small pores and/or granular type islands, pyramidal shaped holes. The reason for using porous material as a relative humidity sensor is that the immense surface-to-volume ratio and the abundant void fraction which leads to very high sensitivities. Structural features were characterized by

using optical microscopy, scanning electron microscopy (SEM), and Raman spectroscopy techniques.

Raman spectroscopy and microscope images processed in MATLAB are utilized for the dimensional characterization of porous silicon structure produced in different formation parameters. Samples are prepared at current densities of 2.2 $mA \cdot cm^{-2}$, 4.4 $mA \cdot cm^{-2}$, 8.8 $mA \cdot cm^{-2}$, 9.7 $mA \cdot cm^{-2}$, 10 $mA \cdot cm^{-2}$, 22.0 $mA \cdot cm^{-2}$ and 33.1 $mA \cdot cm^{-2}$ with duration of times of 5 min, 10 min, 20 min, 30 min, 45 min, 60 min, and 75 minutes. The concentrations of solution are 1:1:1 (H_2O:HF:C_2H_5OH) and ½:½:1 (H_2O:HF:C_2H_5OH). The diameter of the silicon nanocrystallites are ranging from 2 nm to 30 nm and the diameter of pores in between the nanocrystallites are ranging from 2 nm to 5 µm which is resulted from the analysis of Raman spectroscopy, photoluminescence spectroscopy, and image processing of scanning electron microscopy and optical microscopy images.

Finally, silicon nanocrystallites and pore diameter obtained from either optical microscope or scanning electron microscope images processed in MATLAB are compared with the diameter values calculated from Raman spectra parameters.

Comparison of Raman spectra of all the samples with the Raman spectrum of crystalline silicon showed a red (down) shift in the optical phonon mode after porous silicon formation due to the phonon confinement effect. This indicates that nanometer sized silicon crystallites in the silicon samples were formed as a result of electrochemical anodization process. Such structures exhibit red shifts from crystalline silicon (c-Si) in Raman spectra when nanometer sized structures are present.

Enhancement of the Raman spectra intensity due to increased density of nanometer sized crystalline silicon inside the structure of anodized silicon samples was also observed and was given in this section. Raman intensity values together with the depth of porous silicon structure are also found to be highly correlated.

The dimensions of the porous silicon skeleton in the order of micrometer to nanometer sizes are very small to be resolved by microscopy techniques that generate a direct image of the morphology, e.g. SEM. However, an understanding of the morphology of porous

silicon has emerged from a superposition of results obtained from different techniques such as SEM, and Raman spectroscopy. On the other hand, porous silicon skeleton in the order of tens of micrometer sizes can easily be observed by optical microscopy [122].

The Raman spectrum obtained from porous silicon (PSi), which, due to its microstructure, contains a massive surface area to volume ratio, was presented. Moreover, MATLAB Image Processing Toolbox is used in order to analyse the microscope images to determine the porous silicon structure features such as pore diameter, hole diameter and porosity.

Porous silicon samples are prepared at current densities 2.2 $mA\cdot cm^{-2}$, 4.4 $mA\cdot cm^{-2}$, 8.8 $mA\cdot cm^{-2}$, 9.7 $mA\cdot cm^{-2}$, 10 $mA\cdot cm^{-2}$, and 22.0 $mA\cdot cm^{-2}$ and 33.1 $mA\cdot cm^{-2}$ with duration of times of 5 min, 10 min, 15 min, 20 min, 30 min, 45 min, 60 min, and 75 min. The concentrations of solution are 1:1:1 ($H_2O:HF:C_2H_5OH$) and ½:½:1 ($H_2O:HF:C_2H_5OH$). Sets of samples prepared at different current density values, at different duration of times, and at different concentrations of anodization solution.

Table 4. 7 Formation conditions of porous silicon samples prepared from c-Si wafer with <100> orientation

Sample name	Wafer orientation	Wafer resistivity Ω.cm	$HF:H_2O:C_2H_5OH$ concentration %	Current mA (Current density $mA.cm^{-2}$)	Time min.	Pentane drying Thermal treatment
PS050	<100>	1-30	25:25:50	5.0 (2.2)	30	Y Y
PS026	<100>	1-30	25:25:50	5.0 (2.2)	7	Y N
PS025	<100>	1-30	25:25:50	5.0 (2.2)	7	Y N
PS022	<100>	1-30	25:25:50	5.0 (2.2)	6	Y N
PS020	<100>	1-30	25:25:50	5.0 (2.2)	6	Y N
PS019	<100>	1-30	25:25:50	5.0 (2.2)	4	Y N
PS018	<100>	1-30	25:25:50	5.0 (2.2)	1	Y N
PS015	<100>	1-30	25:25:50	5.0 (2.2)	5	Y N
PS051	<100>	1-30	12.5:1.25:75	5.0 (2.2)	30	Y Y

Table 4. 8. Formation conditions of porous silicon samples prepared from c-Si wafer with <111> orientation.

Sample name	Wafer orientation	Wafer resistivity Ω.cm	$HF:H_2O:C_2H_5OH$ concentration %	Current mA (Current density mA·cm^{-2})	Time min.	Pentane drying Thermal treatment
PS013	<111>	2-20	25:25:50	5.0 (2.2)	3	Y N
PS007	<111>	2-20	25:25:50	20.0 (8.8)	5	N N
PS005	<111>	2-20	25:25:50	75.0 (33.1)	20	N N
PS004	<111>	2-20	25:25:50	50.0 (22.0)	20	N N
PS002 PS009	<111> <111>	2-20 2-20	25:25:50 25:25:50	20.0 (8.8) 10.0 (4.4)	20 5	N N N N
PS003	<111>	2-20	25:25:50	10.0 (4.4)	5	N N

Table 4. 9. Raman spectrum evaluation of the porous silicon samples prepared from c-Si wafer with <100> orientation.

Sample name	Wafer resistivity Ω.cm	$HF:H_2O:C_2H_5OH$ concentration %	Current mA (Current density mA.cm^{-2})	Time min.	Pentane drying Thermal treatment	Raman peak wavenumber cm^{-1}	Raman wavenumber shift cm^{-1}	Raman spectra FWHM cm^{-1}	Diameter from Raman spectrum analysis nm	Diameter from MATLAB Image Processing nm
PS050	1-30	25:25:50	5.0 (2.2)	30	Y Y	511.94	9.06	10.92	1.71	588.2
PS026	1-30	25:25:50	5.0 (2.2)	7	Y N	514.96	6.04	8.02	2.27	235.2 588.2
PS025	1-30	25:25:50	5.0 (2.2)	7	Y N	511.94	9.06	9.42	1.71	235.2 588.2
PS022	1-30	25:25:50	5.0 (2.2)	6	Y N	511.94	9.06	11.09	1.71	235.2 588.2
PS020	1-30	25:25:50	5.0 (2.2)	6	Y N	511.94	9.06	10.79	1.71	588.2 705.8
PS015	1-30	25:25:50	5.0 (2.2)	5	Y N	511.94	9.06	10.14	1.71	235.2 588.2 705.8

										823.6
PS019	1-30	25:25:50	5.0 (2.2)	4	Y N	511.94	9.06	9.39	1.71	588.2 705.8 823.6 1058.8
PS018	1-30	25:25:50	5.0 (2.2)	1	Y N	511.94	9.06	11.53	1.71	235.2 588.2
PS051	1-30	12.5:1.25:75	5.0 (2.2)	30	Y Y	514.96	6.04	9.24	2.27	529.2 588.2 705.9

Table 4. 10. Raman spectrum evaluation of the porous silicon samples prepared from p-type c-Si wafer with <111> orientation.

Sample name	Wafer resistivity Ω.cm	$HF:H_2O:C_2H_5OH$ concentration %	Current mA (Current density $mA.cm^{-2}$)	Time min.	Pentane drying Thermal treatment	Raman peak Wavenumber cm^{-1}	Raman wavenumber shift cm^{-1}	Raman spectra FWHM cm^{-1}	Diameter from Raman spectrum analysis nm	Diameter from MATLAB Image Processing nm
PS013	2-20	25:25:50	5.0 (2.2)	3	Y N	511.94	9.06	11.67	1.71	235.2
PS007	2-20	25:25:50	20.0 (8.8)	5	N N	511.94	9.06	11.99	1.71	--
PS005	2-20	25:25:50	75.0 (33.1)	20	N N	511.94	9.06	10.92	1.71	--
PS004	2-20	25:25:50	50.0 (22.0)	20	N N	514.96	6.04	8.99	2.27	--
PS002 PS009	2-20 2-20	25:25:50 25:25:50	20.0 (8.8) 10.0 (4.4)	20 5	N N N N	514.96	6.04	9.78	2.27	411.6 529.2
PS003	2-20	25:25:50	10.0 (4.4)	5	N N	511.94	9.06	11.64	1.71	294.1 352.9

Table 4. 11. Porous silicon samples prepared at different conditions

Sample name	Wafer orientation	Wafer resistivity Ω.cm	$HF:H_2O:C_2H_5OH$ concentration %	Current mA (Current density $mA.cm^{-2}$)	Time min.	Pentane drying Thermal treatment
PS060	<100>	1-30	25:25:50	5.0 (2.2)	15	Y N
PS061	<100>	1-30	25:25:50	5.0 (2.2)	30	Y N

PS062	<100>	1-30	25:25:50	5.0 (2.2)	45	Y N
PS063	<100>	1-30	25:25:50	5.0 (2.2)	60	Y N
PS064	<100>	1-30	25:25:50	22.0 (9.7)	15	Y N
PS065	<100>	1-30	25:25:50	22.0 (9.7)	30	Y N
PS066	<100>	1-30	25:25:50	22.0 (9.7)	45	Y N
PS067	<100>	1-30	25:25:50	22.0 (9.7)	60	Y N
PS068	<100>	1-30	12.5:1.25:75	22.0 (9.7)	15	Y N
PS069	<100>	1-30	12.5:1.25:75	22.0 (9.7)	30	Y N
PS070	<100>	1-30	12.5:1.25:75	22.0 (9.7)	45	Y N
PS071	<100>	1-30	12.5:1.25:75	22.0 (9.7)	60	Y N

Table 4. 12. Three set of porous silicon samples prepared at different conditions.

Sample name	Wafer orientation	Wafer resistivity Ω.cm	$HF:H_2O:C_2H_5OH$ concentration %	Current mA (Current density $mA.cm^{-2}$)	Time min.	Pentane drying Thermal treatment
A1	<100>	1-20	25:25:50	5.0 (2.2)	15	Y N
A2	<100>	1-20	25:25:50	5.0 (2.2)	30	Y N
A3	<100>	1-20	25:25:50	5.0 (2.2)	45	Y N
A4	<100>	1-20	25:25:50	5.0 (2.2)	60	Y N
A5	<100>	1-20	25:25:50	5.0 (2.2)	75	Y N
B1	<100>	1-20	25:25:50	22.69 (10.0)	15	Y N
B2	<100>	1-20	25:25:50	22.69 (10.0)	30	Y N
B3	<100>	1-20	25:25:50	22.69 (10.0)	45	Y N
B4	<100>	1-20	25:25:50	22.69 (10.0)	60	Y N
B5	<100>	1-20	25:25:50	22.69 (10.0)	75	Y N
C1	<100>	1-20	1.25:1.25:75	22.69 (10.0)	15	Y N
C2	<100>	1-20	1.25:1.25:75	22.69 (10.0)	30	Y N
C3	<100>	1-20	1.25:1.25:75	22.69 (10.0)	45	Y N
C4	<100>	1-20	12.5:1.25:75	22.69 (10.0)	60	Y N
C5	<100>	1-20	1.25:1.25:75	22.69 (10.0)	75	Y N

Table 4. 13. Raman spectroscopy and MATLAB Image Processing Analysis of Porous silicon samples prepared at different conditions. (calculated using [179] and 181])

Sample name	Current mA (Current density $mA.cm^{-2}$)	Time min.	Raman peak wavenumber cm^{-1}	Raman wavenumber shift cm^{-1}	Raman spectra FWHM cm^{-1}	Diameter from Raman spectra analysis nm	Diameter from MATLAB Image Processing nm
A1	5.0 (2.2)	15	518.67	2.33	5.95	4.4	24
A2	5.0 (2.2)	30	519.26	1.74	5.72	5.4	27
A3	5.0 (2.2)	45	519.59	1.41	5.72	6.2	30
A4	5.0 (2.2)	60	519.77	1.23	5.35	6.9	39
A5	5.0 (2,2)	75	519.63	1.37	5.56	6.4	28
B1	22.69 (10.0)	15	519.31	1.69	14.0	5.5	--*
B2	22.69 (10.0)	30	519.31	1.69	17.0	5.5	--*
B3	22.69 (10.0)	45	521.00	0.00	19.0	--	--*
B4	22.69 (10.0)	60	521.00	0.00	21.5	--	--*
B5	22.69 (10.0)	75	521.00	0.00	16.0	--	--*
C1	22.69 (10.0)	15	521.00	0.00	14.0	--	--*
C2	22.69 (10.0)	30	521.00	0.00	14.5	--	--*
C3	22.69 (10.0)	45	521.00	0.00	15.0	--	--*
C4	22.69 (10.0)	60	521.00	0.00	15.5	--	--*
C5	22.69 (10.0)	75	521.00	0.00	15.5	--	--*

*Diamater values cannot be calculated because Raman shift was not observed in these samples, which have mainly micrometer sized pores. But they yielded photoluminescence signals and PL peak energy values were used for the calculation of the diameter of the nanometer sized granular silicon crystallites.

4.5.1. Raman Peak Wavenumber Variation

Raman spectra obtained from each A series sample produced at fixed current value but variable anodization times (15 -75 minutes) are given in Figure 4.34, and Figure 4.35.

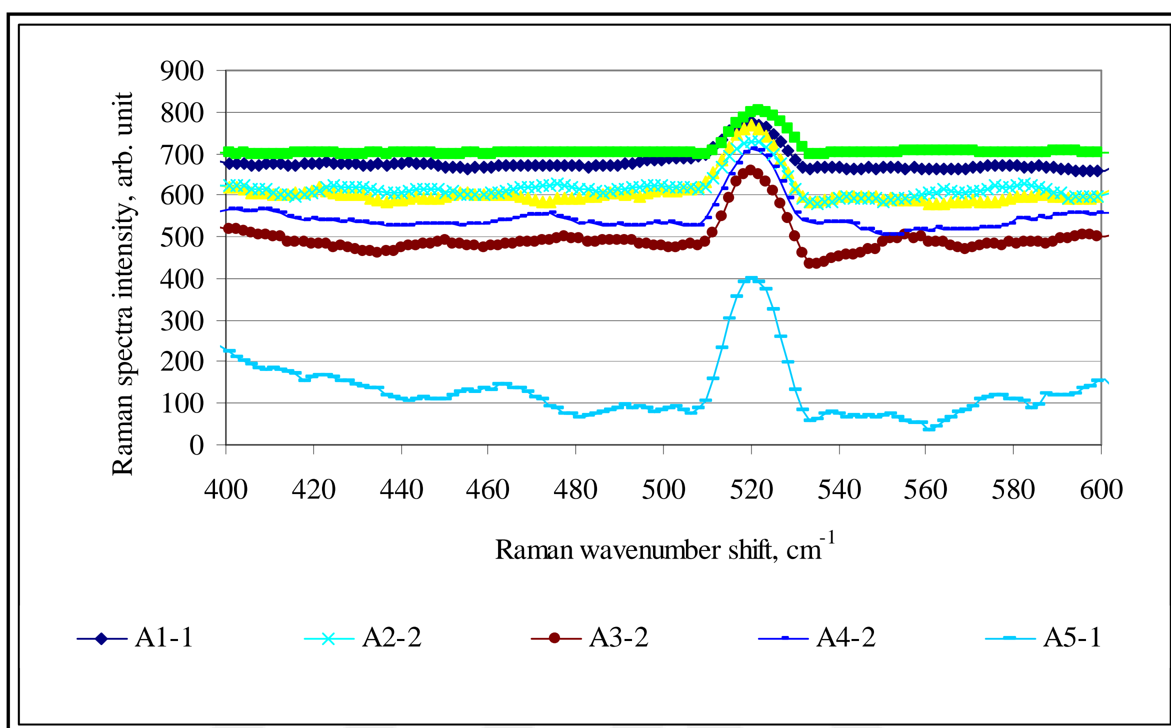

Figure 4. 34 Original Raman spectra of A series samples

These spectra depict the main Raman spectral peak characteristic of each nanoporous silicon sample with respect to the spectrum of strain-free crystalline silicon (c-Si), the latter are represented as diamond-shaped markers in the graph. The Raman spectrum of strain-free crystalline silicon (c-Si) exhibits a specific peak at 521 cm^{-1}. The peaks of Figure 4.34 were compared by overlapping them and limiting the wavenumber range from 500 cm^{-1} to 540 cm^{-1}, as shown in Figure 4.40.

Comparison of Raman spectra of all the samples with the Raman spectrum of crystalline silicon showed a red (down) shift in the optical phonon mode after porous silicon formation, due to the phonon confinement effect as shown in Figure 4.34 and Figure 4.40. This indicates that nanometer sized structures are formed in the silicon samples as a result of the electrochemical anodization process [25, 26, 30, 31, 37, 41, 42]. These wavenumber shifts of Figure 4.34 are listed in Table 4.14, alongside the nanocrystal diameters calculated from them.

Table 4. 14. Raman (a) Diameter values obtained from MATLAB Image Processing (b) Diameter values calculated from Raman spectra analysis

(a) (b)

Sample number	Anodization time min.	Average diameter obtained from MATLAB Image Processing nm	Raman spectra FWHM values cm^{-1}	Raman wavenumber shift cm^{-1}	Diameter calculated from Raman analysis nm
A1	15	26	15.4	2.33	4.4
A2	30	28	15.1	1.74	5.4
A3	45	29	14.9	1.41	6.2
A4	60	32	14.8	1.23	6.9
A5	75	30	14.9	1.37	6.4

Due to resolution differences, SEM and Raman results clearly differ in the calculated dimensions of the nanocrystals from Figure 4.26 and Figure 4.27, respectively. However, both calculation methods show exactly the same trend; an increase in nanocrystal diameter with anodisation time (15 min., 30 min., 45 min., 60 min., and 75 min.) of the silicon samples during fabrication.

The diameter values obtained both from MATLAB Image Processing environment and Raman spectra parameters are given in Table 4.14. The results of MATLAB Image Processing are given in part (a) of Table 4.14, while that of Raman spectral analysis are given in part (b) of Table 4.14. The calculated diameters of part a) SEM analysis displayed a correlation of 96 % with part b) Raman analysis.

The diameters in Table 4.14 are also given in the graph of Figure 4.35. These shows a steady increase in the dimensions of the nanocrystals with anodization time up to 60 minutes, which is also depicted in the photographs of Figure 4.26 and Figure 4.27. After this anodisation time, the nanocrystallite diameters decrease.

This is thought to be caused by the HF dissolving the silicon until its concentration exceeds solubility; the concentration then exceeds the critical limit, allowing it to nucleate. This is followed by diffusion limited growth in which the average nanocrystal radius Rav

increases with the square root of treatment time ($R_{av} \propto t^{1/2}$) [248]. Finally, after the available concentration of reactants has dropped below a critical level, Ostwald ripening or coarsening sets in: larger particles grow at the expense of smaller particles. Since the graph of Figure 4.44 is linear, it must depict the Ostwald ripening stage; diffusion limited growth must occur prior to 20 minutes. The growth of the particles may be inhibited after 60 minutes due to diffusion of HF away from them into the increasingly deeper nanopores. It may also be caused by the disintegration of the nanocrystallites due to structural collapse.

Analysing samples using Raman spectroscopy provide information about the structural features of porous silicon, especially the pore diameter. These parameters are interrelation with the full width half maximum (FWHM), maximum peak intensity, and Raman shift values.

To obtain information about the structure, in particular the pore diameter, the FWHM, peak intensity, and Raman shift values are evaluated by a model which relates the photon-phonon interaction in crystals with the aid of Origin software. The correlation between the results obtained from both methods as given in Table 4.14 show that they are highly correlated and calculated to be 0.96.

Finally, pore diameter obtained from either optical microscope or scanning electron microscope images are compared with the information gathered from Raman spectra. Microscope images were analysed with MATLAB Image Processing Toolbox to obtain the pore diameter, and porosity. Diameter values obtained from MATLAB image processing and Raman spectroscopy measurements given in Table 4.14 was also depicted in Figure 4.35.

Raman spectra wavenumbers at peak intensity value were also compared with the literature and it was given in Figure 4.36. Raman peak shift versus crystallite size follows the same trend as given in ref [181].

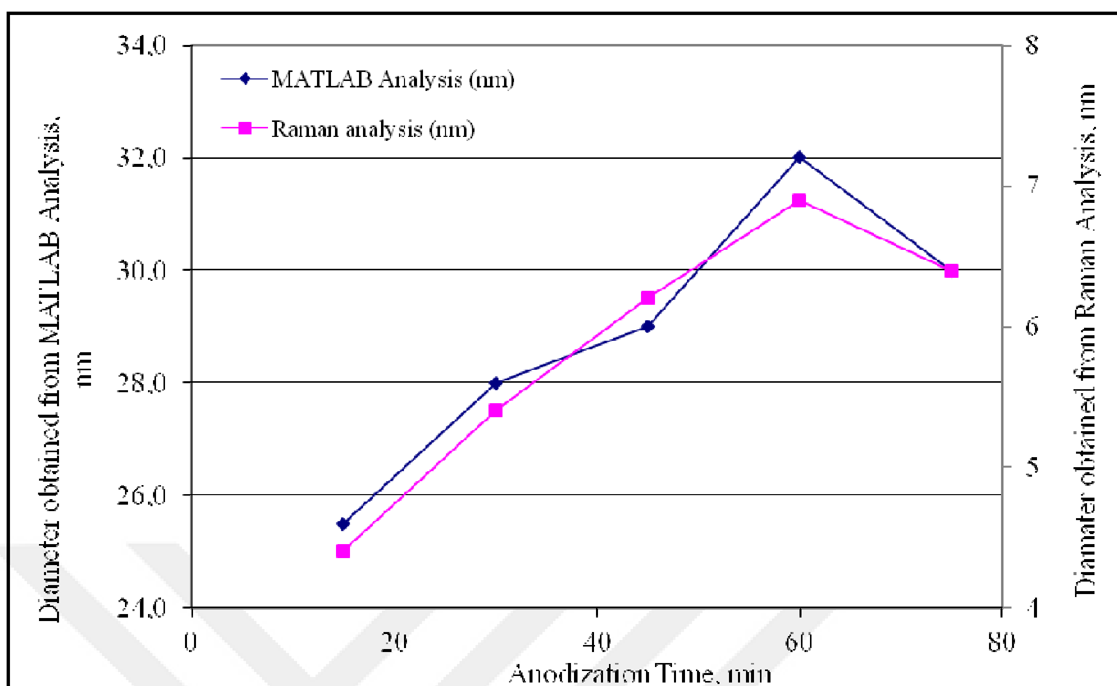

Figure 4. 35 Diameter of structures from Raman and MATLAB analysis

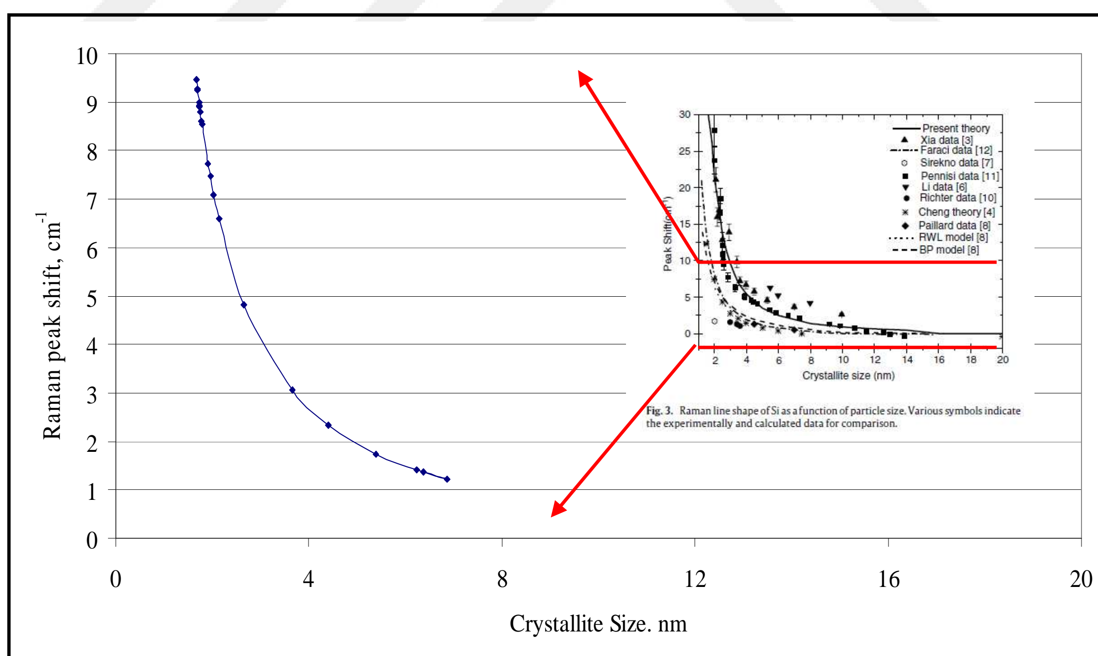

Figure 4. 36 Raman spectra peak shift versus calculated crystallite sizes compared with the literature [181]

4.5.2. Raman Peak Width (FWHM)

Increase of the Raman intensity and FWHM values are the consequence of increase of the nanometer sized porous structure in the samples.

Porous silicon samples were anodized at specified anodization times with varying current density values of 2.2 $mA \cdot cm^{-2}$, 4.4 $mA \cdot cm^{-2}$, 8.8 $mA \cdot cm^{-2}$, 9.7 $mA \cdot cm^{-2}$, 10.0 $mA \cdot cm^{-2}$, 22.0 $mA \cdot cm^{-2}$, and 33.1 $mA \cdot cm^{-2}$. Intensity of Raman spectra and FWHM values from porous silicon samples were increased with respect to single crystalline silicon spectra values. Increase of the Raman intensity and FWHM values are the consequence of nanometer sized porous structure in the samples.

4.5.3. Raman Peak Shift vs FWHM

Raman peak shift values versus FWHM values given in tables from Table 4.7 to Table 4.13 were analysed and given in Figure 4.37. Raman peak shift values versus FWHM values calculated from the above graphs were compared with the literature and they were found to be in good aggrement.

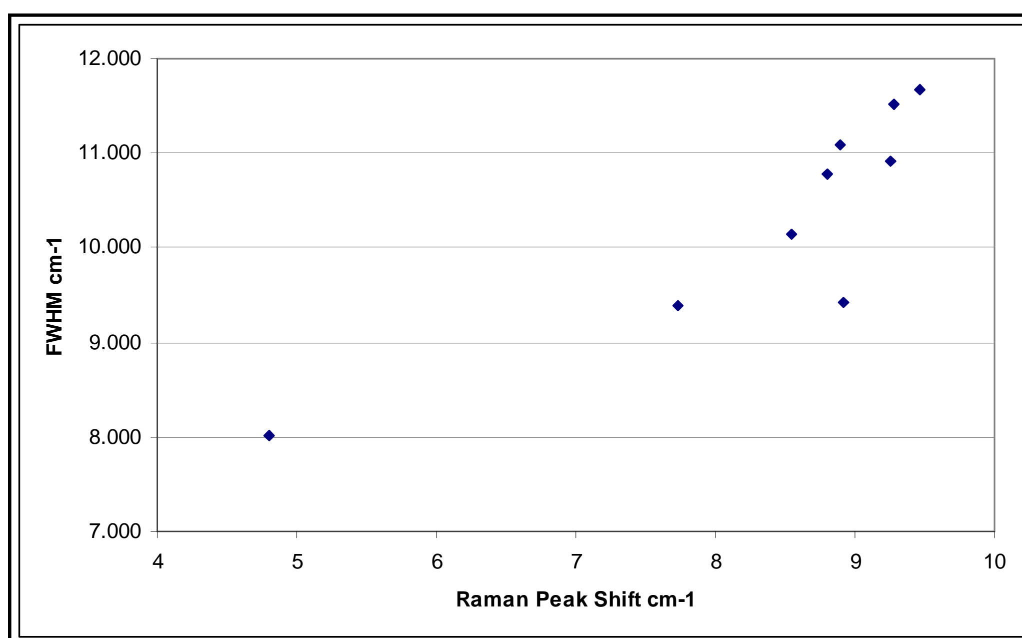

Figure 4. 37 Experimental Raman peak shift values versus calculated FWHM values

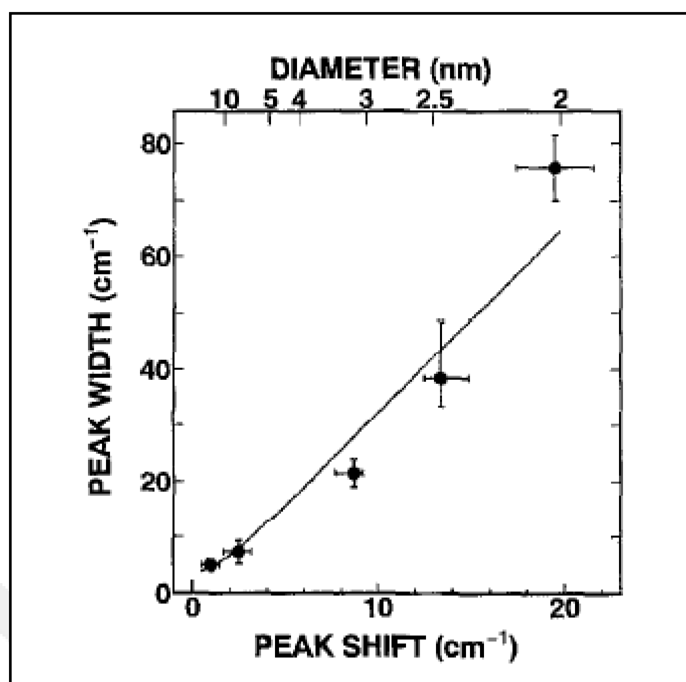

Figure 4. 38 Raman peak shift versus FWHM values found in literature [179-181, 246]

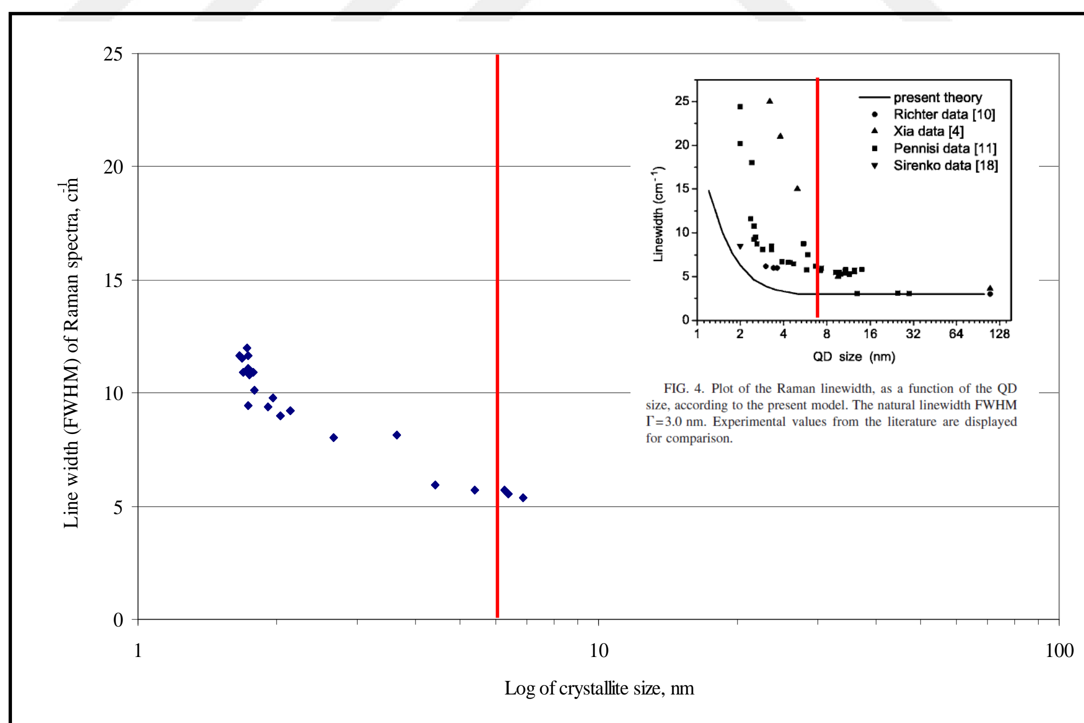

Figure 4. 39 Raman spectra FWHM values versus calculated crystallite sizes compared with the literature [181]

4.5.4. Raman Intensity Variation

Porous silicon layers were formed on p-type silicon wafers having a resistivity of 1-20 Ω.cm and (100) orientation, by anodizing in an hydrofluoric (HF) acid 48 wt. % in H_2O and ethanol (C_2H_5OH) of 1:1 volume per volume (v/v) mixture. Anodization times were set to 15 min., 30 min., 45 min., 60 min., and 75 min. at 2.2 $mA \cdot cm^{-2}$ current density. The anodized samples were named as A1, A2, A3, A4, and A5 respectively. As a result of prescribed anodization parameters, thicknesses of the porous silicon samples were ranged from 2.9 μm to 13.9 μm. Pentane drying was applied to all of the samples to prevent cracking of the porous structure due to evaporation of water from nanometer sized porous structure. Therefore, they were first rinsed with deionized water and then kept in deionized water, in ethanol and in pentane for five minutes consecutively. Entire pentane was evaporated just before characterization measurements. All samples were formed on the same silicon substrate in order to eliminate the effects of doping concentration, resistivity, and orientation parameter on the structure. Other parameters affecting the formation of porous silicon structures such as temperature, and pH value of anodization solution were assumed to be same by keeping concentration of anodizing solution constant during preparation of all the samples. Samples were prepared in the dark. Similar granular-type structures produced on both p-type and n-type silicon substrates can also be found in the literature.

Intensity of Raman spectra and FWHM values from porous silicon samples were increased with respect to single crystalline silicon spectra values with the increase of anodization time. This is most likely to be caused by an increased number of nanocrystals inside the anodized silicon samples as the depth of the nanoporous region (and thus nanopore lengths) below the sample surface increases (shown in Figure 4.40 for the A-series samples). Table 4.14 shows anodization times versus the corresponding depth of porous silicon that is caused by this treatment. Clearly displayed is an increase in NPS depth with anodization time; this is also corroborated by the literature [247].

Superimposed Raman spectra of the samples (A1, A2, A3, A4, and A5) were given in Figure 4.40.

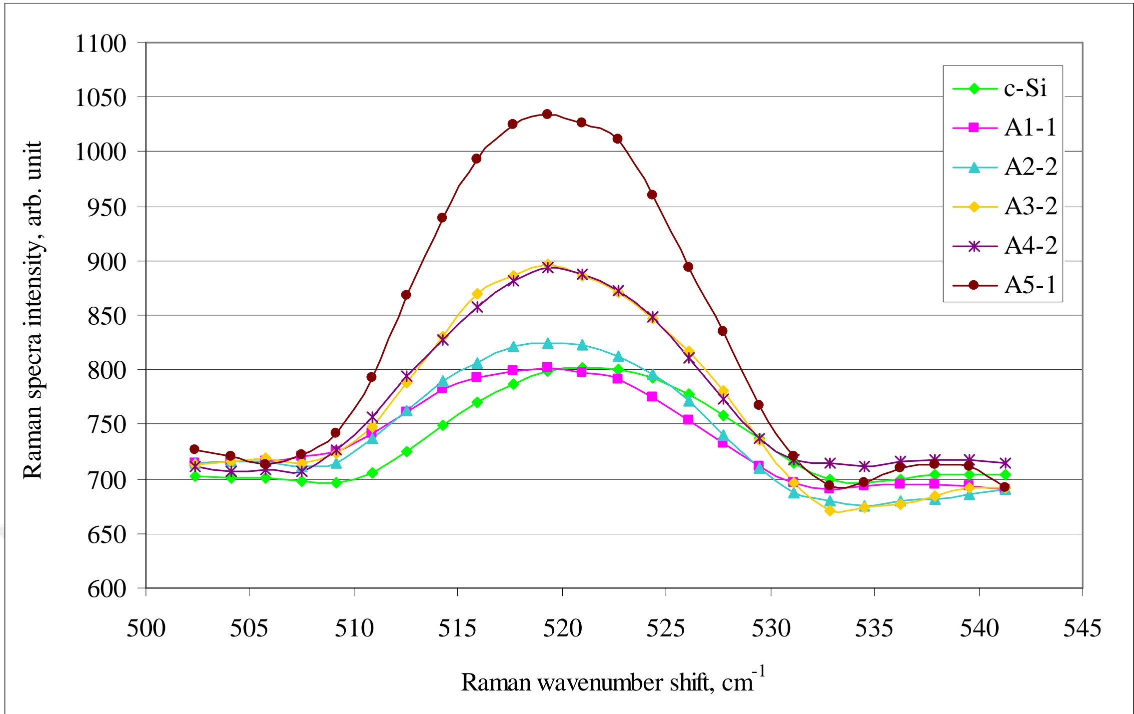

Figure 4. 40 Raman spectra of samples A1, A2, A3, A4, A5

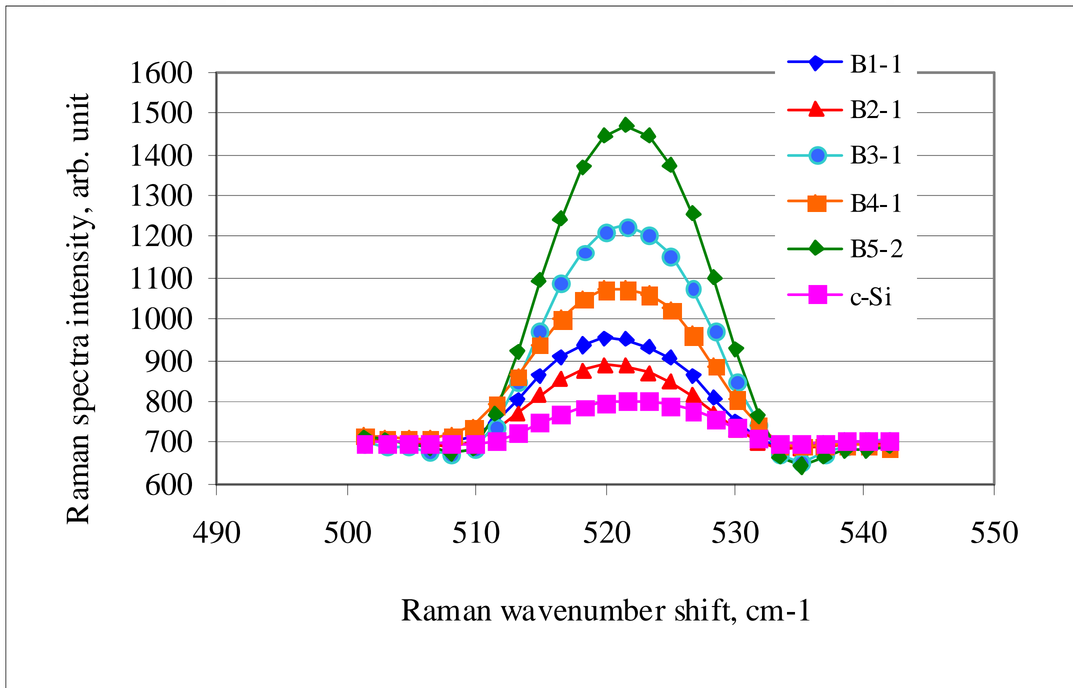

Figure 4. 41 Raman spectra of samples B1, B2, B3, B4, and B5

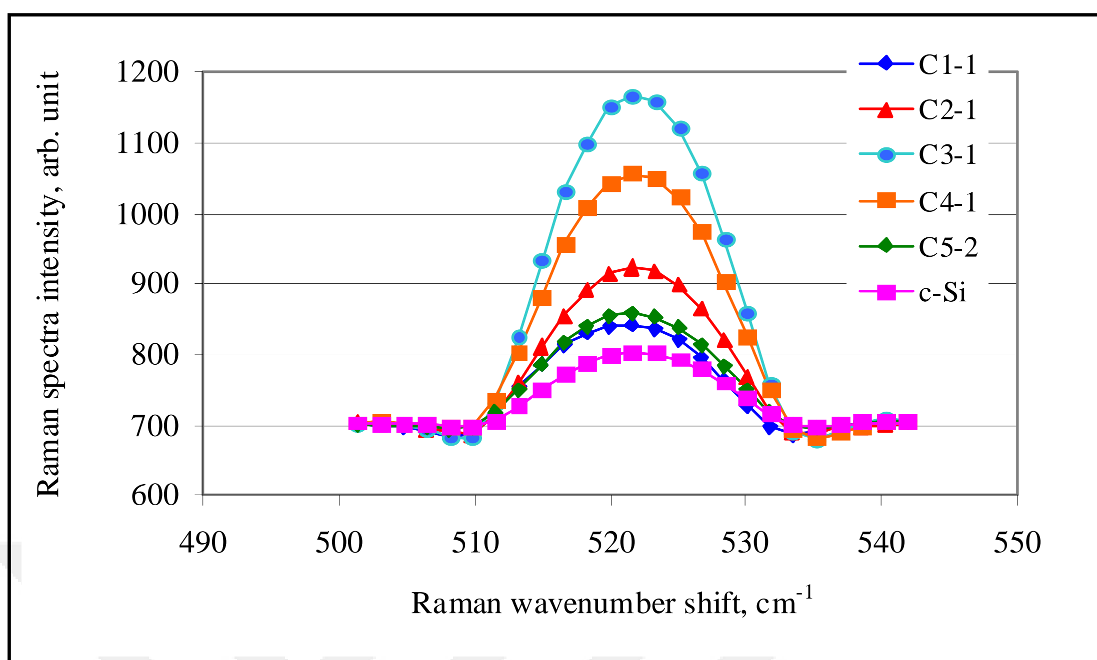

Figure 4. 42 Raman spectra of samples C1, C2, C3, C4, and C5

Raman spectra of B-series (10.0 mA·cm^{-2}) and C-series (10.0 mA·cm^{-2} with half of HF concentration) samples show no Raman wavenumber shift except B1 and B2. This result is expected from the SEM images of B-series (B3, B4, and B5) which show micrometer sized pyramidal shaped pores and hole arrays perpendicular to the surface. C-series samples also show no Raman wavenumber shift which have micrometer sized hole arrays perpendicular to the surface.

In order to verify the current value (2.2 mA·cm^{2}) which was found to be suitable for the formation of nanometer sized porous structure, an intermediate current value (4.4 mA·cm^{2}) was also applied to get Raman spectra having wavenumber shift. Raman spectra wavenumber shift was also observed at 4.4 mA·cm^{2} and depicted in Figure 4.43.

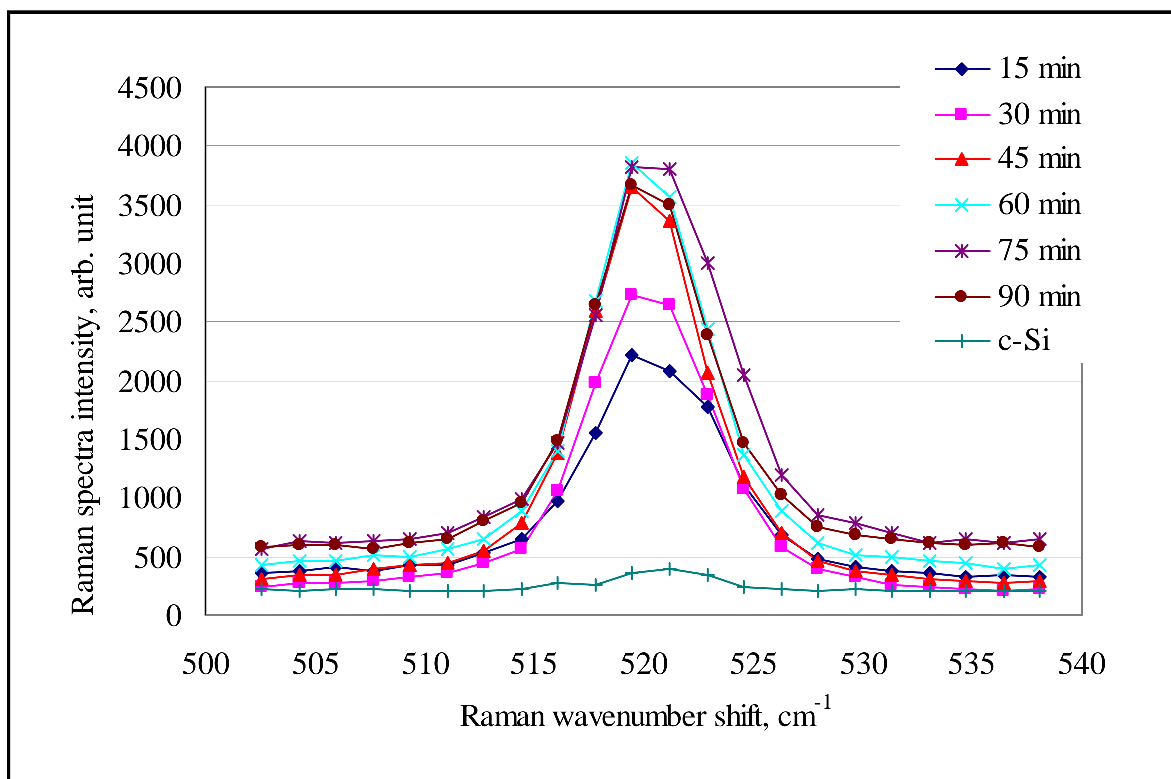

Figure 4. 43 Raman spectra of samples anodized at constant current density of 10 mA.cm^{-2} with different anodization times

Table 4. 15. Raman depth of porous silicon structures in the samples at different anodization times obtained from cross section images obtained from SEM

Sample number	Anodization time min.	Depths of porous silicon structure in the samples from SEM images µm	Raman spectra intensity arb.unit
A1	15	2.9	802.4
A2	30	4.0	824.6
A3	45	4.8	863.4
A4	60	5.1	904.9
A5	75	13.8	1034.2

Raman peak intensities together with the depth of the porous silicon structure of set-A series samples are shown in Table 4.15.

The graph of Raman peak intensities together with the depth of the porous silicon structure displays a quadratic increase ($I = 25{,}5d^2-160d+1053$) in Raman peak intensity (I) as the depth (d) of the SNC region below the sample surface increases as depicted in Figure 4.38. Although Raman cannot theoretically penetrate more than 0.5 μm, it does seem surprisingly that it can sense a quadratic increase in the number of SNC formed down to SNP depths of 5.1 μm. At greater depths, this quadratic dependence can no longer be detected and the graph levels off at 13.8 μm; perhaps indicating that Raman cannot sense as well beyond 5 μm. This means that either Raman can sense below the surface by 10 times more than its theoretical limit, or the SNC density itself varies with anodisation time as shown in Figure 4.44.

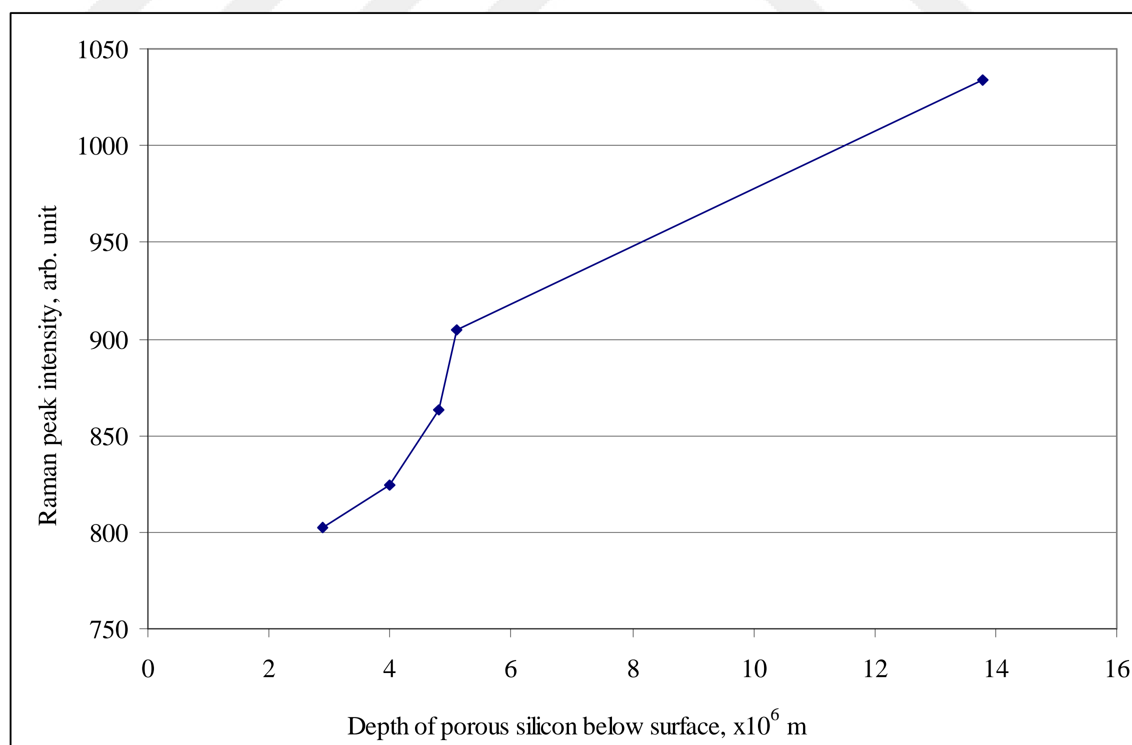

Figure 4. 44 Raman peak intensities together with the depth of the porous silicon structure

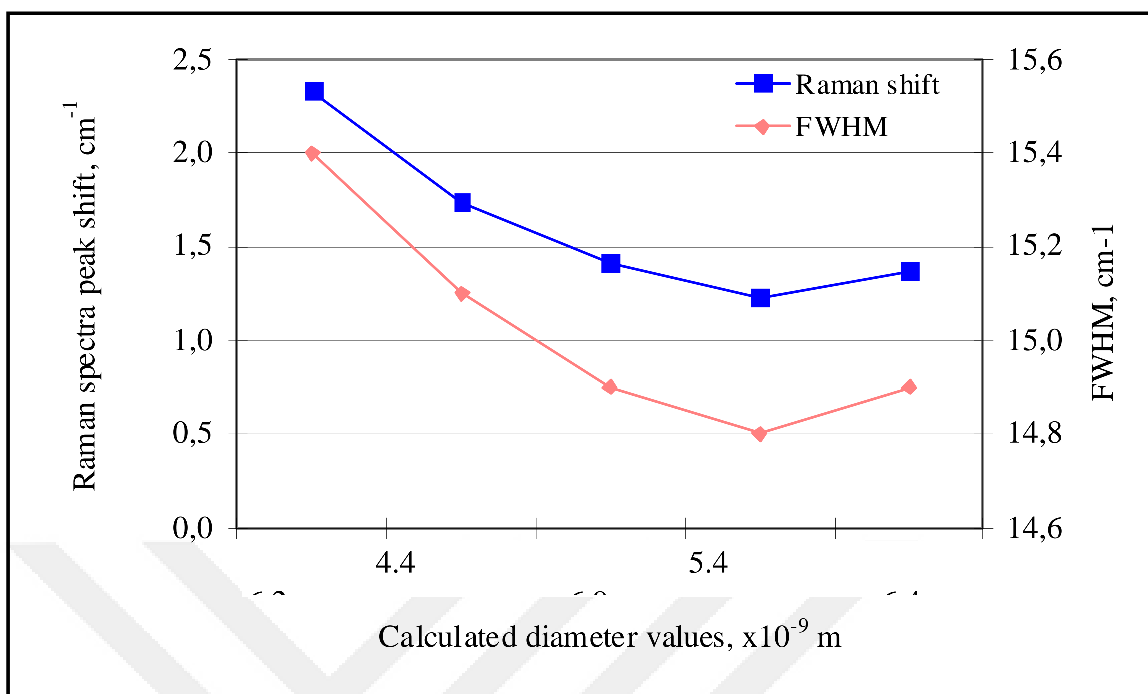

Figure 4. 45 Raman spectra intensity values and depths of porous structures of the set-A samples

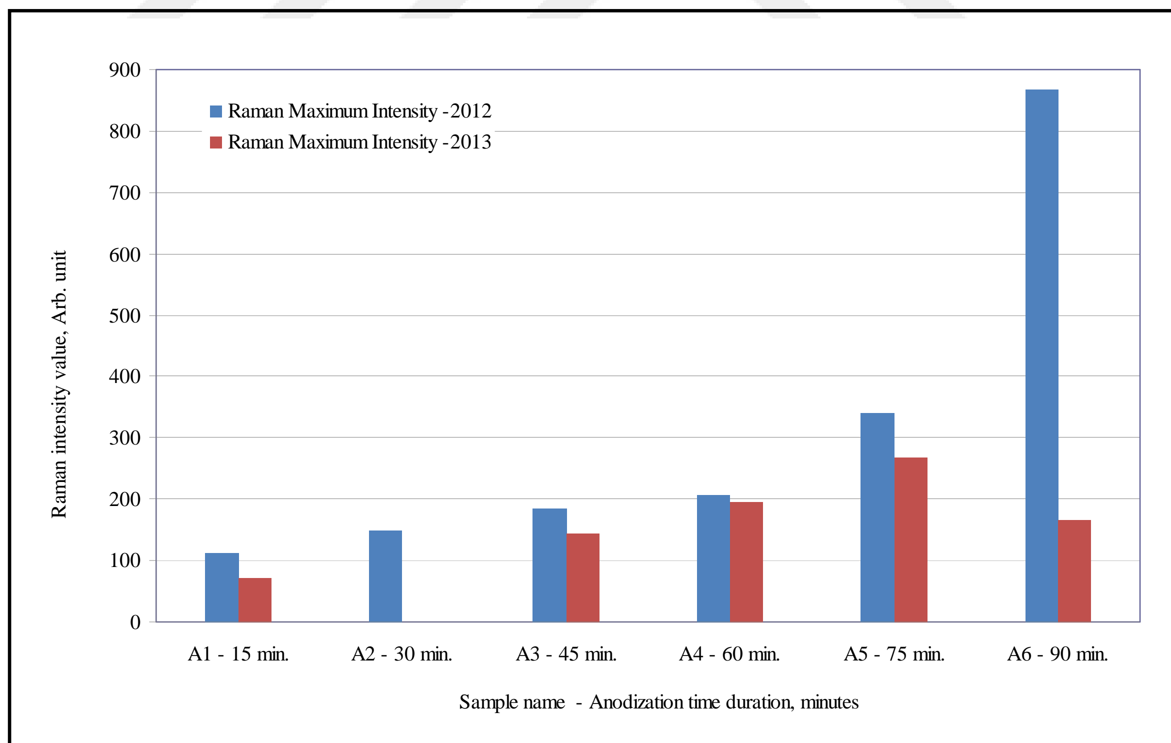

Figure 4. 46 Raman spectra intensity degradation over 3 months

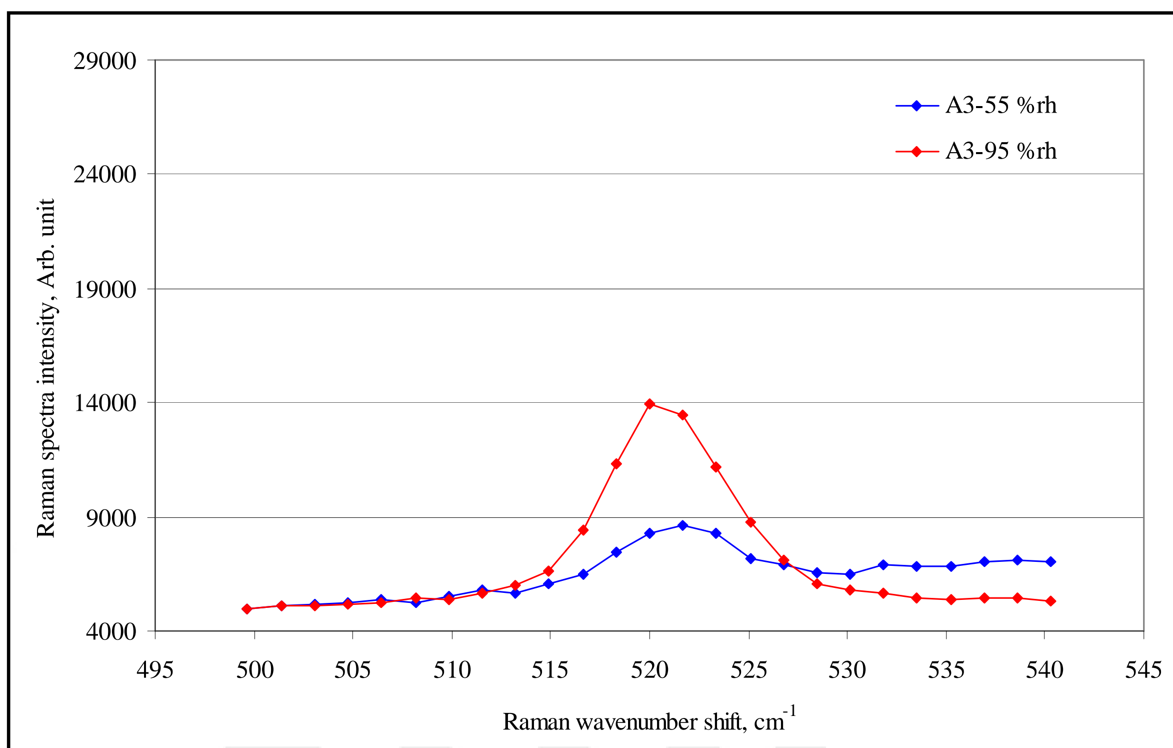

Figure 4. 47 Raman spectra intensity of sample A3 at 55 %rh and 95 %rh

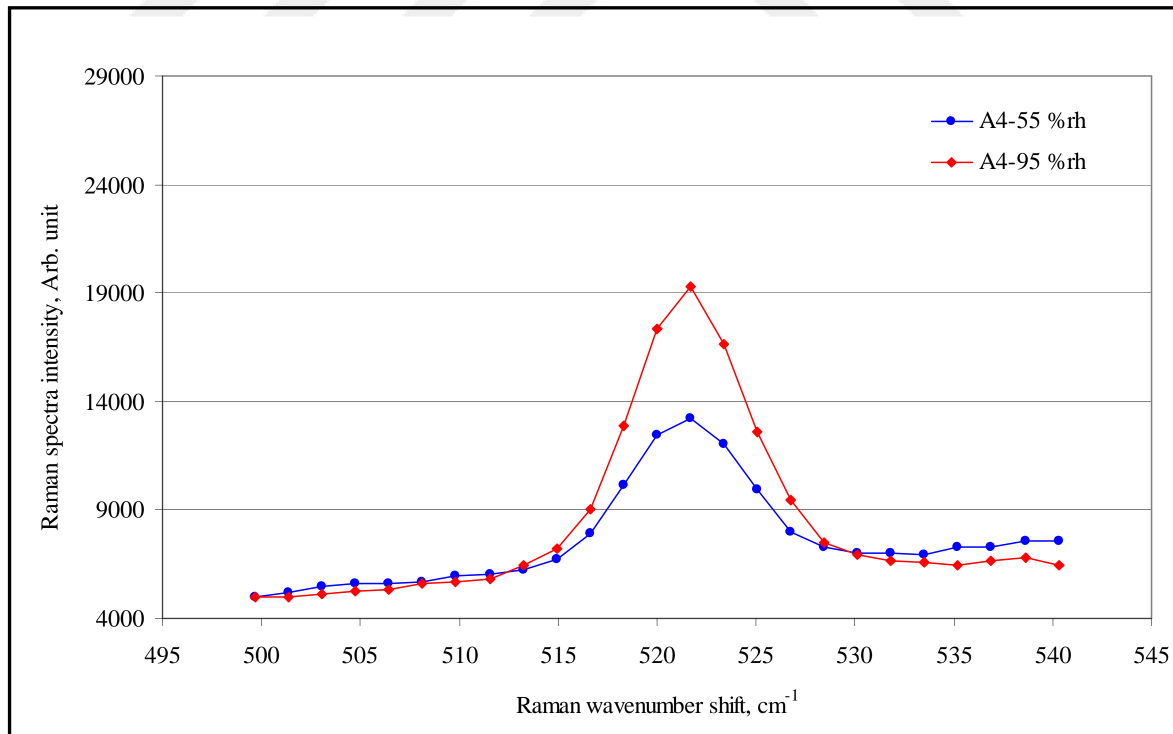

Figure 4. 48 Raman spectra intensity of sample A4 at 55 %rh and 95 %rh

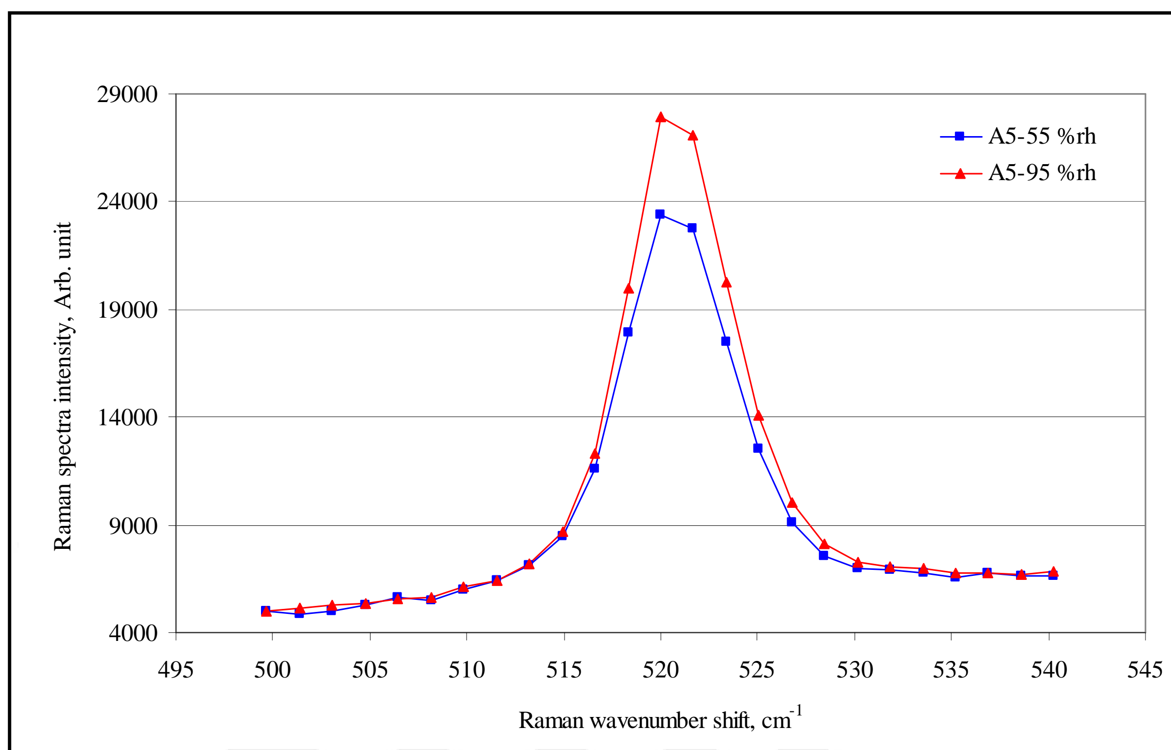

Figure 4. 49 Raman spectra intensity of sample A5 at 55 %rh and 95 %rh

4.5.5. Comparison of Raman and SEM Results

From the graphs given in Figure 4.35, although SNC diameters determined from the Raman spectral analysis increase with anodisation time, they decrease after 60 minutes: this is also the case for the SEM results given in Table 4.15.

The difference in diameter computed from MATLAB and Raman spectra is a consequence of the different resolution of the two characterization techniques.and also image processing of SEM images sets up spherical shapes with well-defined edges. SEM only scans the surface where larger structures may occur due to longer exposure to the chemicals. It is likely that the surface nanocrystals and pores decrease in diameter downwards into the silicon wafer. In the images obtained from SEM (Figure 4.26) 25 nm to 40 nm diameter granular islands are actually composed of much smaller SNC. Certainly, their cross section images in Figure 4.27 show that the diameter of the granular islands decreases from the surface down to the bottom of the porous structure. A variation in pore diameter dimensions is usual in porous silicon structures, since there are basically two independent

formation mechanisms which may coexist simultaneously. This results in a superposition of pore structures of nanometer and micrometer size [142].

Raman spectroscopy can resolve structures from 3 nm to 20 nm, matching the Kelvin pore dimensions for up to 95% rh (Figure 1.12), as predicted by the phonon confinement model predicted by Richter et. al. [185].

4.6. CAPACITANCE MEASUREMENT RESULTS

Porous silicon humidity sensors fabricated by electrochemical anodization from the four basic steps as given in section the first section of the experimental part are shown in Figure 4.50.

Figure 4. 50 Fabricated porous silicon humidity sensors

Electrical characterization of porous silicon humidity sensors were performed in a temperature and humidity controlled environment using a LCR meter. Capacitance measurements were performed for the determination of relative humidity sensitivity of porous silicon sensor. LCR meter was used for electrical parameter measurements, especially capacitance versus frequency, and relative humidity versus frequency. Electrical characterization of porous silicon humidity sensor was performed using a relative humidity generator working two-pressure and two-temperature principle by controlling both pressure and temperature values both in the chamber and the humidifying unit (saturator). Measurement setup is given in Figure 4.51.

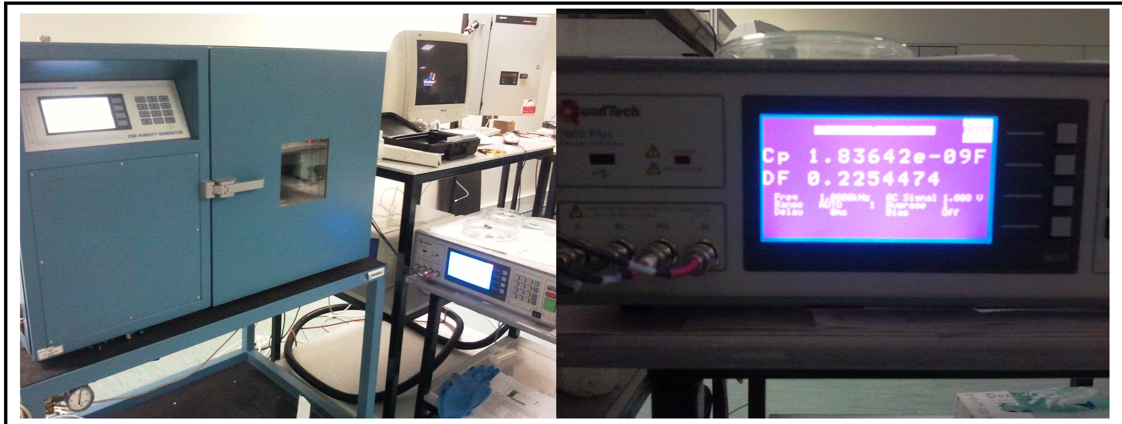

Figure 4. 51 Measurement setup for electrical caharacterization of porous silicon humidity sensor in a humidity generator using an LCR meter.

4.6.1. Equivalent Circuit Model for Porous Silicon Humidity Sensor

Capacitance value of porous silicon relative humidity sensors depend on measurement frequency since dielectric permeability of porous structure depends on frequency. This resulted from the long relaxation time of dipole moment of water molecules absorbed by porous structure. In addition corresponding equivalent circuit is much complex than stated.

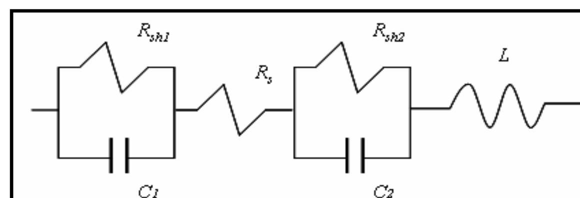

Figure 4. 52 Equivalent circuit model for porous silicon humidity sensor

Equivalent circuit model for metal/PSi/metal structure is composed of serial resistance R_s, a parallel resistance R_{sh2}, capacitance C_2, and induction L (regarding cables). Porous silicon layer was designated by a parallel resistance R_{sh1} and capacitance C_1 in the proposed electrical circuit.

A simplified schematic for capacitor action for humidity sensing of porous silicon sensor is given in Figure 4.53.

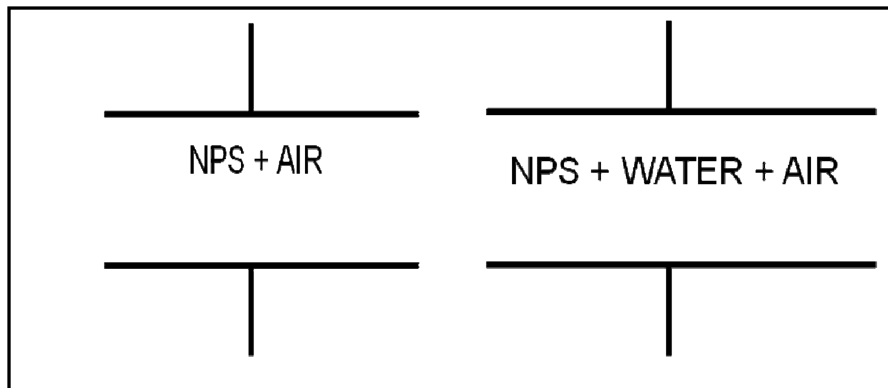

Figure 4. 53 Capacitor action for humidity sensing of porous silicon sensor

4.6.2. Response Determination by Variying Frequencies

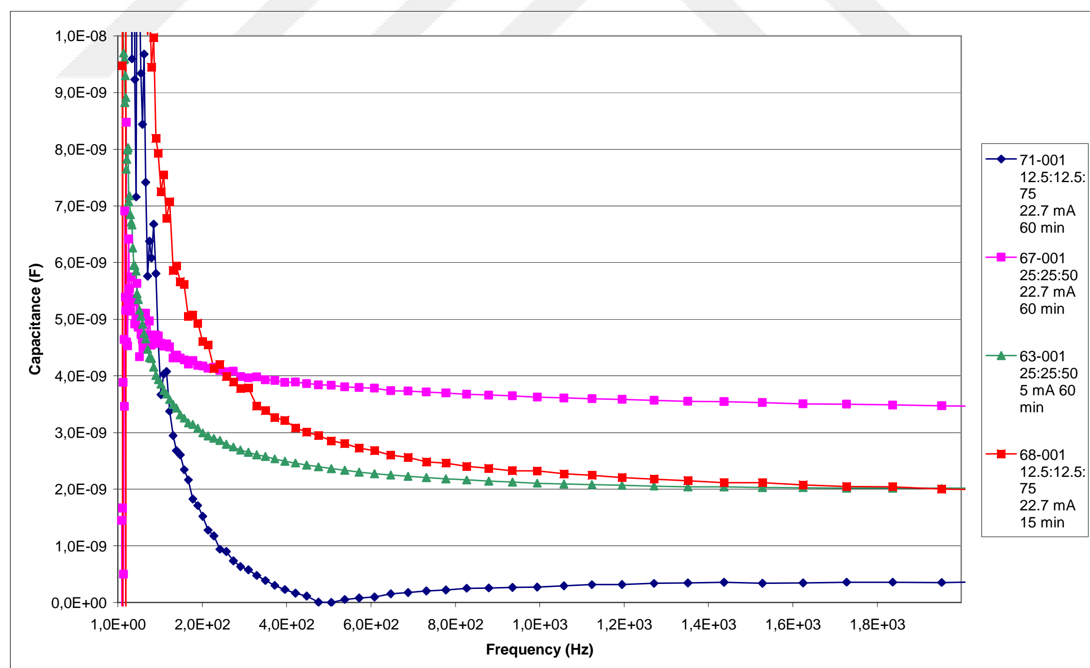

Figure 4. 54 Frequency sweep versus capacitance values of porous silicon relative humidity sensors at 23 °C and 50 %rh.

At a specific voltage value (1 V) frequency values ranging from 10 Hz to 1 MHz was applied in order to determine the response of relative humidity sensors as given in Figure 4.54.

In addition, specific frequency value was determined where maximum capacitance change occurs in the above mentioned frequency range. This frequency value was then chosen to be used for rest of the measurements. From the capacitance versus frequency data, a frequency parameter was found to be 1 kHz for varying relative humidity values from 20 %rh to 95 %rh at a temperature value of 23 °C. Relative humidity versus capacitance values at three specific frequency values was given in Figure 4.55.

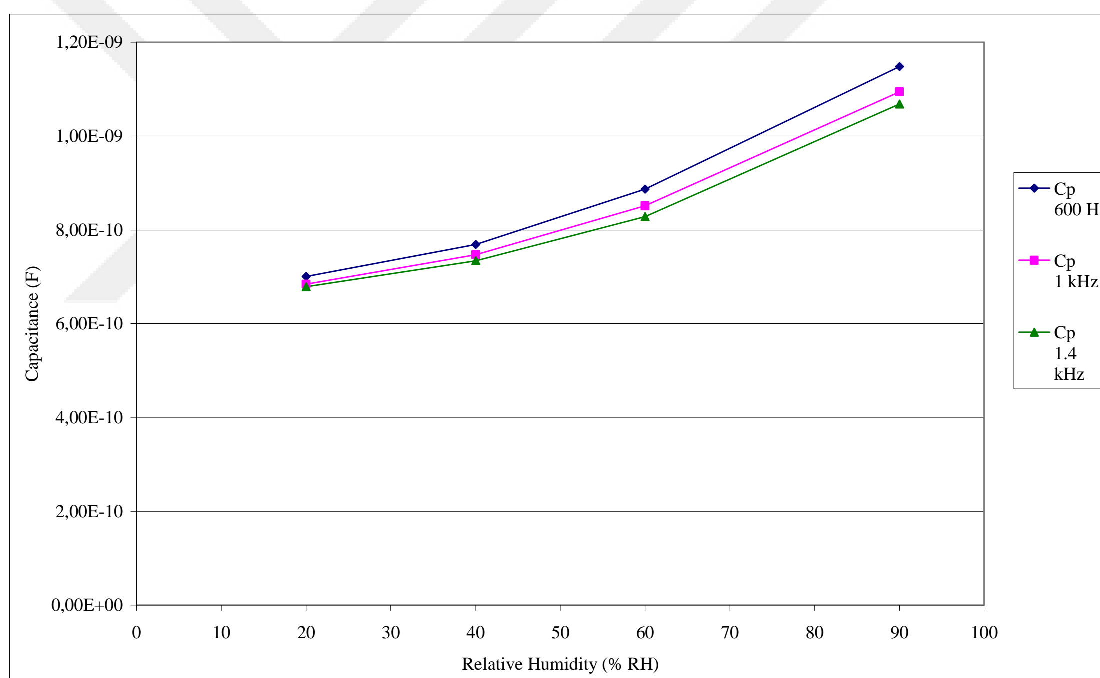

Figure 4. 55 Relative humidity versus capacitance graph of porous silicon humidity sensor at three specific frequency values around 1 kHz.

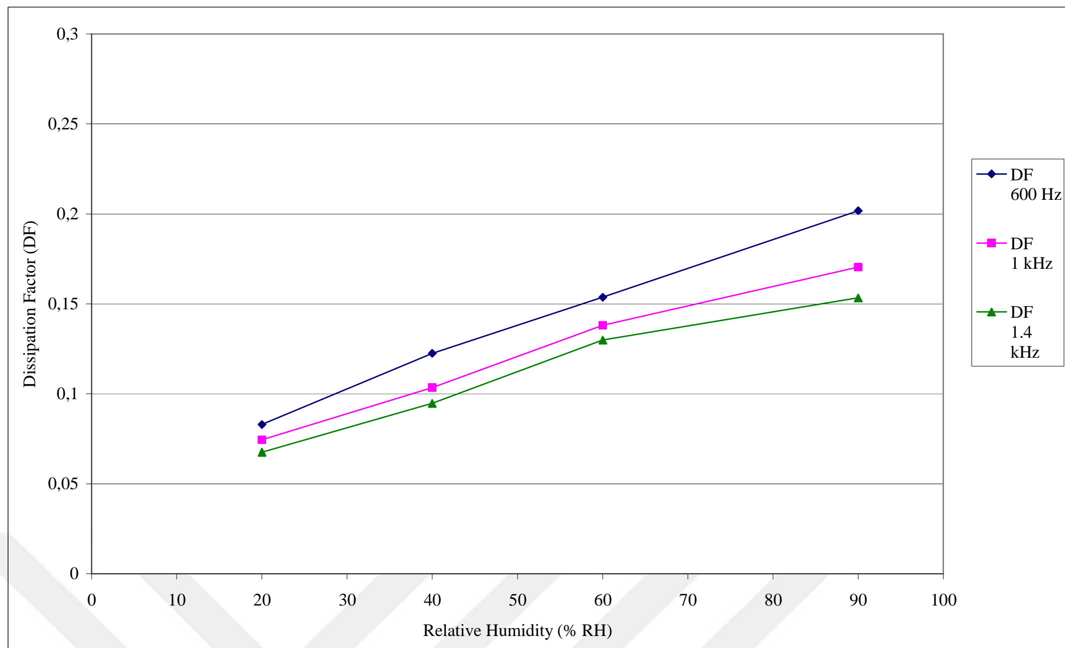

Figure 4. 56 Relative humidity versus dissipation factor graph of porous silicon humidity sensor at three specific frequency values around 1 kHz.

4.6.3. Sensitivity Determination of Sensors

Relative humidity sensors were characterized in terms of their sensitivity. Sensitivity is the change in capacitance with relative humidity. Sensitivity values were given in Table 4.17.

$$S = \frac{\Delta C_p}{\Delta RH} = \frac{C_{pf} - C_{pi}}{RH_f - RH_i} \tag{4.2}$$

Capacitance measurements were carried out with an LCR meter (QuadTech – Model 7600) in a thermally isolated chamber of a humidity generator from Thunder Scientific (Model 2500ST).

4.6.4. Response Time Determination of Sensors

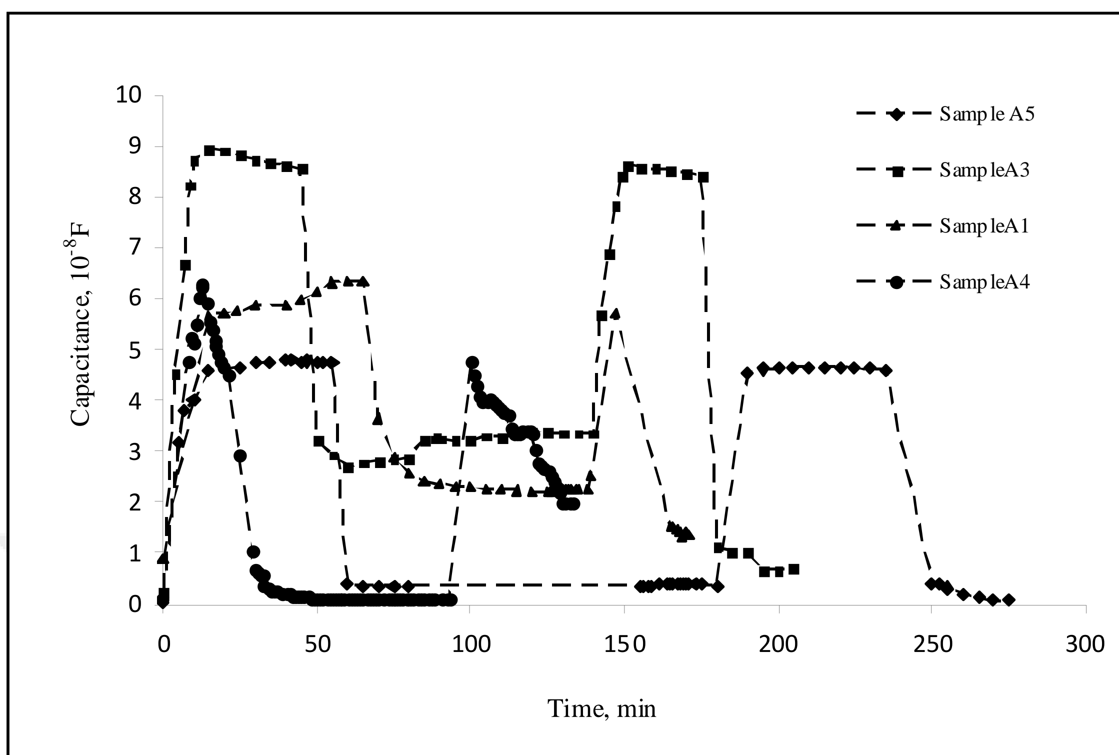

Figure 4. 57 Response time measurements of the sensors at varying RH values from 5 %rh to 95 %rh

Response time of the sensors were carried out with an LCR meter (7600 from QuadTech) at nitrogen atmosphere in a closed container with relative humidity values of 5 %rh, and at 50 %rh, and 95 %rh relative humidity value. The measurement results were given in Figure 4.57.

4.6.5. Capacitance Measurements of Sensors

Capacitance measurements were carried out with an LCR meter (7600 from QuadTech) at a frequency of 1 kHz in a thermally isolated chamber of a humidity generator from Thunder Scientific.

Relative humidity sensors are characterised mostly in terms of their sensitivity, linearity, and capacitance change. Nanoporous silicon relative humidity sensors are characterized in terms of normalized percentage capacitance change (NPCC) in the range from 20 %rh to 95 %rh. Normalized percentage capacitance change was calculated and listed in Table

4.17. Two of the sensor samples A2 and A4 were broken during measurements, so only the three remaining samples (A1, A3 and A5) were used for final measurements at a temperature of 23 °C. The sensitivity of the sensors was calculated as 0.66 $\%rh^{-1}$, 0.74 $\%rh^{-1}$, 0.45 $\%rh^{-1}$ in the range from 20 %rh to 95 %rh at 23 °C.

Table 4. 16. Capacitance values of porous silicon relative humidity sensors at different anodization times

Sample name	Anodization time min.	Capacitance values of porous silicon samples x10^{-9} F						
		0 %rh	20 %rh	40 %rh	50 %rh	60 %rh	80 %rh	95 %rh
A1	15	6.52	13.45	29.30	37.50	43.26	56.56	63.18
A2	30	-	8.12	15.25	22.37	29.69	36.91	54.86
A3	45	0.27	10.49	17.22	24.02	31.78	48.75	66.30
A4	60	0.76	1.39	12.56	25.77	44.14	55.32	66.95
A5	75	0.16	0.49	2.51	5.43	10.21	23.95	34.22

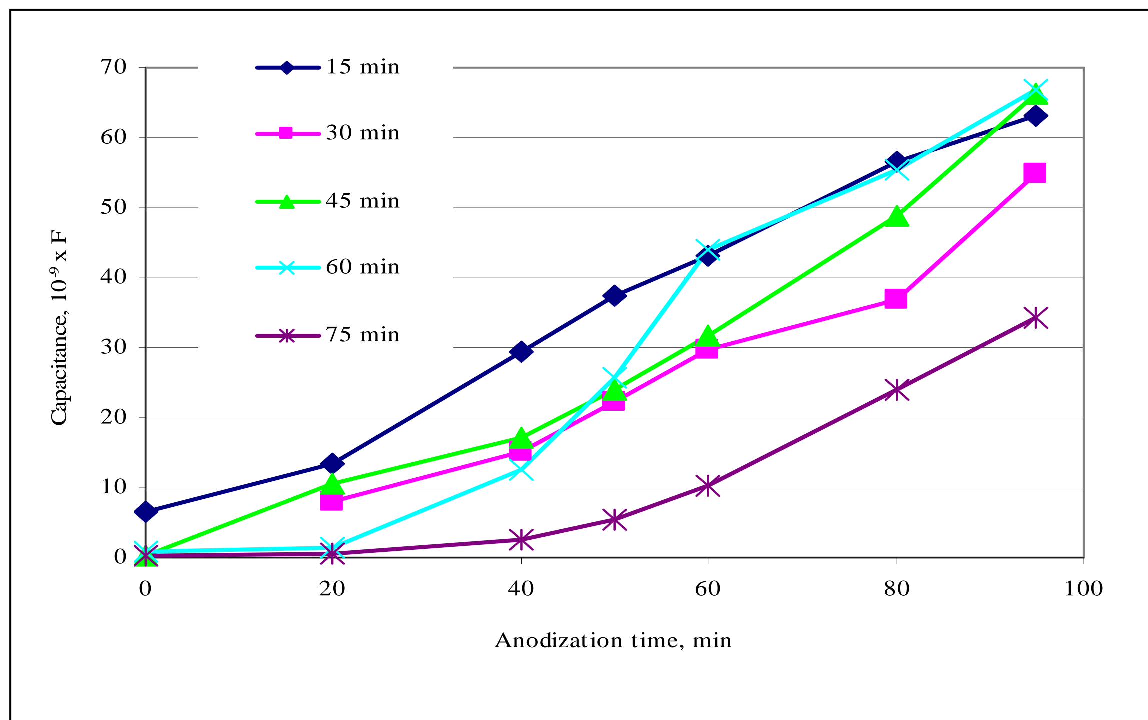

Figure 4. 58 Capacitance values of A-series samples from 0 %rh to 95 %rh

4.6.6. Capacitance and Raman Spectra Intensity Change Over Three Months To Gauge Mechanical Stability

Capacitance measurements also gauge the quality of the mechanical structure of the NPS layers. This is critically important, since it determines the time period over which the sensor can be reliably utilised. Thus, after the measurements were completed on each sample, they were kept at ambient conditions for three months and their performance over the humidity range was again determined to gauge their mechanical stability over time.

The changes in capacitance for each sample were used to determine deterioration in mechanical structure over three months. The maximum deviations in the measured capacitance values over three months were ± 7 nF for A1, ± 5 nF for A3, ± 5 nF for A5 from 20 %rh to 95 %rh. 27 %, 25 %, and 96 % change in mechanical structure was calculated according to the changes in the capacitance values of A1, A3 and A5.

Table 4. 17. Capacitance change of samples over three months with corresponding percentage deteoriation values of mechanical structure

Sample name	Anodization time min.	Capacitance value of porous silicon samples at 50 %rh at 23 °C – 2012 after preparation $x10^{-9}$ F	Sensitivity nF · rh^{-1}	Capacitance value of porous silicon samples at 50 %rh at 23 °C – 2013 after 3 months $x10^{-9}$ F	Differences in capacitance values of porous silicon samples at 50 %rh at 23 °C $x10^{-9}$ F	Mechanical degradation in percentage after 3 months at 20 %rh $x10^{-9}$ F	Mechanical degradation in percentage after 3 months at 50 %rh $x10^{-9}$ F	Mechanical degradation in percentage after 3 months at 95 %rh $x10^{-9}$ F
A1	15	37.50	0.66	33.27	4.23	26.5	11.3	10.8
A2	30	22.37	0.62	-	-	-	-	-
A3	45	24.02	0.74	19.86	4.16	25.4	17.3	5.1
A4	60	27.97	0.87	23.45	4.52	10.4	16.2	15.7
A5	75	5.43	0.45	3.17	2.26	95.9	41.6	13.4

Table 4.17 depicts a decrease in performance of the samples due to the mechanical degradation of the porous structure. Raman spectra of the same samples after three months show a similar intensity decrease for all samples in Figure 4.46 and correlate with the mechanical degradation depicted by the capacitance measurements.

The Raman results are also indicative of a decrease in the number of nanocrystals in the samples as a result of structural collapse. This shows that using Raman, information about the decay in numbers and dimensions of nanopores in the NPS humidity sensors can be obtained, offering a distinct advantage over capacitance measurements.

As the depth of the porous structure is increased, the probability of collapse increases due to insufficient infiltration of the pentane during the drying stage of the fabrication process.

4.6.7. Comparison of Capacitance Sensitivity and Raman Results

Contrary to the increase in intensity of the Raman peak with depth of SNP structure, Figure 4.58 shows that the capacitance does not follow this trend.

Comparing Tables 4.15, 4.16 and 4.17 clearly shows the two opposing trends. This is surprising since deeper and larger pores are expected to be able to accommodate more water droplets and so an increasing dielectric constant and capacitance. This may indicate either blockage of pores at the pore surface or the collapse of the SNP structure beneath the surface. It is known that evaporation of water vapour can cause vapour pressures of some MPa [114] within the sensing SNP. This itself is a potential cause of collapse of the SNP structure, however Table 4.17 shows that the capacitance increases linearly with RH, so the sensing process itself is not thought to cause destruction of the SNP structure. The only remaining possibility is that the collapse occurs as a direct result of longer anodisation times; this would cause less nanopores, but more nanocrystallites, hence the increase in the Raman intensity, but decrease in capacitance as less nanopores are available for water droplets. In Table 4.16 there is almost complete saturation at 95 %rh, and all the samples show the same capacitance reading. However, at 0 %rh, when there is no water, the decreasing capacitance trend with anodisation time of the sample is still apparent. This

shows that the effective cross section area, A in the capacitance equation $C= \varepsilon A/d$ must be decreasing; this is another clue for SNP structural collapse.

Table 4. 18. Peak intensity degradation of Raman spectra from porous silicon humidity sensors fabricated at different anodization times

Sample name	Anodization time min.	Raman spectra peak intensity - 2012 arb. unit	Raman spectra peak intensity - 2013 arb. unit	Decrease in Raman spectra peak intensity arb. unit
A1	15	112.0	72.0	40.0
A2	30	149.0	--	--
A3	45	185.7	146.0	39.7
A4	60	207.7	197.0	10.7
A5	75	341.6	268.0	73.6

The calculated sensitivity, S of the sensor samples is calculated in Table 4.17 in the range from 20 %rh to 95 %rh at 23 °C. Sample A4 with 60 minutes anodisation time was found to be the most linear one having 0.87 nF.%rh^{-1}. As the nanocrystal size decreases after 60 minutes of anodization (Figure 4.45), it causes the nanopore sizes to decrease, which may lead to the lower sensitivity observed for sample A5 (Figure 4.57).

Sensitivity of both measurement methods was also compared and sensitivity ratio was calculated according to the equation given below.

$$S_{Raman} = \left(\left(I_{R@95rh} / \delta I_{R@95rh}\right) - \left(I_{R@50rh} / \delta I_{R@50rh}\right)\right) / \left(RH_{\max} - RH_{\min}\right) \quad (4.3a)$$

$$S_{Cap} = \left(\left(C_{\max@95rh} / \delta C_{@95rh}\right) - \left(C_{\min@50rh} / \delta C_{@50rh}\right)\right) / \left(RH_{\max} - RH_{\min}\right) \quad (4.3b)$$

$$\frac{S_{Raman}}{S_{Cap}} = \frac{\left(\left(I_{R@95rh} / \delta I_{R@95rh}\right) - \left(I_{R@50rh} / \delta I_{R@50rh}\right)\right) / \left(RH_{\max} - RH_{\min}\right)}{\left(\left(C_{\max@95rh} / \delta C_{@95rh}\right) - \left(C_{\min@50rh}\right) / \delta C_{@50rh}\right)\right) / \left(RH_{\max} - RH_{\min}\right)} \quad (4.3c)$$

In the above equation, S_{Raman}, and S_{Cap} are sensitivity values of Raman spectra measurements and capacitance measurements, respectively. I_{Rmax}, I_{Rmin}, C_{max}, C_{min}, RH_{max},

RH_{min} are maximum Raman intensity at 95 %rh, minimum Raman intensity at 50 %rh, maximum capacitance value at 95 %rh, minimum capacitance value at 50 %rh, maximum relative humidity value, 95 %rh, and minimum relative humidity value, 50 %rh, respectively. I_R is Raman intensity peak height from baseline which is divided by signal noise $\delta I_{R.}$ δI_R, and δC are lowest possible Raman signal and capacitance values obtained during measurements.

Ratio of sensitivity values of both Raman spectroscopy and capacitance measurements were calculated and given in Table 4.19. The Raman sensitivity values of samples A3, A4, and A5 was found to be greater in one order of magnitude, which means that Raman spectroscopy measurements can be used for the characterization of relative humidity sensors instead of capacitance characterization. Therefore, Raman measurements can be placed by capacitance measurements.

Table 4. 19. Sensitivity of Raman spectroscopy and capacitance measurements and their ratio values

Sample name	$I_{R@50rh}$ Arb. unit	$I_{R@95rh}$ Arb. unit	$\delta I_{R@50\text{rh}}$ Arb. unit	$\delta I_{R@95\text{rh}}$ Arb. unit	Sensitivity values of Raman spectra measurements $\%^{-1}$	Sensitivity values of capacitance measurements $\%^{-1}$	Ratio of both sensitivity values
A1	--	--	--	--	--	1.1	--*
A2	--	--	--	--	--	--	--*
A3	2113.1	7857.8	20.1	6.5	24.3	2.3	10.7
A4	4948.4	11741.9	18.7	18.6	8.2	--	--*
A5	15862.3	19809.4	18.6	15.6	9.2	6.6	1.4

*as sample is broken sensitivity values are not given

4.7. AFM ANALYSIS

AFM images were given in the following figures. The results were given in Table 4.20 and from Figure 4.59 to Figure 4.55. AFM measurements which were carried out over 10 μm^2 region provided information about the uniformity of the porous silicon surface. Average

rougness values of the samples from set-A calculated from AFM measurements were found to be highly correlated with the average diameter values of the same samples calculated from image processing software.

Average roughness values of set-B and set-C samples also provided insight about the structure that they did not have the required specifications for relative humidity sensor.

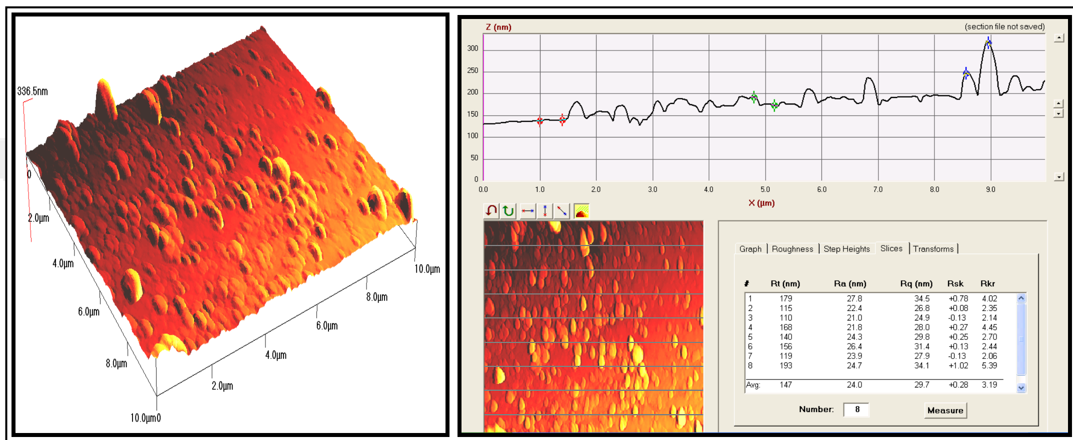

Figure 4. 59 AFM of sample A1 with surface roughness values

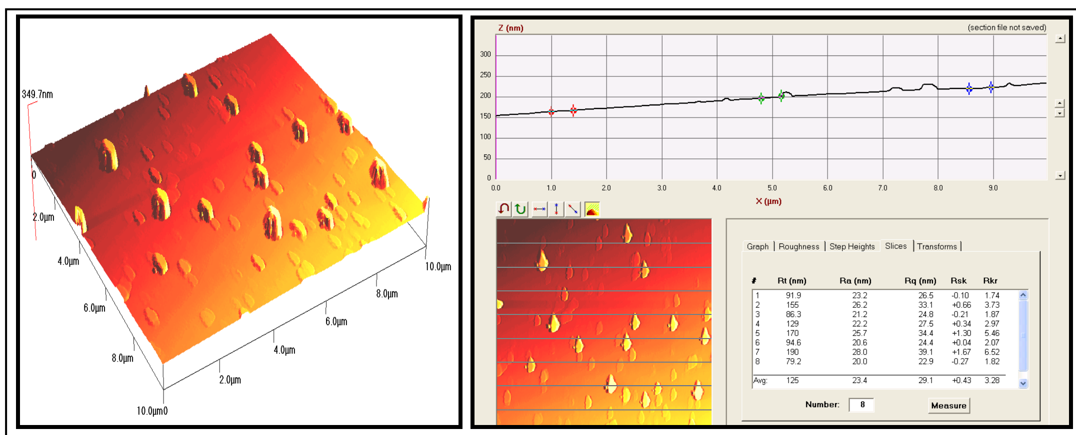

Figure 4. 60 AFM of sample A2 with surface roughness values

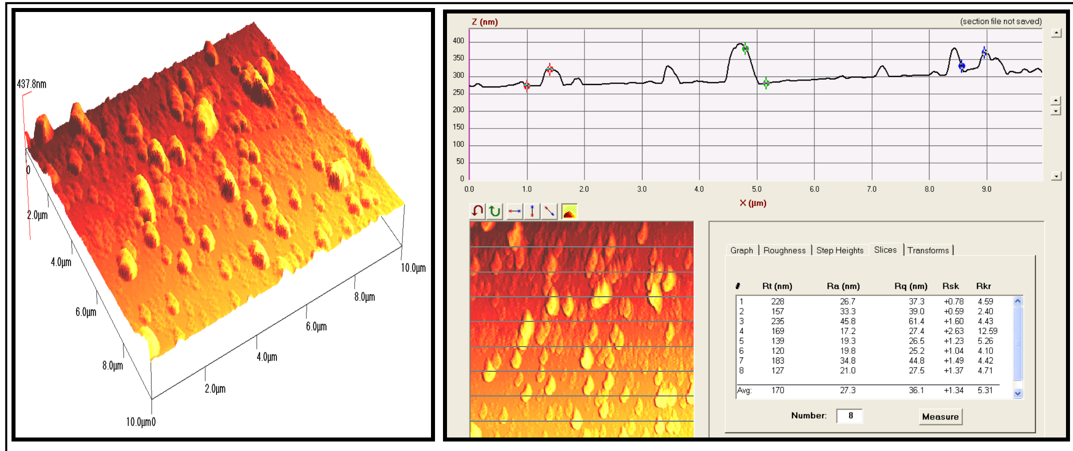

#	Rt (nm)	Ra (nm)	Rq (nm)	Rsk	Rkr
1	228	26.7	37.3	+0.78	4.59
2	157	33.3	39.0	+0.59	2.40
3	235	45.8	61.4	+1.60	4.43
4	169	17.2	27.4	+2.63	12.59
5	139	19.3	26.5	+1.23	5.26
6	120	19.8	25.2	+1.04	4.10
7	183	34.8	44.8	+1.49	4.42
8	127	21.0	27.5	+1.37	4.71
Avg:	170	27.3	36.1	+1.34	5.31

Figure 4. 61 AFM of sample A3 with surface roughness values

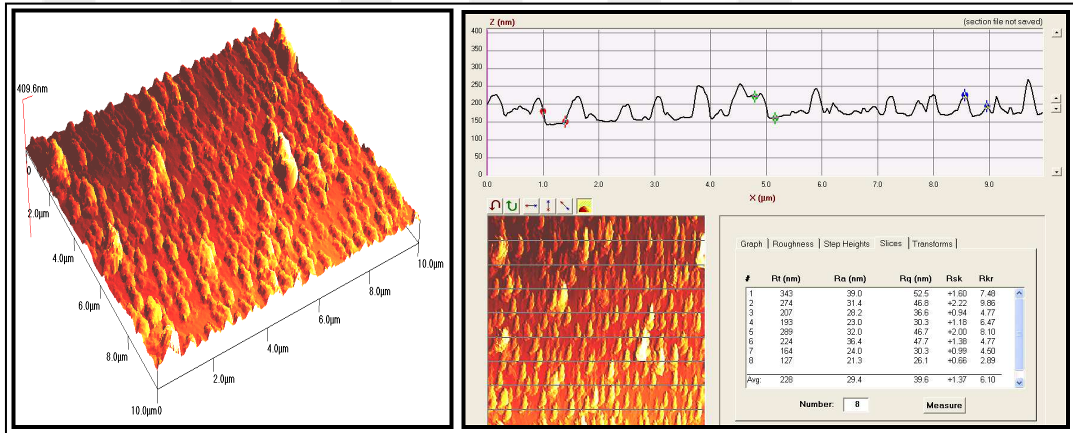

#	Rt (nm)	Ra (nm)	Rq (nm)	Rsk	Rkr
1	343	39.0	52.5	+1.60	7.48
2	274	31.4	46.8	+2.22	9.86
3	207	28.2	36.6	+0.94	4.77
4	193	23.0	30.3	+1.18	6.47
5	289	32.0	46.7	+2.00	8.10
6	224	36.4	47.7	+1.38	4.77
7	164	24.0	30.3	+0.99	4.50
8	127	21.3	26.1	+0.66	2.89
Avg:	228	29.4	39.6	+1.37	6.10

Figure 4. 62 AFM of sample A4 with surface roughness values

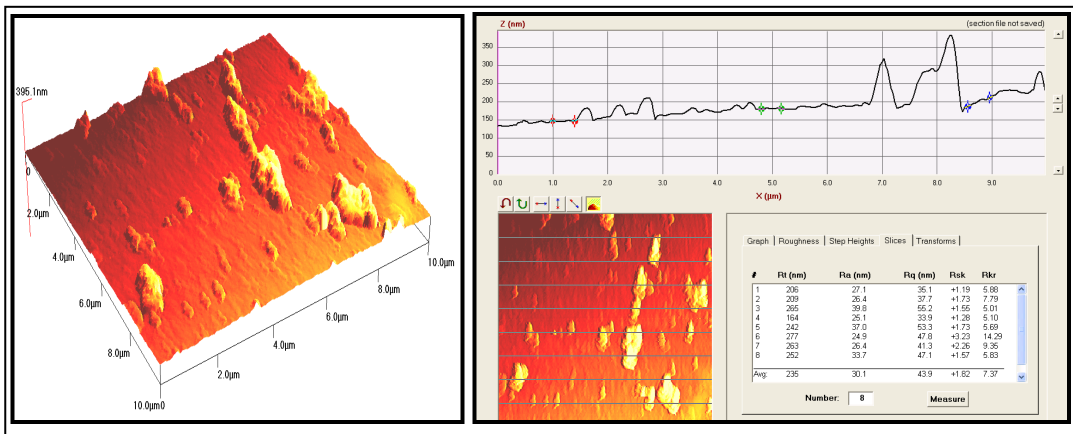

#	Rt (nm)	Ra (nm)	Rq (nm)	Rsk	Rkr
1	206	27.1	35.1	+1.19	5.88
2	209	26.4	37.7	+1.73	7.79
3	265	39.8	55.2	+1.55	5.01
4	164	25.1	33.9	+1.28	5.10
5	242	37.0	53.3	+1.73	5.69
6	277	24.9	47.8	+3.23	14.29
7	263	26.4	41.3	+2.26	9.35
8	252	33.7	47.1	+1.57	5.83
Avg:	235	30.1	43.9	+1.82	7.37

Figure 4. 63 AFM of sample A5 with surface roughness values

Average roughness values of samples were tabulated in Table 4.20 and given in Figure 4.64 and Figue 4.65. Set-A samples were anodized in a solution containing 1:1:1 $HF:H_2O:C_2H_5OH$ at 2.2 $mA{\cdot}cm^{-2}$ with different anodization times form 15 min, 30 min., 45 min., 60 min., and 75 min., labeled starting from A1 to A5. Set-B samples were anodized in a solution containing 1:1:1 $HF:H_2O:C_2H_5OH$ at 10.0 $mA{\cdot}cm^{-2}$ with different anodization times form 15 min, 30 min., 45 min., 60 min., and 75 min., labeled starting from B1 to B5. Set-C samples were anodized in a solution containing 1:1/2:1/2 $HF:H_2O:C_2H_5OH$ at 10.0 $mA{\cdot}cm^{-2}$ with different anodization times form 15 min, 30 min., 45 min., 60 min., and 75 min., labeled starting from C1 to C5.

Table 4. 20. Average roughness values of samples anodized at different current densities and anodization times

Anodization time, min	Sample name	Average roughness R_a, nm	Sample name	Average roughness R_a, nm	Sample name	Average roughness R_a, nm
15	A1	24.0	B1	26.4	C1	125.0
30	A2	23.4	B2	34.1	C2	341.0
45	A3	27.3	B3	105.0	C3	410.0
60	A4	32.2	B4	115.0	C4	420.0
75	A5	30.1	B5	117.0	C5	419.0

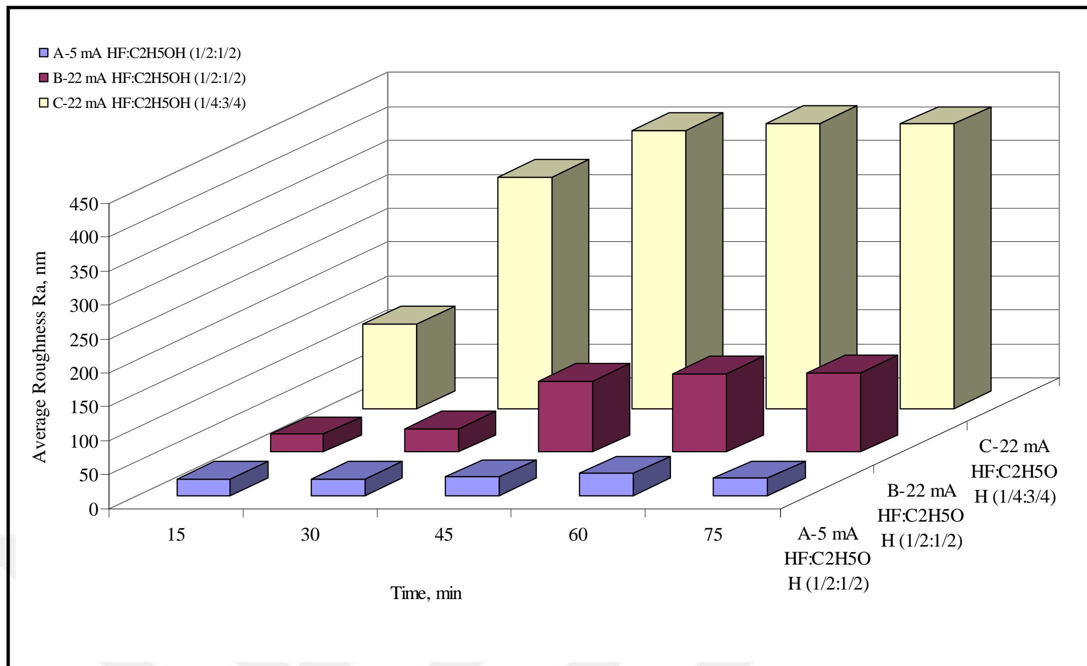

Figure 4. 64 AFM results of samples A1 to A5, B1 to B5, and C1 to C5

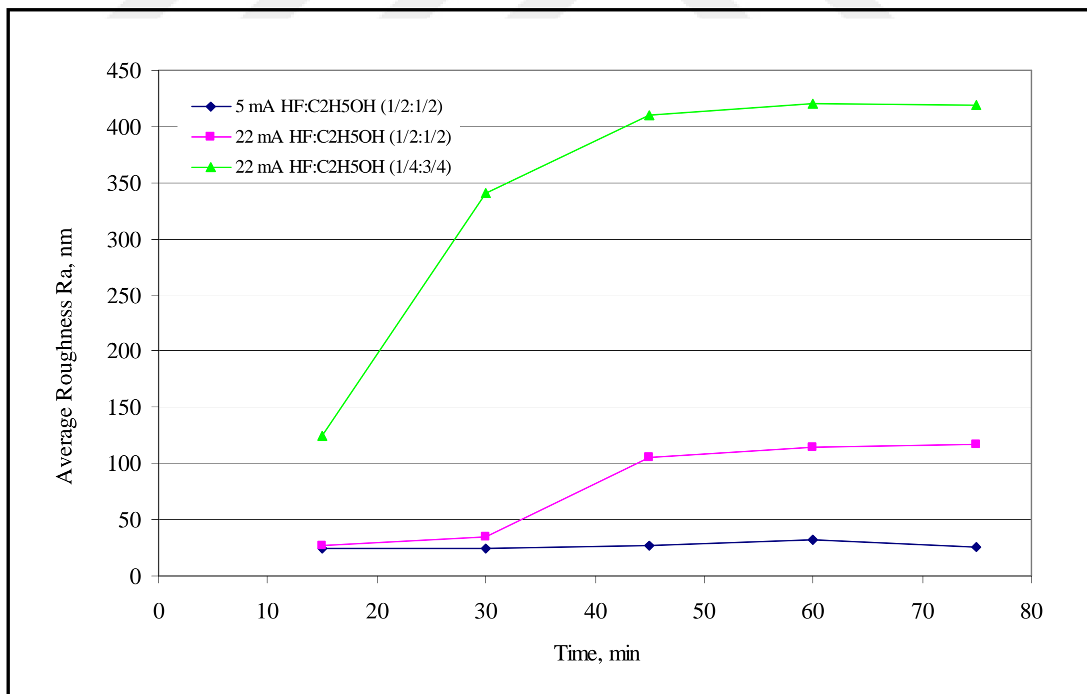

Figure 4. 65 Average roughness values from AFM analysis of samples A1 to A5, B1 to B5, and C1 to C5

Average roughness values of set-A samples were found to be in good correlation with the diameter values obtained from image processing of SEM images. Since the structure of set-B and set-C samples, except B1 and B2, have micrometer sized pore arrays, their roughness values are rather greater than the A series roughness values, as it was expected.

4.8. PHOTOLUMINESCENCE ANALYSIS

The photoluminescence spectra were obtained using a PC controlled MMS spectrometer. Light from a UV lamp (Konrad-Benda) of wavelength 366 nm was used as photoluminescence excitation. All spectral measurements were taken at room temperature. Photoluminescence spectroscopy measurements of the samples and the analysis were given in the following graphs and tables. Diameter values calculated from photoluminescence spectra parameters were given in the Table 4.21, Table 4.22, and Table 4.23.

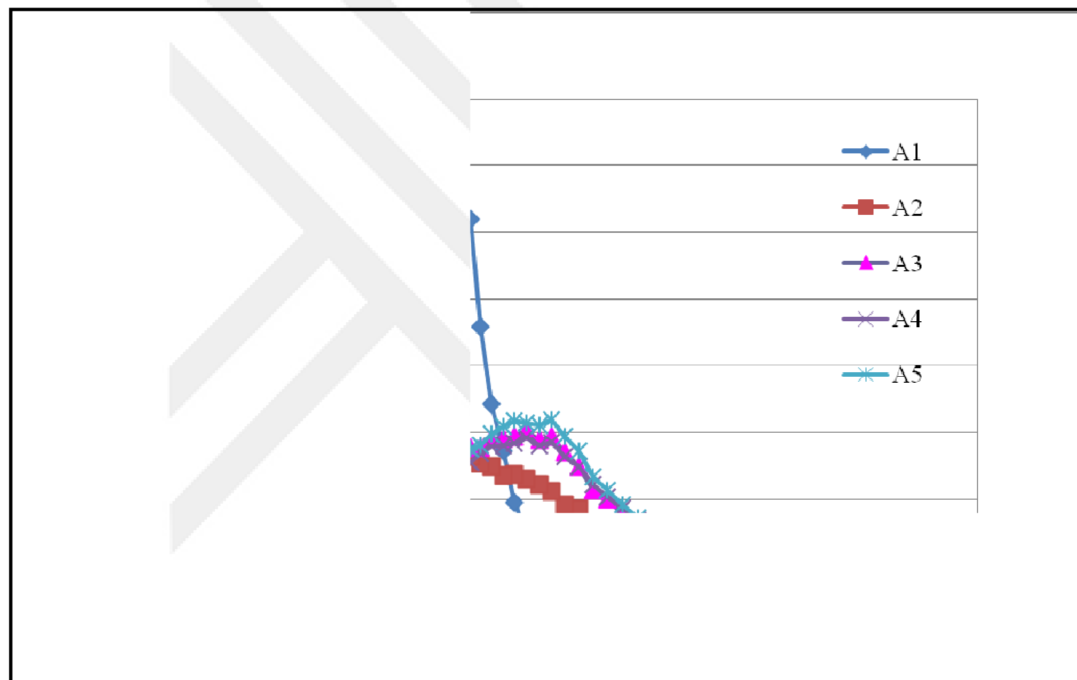

Figure 4. 66 Photoluminescence spectra of samples from A1 to A5

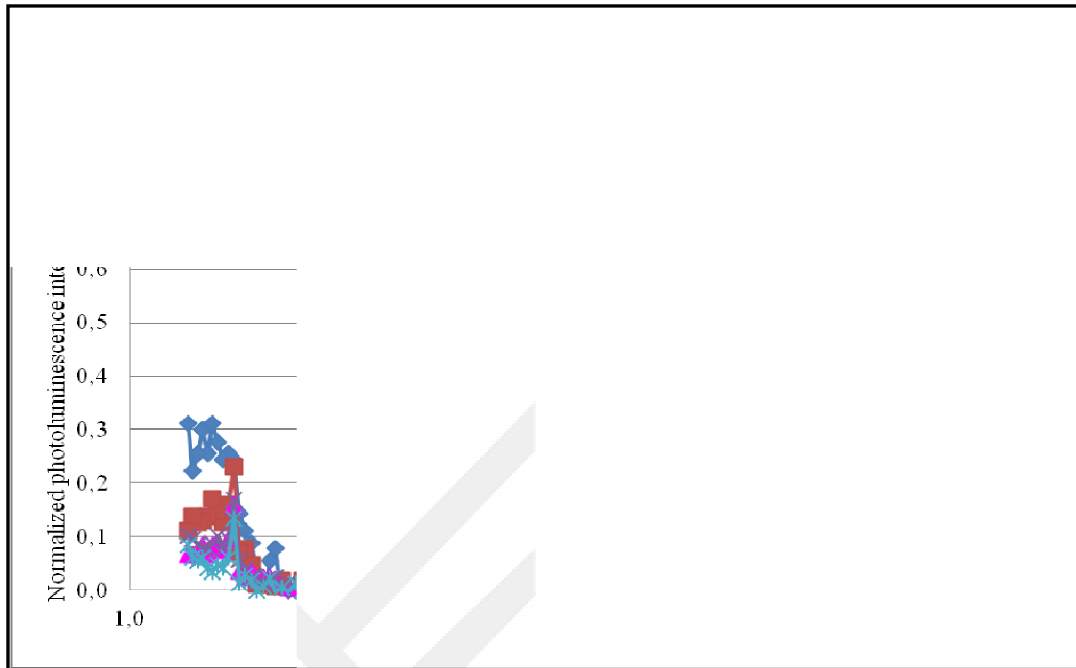

Figure 4. 67 Normalized photoluminescence spectra of samples from A1 to A5

Table 4. 21. Diameter values calculated using photoluminescence parameters

Sample name	Anodization time, min	Energy at maximum PL intensity (I), eV	Diameter values calculated from PL parameters, nm
A1	15	1.71	4.2
A2	30	1.78	3.8
A3	45	1.91	3.2
A4	60	1.91	3.2
A5	75	1.98	3.0

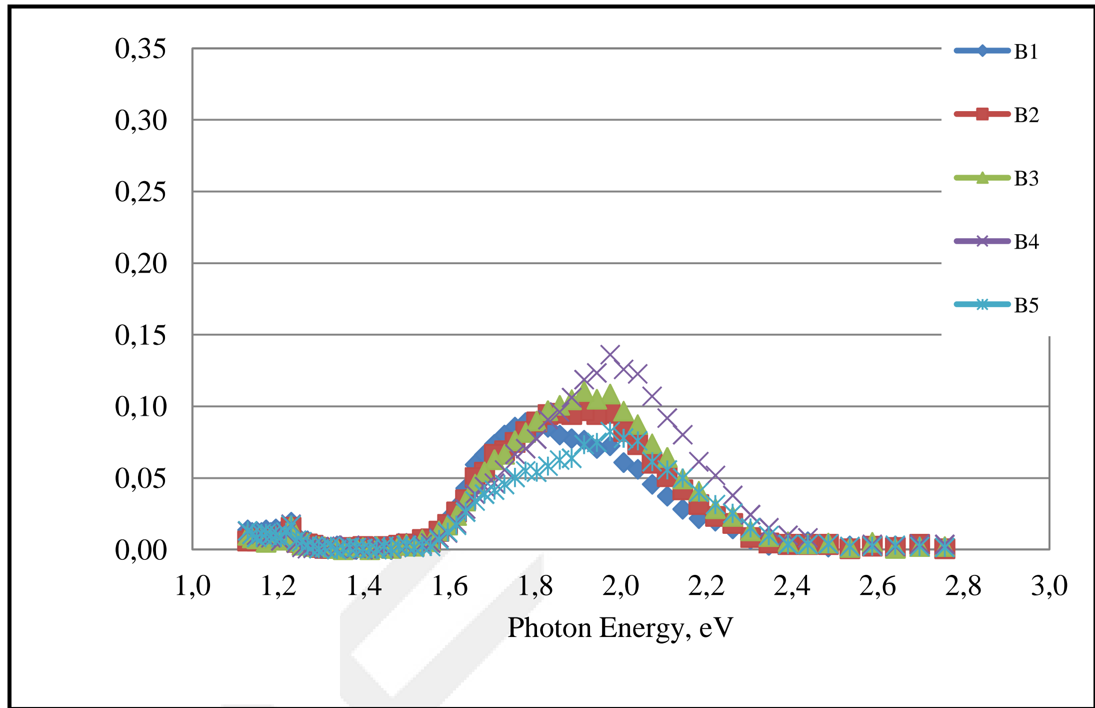

Figure 4. 68 Photoluminescence spectra of samples from B1 to B5

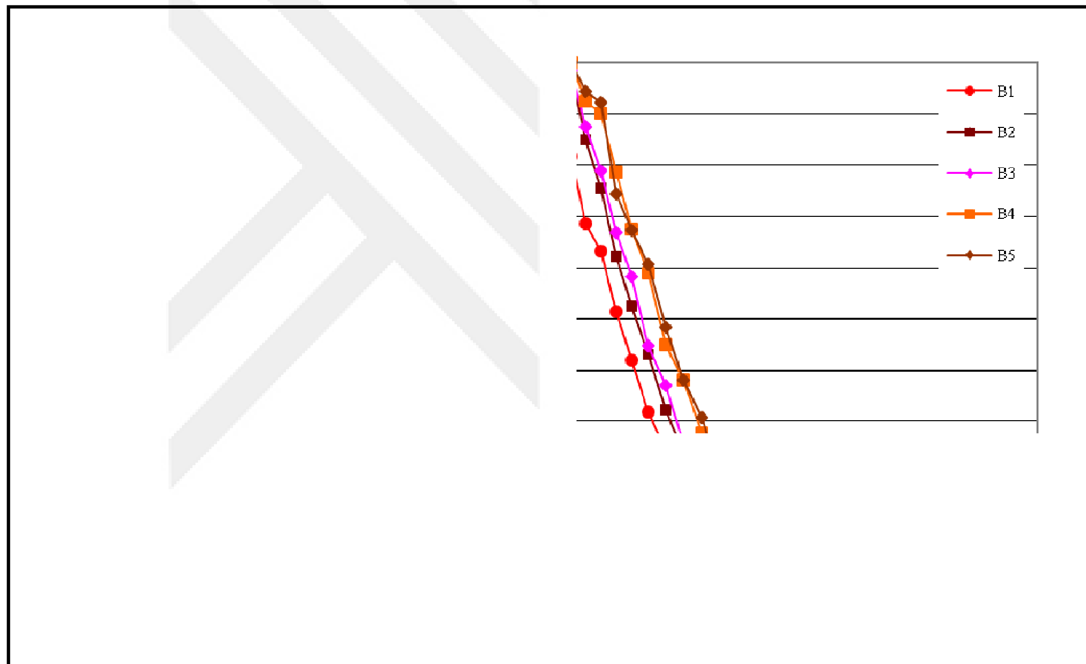

Figure 4. 69 Normalized photoluminescence spectra of samples from B1 to B5

Table 4. 22. Diameter values calculated using photoluminescence parameters

Sample name	Anodization time, min	Energy at maximum PL intensity (I_{PLmax}), eV	Diameter values calculated from PL parameters, nm
B1	15	1.78	3.8
B2	30	1.91	3.2
B3	45	1.91	3.2
B4	60	1.98	3.0
B5	75	1.98	3.0

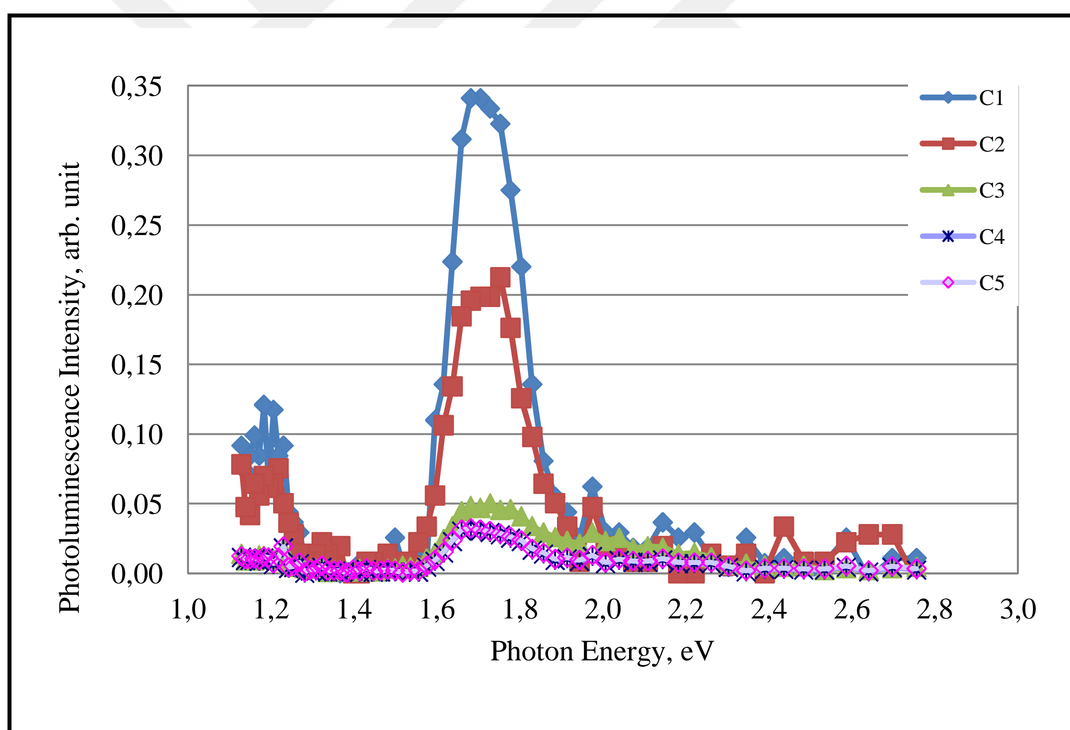

Figure 4. 70 Photoluminescence spectra of samples from C1 to C5

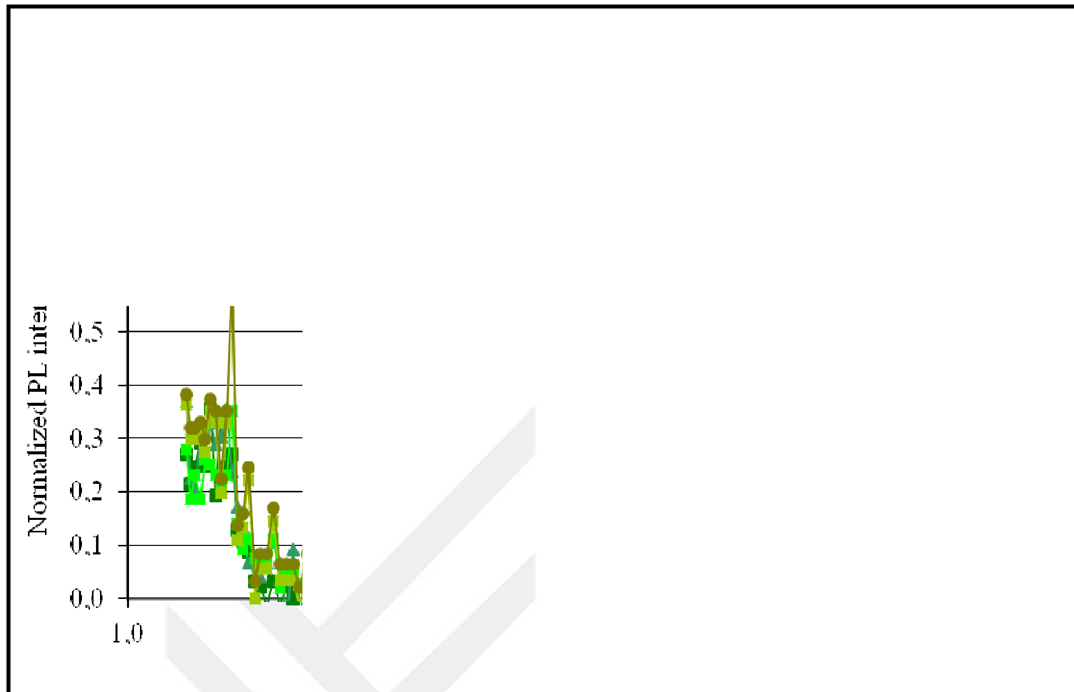

Figure 4. 71 Normalized photoluminescence spectra of samples from C1 to C5

Table 4. 23. Diameter values calculated using photoluminescence parameters

Sample name	Anodization time, min	Energy at maximum PL intensity (I), eV	Diameter values calculated from PL parameters, nm
C1	15	1.68	4.3
C2	30	1.75	3.9
C3	45	1.73	4.1
C4	60	1.68	4.3
C5	75	1.68	4.3

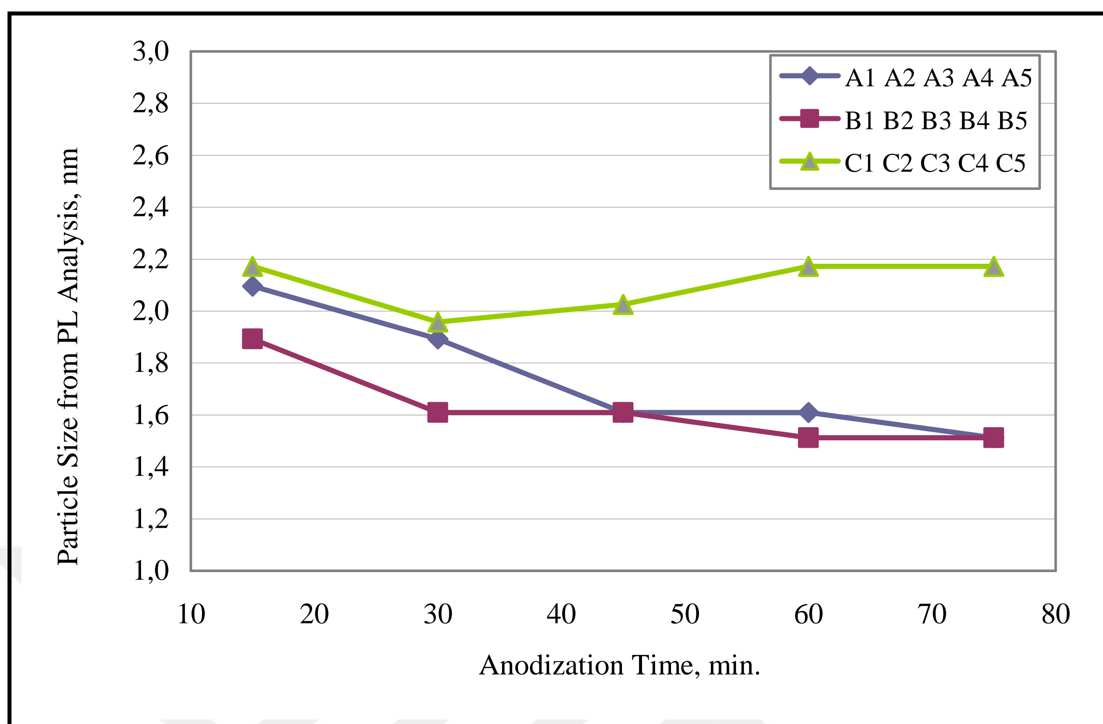

Figure 4. 72 Anodization time versus particle size calculated from photoluminescence parameters

Shift in the peak of the photon energy was observed which means that photoluminescence wavelength can be tuned by changing the formation conditions such as anodisation current density, anodisation time, and concentration of HF in the anodisation solution.

Decreasing HF concentration leads to decrease in the maximum photon energy for all durations of the anodization time. Increasing anodization time was resulted an increase in the photon energies in set-A and set-B series which have granular structure.

In set-A samples, as the anodization time increased through 15 minutes to 75 minutes, an increase in photon energies was observed. These samples show a similar surface structure regarding scanning electron microscope images.

In set-B samples, as the anodization time increased through 15 minutes to 75 minutes, photon energies were also increased. These five samples show a dissimilar surface structure regarding scanning electron microscope images.

In set-C samples, maximum photon energy occurs at the anodization time of 30 minutes, after that photon energy tends to decrease. These samples show micrometer sized regular pore arrays which are dissimilar surface structure with respect to A- and B-series samples regarding scanning electron microscope images.

5. CONCLUSION

It was shown that the image processing of SEM images developed in this work was successful at determining and sizing surface features. Comparison of Raman spectra of all the samples with the Raman spectrum of crystalline silicon showed a red shift of the optical phonon mode after porous silicon formation, this indicates the formation of nanocrystallites which causes phonon confinement effects. An increase in Raman spectral intensity was reliable evidence for the development of silicon nanocrystals during anodisation. Raman spectral red shifts were found to provide data which was reliable enough to compute sub-surface SNC dimensions. The SNC diameter within the NPS sensor region increases with anodisation time up until 60 minutes, at longer anodisation times the diameter suddenly decreases. Both SEM image processing and Raman spectral determinations exhibit the same trend with a high degree of correlation; demonstrating that both surface and sub-surface SNC exhibit the same behaviour.

The SEM images show that the SNC form as uniform spheres of similar dimension to the nanopores in-between them. This can only occur when the silicon crystal is dissolved by HF and allowed to re-crystallise as nanocrystals; the permeance time of anodisation allows the nanocrystals time to grow. Thus, longer anodisation times are associated with larger diameter SNC. However, after 60 minutes, the SNC diameter decrease of sample A5 corresponds to a limiting mechanism for the nanocrystal growth rate. This may be caused when a higher mass of chemically dissolved silicon is carried away by diffusion of HF acid; since the sub-surface NPS layer deepens with anodisation time also. This may start to limit the nanocrystal growth rate, but causing much larger pores. This seems to be borne out by the capacitance measurements also. Sample A3 was the most sensitive to changes in relative humidity (74 $nF\%.rh^{-1}$), followed closely by sample A1. However, sample A1 displayed the most linear capacitance response. It was found that a lower anodisation time resulted in a more reliable mechanical structure and smaller pore dimensions.

Raman and SEM trends with increasing anodisation time correlated within 0.98, showing the robustness of Raman analysis. The results show that nanocrystallite sizes on the surface and within the deeper layers increase with anodization time, reaching a maximum value at 60 minutes, and then decreasing. The decrease of diameter values after 60 minutes can be

explained by Ostwald ripening, where a longer permanence time of silicon in HF solution results in larger diameter crystals at the expense of smaller ones. However, as the anodized silicon layer gets thicker, diffusion of HF acid may start to limit the growth of the crystals because of diffusion of HF into the increasingly deeper nanopores.

However, the magnitudes of the crystal sizes detected are different. The difference in granule sizes computed from MATLAB and Raman spectra is a consequence of different resolution values of two characterization techniques: 10 nm for SEM, and 1 nm for Raman spectroscopy. In addition, Raman characterization has a probing volume of 2 μm^3, and together with the model used in this paper, changes in nanocrystallite diameters of 1 nm could be detected. Image processing has also limiting aspects arising from the method chosen to determine the diameter of granular islands. During image processing, edges of the granular islands have to be enhanced in order to specify the edges of the granular islands which cause deterioration of inner structures of the granular islands. This will also limit the detection of granular islands smaller than 10 nm.

This difference between the two techniques allows the Raman spectra to detect much smaller nanocrystalline sizes (down to 1 nm) within a specified volume of the samples, whilst the SEM technique detected much larger (10 nm or greater) nanocrystalline on the surface due to its resolution limit and method used during image processing of SEM images of the samples.

The image processing techniques is only capable of determining spherical shapes with well defined edges. The differences in diameter values found from MATLAB analysis (24-30 nm), and in Raman spectra graphs (3-6 nm) were mainly due to different anodization times (15 min., 30 min., 45 min., 60 min., and 75 min.) of the silicon samples while other parameters including anodization current density and anodization solution concentration kept constant as 5 $mA \cdot cm^{-2}$ and 1:1 volume per volume (v/v) mixture of hydrofluoric (HF) acid 48 wt. % in H_2O and ethanol (C_2H_5OH) respectively. Anodization times and the corresponding thickness of porous silicon structures stated that as anodization time increased thickness of porous silicon structure increased.

SEM images of set-A, B1, and B2 samples showed that they have nanometer sized granular type structure, so both Raman and PL spectra respond. Raman spectra of samples (A1, A2, A3, A4, A5, B1, and B2) having granular structure introduce a red shift which is caused as a result of quantum confinement in the porous silicon structure. Photoluminescence (PL) spectra obtained from set-A series samples also give evidence of the quantum confinement due to nanometer sized structure inside the set-A series samples. They have photon energies at maximum PL intensity ranging from 1.71 eV (728.2 nm) to 1.98 eV (628.7 nm). However, the remaining B3, B4, B5, and set-C samples have micrometer sized holes inside the structure as seen from SEM images, give no response to Raman spectroscopy, but do give PL spectra. It is possible that PL spectroscopy gives average PL spectra over all of the surface structure (including silicon nanocrystallite granules and pores). In PL spectra measurements a UV lamp of much lower intensity than the Raman laser was used, and all the sample area was illuminated meaning the intensity was even lower for PL spectra of the sample. However, in Raman measurements all the laser beam of area 2 μm^2 makes a contribution to the Raman spectra. Raman spectroscopy compared with PL spectroscopy penetrates much deeper, but it measures less volume meaning less structure, so Raman spectra is not observed for structures having micrometer sized pores.

PL and Raman spectroscopy measurements were taken at different excitation wavelengths resulting different penetration depths in porous silicon structure. PL measurements were carried out at an excitation wavelength of 366 nm which have emission from 728 nm to 628 nm. While Raman spectroscopy measurements were carried out at excitation wavelength of 514 nm and emit radiation from 526.6 nm to 527.2 nm. Therefore any discrepancies from Raman and PL spectra could be attributed to the different penetration depths and different mechanisms of the two techniques.

Photoluminescence spectra of the porous silicon samples give confirmation that the structure of the samples has nanometer sized silicon crystallites. After SEM and Raman spectra measurements, it can be concluded that the structure contains nanometer sized silicon crystallites. In set-A samples both Raman and PL spectra were found to be in good agreement in terms of the diameter values calculated from both spectral parameters. In set-B and set-C samples which have micrometer sized regular pore arrays in the structure did

not show Raman wavenumber shift but they exhibit PL spectra. It was easily seen from the SEM images of these samples that although they have micrometer sized pores, the remaining structure (pore walls and area in between pores) composed of nanometer sized granular islands which exhibits room temperature PL. It is concluded that Raman spectroscopy together with other techniques such as SEM or PL spectroscopy is sufficient to determine that the structure contains nanometer sized granules.

It is concluded that Raman and photoluminescence spectroscopy can placed by capacitance measurements to characterize the structure of porous silicon which is suitable for humidity sensing, and its long term stability. However, PL spectroscopy and its interaction with the porous silicon nanocrystallites must be studied in more detail.

Raman spectroscopy is an indirect method which can resolve structures from 1 nm to 100 nm, but is also capable of probing much deeper below the surface, while SEM can only probe surface area. In images obtained from SEM, 25 nm to 40 nm diameter granular islands are composed of tiny islands having smaller diameters. Their cross section images show that the diameter of the granular islands decreases from the surface down to the bottom of the porous structure. A variation in pore size diameter values is usual in porous silicon structures, since there are basically two independent formation mechanisms which may coexist simultaneously. This results in a superposition of structures of nanometer to micrometer sized pores. From the results of Raman spectroscopy and SEM the pores were determined to be micropores and nanopores, the latter of dimensions 3-6 nm to 26-32 nm, respectively. This matches the ideal pore dimensions ranging from 1 nm to 40 nm determined from the Kelvin equation for humidity sensing in the range 20 %rh to 95 %rh. Whereas Raman analysis is a volume detection technique and can detect structures down to 1 nm resolution, SEM images have a resolution of 10 nm or greater and can probe only a surface area of approximately 1μm^2. Image processing also has limiting aspects since edges of the granular islands have to be enhanced to the detriment of smaller structures.

Enhancement of the Raman spectra intensity due to nanometer sized crystalline silicon inside the structure of anodized silicon samples was also observed by SEM images. It was supported with the thickness of the porous silicon structures obtained from the cross section SEM images. As the NP structure below the sensor surface deepened with

anodisation time, the Raman spectral intensities increased in sympathy with correlation value of 0.96. This implies that an increasing number of nanocrystallites is being synthesised. The capacitance, surprisingly, does not follow this trend. The only explanation is that although more and larger nanocrystals are produced, the nanopores are blocked with water droplets at the top, preventing further droplets entering; thus, the capacitance drops off. This is important to study further because it indicates a limiting mechanism for humidity sensing.

A parallel plate model with three layers and multiple series capacitances per layer was proposed in this work and could simulate the variation in capacitance with relative humidity of SNP sensors.

The response times for reaching 63% of the step humidity function are extended if the nanopore sizes are too small. This effect deteriorates six fold for step decreases, since it is much harder for a drying gas to reach the inner nanopore structure. Samples A5 and A3 respond fastest to step increase in humidity at $3.1 s \cdot \%rh^{-1}$; their responses are only slightly retarded for step decreases. This makes their structures suitable for fast response humidity sensors.

Thus, a lower anodisation time resulted in a more reliable mechanical structure and smaller pore dimensions.

Mechanical degradation gauged through decrease in capacitance over 3 months ranged from ± 4.0 nF from 20 %rh to 95 %rh. Samples A1 and A3 exhibited a much better mechanical degradation than sample A5. This shows that after 60 minutes of anodization, the resulting SNP structure of the sensor is inherently unstable, making it unsuitable as a RH sensor. Both A1 and A3 had the best mechanical stability, although A3 was about 11% more sensitive, but with a non-linear response.

Hysteresis results showed the greatest hysteresis to occur at 95 %rh. A1 had the least hysteresis at 3.6 % and the maximum value is calculated to be 4.2 nF (4.6 %) for sample A5. Thus, with the smallest average SNC size (and hence nanopore), sample A1 appears to contain the best structure, displaying adequate sensitivity, the most linear response, the

least hysteresis and a robust mechanical structure. The only disadvantage is that response time for step decreases in humidity is on average four times worse than the other structures; this may be improved by anodisation procedures that slightly increase this pore diameter to ≤ 5 nm, since sample A2 has the next lowest pore diameter at 5.5 nm. The average dimensions of surface SNC size are 25 nm as determined by SEM; Raman analysis shows that this corresponds to an average sub-surface pore diameter of 4.5 nm.

Capacitance results show that relative humidity sensor A4 having nanocrystalline structure with surface nanocrystallite dimensions of 29 nm (due to SEM) and 6.2 nm (due to Raman), produce the best sample sensitivity of 0.74 $nF.rh^{-1}$. It has only moderate mechanical deterioration as calculated from capacitance changes over three months and Raman peak intensity change over this time.

It was found that the capacitance value does increase with RH, with samples A1, A3 and A4, providing the most linear sensor elements. The increase in nanocrystal and so nanopore size with anodisation time observed for Raman and SEM and may also explain the decrease in sensitivity for sample A5, as due to its decreased nanopore size.

Dielectric properties which gauge mechanical structure of porous silicon layers are presented. The sensitivity of the sensors was calculated as 0.66 $\%rh^{-1}$, 0.74 $\%rh^{-1}$, 0.45 $\%rh^{-1}$ in the range from 20 %rh to 95 %rh at 23 °C. The normalized percentage capacitance values were also calculated as 4.93 % rh^{-1}, 7.09 % rh^{-1}, 91.78 % rh^{-1} in the range from 20 %rh to 95 %rh at 23 °C. The capacitance measurements were carried out at 1 kHz.

A study of deterioration in the NPS structure over three months showed that the range of deviation in the measured capacitance values over three months was ± 4.0 nF from 20 %rh to 95 %rh. Sample A1 provided the most mechanically stable structure due to the fact it was subjected to anodization for the least time of 15 minutes. Sample A5 cannot be utilised as it has a 22 % change in Raman intensity, and the lowest sensitivity value compared with the remaining sensors over three months. Capacitance results show that relative humidity sensor A4 having nanocrystalline structure with surface nanocrystallite dimensions of 29 nm (due to SEM) and 6.2 nm (due to Raman), produce the best sample sensitivity of 0.74

nF.rh^{-1}. It has only moderate mechanical deterioration as calculated from capacitance changes over three months and Raman peak intensity change over this time.

Considering all the factors it appears that a smaller pore size produced over a shorter anodisation time produces the best silicon nanoporous sensor, since A1 performed the best over all three parameters studied in this work; linearity, sensitivity, and mechanical stability.

Development of more ordered porous silicon formation by template transfer technology/ photolithography is essential to apply the immense sensing potential of porous silicon for commercial purposes.

6. REFERENCES

1. Wiederhold, P. R., *Water Vapor Measurement Methods and Instrumentation*, Marcel Dekker, Inc., New York, 1997.
2. http://www.warensortiment.de/technische-daten/aspirations-psychrometer-pce-apa1.htm.
3. http://www.michell.com/us/technology/chilled-mirror.htm.
4. Wade Jr., L. G., *Organic Chemistry*, Prentice Hall, NJ, 2001.
5. Chen, Z., Lu, C., "Humidity Sensors A Review of Material and Mechanisms", *Sensor Letters*, Vol. 3, pp. 274-295, 2005.
6. Lee, C. W., Rhee, H. W., Gong, M. S., "Humidity Sensitive Properties of Copolymers Containing Phosphonium Salts", *Synthetic Metals*, Vol. 106, No. 3, pp. 177-182, 1999.
7. Lee, C. W., Gong, M. S., "Resistive Humidity Sensor Using Phosphonium Salt-Containing Polyelectrolytes Based on the Mutually Cross-linkable Copolymers" *Macromolecular Research*, Vol. 11, No. 5, pp. 322-327, 2003.
8. Gong, M. S., Park, J. S., Lee, M. H., Rhee, H. W., "Humidity Sensor Using Cross-Linked Polyelectrolyte Prepared From Mutually Reactive Copolymers Containing Phosphonium Salt", *Sensors and Actuators B: Chemical*, Vol. 86, pp. 160–167, 2002.
9. Gupta, N., Sharma, S., Mir, I. A., Kumar, D., "Conductive Polymer-Based Humidity Sensors", *Journal of Scientific and Industrial Research*, Vol. 65, pp. 549-557, 2006.
10. Gerlach, G., Sager, K., "A Piezoresistive Humidity Sensor", *Sensors and Actuators A: Physical*, Vol. 43, Issues 1–3, pp. 181-184, 1994.
11. Buchhold, R., Nakladal, A., Gerlach, G., Neumann, P., "Design Studies on Piezoresistive Humidity Sensors", *Sensors and Actuators B: Chemical*, Vol. 53, Issues 1–2, pp. 1–7, 1998.
12. Tashtoush, N. M., Cheeke, J. D. N., Eddy, N., "Surface Acoustic Wave Humidity Sensor Based on a Thin PolyXIO Film", *Sensors and Actuators B: Chemical*, Vol. 49, Isuue 3, pp. 218-225, 1998.
13. Penza, M., Cassano, G., "Relative Humidity Sensing by PVA-Coated Dual Resonator SAW Oscillator", *Sensors and Actuators B: Chemical*, Vol. 68, Issues 1-3, pp. 300-306, 2000.

14. Ippolito, S. J., Ponzoni, A., Zadeh, K. K., Wlodarski, W., Comini, E., Faglia G., Sberveglieri, G., "Layered WO3/ZnO/36° LiTaO3 SAW Gas Sensor Sensitive Towards Ethanol Vapour and Humidity", *Sensors and Actuators B: Chemical*, Vol. 117, Issue 2, pp. 442-450, 2006.
15. Wu, T. T., Chen Y. Y., Chou, T. H., "A High Sensitivity Nanomaterial Based SAW Humidity Sensor", *Journal of Physics D: Applied Physics*, Vol. 41, No. 8, p. 085101, 2008.
16. Sheng, L., Dajing, C., Yuquan, C., "A Surface Acoustic Wave Humidity Sensor with High Sensitivity Based on Electrospun MWCNT/Nafion Nanofiber Films", *Nanotechnology*, Vol. 22, No. 26, p. 265504, 2011.
17. Ramakrisnan, N., Vamsi, T., Khan, A., Nemade, H. B., Palathinkal, R. P., "Humidity Sensor Using NIPAAM Nanogel as Sensing Medium in SAW Devices", *International Journal of Nanoscience*, Vol. 1, No. 1, pp. 1–4, 2007.
18. http://www.sensorwiki.org/doku.php/sensors/hygrometer; http://www.sensorsmag.com/sensors/humidity-moisture/choosing-a-humidity-sensor-a-review-three-technologies-840.
19. Farahani, H., Wagiran, R., Hamidon, M. N., "Humidity Sensors Principle, Mechanism, and Fabrication Technologies: A Comprehensive Review", *Sensors*, Vol. 14, pp. 7881-7939, 2014.
20. Coran, A. Y., "Chemistry of the Vulcanization and Protection of Elastomers: A Review of the Achievements", *Journal of Applied Polymer Science*, Vol. 87, Issue 1, pp. 24-30, 2003.
21. Sakai, Y., Sadaoka, Y., Matsuguchi, M., "Humidity Sensors Based on Polymer Thin Films", *Sensors and Actuators B: Chemical*, Vol. 35, Issues 1-3, pp. 85-90, 1996.
22. Gong, M. S., Lee, C. W., Rhee, H. W., "Humidity Sensor Using Cross-Linked Copolymers Containing Viologen Moiety", *Sensors and Actuators B: Chemical*, Vol. 73, Issues 2-3, pp. 185-191, 2001.
23. Park, S.H., Park, J. S., Lee, C. W., Gong, M. S., "Humidity Sensor Using Gel Polyelectrolyte Prepared From Mutually Reactive Copolymers", *Sensors and Actuators B: Chemical*, Vol. 86, Issue 1, pp. 68-74, 2002.
24. Lee, C. W., Kim, O. Y., Gong, M. S., "Humidity-Sensitive Properties of New Polyelectrolytes Based on the Copolymers Containing Phosphonium Salt and

Phosphine Function", *Journal of Applied Polymer Science*, Vol. 89, Issue 4, pp. 1062-1070, 2003.

25. Macdiarmid, A. G., "Conducting polymers: What does the future hold?", *Synthetic Metals*, Vol. 21, Issues 1-3, pp. 79–83, 1987.
26. Bredas, J. L., Silbey, R., *Conjugated Polymers*, Kluwer Academic Publishers, The Netherlands, 1991.
27. Munn, R. W., Miniewicz, A., Kuchta, B., *Electrical and Related Properties of Organic Solids*, Kluwer Academic Publishers, Netherlands, 1997.
28. Schopf, G., Kobmehl, G., *Polythiophenes - Electrically Conductive Polymers*, Springer, Berlin, 1997.
29. Nalwa, E. H. S., *Handbook of Organic Conductive Molecules and Polymers*, Wiley and Sons, NJ, 1997.
30. Braun, D., Heeger, A. J., "Visible Light Emission from Semiconducting Polymer Diodes", *Applied Physics Letters*, Vol. 58, pp. 1982-1984, 1991.
31. Liang, Y., Wu, Y., Feng, D., Tsai, S. T., Son, H. J., Li, G., Yu, L., "Development of New Semiconducting Polymers for High Performance Solar Cells", *Journal of the American Chemical Society*, Vol 131, No. 1 , pp.56-57, 2009.
32. Muccini, M., "A Bright Future for Organic Field-Effect Transistors", *Nature Materials*, Vol. 5, pp. 605-613, 2006.
33. Bearzotti, A., "Fast Humidity Response of a Metal Halide-Doped Novel Polymer", *Sensors and Actuators B: Chemical*, Vol. 7, Issues 1-3, pp. 451-454, 1992.
34. Shah, H. V., Hanson, E. L., Arbuckle-Keil, G. A., "Vapor-Phase Fuming Sulfuric Acid-Doped Poly(P-Phenylene Vinylene) as a Potential Humidity Sensor", *Journal of Electrochemical Society*, Vol. 148, Issue 9, pp. H120-H127, 2001.
35. McGovern, S. T., Spinks, G. M., Wallace, G. G., "Micro-Humidity Sensors Based on a Processable Polyaniline Blend", *Sensors and Actuators B: Chemical*, Vol. 107, pp. 657-665, 2005.
36. Angelopoulos, M., Ray, A., Macdiarmid, A. G., "Polyaniline: Processability From Aqueous Solutions and Effect of Water Vapor on Conductivity", *Synthetic Metals*, Vol. 21, Issues 1–3, pp. 21–30, 1987.
37. Nechtschein, M., Santier, C., Travers, J.P., Chroboczek, J., Alix, A., Ripert, M., "Water Effects in Polyaniline: NMR and Transport Properties", *Synthetic Metals*, Vol. 18, Issues 1–3, pp. 311–316, 1987.

38. Travers, J. P., Nechtschein, M., “Water Effects in Polyaniline: A New Conduction Process”, *Synthetic Metals*, Vol. 21, Issues 1–3, pp. 135–141, 1987.

39. Ogura, K., Tonosaki, T., Shiigi, H., “AC Impedance Spectroscopy of Humidity Sensor Using Poly(O-Phenylenediamine)/Poly(Vinyl Alcohol) Composite Film”, *Journal of Electrochemical Society*, Vol. 148, Issue 3, pp. H21-H27, 2001.

40. Tonosaki, T., Oho, T., Isomura, K., Ogura, K., “Effect of the Protonation Level of Poly(O-Phenylenediamine) (PoPD) on the AC Impedance of Humidity-Sensitive PoPD/poly(vinyl alcohol) Composite Film”, *Journal of Electroanalytical Chemistry*, Vol. 520, Issues 1-2, pp. 89-93, 2002.

41. Ogura, K., Shiigi, H., Nakayama, M., Ogawa, A., “Thermal Properties of Poly(anthranilic acid) (PANA) and Humidity-Sensitive Composites Derived From Heat-Treated PANA and Poly(Vinyl Alcohol)”, *Journal of Polymer Science Part A: Polymer Chemistry*, Vol. 37, Issue 23, pp. 4458-4465, 1999.

42. Ogura, K., Patil, R. C., Shiigi, H., Tonosaki, T., Nakayama, M., “Response of Protonic Acid-Doped Poly(O-Anisidine)/Poly(Vinyl Alcohol) Composites to Relative Humidity and Role of Dopant Anions”, *Journal of Polymer Science Part A: Polymer Chemistry*, Vol. 38, Issue 24, pp. 4343-4352, 2000.

43. Li, Y., Yang, M., “Humidity Sensitive Properties and Sensing Mechanism of π-Conjugated Polymer P-Diethynylbenzene-Co-Propargyl Alcohol”, *Synthetic Metals*, Vol. 128, Issue 3, pp. 293-298, 2002.

44. Li, Y., Yang, M., “Humidity Sensitive Properties of a Novel Soluble Conjugated Copolymer: Ethynylbenzene-Co-Propargyl Alcohol”, *Sensors and Actuators B: Chemical*, Vol. 85, Issues 1-2, pp. 73-78, 2002.

45. Sakai, Y., Sadaoka, Y., Matsuguchi, M., “Humidity Sensors Based on Polymer Thin Films”, *Sensors and Actuators B: Chemical*, Vol. 35, Issues 1-3, pp. 85-90, 1996.

46. Harrey, P. M., Ramsey, B. J., Evans, P. S. A., Harrison, D. J., “Capacitive-Type Humidity Sensors Fabricated Using the Offset Lithographic Printing Process”, *Sensors and Actuators B: Chemical*, Vol. 87, Issue 2, pp. 226-232, 2002.

47. Ralston, A. R. K., Klein, C. F., Thoma, P. E., Denton, D. D., “A Model for the Relative Environmental Stability of a Series of Polyimide Capacitance Humidity Sensors”, *Sensors and Actuators B: Chemical*, Vol. 34, Issues 1-3, pp. 343-348, 1996.

48. Dokmeci, M., Najafi, K., “A High-Sensitivity Polyimide Capacitive Relative Humidity Sensor for Monitoring Anodically Bonded Hermetic Micropackages”, *Journal of Microelectromechanical Systems*, Vol. 10, Issue 2, pp. 197-204, 2001.

49. Ingram, J. M., Greb, M., Nicholson, J. A., W. Fountain, A., “Polymeric Humidity Sensor Based on Laser Carbonized Polyimide Substrate”, *Sensors and Actuators B: Chemical*, Vol. 96, Issues 1–2, pp. 283–289, 2003.

50. Grange, H., Bieth, C., Boucher, H., Delapiere, G., “A Capacitive Humidity Sensor with Every Fast Response Time and Very Low Hysteresis”, *Sensors and Actuators*, Vol. 12, Issue 3, pp. 291–296, 1987.

51. Ducéré, V., Bernès, A., Lacabanne, C., “A Capacitive Humidity Sensor Using Cross-Linked Cellulose Acetate Butyrate”, *Sensors and Actuators B: Chemical*, Vol. 106, Issue 1, pp. 331-334, 2005.

52. Romana, C., Bodea, O., Prodana, N., Levia, A., Cordosa, E., Manoviciub I., “A Capacitive-Type Humidity Sensor Using Crosslinked Poly(Methyl Methacrylate-Co-(2 Hydroxypropyl)-Methacrylate)”, *Sensors and Actuators B: Chemical*, Vol. 25, Issues 1-3, pp. 710-713, 1995.

53. Jia, S., Lia, Y., Yanga, M., “Gas Sensing Properties of a Composite Composed of Electrospun Poly(Methyl Methacrylate) Nanofibers and in Situ Polymerized Polyaniline”, *Sensors and Actuators B: Chemical*, Vol. 133, Issue 2, pp. 644–649, 2008.

54. Matsuguchi, M., Sadaoka, Y., Nuwa, Y., Shinmoto, M., Sakai, Y., Kuroiwa, T., “Capacitive□Type Humidity Sensors Using Polymerized Vinyl Carboxylate”, The Journal of the Electrochemical Society, Vol. 141, Issue 3, pp. 614-618, 1994.

55. Reddy, A. S. G., Narakathua, B. B., Atashbara, M.Z., Rebrosb, M., Rebrosovab, E., Joyce, M.K. “Fully Printed Flexible Humidity Sensor”, Procedia Engineering, Vol. 25, pp. 120-123, 2011.

56. Matsuguchi, M., Umeda, S., Sadaoka, Y., Sakai, Y., “Characterization of Polymers for a Capacitive-Type Humidity Sensor Based on Water Sorption Behavior”, *Sensors and Actuators B: Chemical*, Vol. 49, pp. 179-185, 1998.

57. Matsuguchi, M., M. Shinmoto, Y. Sadaoka, T. Kuroiw, Y. Sakai, “Effect of the Degree of Cross-Linking on the Characteristics of a PVCA Capacitive-Type Humidity Sensor”, *Sensors and Actuators B: Chemical*, Vol. 34, pp. 349-355, 1996.

58. Matsuguchi, M., S. Kubo, Y. Sakai, “A Capacitive-type Relative Humidity Sensor Having a Double Layer Structure Consisting of a Photocrosslinked PVCA and a PMMA Film”, Electrochemistry, Vol. 67, pp. 170-174, 1999.
59. Matsuguchi, M., Y. Sadaoka, K. Nosaka, M. Ishibashi, Y. Sakai, T. Kuroiwa, A. Ito, “Effect of Sorbed Water on the Dielectric Properties of Acetylene Terminated Polyimide Resins and Their Application to a Humidity Sensor”, Journal of the Electrochemical Society, Vol. 140, pp. 825-829, 1993.
60. Liu, X., Eriksent, G. F., Leistikot, O., “A New a Water Permeability Sensor for Testing Thin Films”, Journal of Micromechanics and Microenginnering, Vol. 5, pp. 147-149, 1995.
61. Kuroiwa, T., Miyagishi, T., Ito, A., Matsuguchi, M., Sadaokab, Y., Sakai, Y., “A Thin-Film Polysulfone-Based Capacitive-Type Relative-Humidity Sensor”, *Sensors and Actuators B: Chemical*, Vol. 25, pp. 692-695, 1995.
62. Tetelin, A., Pellet, C., Laville, C., N’Kaoua G., “Fast Response Humidity Sensors for a Medical Microsystem”, *Sensors and Actuators B: Chemical*, Vol. 91, pp. 211-218, 2003.
63. F. Kraus, S. Cruz, J. Muller, “Plasmapolymerized Silicon Organic Thin Films from HMDSN for Capacitive Humidity Sensors”, *Sensors and Actuators B: Chemical*, Vol. 88, pp. 300-311, 2003.
64. Seiyama, T., Yamazoe, N., Arai, H., “Ceramic Humidity Sensors”, *Sensors and Actuators*, Vol. 4, pp. 85-96, 1983.
65. de Grotthuss, C. J. T., “Sur la Décomposition de l’eau et des Corps Qu’elle Tient en Dissolution à l’aide de l’électricité”, *Galvanique. Ann. Chim.* **LVIII**, 54-74, 1806.
66. Masuda, H., Fukuda, K., “Ordered Metal Nanohole Arrays Made by a Two-Step Replication of Honeycomb Structures of Anodic Alumina”, *Science*, Vol. 268, pp. 1466-1468, 1995.
67. Varghese, O. K., Grimes, C. A., “Metal Oxide Nanoarchitectures for Environmental Sensing”, *Journal of Nanoscience and Nanotechnology*, Vol. 3, pp. 277-293, 2003.
68. McCafferty, E., Zettlemoyer, A. C., “Adsorption of water vapour on α-Fe_2O_3”, *Discussions of the Faraday Society,* Vol. 52, pp. 239-254, 1971.
69. Krutovertsev, S. A., Tarasova, A. E., Krutovertseva, L. S., Zorin, A. V., “Integrated Multifunctional Humidity Sensor”, *Sensors and Actuators A*: Physical, Vol. 62, pp. 582-585, 1997.

70. Lin, J., Heurich, M., Obermeier, E., "Manufacture and Examination of Various Spin-on Gass Films with respect to Their Humidity-Sensitive Properties", *Sensors and Actuators B: Chemical*, Vol. 13, pp. 104-106, 1993.
71. D'Apuzzo, M., Aronne, A., Esposito, S., Pernice, P., "Sol-Gel Synthesis of Humidity-Sensitive P_2O_5-SiO_2 Amorphous Films", *Journal of Sol–Gel Science and Technology*, Vol. 17, pp. 247-254, 2000.
72. Kong, L. B., Zhang, L. Y., Yao, X., "Preparation and Properties of a Humidity Sensor Based on LiCl-Doped Porous Silica", *Journal of Material Science Letters*, Vol. 16, pp. 824-826, 1997.
73. Arshaka, K., Twomey, K., Egan, D., "A Ceramic Thick Film Humidity Sensor Based on MnZn Ferrite", *Sensors*, Vol. 2, pp. 50-61, 2002.
74. Gusmano, G., Montesperelli, G. Traversa, E., "Magnesium Aluminium Spinel Thin Film as a Humidity Sensor", *Sensors and Actuators B: Chemical*, Vol. 7, pp. 460-463, 1992.
75. Qu, W., Meyer, J. U., "Thick-Film Humidity Sensor Based on Porous Material", *Measurement Science and Technology*, Vol. 8, pp. 593-600, 1997.
76. Qu, W., Meyer, J. U., "A Novel Thick-Film Ceramic Humidity Sensor", *Sensors and Actuators B: Chemical*, Vol 40, pp. 175-182, 1997.
77. Boyle J. F., Jones, K. A., "The Effects of CO, Water Vapor and Surface Temperature on the Conductivity of a SnO_2 Gas Sensor", *Journal of Electronic Materials*, Vol. 6, pp. 717-733, 1977.
78. Advani G. N., Nanis, L., "Effects of Humidity on Hydrogen Sulfide Detection by SnO_2 Solid State Gas Sensors", *Sensors and Actuators*, Vol 2, pp. 201-206, 1981.
79. Yamazoe, N., Fuchigami, J., Kishikawa, M., Seiyama, T., "Interactions of Tin Oxide Surface with O_2, H_2O and H_2", *Surface Science*, Vol. 86, pp. 335-344, 1979.
80. Shimizu, Y., Shimabukuro, M., Arai, H., "The Sensing Mechanism in a Semiconducting Humidity Sensor with Pt Electrodes", *Journal of Electrochemical Society*, Vol. 136, Issue 12, pp. 3868-3871, 1989.
81. Mukode, S., Futata, H., "Semiconductive Humidity Sensor", *Sensors and Actuators*, Vol. 16, pp. 1-11, 1989.
82. Wang, J., Wan, H., Lin, Q., "Properties of a nanocrystalline barium titanate on silicon humidity sensor", *Measurement Science and Technology*, Vol. 14, pp. 172-175, 2003.

83. Wang, W., Virkar, A. V., "A Conductimetric Humidity Sensor Based on Proton Conducting Perovskite Oxides", *Sensors and Actuators B: Chemical*, Vol. 98, pp. 282-290, 2004.

84. Shimizu, Y., Shimabukuro, M., Arai, H., Seiyama, T., "Humidity Sensitive Characteristics of La3+ Doped and Undoped SrSnO3", *Journal of Electrochemical Society*, Vol. 136, Issue 4, pp. 1206-1210, 1989.

85. Viviani, M., Buscaglia, M. T., Buscaglia, V., Leoni, M., Nanni, P., "Barium perovskites as humidity sensing materials", *Journal of European Ceramic Society*, Vol. 21, Issues 10-11, pp. 1981-1984, 2001.

86. Holc, J., Hrovat, M., Slunecko, J., "Temperature Characteristics of Electrical Properties of (Ba, Sr)TiO_3 Thick Film Humidity Sensors", *Sensors and Actuators B: Chemical*, Vol. 26, pp 99-102, 1995.

87. Qu, W., Green, R., Austin, M., "Development of Multi-Functional Sensors in Thick-Film and Thin-Film Technology", *Measurement Science and Technology*, Vol. 11, No. 8, pp. 1111-1118, 2000.

88. Kleperis, J., Kundzins, M., Vitins, G., Eglitis, V., Vaivars, G., Lusis, A., "Gas-Sensitive Gap Formation by Laser Ablation in In2O3 Layer: Application as Humidity Sensor", *Sensors and Actuators B: Chemical*, Vol. 28, pp. 135-138, 1995.

89. Vaivars, G., Kleperis, J., Zubkans, J., Vitins, G., Liberts, G., Lusis, A., "Influence of Thin Film Coatings on the Gas Sensitivity Properties of Narrow Laser Cut Gap in In_2O_3 on Glass Substrate", *Sensors and Actuators B: Chemical*, Vol 33, pp. 173-177, 1996.

90. Arshak, K., Twomey, K., "Thin Films of In_2O_3/SiO for Humidity Sensing Applications", *Sensors*, Vol. 2, pp. 205-218, 2002.

91. Raj, A. M. E. S., Magdalane, C. M., Nagaraja, K. S., "Zinc(II) Oxide–Yttrium(III) Oxide Composite Humidity Sensor", *Physica Status Solidi (a)*, Vol. 191, Issue 1, pp. 230-234, 2002.

92. Raj, A. M. E. S., Mallika, C., Swaminathan, K., Sreedharan, O. M., Nagaraja, K. S., "Zinc(II) Oxide-Zinc(II) Molybdate Composite Humidity Sensor", *Sensors and Actuators B: Chemical*, Vol 81, pp. 229-236, 2002.

93. Bell, S., *A Beginner's Guide to Humidity Measurement*, NPL, 2011.

94. Pickering, C, Beale M I J, Collins D J, Pearson P J, Greef R., "Optical Studies of the Structure of Porous Silicon Films Formed in p-Type Degenerate and Non-Degenerate Silicon", *Journal of Physics C: Solid State Physics*, Vol. 17, pp. 6535-6552, 1984.

95. Canham, L. T., "Silicon Quantum Wire Array Fabrication by Electrochemical and Chemical Dissolution of Wafers", *Applied Physics Letters*, Vol. 57, No.10, pp. 1046-1048, 1990.

96. Gregg, S. J., Sing, K. S. W., *Adsorption, Surface Area and Porosity*, AP, 1982.

97. Uhlir, A., "Electrolytic Shaping of Germanium and Silicon", *Bell System Technical Journal*, Vol. 35, Issue 2, pp. 333-347, 1956.

98. Turner, D.R., "Electropolishing Silicon in Hydrofluoric Acid Solutions", *Journal of the Electrochemical Society*, Vol. 105, pp. 402-408, 1958.

99. Theunissen, M. J J., "Etch Channel Formation during Anodic Dissolution of n-Type Silicon in Aqueous Hydrofluoric Acid", *Journal of the Electrochemical Society*, Vol. 19, No.3, pp.351-359, 1972.

100. Bomchil, G., Halimaoui, A., Herino, R., "Porous Silicon: the Material and its Applications in Silicon-on-Insulator Technologies", *Applid Surface Science*, Vol. 41/42, pp. 604-613, 1989.

101. Santos, A. H., Bimbo, M. L., Lehto, V. P., Airaksinen, J. A., Salonen, J., Hirvonen, J., "Multifunctional Porous Silicon for Therapeutic Drug Delivery and Imaging", *Current Drug Discovery Technologies*, Vol. 8, No. 3, pp. 228-249, 2011,

102. De Stefano L., Moretti, L., Rendina, I., Rossi, A. M., "Quantitative Optical Sensing in Two-Component Mixtures Using Porous Silicon Microcavities", *Physica Status Solidi (a)*, Vol. 201, Issue 5, pp. 1011–1016, 2004.

103. Angelescu, A., Kleps, I., Mihaela, M., "Porous Silicon Matrix for Applications in Biology", *Reviews on Advanced Material Science*, Vol.5, pp. 440-449, 2003.

104. Stewart, M. P., Buriak, J. M., "Chemical and Biological Applications of Porous Silicon Technology", *Advanced Materials*, Vol. 12, No. 12, pp. 859-869, 2000.

105. Arita, Y., Sunohara, Y., "Formation and Properties of Porous Silicon Film", *Journal of the Electrochemical Society*, Vol. 124, Issue 2, pp. 285-295, 1977.

106. Unagami, T., "Formation Mechanism of Porous Silicon Layer by Anodization in HF Solution", *Journal of Electrochemical Society: Solid-State Science and Technology*, Vol. 127, No. 2, pp. 476-483, 1980.

107. Beale, M.I.J., Benjamin, J.D., Uren, M.J., Chew, N.G., Cullis, A.G., “An Experimental and Theoretical Study of the Formation and Microstructure of Porous Silicon”, *Journal of Crystal Growth*, Vol. 73, pp. 632-636, 1985.
108. Smith, R. L., S. -F. Chuang, S. D. Collins, “A Theoretical Model of the Formation Morphologies of Porous Silicon”, *Journal of Electronic Materials*, Vol. 17, Issue 6, pp 533-541, 1988
109. Zhang, X. G., S. D. Collins, R. L Smith, “Porous Silicon Formation and Electropolishing of Silicon by Anodic Polarization in HF Solution”, Journal of the Electrochemical Society, Vol. 136, Issue 5, pp. 1561-1565, 1989.
110. Smith, R. L., “Porous Silicon Morphologies and Formation Mechanism”, Sensors and Actuators A: Physical, Vol. 23, Issues 1-3, pp. 825–829, 1990.
111. Lehmann, V., Gösele, U., “Porous Silicon Formation: A Quantum Wire Effect”, *Applied Physics Letters*, Vol. 58, Issue 8, pp. 856- 1991.
112. Smith, R. L., Collins, S. D., “Porous Silicon Formation Mechanisms”, *Journal of Applied Physics*, Vol. 71, No. 8, pp. R1-R22, 1992.
113. Cullis, A. G., Canham, L. T., Calcott, P. D. J., “The Structural and Luminescence Properties of Porous Silicon”, *Journal of Applied Physics*, Vol. 82, No.3, pp. 909-965, 1997.
114. Bisi, O., Ossicini, S., Pavesi, L., “Porous Silicon: A Quantum Sponge Structure for Silicon Based Optoelectronics”, *Surface Science Reports*, Vol. 38, pp. 1-126, 2000.
115. Goryachev, D. N., Belyakov, L. V., Sreseli, O. M., “On the Mechanism of Porous Silicon Formation”, *Semiconductors*, Vol. 34, Issue 9, pp. 1090-1093, 2000.
116. Föll, H., Christophersen, M., Carstensen, J., Hasse, G., “Formation and Application of Porous Silicon”, *Materials Science and Engineering Reports*, Vol. 39, pp. 93-141, 2002.
117. Zhang, X. G., “Morphology and Formation Mechanisms of Porous Silicon”, *Journal of Electrochemical Society*, Vol. 151, Issue 1, pp. C69-C80, 2004.
118. Torres-Costa, “Application of Nanostructured Porous Silicon in the Field of Optics. A Review”, *Journal of Materials Science*, Vol. 45, Issue 11, pp. 2823-2838, 2010.
119. Feng, Z. C., Tsu, R., *Porous Silicon*, World Scientific, 1994.
120. Canham, L., *Properties of Porous Silicon*, INSPEC, 1997.

121. Amato, G., Delerue, C., VonBardeleben, H. J., *Structural and Optical Properties of Porous Silicon Nanostructures - Optoelectronic Properties of Semiconductors and Superlattices,* Vol 5, Gordon and Breach Science Publishers, 1998.

122. Lehmann¸ V., *Electrochemistry of Silicon: Instrumentation, Science, Materials and Applications*, Wiley-VCH Verlag GmbH, 2002.

123. Kumar, V., *Nanosilicon*, Elsevier, 2008.

124. Sailor, M. J., *Porous Silicon in Practice*, Wiley-VCH Verlag GmbH, 2012.

125. Sailor, M. J., Wu, E. C., "Photoluminescence-Based Sensing With Porous Silicon Films, Microparticles, and Nanoparticles", *Advanced Functional Materials*, Vol. 19, Issue 20, pp. 3195–3208, 2009.

126. Erson R. C., Muller, R. S., Tobias, C. W., "Investigations of Porous Silicon for Vapor Sensing", *Sensors and Actuators A: Physical*, Vol. 23, Issues 1–3, pp. 835–839, 1990.

127. O'Halloran, G. M., Sarro, P. M., Groeneweg, J., Trimp, P. J., French, P. J., "A Bulk Micromachined Humidity Sensor Based on Porous Silicon", *Solid State Sensors and Actuators*, Transducers '97 International Conference, Vol. 1, pp. 563-566, 1997.

128. Foucaran, A., Sorli, B., Garcia, M., Pascal-Delannoy, F., Giani, A., Boyer, A., "Porous Silicon Layer Coupled With Thermoelectric Cooler: A Humidity Sensor", *Sensors and Actuators*, Vol. 79, pp. 189-193, 2000.

129. Kim, S. J., Park, J. Y., Lee, S. H., Yi, S. H., "Humidity Sensors Using Porous Silicon Layer With Mesa Structure", *Journal of Physics D: Applied Physics*, Vol. 33, pp. 1781-1784, 2000,

130. Mai, L. H., Hoa, P. T. M., Binh, N. T., Ha, N. T. T., An, D. K., "Some Investigation Results of the Instability of Humidity Sensors Based on Alumina and Porous Silicon Materials", *Sensors and Actuators B: Chemical*, Vol. 66, pp. 63-65, 2000.

131. Rittersma, Z. M., Zaagman, W. J., Zetstra, M., Benecke, W., "A Monitoring Instrument with Capacitive Porous Silicon Humidity Sensors", *Smart Material Structure*, Vol. 9, pp. 351-356, 2000.

132. Das, J., Hossain, S. M., Chakraborty, S., Saha, H., "Role of Parasitics in Humidity Sensing by Porous Silicon", *Sensors and Actuators A: Physical*, Vol. 94, pp. 44-52, 2001.

133. Connolly, E. J., O'Halloran, G. M., Pham, H. T. M., Sarro, P. M., French, P. J., "Comparison of Porous Silicon, Porous Polysilicon and Porous Silicon Carbide as

Materials for Humidity Sensing Applications", *Sensors and Actuators A: Physical*, Vol. 99, pp. 25-30, 2002.

134. Fürjes, P., Kovács, A., Dücsö, Cs., Ádám, M., Müller B., Mescheder, U., "Porous Silicon-Based Humidity Sensor with Interdigital Electrodes and Internal Heaters", *Sensors and Actuators B: Chemical*, Vol. 95, pp. 140-144, 2003.
135. Yarkin, D. G., "Impedance of Humidity Sensitive Metal/Porous Silicon/n-Si Structures", *Sensors and Actuators A: Physical*, Vol. 107, pp. 1-6, 2003.
136. Bjorkqvist, M., Salonen, J., Paski, J., Laine, E., "Characterization of Thermally Carbonized Porous Silicon Humidity Sensor", *Sensors and Actuators A: Physical*, Vol. 112, pp. 244-247, 2004.
137. Di Francia, G., Castaldo, A., Massera, E., Nasti, I., Quercia, L., Rea, I., "A Very Sensitive Porous Silicon Based Humidity Sensor", S*ensors and Actuators B: Chemical*, Vol. 111-112, pp. 135-139, 2005.
138. Xu, Y.Y., Li, X. J., He, J. T., Hu, X., W., H. Y., "Capacitive Humidity Sensing Properties of Hydrothermally-Etched Silicon Nano-Porous Pillar Array", *Sensors and Actuators B: Chemical*, Vol. 105, pp. 219-222, 2005.
139. Bjorkqvist, M., Paski, J., Salonen, J., Lehto, V. P., "Studies on Hysteresis Reduction in Thermally Carbonized Porous Silicon Humidity Sensor", *IEEE Sensors Journal*, Vol. 6, No. 3, pp. 542-547, 2006.
140. Salonen, J., Tura, J., Björkqvist, M., Lehto, V.-P., "Sub-ppm Trace Moisture Detection with a Simple Thermally Carbonized Porous Silicon Sensor", *Sensors and Actuators B: Chemical*, Vol. 114, pp. 423-426, 2006.
141. Islam, T., Saha, H., "Study of Long-Term Drift of a Porous Silicon Humidity Sensor and Its Compensation Using ANN Technique, *Sensors and Actuators A: Physical*, Vol. 133, pp. 472-479, 2007.
142. Zhang, X. G., *Electrochemistry of Silicon and Its Oxide*, Kluwer Academic/Plenum Publishers, 2001.
143. Somashekhar, A., O'Brien, S., "Etching SiO_2 Films in Aqueous 0.49% HF", *Journal of Electrochemical Society*, Vol. 143, Issue 9, pp. 2885-2891, 1996.
144. Kolasinski, K. W., "Etching of Silicon in Fluoride Solutions", *Surface Science*, Vol. 603, pp. 1904-1911, 2009.
145. Föll, H., "Properties of Silicon-Electrolyte Junctions and Their Application to Silicon Characterization", Applied Physics A, Vol. 53, Issue 1, pp 8-19, 1991.

146. Carstensen, J., Prange, R., Föll, H., “A Model for Current-Voltage Oscillations at the Silicon Electrode and Comparison with Experimental Results”, Journal of the Electrochemical Society, Vol. 146, pp. 1134-1140, 1999.

147. Serre, C., Barret, S., Herino R., “Characterization of the Electropolishing Layer During Anodic Etching of p-Type Silicon in Aqueous HF Solutions” *Journal of the Electrochemical Society*, Vol. 141, Issue 8, pp. 2049-2053, 1994.

148. Chazalviel, J. N., Da Fonseca, C., Ozanam, F., “In Situ Infrared Study of the Oscillating Anodic Dissolution of Silicon in Fluoride Electrolytes”, *Journal of the Electrochemical Society*, Vol. 145, Issue 3, pp. 964-973, 1998.

149. Lehmann, V., “On the Origin of Electrochemical Oscillations at Silicon Electrodes”, *Journal of the Electrochemical Society*, Vol. 143, Issue 4, pp. 1313-1318, 1996.

150. Grüning, U., Yelon A., “Capillary and Van der Waals Forces and Mechanical Stability of Porous Silicon”, *Thin Solid Films*, Vol. 255, Issues 1–2, pp. 135–138, 1995.

151. Kim, H., Cho, N., “Morphological and Nanostructural Features of Porous Silicon Prepared by Electrochemical Etching”, *Nanoscale Research Letters*; Vol. 7 No. 1, pp. 408-, 2012.

152. Rouquerol, J., Avnir, D., Fairbridge, C. W., Everett, D. H., Haynes, J. H., Pernicone, N., Ramsay, J. D. F., Sing, K. S. W., Unger, K. K., “Recommendations for the Characterization of Porous Solids”, *Pure and Applied Chemistry*, Vol. 66, No. 8, pp. 1739-1758, 1994.

153. Sweryda-Krawiec, B., Cassagneau, T., Fendler, J. H., “Ultrathin Electroactive Junctions Assembled from Silicon Nanocrystallites and Polypyrrole”, *Advanced Materials*, Vol. 11, Issue 8, pp. 659–664, 1999.

154. Lehmann, V., Gösele, U., “Formation Mechanism of Microporous Silicon: Predictions and Experimental Results”, *MRS Fall Meeting. Symposium F – Microcrystalline Semiconductors–Materials Science and Devices MRS Proceedings*, Vol. 283, 1992.

155. Beale, M. I. J., Benjamin, J. D., Uren, M. J., Chew, N. G., Cullis A. G., “An Experimental and Theoretical Study of the Formation and Microstructure of Porous Silicon”, *Journal of Crystal Growth*, Vol. 73, pp. 622-636, 1985.

156. Lehmann, V., *Chapter 1: Microporous Silicon: Formation Mechanism and Preparation Method in Optical Properties of Low Dimensional Silicon Structures*, NATO ASI Series, Vol. 244, pp. 1-9, 1993.
157. Karavanskii, V. A., Kachalov, M. A., Maslov, A. P., Petrov, Yu. N., Seleznev, V. N., Shuvalov, A. O., "Morphology of Quantum Wires of Porous Silicon", *Journal of Experimental and Theoretical Physics Letters*, Vol. 57, No. 4, pp. 239-243, 1993.
158. Nakajima, A., Ohshima, Y., Itakura, T., Goto, Y., "Microstructure of Porous Silicon", *Applied Physics Letters*, Vol. 62, pp. 2631-2633, 1993.
159. Parkhutik, V., "Porous Silicon - Mechanisms of Growth and Applications", *Solid-State Electronics*, Vol. 43, pp. 1121-1141, 1999.
160. Prabakaran, R., Kesavamoorthy, R., Singh, A., "Optical and Microstructural Investigations of Porous Silicon", *Bulletin of Material Science*, Vol. 28, No. 3, pp. 219-225, 2005.
161. Du, X. W., Lu, Y. W., Kulinich, S. A., Sun, J., Yao, P., "Microporous Silicon connected with Silicon Wires", *Semiconductor Science and Technology*, Vol. 21, pp. 498-500, 2006.
162. Huang, Y. M., Zhai, B-G., Zhou, F-F., "Correlation of excitation-wavelength dependent photoluminescence with the fractal microstructures of porous silicon", *Applied Surface Science*, Vol. 254, pp. 4139-4143, 2008.
163. Lu, J., Cheng, X., Zhang, Y., Zhud, X., "Correlations of Electrochemical Behavior, Microstructure and Chemical Composition of Porous Silicon", *Electrochimica Acta*, Vol. 55, pp. 5084-5090, 2010.
164. Fronhoff, S., Marsa, M., Berger, M. G., Thönissen, M., Lüth, H., Münder, H., "An Extended Quantum Model for Porous Silicon Formation", *Journal of the Electrochemical Society*, Vol. 142, pp. 615-620, 1995.
165. Lehmann, V., Stengl, R., Luigart, A., "On the Morphology and the Electrochemical Formation Mechanism of Mesoporous Silicon", *Materials Science and Engineering B*, Vol. 69–70, pp. 11–22, 2000.
166. Ponomarev, E. A., Levy-Clement, C., "Macropore Formation on p-Type Si in Fluoride Containing Organic Electrolytes", *Electrochemical Solid-State Letters*, Vol. 1, pp. 42-45, 1998

167. Wehrspohn, R. B., Chazalviel, J.-N., Ozanam, F., “Macropore Formation in Highly Resistive p-Type Crystalline Silicon”, *Journal of Electrochemical Society*, Vol. 145, pp. 2958–2961, 1998.

168. Lehmann, V., Rönnebeck, S., “The Physics of Macropore Formation in Low-Doped p-Type Silicon”, *Journal of Electrochemical Society*, Vol. 146, pp. 2968-2975. 1999.

169. Carstensen, J., Christophersen, M., Föll, H., “Pore Formation Mechanism for the Si-HF System”, *Material Science Engineering B*, Vol. 69-70, pp. 23-30, 2000.

170. Probst, E. K., Kohl, P. A., “The Electrochemical Oxidation of Silicon and Formation of Porous Silicon in Acetonitrile”, *Journal of Electrochemical Society*, Vol. 141, pp. 1006-1013, 1994.

171. Rieger, M. M., Kohl, P. A., “Mechanism of (111) Silicon Etching in HF-Acetonitrile”, Journal of Electrochemical Society, Vol. 142, pp. 1490-1495, 1995.

172. Wehrspohn, R. B., Chazalviel, J.-N., Ozanam, F., Solomon, I., “Electrochemistry and Photoluminescence of Porous Amorphous Silicon”, *Thin Solid Films*, Vol. 297, pp. 5-8, 1997.

173. Chao, K. J., Kao, S. C., Yang, C. M., Hseu, M. S., Tsai, T. G., “Formation of High Aspect Ratio Macropore Array on p-Type Silicon”, *Electrochemical Solid-State Letters*, Vol. 3, pp. 489-492, 2000.

174. Christophersen, M., Carstensen, J., Feuerhake, A., Föll, H., “Crystal Orientation and Electrolyte Dependence for Macropore Nucleation and Stable Growth on p-Type Si”, *Material Science and Engineering B*, Vol. 69–70, pp. 194-198, 2000.

175. http://www.leica-microsystems.com/products/light-microscopes/clinical/upright-microscopes/details/product/leica-dm4000-b/

176. http://www.jeol.co.jp/en/products/list_sem.html.

177. http://caur.uga.edu/semnote1.htm.

178. MATLAB, *Image Processing Toolbox User’s Guide*, MathWorks, 2014. (http://www.mathworks.co.uk/help/pdf_doc/images/images_tb.pdf)

179. Zi, J., Büscher, H., Falter, C., Ludwig, W., Zhang, K., Xie, X., “Raman Shifts in Si Nanocrystals”, *Applied Physics Letters*, Vol. 69, pp. 200-202, 1996.

180. Faraci, G., Gibilisco, S., Russo, P., Penisi, R., “Modified Raman Confinement Model for Si Nanocrystals”, *Physical Review B*, Vol. 73, pp. 033307-1-033307-4, 2006.

181. Gupta, S. K., Jha, P. K., “Modified Phonon Confinement Model for Size Dependent Raman Shift and Linewidth of Silicon Nanocrystals”, *Solid State Communications*, Vol. 149, pp. 1989-1992, 2009.
182. Lu, J., Cheng, X., Zhang, Y., Zhu, X., “Correlations of Electrochemical Behavior, Microstructure and Chemical Composition of Porous Silicon”, *Electrochimica Acta*, Vol. 55, pp. 5084-5090, 2010.
183. http://resources.renishaw.com/en/details/invia-raman-microscopes--5866
184. http://www.horiba.com/fileadmin/uploads/Scientific/Documents/Raman/Semiconductors01.pdf
185. Richter, H., Wang, Z. P., Ley, L., “The One Phonon Raman Spectrum in Microcrystalline Silicon”, *Solid State Communications*, Vol. 39, Issue 5, pp. 625-629, 1981.
186. Cruz, M., Wang C., “Raman Response of Porous Silicon”, *Physica A: Statistical Mechanics and its Applications*, Vol. 207, Issues 1-3, pp. 168-173, 1994.
187. Raman, C. V., Krishnan, K. S., “A New Type of Secondary Radiation”, *Nature*, Vol. 121, pp. 501-502, 1928.
188. Parker, Jr, J. H., Feldman, D. W., Ashkin. M., “Raman Scattering by Silicon and Germanium”, *Physical Review*, Vol. 155, pp. 712-714, 1967.
189. Campbell, I.H., Fauchet, P.M., “The Effects of Microcrystal Size and Shape on the One Phonon Raman Spectra of Crystalline Semiconductors”, *Solid State Communications*, Vol. 58 No. 10, pp. 739-741, 1986.
190. Liu, F. M., Ren, B., Wu, J. H., Yan, J. W., Xue, X. F. W., Mao, B., Tian, Z. Q., “Enhanced-Raman Scattering from Silicon Nanoparticle Substrates”, *Chemical Physics Letters*, Vol. 382, Issues 5-6, pp. 502-507, 2003.
191. Zhong, F., Jia, Z.,”Raman Scattering Study on Pristine and Oxidized n-Type Porous Silicon”, *Physica B*, Vol. 411, pp. 77-80, 2013.
192. Kearney, S. P., Serrano, J. R., Phinney, L. M., Graham, S., Beecham, T., Abel, M. R., “Noncontact Surface Thermometry for Microsystems” LDRD Final Report, Sandia Report, SAND2006-6369, 2006.
193. Kittel, C., *Introduction to Solid State Physics*, Wiley, 2005.
194. Yu, p. Y., Cardona, M., *Fundamentals of Semiconductors, Physics and Materials Properties*, Springer, 2010.

195. Cardona, M., *Light Scattering in Solids I, Introductory Concepts*, Springer-Verlag, 1983.

196. Cardona, M., Güntherodt, G., *Light Scattering in Solids VII, Crystal-Field and Magnetic Excitations*, Springer, 2000.

197. Hamaguchi, C., *Basic Semiconductor Physics*, Springer, 2010.

198. Burstein, E., *Raman Spectroscopy of Solids*, Defense Technical Information Center, 1980.

199. Smith, J. E., Brodsky, Jr., M. H., Crowder, B. L., Nathan, M. I., Pinczuk, A., “Raman Spectra of Amorphous Si and Related Tetrahedrally Bonded Semiconductors”, *Physical Review Letters*, Vol. 26, pp. 642-645, 1971.

200. Hedley, J., Zhongxu, H., Arce-Garcia, I., Gallacher, B.J., “Mode Shape and Failure Analysis of High Frequency MEMS/NEMS Using Raman Spectroscopy”, *3rd IEEE International Conference on Nano/Micro Engineered and Molecular Systems 2008, (NEMS 2008)*, pp. 842 - 846, 2008.

201. Loudon, R., “The Raman Effect in Crystals”, *Advances in Physics*, Vol. 13, Issue 52, pp. 423-482, 1964.

202. Narayanan, S., Kalidindi, S.R., Schadler, L.S., “Determination of Unknown Stress States in Silicon Wafers Using Microlaser Raman Spectroscopy”, *Journal of Applied Physics*, Vol. 82, Issue 5, pp. 2595-2602, 1997.

203. Kaviany, M., *Heat Transfer Physics*, Cambridge University Press, 2008.

204. Madou, M. J., *Solid-State Physics, Fluidics, and Analytical Techniques in Micro- and Nanotechnology*, CRC Pres, 2011.

205. Vial, J.-C., Derrien, J., *Porous Silicon Science and Technology*, Springer-Verlag, 1995.

206. Temple, P. A., Hathaway, C. E., “Multiphonon Raman Spectrum of Silicon”, *Physical Review B*, Vol. 7, No. 8, pp. 3685-3697, 1973.

207. Bermejo, D., Cardona, M., “Raman Scattering in Pure and Hydrogenated Amorphous Germanium and Silicon”, *Journal of Non-Crystalline Solids*, Vol. 32, Issues 1–3, pp. 405-419, 1979.

208. Dresselhaus, M. S., Solid State Physics Part II Optical Properties of Solids, http://web.mit.edu/6.732/www/opt.pdf.

209. Delerue, C., Allan, G., Lannoo, M, “Theoretical Aspects of the Luminescence of Porous Silicon”, *Physical Review B*, Vol. 48, No. 15, pp. 11024-11036, 1993.

210. Delerue, C., Martin, E., Lampin, J.-F., Allan, G., Lannoo, M, “Luminescence of Silicon Crystallites”, *Journal de Physique IV*, Vol. 3, pp. 359-362, 1993.
211. Canham, L. T., Cullis, A. G., Pickering, C., Dosser, O. D., Cox, T. I., Lynch, T. P., “Luminescent Anodized Silicon Aerocrystal Networks Prepared by Supercritical Drying ”, *Nature*, Vol. 368, pp. 133-135, 1994.
212. Gole, J. L., Dudel, F. P., Grantier, D., “Origin of Porous Silicon Photoluminescence: Evidence for a Surface Bound Oxyhydride-like Emitter”, *Physical Review B*, Vol.56, No. 4, pp. 2137-2153, 1997.
213. Qin, G. G., Qin, G., “Multiple Mechanism Model for Photoluminescence from Oxidized Porous Si”, *Physica Status Solidi (A)*, Vol. 182, pp. 335-339, 2000.
214. Canham, L. T., “Luminescence Bands and their Proposed Origins In Highly Porous Silicon”, *Physica Status Solidi (A)*, Vol. 190, Issue 1, pp. 9-14, 1995.
215. Ossicini, S., Bertoni, C. M., Biagini, M., Lugli, A., Roma, G., Bisi, O., “Optical Properties of Isolated and Interacting Silicon Quantum Wires”, *Thin Solid Films*, Vol. 297, Issues 1-2, pp. 154-162, 1997.
216. Degoli, E., Luppi, M., Ossicini, S., “From Undulating Si Quantum Wires to Si Quantum Dots: A Model for Porous Silicon”, *Physica Status Solidi (A)*, Vol. 182, Issue 1, pp. 301-306, 2000.
217. Fauchet, P. M., “The Integration of Nanoscale Porous Silicon Light Emitters: Materials Science, Properties, and Integration with Electronic Circuitry”, *Journal of Luminescence*, Vol. 80, Issues 1-4, pp. 53-64, 1998.
218. Saar, A., “Photoluminescence from Silicon Nanostructures: The Mutual Role of Quantum Confinement and Surface Chemistry”, *Journal of Nanophotonics*, Vol. 3, Issue 1, pp. 032501, 2009.
219. Kayahan, E., “The Role of Surface Oxidation on Luminescence Degradation of Porous Silicon”, *Applied Surface Science*, Vol. 257, Issue 9, pp. 4311–4316, 2011.
220. Hossaina, S. M., Chakrabortya, S., Duttaa, S. K., Dasa, J., Saha, H., “Stability in Photoluminescence of Porous Silicon”, *Journal of Luminescence*, Vol. 91, pp. 195-202, 2000.
221. Gelloz, B., Loni, A., Canham, L., Koshida, N., “Luminescence of Mesoporous Silicon Powders Treated by High-Pressure Water Vapor Annealing”, *Nano Research Letters*, Vol. 7, pp. 382-383, 2012.

222. Yorikawa, H., Muramatsu, S., "Analysis of Photoluminescence from Porous Silicon: Particle Size Distribution", *Journal of Applied Physics*, Vol. 84, No. 6, pp. 3354-3358, 1998.
223. Ledoux, G., Guillois, O., Porterat, D., Reynaud, C., Huisken, F., Kohn, B., Paillard, V., "Photoluminescence Properties of Silicon Nanocrystals as a Function of Their Size", *Physical Review B*, Vol. 62, pp. 15942-15951, 2000.
224. Kim, Y., Lee, J., Kim, Y., Kim, J., "A Highly Sensitive Humidity Sensor Using A Modified Polyimide Film", *Journal of Semiconductor Technolgy and Science*, Vol. 4, pp. 128-132, 2004.
225. Y. Wang, S. Park, J. Yeow, A. Langner, F. Müller, "A Capacitive Humidity Sensor Based on Ordered Macroporous Silicon with Thin Film Surface Coating", *Sensor and Actuators B: Chemical*, Vol. 149, pp. 136-142, 2010.
226. Giancolli, D. C., *Physics for Scientists and Engineers*, 4th Edition, Pearson, p. 631, 2009.
227. Ádám, M., Mohácsy, T., Jónás, P., Dücső, C., Vázsonyi, É., Bársony, I., "CMOS Integrated Tactile Sensor Array by Porous Si Bulk Micromachining", *Sensors and Actuators A: Physical*, Vol. 142, Issue 1, pp. 192–195, 2008.
228. Dhanekar, S., Jain, S., "Porous Silicon Biosensor: Current Status", *Biosensors and Bioelectronics*, Vol. 41, pp. 54–64, 2013.
229. Harraz, F. A., "Porous Silicon Chemical Sensors and Biosensors: A Review", *Sensors and Actuators B: Chemical*, Vol. 202, pp. 897–912, 2014.
230. Weiss, S. M., Rong, G., Lawrie, J. L., "Current Status and Outlook for Silicon-Based Optical Biosensors", *Physica E: Low-dimensional Systems and Nanostructures*, Vol. 41, Issue 6, pp. 1071–1075, 2009.
231. Faivre, C., Bellet, D., "Orientation Effect of the Wafer on the Structural Properties of p^+ Type Porous Silicon Layers", *Journal of Porous Materials*, Vol. 7, pp. 357–361, 2000.
232. Grüning, U., Yelon, A., "Capillary and Van der Waals Forces and Mechanical Stability of Porous Silicon", *Thin Solid Films*, Vol. 255, pp. 135-138, 1995.
233. Bouchaour, M., Ould-Abbas, A., Diaf, N., Chabane Sari, N., "Effect of Drying on Porous Silicon", *Journal of Thermal Analysis and Calorimetry*, Vol. 76, pp. 677-684, 2004.

234. Amato, G., Brunetto, N., “Porous Silicon via Freeze Drying”, *Materials Letters*, Vol. 26, pp. 295-298, 1996.

235. Lerondel, G., Amato, G., Parisini, A., Boarino, L., “Porous Silicon Nanocracking”, *Materials Science and Engineering*, Vol. B69-70, pp. 161-166, 2000.

236. Fronhoff, St., Arens-Fischer, R., Heinrich, T., Fricke, J., Arntzen, M., Theiss, W., “Characterization of Supercritacally Dried Porous Silicon”, *Thin Solid Films*, Vol. 255, pp. 115-118, 1995.

237. Bouchaour, M., Diaf, N., Ould-Abbas, A., Benosman, M., Merad, L., Chabane Sari, N-E., “The Role of Supercritical CO_2 in the Drying of Porous Silicon”, *Revue des Energies Renouvelables*, Vol. Special ICPWE, pp. 99-102, 2003.

238. Björkqvist, M., Salonen, J., Laine, E., Niinisto, L., “Comparison of Stabiliing Treatments on Porous Silicon for Sensor Applications”, *Physica Statu Solidi (A)*, Vol. 197, No. 2, pp. 374-377, 2003.

239. Boukherroub, R., Morin, S., Wayner, D. D. M., Lockwood, D. J., “Thermal Route for Chemical Modification and Photoluminescence Stabilization of Porous Silicon” *Physica Statu Solidi (A)*, Vol. 182, pp. 117-121, 2000.

240. Buriak, J. M., Allen, M. J., “Lewis Acid Mediated Functionalization of Porous Silicon with Substituted Alkenes and Alkynes”, *Journal of American Chemical Society*, Vol. 120. No. 6, pp. 1339-1340, 1998.

241. Tuura, J., Björkqvist, M., Salonen, J., Lehto, V-P., “Electrically Isolated Thermally Carbonized Porous Silicon Layer for Humidity Sensing Purposes”, *Sensors and Actuators B*, Vol. 131, pp. 627-632, 2008.

242. Tuura, J., Björkqvist, M., Salonen, J., Lehto, V-P., “Long - Term Stability of Thermally - Carbonized Porous Silicon Humidity Sensor”, *Material Research Society Symposium Proceedings*, Vol. 876E, R8.8.1, 2005.

243. Oğuz Aytekin, S., Ince, R., Kodolbaş, A. O., “Characterization of Porous Silicon Structures Using Raman Spectroscopy and Scanning Electron Microscopy”, *Balkan Physics Letters*, Vol. 22, pp. 10-23, 2014.

244. Oğuz Aytekin, S., Ince, R., International Journal of Thermophysics, Submitted.

245. Cruz, M., Wang, C., “Raman Response of Porous Silicon”, *Physica A: Statistical Mechanics and its Applications*, Vol. 207, Issue 1, pp. 168-173, 1994.

246. Sui, Z., Leong, P. P., Herman, I. P., Higashi, G. S., Temkin, H., “Raman Analysis of Light-Emitting Porous Silicon”, *Applied Physics Letters*, Vol. 60, No 17, pp. 2086-2088, 1992.

247. Miranda, C. R. B., Baldan, M. R., Beloto, A. F., Ferreira, N. G., *Journal of Brazilian Chemical Society*, Vol 19, No. 4, pp. 769-771, 2008.

248. Ekimov, A. I., Onushchenko, A. A., *JETP Letters*, Vol. 34, pp 345-347, 1981.

APPENDIX A: MATLAB IMAGE PROCESSING CODES FOR DIAMETER DETERMINATION

MATLAB files used in diameter determination as follows;

```
%%%%%%%%%%%%%%%%%%%%%%%%%%%%%%%%%%%%%%%%%%%%%%%%%%%%%%%%%%%
%%--Granulometry based program to calculate diameter of--%%
%%--granular islands in porous silicon structure using --%%
%%--SEM images                                         --%%
%%%%%%%%%%%%%%%%%%%%%%%%%%%%%%%%%%%%%%%%%%%%%%%%%%%%%%%%%%%

im=imread('A1-22-75.png');
figure,imshow(im);title('original A1-22-75.png');
background = imopen(im,strel('disk',82));
I2 = im - background;
I3=I2(:,:,1);
I4 = imadjust(I3);
figure, imshow(I4); title('adjust');
I5 = medfilt2(I4);
figure, imshow(I5); title('medfilt');

%%------Matlab function for Granulometry---%%

for counter = 0:80;
    remain = imopen(I5, strel('disk', counter));
    int_area(counter + 1) = sum(remain(:));
end
figure, plot(int_area, 'm - *'), grid on;
title('Sum of pixel values in opened image as a function of
radius');
xlabel('radius of opening (pixels)');
ylabel('pixel value sum of opened objects (intensity)');

%%--the first derivative of the intensity surface area--%%
%%--array, which contains the size distribution of    --%%
%%--the pores in the image.                           --%%

int_area_prime= diff(int_area);
figure,plot(int_area_prime, 'm - *'), grid on;
title('Granulometry (Size Distribution) of Porous Silicon');
set(gca, 'xtick', [0 2 4 6 8 10 12 14 16 18 20 22 24 26 28 30
32 34 36 38 40 42 44 46 48 50 52 54 56 58 60 62 64 66 68 70
72 74 76 78 80]);
xlabel('radius of pores (pixels)');
ylabel('Sum of pixel values in pores as a function of
radius');

%%--The minima tell you that pores/islands in the image --%%
%%--have those radii. The more negative the minimum     --%%
%%--point, the higher the pores/islands'cumulative      --%%
%%--intensity at that radius.                           --%%
```

```
j=0;
for i=2:69
    if (int_area_prime(i-1) > int_area_prime(i)) &
(int_area_prime(i+1) > int_area_prime(i))
        j = j + 1;
        minpointindex(j) = i;
    end
end
figure, stem(minpointindex), title('radius of minimum
points');
[row col] = size(I5);
totalarea = row*col;
for k=1:j % j is the length of minpointindex
    if k==1
        temp = imopen(I5, strel('disk', minpointindex(k)));
        imtemp = I5 > temp;
        arearatio = 100*(length(find(imtemp==1)) /
totalarea);
        [label num] = bwlabel(imtemp);
        numofobjects(k) = num;
        arearatiovector(k) = arearatio;
    else
        temp1 = imopen(I5, strel('disk', minpointindex(k-
1)));
        temp2 = imopen(I5, strel('disk', minpointindex(k)));
        imtemp = temp1 > temp2;
        [label num] = bwlabel(imtemp);
        numofobjects(k) = num;
        arearatio = 100*(length(find(imtemp==1)) /
totalarea);
        arearatiovector(k) = arearatio;
    end
end

figure, stem(minpointindex,numofobjects),title('radius of
minimum points vs number of objects at that radius');
xlabel('radius of minimum radius value(pixels)');
ylabel('number of objects in image)');
figure, stem(minpointindex,arearatiovector),title('radius of
minimum points vs area ratio at that radius');
xlabel('radius of minimum radius value (pixels)');
ylabel('area ratio at that radius)');
```

```
%%--Convert grayscale image to balck-white to determine --%%
%%--porosity                                            --%%

eul = bweuler(I5,8);
im=I5(:,:,1);
figure,imshow(im); hold on;
level=graythresh(im);
imcbw=im2bw(im,level);
figure,imshow(imcbw);
white=numel(find(imcbw==1));
black=numel(find(imcbw==0));
whitepercent=100*white/(black+white);
blackpercent=100-whitepercent;

imlabel=bwlabel(imcbw);
segmentnum=max(imlabel(:));
[row col]=size(im);
totalarea=0;
minarea=row*col;
maxarea=0;
for i=1:segmentnum
    temp=imlabel(imlabel==i);
    temparea=bwarea(temp);
    if temparea<minarea
        minarea=temparea;
    end
    if temparea>maxarea
        maxarea=temparea;
    end
    totalarea=totalarea+temparea;
end
averagearea=totalarea/segmentnum;

im2=I5(:,:,1);
figure,imshow(im2); hold on;
level=graythresh(im2);
im2cbw=im2bw(im2,level);
im3=imcomplement(im2cbw);
figure,imshow(im3); hold on;

im4=imcomplement(im2);
figure,imshow(im4); hold on;

%%---------------------------------------------------------%%
%%---------------------------------------------------------%%
```